



# New morphing blade section designs and structural solutions for smart blades

## Authors:

Anargyros A. Karakalas (University of Patras), Theodore Machairas (University of Patras), Alexandros Solomou (University of Patras), Dimitrios A. Saravanos (University of Patras), Xavier Lachenal (UBristol), Paul M. Weaver (UBristol), Peter Berring (DTU), Kim Branner (DTU)

Edited by: Denja J. Lekou (CRES), Georgios Roukis (CRES), Andreas Makris (CRES)

## Deliverable 2.23

June, 2016

Agreement n.:	308974
Duration	November 2012 – October 2017
Co-ordinator:	Mr Peter Hjuler Jensen
Supported by:	EU 7th Framework Programme



The research leading to these results has received funding from the European Community's Seventh Framework Programme under grant agreement 308974

---

### PROPRIETARY RIGHTS STATEMENT

This document contains information, which is proprietary to the "INN WIND.EU" Consortium. Neither this document nor the information contained herein shall be used, duplicated or communicated by any means to any third party, in whole or in parts, except with prior written consent of the "INN WIND.EU" consortium.

---

## Document information

Document Name:	New morphing blade section designs and structural solutions for smart blades
Confidentiality Class	PU
Document Number:	D2.23
Authors:	Karakalas A., Machairas T., Solomou A., Saravanos D. (UPAT), Lachenal X., Weaver P. M. (UBRISTOL), Berring P., Branner K. (DTU)
Review:	D. J. Lekou, G. Roukis, A. Makris
Date:	29 June 2016
WP:	WP2: Lightweight Rotor
Task:	Task 2.2: Lightweight structural design

## Executive Summary

In order to achieve the primary objectives of the INNWIND project, i.e. the high performance innovative design of a beyond the state-of-the-art 10-20MW offshore wind turbine and hardware demonstrations of some of the key components, new concepts and technologies for better load control are investigated within WP2 “Lightweight rotor”. More specifically, morphing technologies along with control concepts are being investigated under Task 2.3 “Active and passive load control and alleviation (smart blades) design”, against aerodynamic compliance and requirements of the complete wind turbine system.

The stimulus of this approach arises from experimental and numerical studies in helicopter and wind turbine blade research that have shown the potential of using shape morphing in reducing blade loads. As these efforts mature from an aeroelastic and control point of view, in order to get to the next stage of applying those solutions on wind turbine systems, evaluation of the structural requirements of the various proposed concepts and quantification of their potential is required. A part of Subtask 2.2.2 “New structural concepts” of Task 2.2 “Lightweight structural design” aims to investigate the structural consequences of such concepts on the wind turbine blade.

This report includes these efforts performed within Subtask 2.2.2 towards the use of new morphing blade sections designs and the structural solutions for smartblades developed in Task 2.3. The investigations performed on the blade sections with variable geometry airfoils were designed and assessed towards compliance with structural and manufacturing processes constrains. Down selection of concept designs, based on results of analysis, to be input to Task 2.3 was also performed. It should be noted that the research performed and reported here is focused on the integration of the morphing concepts within the blade structure by means of local/global stiffness, strength and fatigue life loss, rather than cover investigations for the complete set of design requirements of smart blades such as the size of the aerodynamic control surface.

Structural solutions for the following concepts were investigated:

- Morphing blade sections with Shape Memory Alloys (SMA) by University of Patras (UPAT)
- Morphing blade sections using an elastomer of zero Poisson ratio by University of Bristol
- Morphing blade sections involving an innovative mechanism by Technical University of Denmark (DTU)

SMA are solid actuators with high power to weight ratio that can provide high stroke and thrust and are currently used in aerospace industry for morphing wing designs. In order to achieve load alleviation control by means of trailing edge deflection, UPAT investigate the implementation of SMA technology in an airfoil of the reference wind turbine (RWT). A numerical tool was developed to perform the necessary simulations and come up with an appropriate solution . Four morphing mechanisms were investigated and a downselection was performed.

University of Bristol performed design and analysis of an active morphing flap using an anisotropic core material (honeycomb) covered by carbon fiber reinforced plastic (CFRP) and polyurethane foam in order to enable large bending deformations with reduced actuation force. Actuation was achieved by a push-pull rod attached to a commercial actuator and the trailing edge, guided through the core with eyelets.

DTU performed preliminary studies of the structural consequences of active and passive mechanisms when attached on the RWT. The RWT’s airfoils were truncated while modal and buckling analyses as well as tip deflection calculations were performed.

The work performed for these three concepts is described in individual chapters in the present report. Section 2 discusses the concept using the shape memory alloys, section 3 describes the

concept using the special properties of the elastomer and section 4 presents the structural investigations on the blade that should support the innovative mechanism. The advantages and disadvantages of these concepts are discussed in the individual sections, while an overall assessment is available in the last section of the report.

The solutions using Shape Memory Alloys, as well as an elastomer of zero Poisson ratio have a quite low technological readiness level (TLR). Both are inspired through the aeronautics sector, yet there are different challenges to address when designing for wind turbine blades. The large size together with the loading of the component combined with low (or even no) maintenance during the 20-30 years of the blade service life makes fatigue of paramount importance for these solutions. Relevant to the morphing blade comprising an innovative mechanism, the focus lays into the elastic stability (buckling) of the supporting structure, i.e. the blade, which needs to be modified to properly accommodate the mechanism.

The technology readiness level (TLR) of the three solutions ranges from 4-6 for wind turbine system applications. Feasibility studies have been undertaken by looking at the complete system by numerical applications and at details of the concepts through dedicated experiments. Through the efforts performed and presented in this report an advance of this level has been achieved. For all cases the investigations have been conducted using the DTU 10MW reference wind turbine as the baseline for research activities. Due to the initial stages of the concept development, several configurations and several sensitivity studies have been performed to support the results. These are all described within the present report.

## TABLE OF CONTENTS

<b>1</b>	<b>INTRODUCTION</b> .....	<b>7</b>
<b>2</b>	<b>STRUCTURAL INVESTIGATIONS FOR NEW MORPHING BLADE SECTIONS INVOLVING SHAPE MEMORY ALLOYS (SMA)</b> .....	<b>9</b>
2.1	STATE OF THE ART AND MOTIVATION .....	9
2.2	BRIEF DESCRIPTION OF THE CONCEPT .....	10
2.2.1	<i>Anticipated PROS and CONS</i> .....	12
2.3	BASIC DESCRIPTION OF SHAPE MEMORY ALLOYS BEHAVIOUR .....	12
2.4	SHAPE MEMORY ALLOY MODELLING TOOLS .....	15
2.4.1	<i>Specialty Beam FE for The Prediction Of SMA Wire Behaviour</i> .....	15
2.4.2	<i>Large Displacement Capabilities (Geometrical Nonlinearities)</i> .....	17
2.4.3	<i>Beam Element with High Order Polynomial for Temperature Prediction</i> .....	19
2.4.4	<i>Evaluation of New Capabilities – Validations</i> .....	20
2.5	MORPHING CONCEPT .....	25
2.5.1	<i>Specifications</i> .....	25
2.6	PRELIMINARY INVESTIGATION OF MORPHING CONFIGURATIONS .....	26
2.6.1	<i>Implementation of Internal Truss Structure</i> .....	26
2.7	IMPLEMENTATION OF MORPHING MECHANISM .....	41
2.7.1	<i>Morphing Mechanism Concept 1a and 1b</i> .....	42
2.7.2	<i>Morphing Mechanism Concept 2</i> .....	43
2.7.3	<i>Morphing Mechanism Concept 3</i> .....	44
2.7.4	<i>Morphing Mechanism Concept 4</i> .....	45
2.8	DOWNSELECTED MORPHING MECHANISM .....	47
2.9	NUMERICAL SIMULATIONS OF THE DOWNSELECTED CONCEPT .....	49
2.9.1	<i>Morphing without Aerodynamic Pressure Loads</i> .....	49
2.10	CONSIDERATION OF STEADY PRESSURE LOADS ON MORPHING MECHANISM .....	65
2.10.1	<i>Compensation of Structural Stiffness Under Aerodynamic Loading</i> .....	67
2.10.2	<i>Investigation of Morphing prior to Aerodynamic Pressure Loading application</i> .....	71
2.11	SELECTION OF SKIN MATERIAL .....	75
2.12	CONCLUSIONS AND RECOMMENDATIONS .....	77
<b>3</b>	<b>STRUCTURAL INVESTIGATIONS PERFORMED OF A MORPHING FLAP DESIGNED FOR LONG FATIGUE LIFE</b> .....	<b>79</b>
3.1	STATE OF THE ART AND MOTIVATION .....	79
3.2	BRIEF DESCRIPTION OF THE CONCEPT .....	80
3.3	DESIGN AND ANALYSIS OF A MORPHING FLAP .....	81
3.3.1	<i>Influence of flap size and tip size</i> .....	81
3.4	DESIGN OF A REDUCED SCALE MORPHING FLAP .....	83
3.4.1	<i>Morphing skin design</i> .....	84
3.4.2	<i>Zero Poisson’s ratio honeycomb core</i> .....	87
3.4.3	<i>Actuator rod attachment and guides</i> .....	88
3.5	MANUFACTURE OF A REDUCED SCALE MORPHING FLAP .....	89
3.5.1	<i>CFRP skin manufacture</i> .....	89
3.5.2	<i>Morphing core manufacture</i> .....	90
3.5.3	<i>Morphing flap assembly</i> .....	92
3.6	MORPHING FLAP TESTS .....	92
3.7	CONCLUSIONS AND RECOMMENDATIONS .....	96
<b>4</b>	<b>NEW MORPHING BLADE SECTIONS INVOLVING INNOVATIVE MECHANISM</b> .....	<b>97</b>
4.1	STATE OF THE ART AND MOTIVATION .....	97

4.2	BRIEF DESCRIPTION OF THE CONCEPT .....	98
4.3	ANALYSIS OF THE CONCEPT .....	99
4.3.1	<i>Software used</i> .....	99
4.3.2	<i>Two modified versions of the reference blade</i> .....	100
4.3.3	<i>Modelling details and mesh</i> .....	100
4.3.4	<i>Load cases</i> .....	101
4.3.5	<i>Simulations</i> .....	102
4.3.6	<i>Results</i> .....	103
4.4	CONCLUSIONS AND RECOMMENDATIONS.....	113
<b>5</b>	<b>CONCLUSIONS</b> .....	<b>115</b>
<b>6</b>	<b>REFERENCES</b> .....	<b>117</b>
	APPENDIX A: .....	120
	MORPHING TRUSS CONFIGURATIONS CONSIDERED IN PRELIMINARY ANALYSIS .....	120

## 1 INTRODUCTION

Within INN WIND.EU new concepts are investigated having the ultimate goal to reduce the cost per kilowatt-hour of the produced energy. With increasing size of wind turbines, new approaches to load control are required to reduce the stresses in blades. Experimental and numerical studies in the fields of helicopter and wind turbine blade research have shown the potential of shape morphing in reducing blade loads. Morphing technologies are currently receiving significant interest from the wind turbine community due to their potential high aerodynamic efficiency, feasible construction and low weight. These technologies, along with other control concepts, are investigated under Task 2.3 of WP “Lightweight Rotor”, against aerodynamic compliance and requirements of the complete wind turbine system.

As these efforts mature from an aeroelastic and control point of view, in order to get to the next stage of applying the solutions on wind turbine systems it is of importance to evaluate the structural needs of the various proposed solutions and quantify their potential. The report includes the efforts performed within Task 2.2 “Lightweight structural design” of INN WIND.Eu work-package WP2 “Lightweight Rotor” regarding the structural solutions necessary to accommodate the requirements of smart blades developed within work-package WP2 Task 2.3 “Active and passive loads control and alleviation (smart blades) design”.

Therefore, the research performed within Task 2.2 and reported herein does not cover investigations for the complete set of design requirements of smart blades, such as aerodynamic control surface size, deflection and position for optimum effectiveness; minimum drag penalty; minimum noise generation; risk of lightning strikes; device failure, cost and power consumption as e.g. identified in [42]. Rather it focuses on answers relevant to integration within the blade structure, i.e. no loss of local/global stiffness or strength and/or fatigue life.

The purpose is to report efforts towards the use of new morphing blade section designs and the structural solutions for smart blades (developed in Task 2.3). The objective is to define, assess and demonstrate innovative concepts for lightweight rotor blades through the synergistic combination of adaptive characteristics from passive built-in geometrical couplings and active control. The investigations performed on the blade sections with variable geometry airfoils were designed and assessed towards compliance with structural constraints and manufacturing processes constraints. Down selection of design based on results of analysis (for input to Task 2.3) was also performed.

Following solutions were investigated:

- Morphing blade sections with Shape Memory Alloys (SMA) by University of Patras (UPAT)
- Morphing blade sections using an elastomer of zero Poisson ratio by University of Bristol (UBRISTOL)
- Morphing blade sections involving an innovative mechanism by Denmark University of Technology (DTU)

The work performed on these three concepts is described in individual chapters of the present report. Section 2 discusses the concept using shape memory alloys, section 3 the concept using the special properties elastomer and section 4 the structural investigations on the blade that should support the innovative mechanism. The advantages and disadvantages of these concepts are discussed in the individual sections, while an overall assessment is performed in the last section of the present report.

It should be noted that the solutions using Shape Memory Alloys, as well as an elastomer of zero Poisson ratio have a quite low technological readiness level. Both are inspired through the aeronautics sector, yet there are different challenges to address when designing for wind turbine blades. The size in addition with the loading on the component combined with low (or even no) maintenance during the 20-30 service life of the blade makes fatigue of special importance for

these solutions. Relevant to the morphing blade comprising an innovative mechanism, the focus lays into the elastic stability (buckling) of the supporting structure, i.e. the blade, which needs to be modified to accommodate the mechanism.

For all cases the investigations have been conducted with reference to the DTU 10MW reference wind turbine used as the baseline for research activities performed within INNWIND.EU. Due to the initial stages of the concept development, several configurations and several sensitivity studies have been performed to support the results. These are all described within the following chapters.

## 2 STRUCTURAL INVESTIGATIONS FOR NEW MORPHING BLADE SECTIONS INVOLVING SHAPE MEMORY ALLOYS (SMA)

In the present section the structural investigations performed by University of Patras for the new morphing blade section based on Shape Memory Alloy (SMA) actuators are described. SMA wires were used to provide the actuation forces aiming to move the trailing edge of the airfoil in both directions. Aim of this morphing airfoil section is to reduce the loads that the blade undergoes and therefore to extend its fatigue life. It must be noted that this work is the first part upon which the work performed in Task 2.3 of INNWIND.Eu project regarding the active load alleviation has been based. In the following sections the steps towards the development of the concept are described.

### 2.1 State of the Art and Motivation

Shape Memory Alloys are mainly used for actuation purposes as they are solid actuators with high power to weight ratio. This renders them adequate for use in systems where space limitations exist. Many applications of aerospace industry take advantage of these materials in order to design aircraft subsystems with higher efficiency at different regimes of the flight envelope. Such subsystems refer mainly to morphing wings which can increase the performance of the future aircraft by adapting the wing configuration to address specific flight regime requirements. Efforts on this direction have been done by many researchers. Martin et al. [13] and Kudva and Carpenter [10] have realized an unmanned combat air vehicle by integrating SMAs in a morphing wing. Barret et al. [6] introduced a pitch active SMA wing UAV with a 2m span. Nam et al. [14] used SMA spars to replace the mechanically actuated variable stiffness spar concept aiming to enhance the aeroelastic performance of the wing. Barbarino et al. [5] investigated an active wing by use of SMAs that deformed its shape to provide a bumped wing geometry. Other aircraft subsystems use also SMA actuators such as the variable geometry chevron developed by Turner et al. [19] aiming to mitigate the noise disturbance. In another effort by Mabe et al. [12] an adaptive chevron has been designed with the use of SMA beams that bend the elastic substrate to the desired configuration. The elastic energy stored at the passive part leads the structure to regain its original shape upon deactivation of the SMA actuators.

The main goal of the research carried out on the wind energy field is to reduce the cost per kilowatt-hour of the produced energy. To this end, the size of the blades has been drastically increased over the last decade. The upscaling of the wind turbines entails higher towers and longer blades in order to take advantage of the faster wind speeds at greater heights. However the side effects revealed from upscaling hinder the realization of bigger wind turbine systems. The main drawback of the upscaling comes from the increased weight which causes higher loading and stresses on the wind turbine components during their function. To overcome this obstacle next generation of wind turbines adopts new approaches for load control and reduction. Research performed [3], [8], [9], [15], [20], [21] has shown that there is significant potential for load alleviation by adapting actively the blade profile at any spanwise location in response to the wind conditions. Many concepts have been developed towards this aim, using trailing edge devices such as microtabs. Microtabs are used for active control purposes as they can be deployed upon triggering, normal to the aerodynamic surface usually close to the trailing edge, changing thus the sectional camber of the blade and the flow conditions [7]. However continuously deformable trailing edges are considered to be aerodynamically more efficient for load control as they can influence lift while the flow is maintained attached to the foil. Similarly to the aerospace industry, Shape Memory Alloy actuators can be used in order to change the shape of the wind turbine trailing edge.

Few efforts have been reported developing active concepts for load control of wind turbine blades using Shape Memory Alloy actuators in the activities of the UPWind project. Quintanilla et al. [17] have developed a small-scale actuator based on Shape Memory Alloy wires able to operate on high rates aiming to control the aerodynamic loads of a blade. This actuator is designed as a beam-like structure with prestrained SMA wires on both sides of the neutral axis in order to deflect

the beam in both directions. In another effort [18] the researchers aim to design a control system for an adaptive WTB airfoil based on SMA actuators for load reduction.

Currently the research work conducted in the field of active control of the aerodynamic loads in the context of the INN WIND.Eu project, aims to design and optimize new morphing concepts for WTB sections using SMA wire actuators. The basic objectives for this activity are:

- the development of blade airfoils and sections with variable geometry capabilities, termed thereafter as morphing section configurations and
- the development of new modelling tools capable of simulating the coupled thermomechanical steady-state and time response of SMA actuators.

The proposed research on the design of morphing blade sections for WTB was organized in WP2 as follows. In WP2.2 and in the present Deliverable 2.23, the development of a morphing WTB section using Shape Memory Alloy actuators in wire form is pursued and described. Various morphing section configurations are specified, analysed numerically and optimized to achieve desirable target airfoil shapes defined by aerodynamic analyses to provide the specified ranges of variations of the lift coefficient  $C_L$  which can provide useful control and alleviation of aerodynamic loads (steady and unsteady) applied on the blade. This aerodynamic input and target shapes were provided by National Technical University of Athens (NTUA).

It is pointed out that the work presented in this deliverable is the first part of the overall work conducted by UPAT on morphing sections, and is focused on the basic morphing functionality required for **steady aerodynamic load control**. The down selected and optimized morphing airfoil section design in this deliverable, was further enhanced in terms of applied actuator excitation and PID controller design (Deliverable D2.31), to achieve the time response required for the **alleviation of unsteady aerodynamic loads**. Additionally the power requirements during operation of the morphing concept were estimated under the same deliverable D2.31.

## 2.2 Brief Description of the Concept

In this subsection the description of the investigated morphing concept and load alleviation control is given. The load alleviation control will be achieved by a change of the lift coefficient which will occur due to a deflection of the trailing edge either upwards or downwards, depending on the position of the blade regarding the air velocity. A section of the blade close to the tip was assumed and further investigated regarding the morphing shapes it can reach. Specifically the airfoil located at 66.711m away from the root of the blade (Figure 1) was chosen due to the presence of high velocities of the wind turbine that increase significantly the developed stresses. The initial geometry profile of the airfoil used for this study has been taken from [4] as well as the structural layout and the material properties.

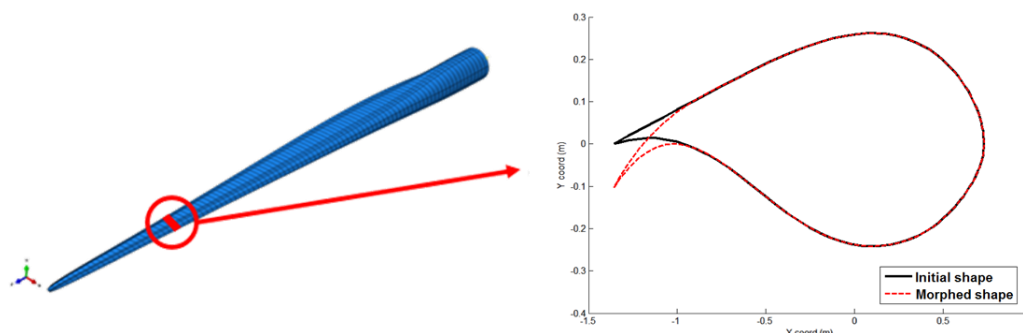


Figure 1: Airfoil shape at 75% (66.711m) of blades length

The aim of this morphing concept was to deform the initial configuration of the airfoil to a given target shape that would contribute beneficially to the scope of load reduction. The target shape has been provided by NTUA after aerodynamic analysis of various aerodynamic cases (Figure 2). The challenge faced is to reach the target shape without overstressing any of the components of the wind turbine blade section.

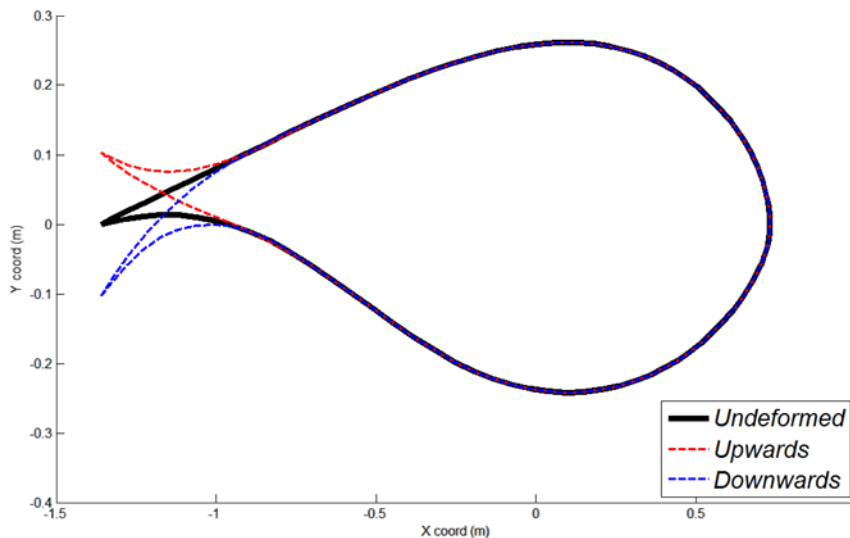


Figure 2: Target morphing shape provided by NTUA for maximum change of lift coefficient

Proper modifications of the geometry were considered in order to incorporate the **Shape Memory Alloy (SMA) actuators** and the accompanying mechanisms into the design. Initial concepts entailed 3 mechanisms, able to move different portion of the trailing edge of the airfoil as it can be seen in Figure 3. Each mechanism was able to move the airfoil to both directions as antagonistic SMA wires were attached to it on the top and bottom side and therefore they move the trailing edge upwards or downwards. Also the SMA wires were providing the stiffness to the slotted airfoil skin.

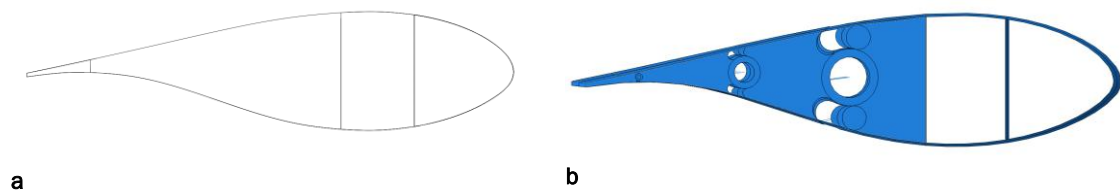


Figure 3: Airfoil configuration (a) pristine and (b) modified morphing airfoil configuration

The SMA materials provide the only available solid-state actuators which are able to provide significant actuation strains (3-6%), forces and power, when they transform from one stable phase to another under application of either thermal or mechanical load. This beneficial phase transformation takes place between the parent phase of Austenite and the phase of Martensite. In order to act as an actuator the SMA must fully or partially be in the martensitic phase which can be reached under mechanical loading of the austenitic phase. Once in martensitic phase, a temperature elevation can provoke the transformation back to the Austenite and therefore the SMA retracts to its initial shape. To provide the actuation force, the SMA wire must be constrained at its both ends such that the constrained recovery results in the exerted actuation forces.

In order to assess the effectiveness of the morphing concept to deliver the scope of contributing to WTB load alleviation numerous finite element simulations have been conducted to evaluate

different designs. As the prediction of the SMA behavior is still an open case, there is not a single constitutive model that can capture its response. Therefore there is not a material model available in the FE program, to be used for the simulation of SMA actuators. To overcome this obstacle a specialty numerical tool is developed that implements the selected constitutive model and is linked to the FE program global solver in order to interact with the remaining elastic parts. Once this material subroutine became available the full model of the morphing wind turbine blade section was built entailing both the passive and the active parts of the morphing concept. The resulting deformed shape was evaluated in each case as well as the developed stresses on the section components.

### 2.2.1 Anticipated PROS and CONS

Shape Memory Alloys are solid state actuators that can provide high stroke and thrust. Therefore they are adequate actuators for applications that require large movements such as the morphing wind turbine blade section. Additionally their high power to weight ratio refrains from the use of bulky and heavy actuators for changing the shape of the airfoil. Also the number of the required actuators is kept to minimum reducing thus the modifications required to be implemented in the WTB section. Therefore the development of a morphing concept based on SMA actuators is envisioned to be feasible.

The developed morphing section is expected to contribute to the load alleviation of the whole wind turbine blade. However, the slow response of the SMA actuators that has been addressed in D2.31: *“New concepts to control the load along the span of the blade, passive, active or mixed”* may hinder the development of a continuous moving airfoil and confines the contribution to the load alleviation only to stand still conditions. Additionally the antagonistic configuration of the actuators may lead to high loading of the SMAs. The modifications required to implement the actuators in the already existing blade are expected to add complexity on the manufacturing process and increase its weight. Finally the actuators themselves as well as some of the required supportive structures introduce undesirable metallic components on the WTB as they may attract lightning.

In the following sections a description of the work performed towards the development of a new morphing airfoil concept using SMA actuators is given. The section is organized in the following six subsections; i) description of shape memory alloys behaviour, ii) description of the numerical tool for the prediction of the thermal and mechanical response of the SMA actuators; iii) the basic principles of the morphing concept; iv) description of the specifications for the design of the morphing concept; v) details and numerical results regarding the structural behaviour of each morphing concept and finally vi) prediction of the response of the downselected concept with and without the consideration of aerodynamic loading .

## 2.3 Basic Description of Shape Memory Alloys Behaviour

Shape Memory Alloys belong to a class of multifunctional materials whose properties can be tuned by altering their composition in order to deliver a specific scope. Although they can be used both as sensors and actuators, their unique capability to retract their initial shape after elongation that can reach up to 8% of their initial length make their use as actuators extremely efficient. Additionally they provide capabilities to apply high induced strains, block stress and high actuation energy density (available work per unit volume), hence they are considered suitable for applications where large movements are required and space limitations apply. The most known and widely used Shape Memory Alloy is the equiatomic NiTi alloy also known as NiTiNol.

### 2.3.1.1 Microscopic Aspects of Shape Memory Alloys

The unique behaviour of SMAs is linked to a shear dominant diffusionless solid state phase transformation between two stable phases; the high temperature and symmetry phase of austenite (*A*) and the lower temperature and symmetry phase of martensite (*M*). The transformation evolves by nucleation and growth of the martensitic phase. The transformation

from austenite to martensite is accompanied by release of latent heat (exothermic reaction) while latent heat is absorbed during the transformation of martensite to austenite (endothermic reaction). Austenitic phase usually has a cubic (B2) unit cell structure, while the martensite can exist in various crystallographic structures depending on the composition of the alloy. Typically in equiatomic NiTi alloys, the martensite has a monoclinic (B19') form.

During the transformation from austenite to martensite every martensitic unit cell can have different crystallographic orientation with respect to the cubic parent face. Hence each unit cell is called martensitic variant and the number of the variants that can be formed depends on the crystal structure of the martensite and its lattice correspondence with the parent unit cell.

Martensite can be found in two different forms; i) twinned martensite or ii) detwinned martensite. Twinned martensite can be reached via cooling of the parent austenitic phase under zero stress levels with no associated macroscopic shape change. In this case the self-accommodated martensite is a mixture of different martensitic variants, arranged in twins aiming to minimize the overall strain energy. When the self-accommodated twinned martensite structure subjects to an applied load a shear stress acts on the twin plane. When this stress becomes greater than a threshold value, the most preferred variant, the one with orientation aligned to the loading axis, evolves in expense of the other variants forming the detwinned structure of martensite. This process is called as the detwinning of martensite and is associated with a macroscopic shape change exhibiting an inelastic strain which persists when the applied load is removed. Both transformations to the martensitic phase are referred to as forward or martensitic transformation while the transformation back to the parent phase of austenite is called reverse transformation. The reverse transformation can occur only by heating of the twinned or detwinned form of martensite. The transformation from the detwinned martensite back to the austenite is accompanied by a macroscopic shape change.

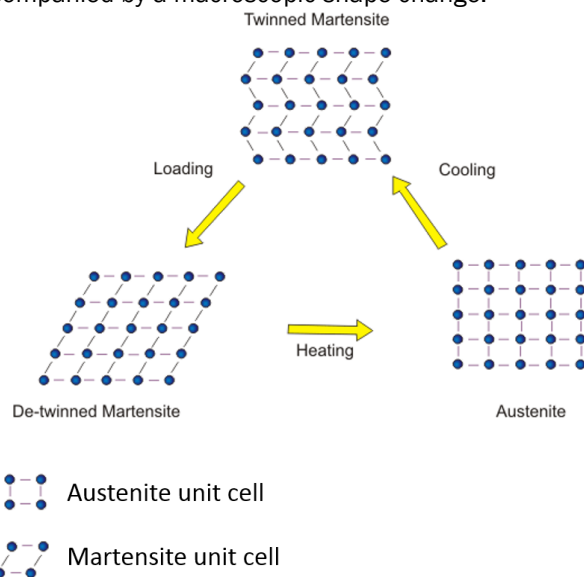


Figure 4: Representation of martensitic twinning and detwinning

### 2.3.1.2 Macroscopic Aspects of Shape Memory Alloys

Aiming to describe the complicated behaviour of SMA a phase diagram on the stress-temperature plane is constructed. The phase diagram consists of equilibrium lines (or phase boundaries) which indicate the conditions under which the two different phases are stable, while phase transformations can occur along these lines. In Figure 5 a typical SMA phase diagram is presented.  $M_s$ ,  $M_f$ ,  $A_s$  and  $A_f$  are the temperatures that consists the threshold values for the initiation and completion of the martensitic transformation and the initiation and completion of

the reverse transformation respectively under zero stress levels. As already mentioned, once the SMA material is cooled while in the austenitic phase it transforms to martensite which is either twinned or detwinned. The form of martensite depends on the applied stress level. If the applied load results in stress that is higher than  $\sigma_f$  (detwinning finish stress) the material transforms to fully detwinned martensite while if the developed stress level is between  $\sigma_f$  and  $\sigma_s$  (detwinning start stress) the material partially transforms to detwinned martensite. Finally if the stress level is below  $\sigma_s$  then the SMA transforms to twinned martensite.

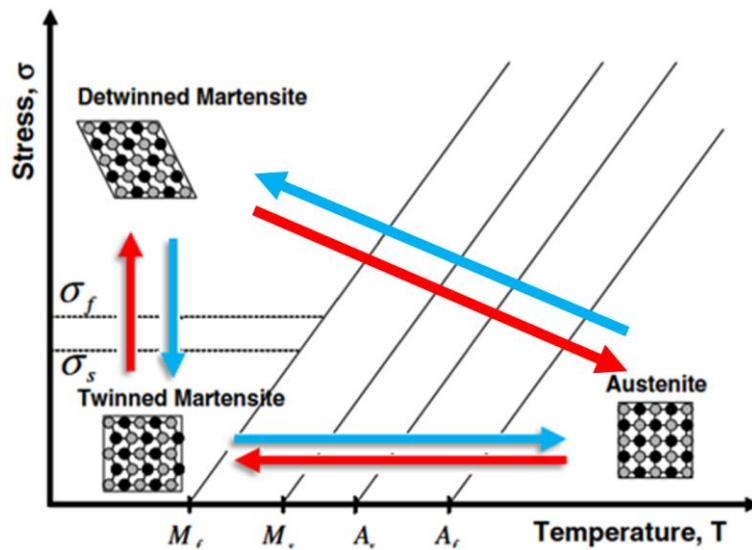


Figure 5: SMA phase diagram

The effect of SMA behaviour that is mainly exploited when they are used as actuators is known as the *one way shape memory effect*. To explain this effect and gain a better insight of the SMA behaviour the stress-strain-temperature response of the material will be explained based on the diagram of Figure 6. The material is considered to be initially at a high temperature under zero stress level on the austenitic phase (point A). A subsequently cooling of the material below  $M_r$  without any load application transforms the material to twinned martensite (point B). Following, a mechanical load is applied and as the resulted stress is higher than the  $\sigma_f$  the SMA transforms to fully detwinned martensite exhibiting the transformation strain ( $\epsilon^t$ ) (point C). Upon unloading the elastic strain is recovered while the transformation strain remains (point D). The transformation strain starts to be recovered as the temperature of the material is elevated and overcomes the threshold value  $A_r$  where the reverse transformation is completed (point A).

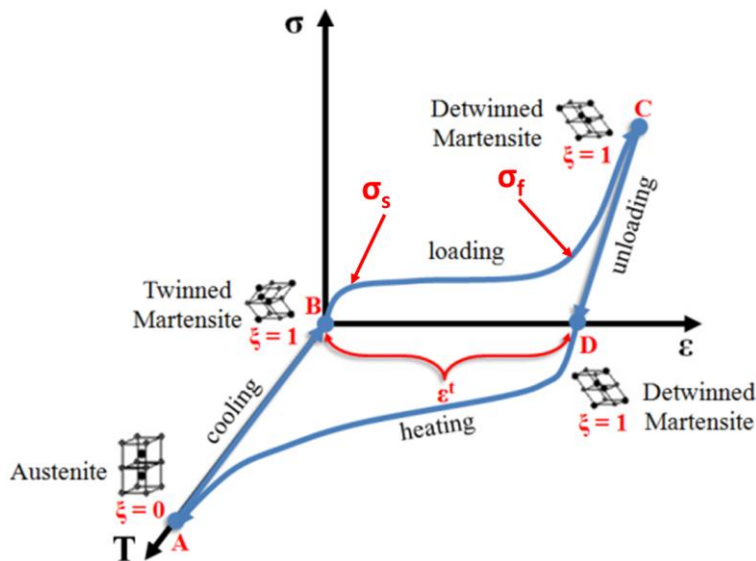


Figure 6: One way shape memory effect on the stress-strain-temperature space

Exploiting the strain recovery upon heating, the SMA can be used as actuator adequate for changing the shape of an airfoil when located at suitable points on the structure. Considering a prestrained SMA wire in the phase of detwinned martensite clamped at its two ends when heated above the critical temperature  $A_s$  the reverse transformation initiates and stresses are being developed. The produced force is used for actuation of the morphing airfoil.

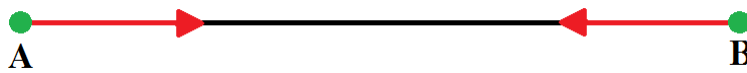


Figure 7: Shape memory alloy constrained recovery

## 2.4 Shape Memory Alloy Modelling Tools

### 2.4.1 Specialty Beam FE for The Prediction Of SMA Wire Behaviour

A critical issue restricting the application of SMA actuators is the lack of robust modelling tools capable to predict their complicated thermomechanical behaviour. Since the early 80s, when significant research efforts focused on the modelling of SMAs, many constitutive models have been developed [22]. Primitive models were based on experimental results and observations and hence they were characterized as phenomenological.

However, still much research is needed in the field of robust and computationally efficient finite elements for beam and wire actuators, and as a consequence none of the already developed models is globally accepted to be implemented in the various finite element (FE) software. The majority of the FE programs offer to the user special subroutines where they can implement any material model with continuum finite elements to provide limited capabilities for conducting simulations entailing SMA actuators.

To overcome this obstacle, a numerical tool for the prediction of SMA behaviour has been developed for the scope of this project. It entails a new multi-field SMA beam finite element which is summarized herein and in D2.31. This numerical tool has already been used to predict the time response of a morphing airfoil section based on SMA actuators. The results of this study and the description of the numerical tool can be found in deliverable D2.31 "New concepts to control the

load along the span of the blade, passive active or mixed". In order to enhance the capabilities of this numerical tool and increase its accuracy some additions have been performed. The additions concern a high order polynomial expression for the prediction of the temperature field on the cross section of the element and the incorporation of large displacements/rotation theory as they are crucial for the prediction of the response of morphing structures that undergo large movements. For the sake of brevity only the additions and enhancements implemented in the numerical tool are presented in this report. More details can be found in deliverable D2.31.

The aforementioned tool implements a phenomenological constitutive model developed by Lagoudas et al. [11]. In order to increase the accuracy of the numerical predictions of the thermomechanical response of SMAs the constitutive model was combined with the development of a specialty beam finite element that accounts for the simultaneous solution of the thermal and mechanical equations considering thus the thermomechanical coupling. The existing geometrical nonlinearities due to the large displacements and rotations which are naturally associated with a morphing section, has been taken into account through the implementation of corotational theory that accounts for large rotations and displacements. Additionally the time response of the SMA actuators can be predicted via the transient thermal response capabilities of this numerical tool. In closing, the development of this robust numerical tool enables the accurate prediction of the response of the SMA wire actuators under the various thermomechanical loads required to morph the WTB section.

To make feasible the interaction of the SMA actuators with the remaining elastic parts of the morphing airfoil concept and finally to predict its structural response the numerical tool has been implemented in Abaqus FE program through the available user element (UEL) subroutine which is interconnected with the user material (UMAT) subroutine that implements the SMA constitutive model. A summary of the developed tool is schematically given in Figure 8.

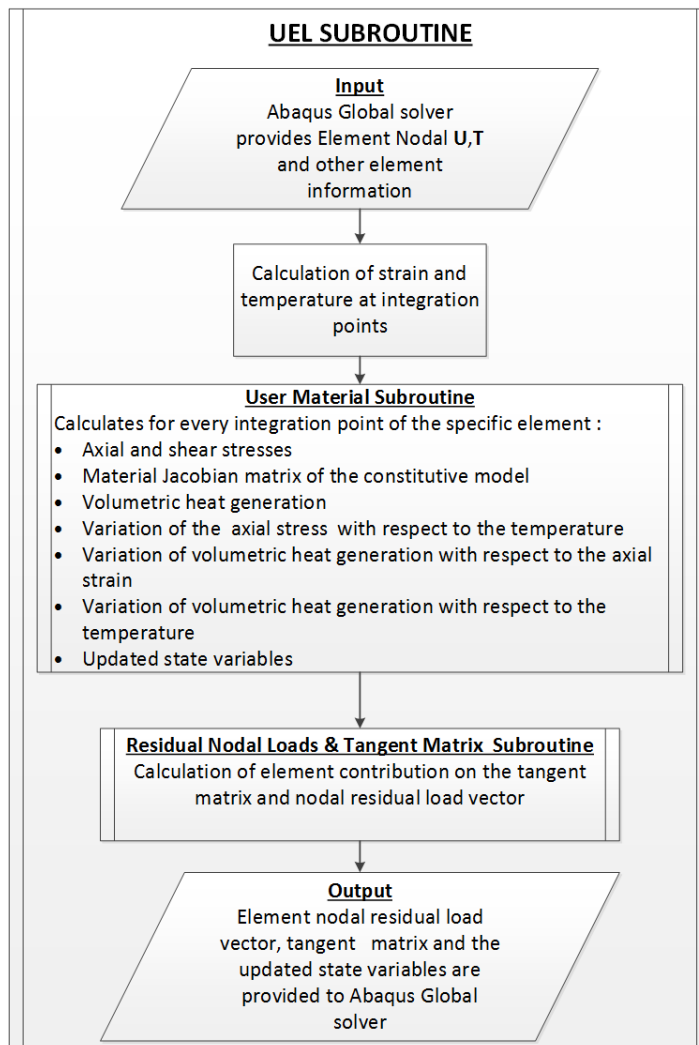


**Figure 8: Summary of the developed numerical tool for prediction of SMA behaviour**

#### 2.4.2 Large Displacement Capabilities (Geometrical Nonlinearities)

The concept of a morphing structure implies a capability to undergo large elastic and rigid body rotations and displacements. Likewise, the capability of SMA to undergo large transformation strains dictates the need of consideration of large displacements and rotations in the modelling tool in order to acquire more reliable results. Hence, the inclusion of large displacement/rotation nonlinear analysis capabilities in modelling tool is of high importance in the development of morphing structures that undergo large movements such as the morphing WTB section concept. To take into account the geometrical nonlinearities, the corotational description of motion has been adopted that assumes small strains with large displacements/rotations. The formulation is based on the polar decomposition theory which assumes that the total deformation of a continuum body can be split into a rigid body motion and a relative deformation. A corotated Cartesian system is attached on each FE element that rotates and translates with the average rigid body motion of the element. In this manner the remaining relative deformation is free from rigid body motion and therefore small enough so that the small strain theory can be used. The geometrical nonlinearity is introduced through the coordinate transformation of the local displacements in terms of the displacement components in fixed global coordinate system.

To demonstrate the corotational framework a two node plane beam FE is considered. Initially the finite element has a  $\theta_0$  angle in respect to the global coordinate system  $(x, z)$  and known nodal coordinates as it can be seen in Figure 9. The decomposition of the total motion of the continuous body into rigid body motion and relative deformation can be achieved by attaching to each element a local coordinate system  $(\hat{x}, \hat{z})$  which rotates with the averaged rigid body motion. In this way, the finite rigid motion that affects significantly the structural response is eliminated from the total displacements.

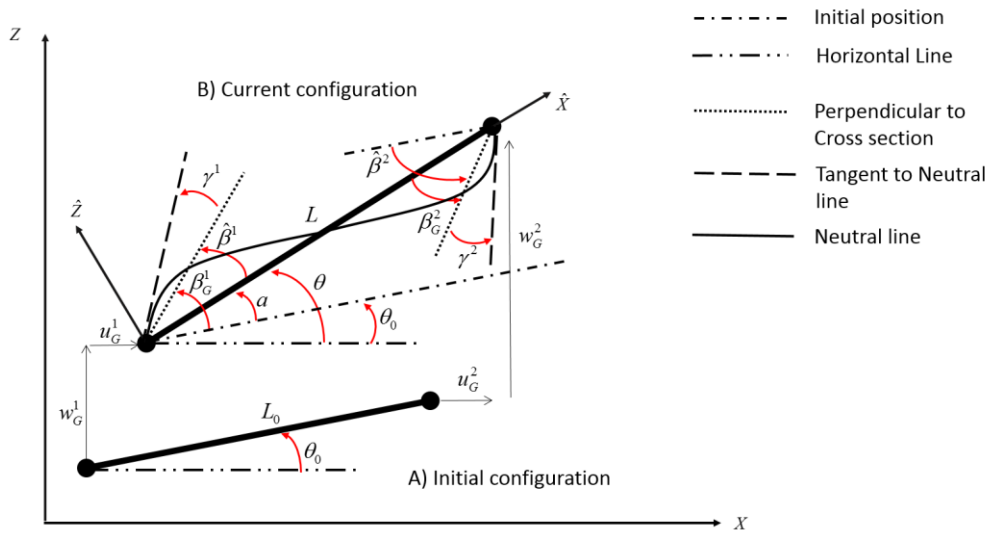


Figure 9: Beam FE kinematics

In the beam finite element formulation the generalized displacement and temperatures in equation (1) are interpolated using  $c^0$  shape functions  $N^i(x)$  which implements 3 displacement and 7 temperature DOFs per node. Without loss of generality, in the remaining section the corotational formulation is presented for a 2 node beam element.

$$\left\{ \hat{u}_0(\hat{x}), \hat{w}(\hat{x}), \hat{\beta}(\hat{x}), T_0(\hat{x}), T_1(\hat{x}), T_2(\hat{x}), T_3(\hat{x}), T_4(\hat{x}), T_5(\hat{x}), T_6(\hat{x}) \right\}^T = \sum_{i=1}^{nodes} N^i(\hat{x}) \left\{ \hat{u}_0^i, \hat{w}^i, \hat{\beta}^i, T_0^i, T_1^i, T_2^i, T_3^i, T_4^i, T_5^i, T_6^i \right\}^T \quad (1)$$

Taking into account the definition of the corotational coordinate frame, the element global displacements in the fixed frame  $\mathbf{U}_e^G$  and local displacements  $\hat{\mathbf{U}}_e$  in the corotational frame are respectively

$$\mathbf{U}_e^G = \left\{ u_{0G}^1, w_G^1, \beta_G^1, u_{0G}^2, w_G^2, \beta_G^2 \right\}^T \quad (2)$$

$$\hat{\mathbf{U}}_e = \left\{ 0, 0, \hat{\beta}^1, \hat{u}_0^2, 0, \hat{\beta}^2 \right\}^T$$

The local elongation  $\hat{u}_0^2$  of the neutral axis of the beam is defined as,

$$\hat{u}_0^2 = \frac{L^2 - L_0^2}{L + L_0} \quad (3)$$

The current beam length  $L$  is calculated using the initial nodal coordinates  $(x_1, z_1, x_2, z_2)$  and the global displacements,

$$L = \sqrt{\left(\left(x_2 + u_{0G}^2\right) - \left(x_1 + u_{0G}^1\right)\right)^2 + \left(\left(z_2 + w_G^2\right) - \left(z_1 + w_G^1\right)\right)^2} \quad (4)$$

While the initial length  $L_0$  is defined by the coordinates of the initial configuration,

$$L_0 = \sqrt{\left(x_2 - x_1\right)^2 + \left(z_2 - z_1\right)^2} \quad (5)$$

The local nodal rotational angles  $\hat{\beta}^i$  of the beam are calculated from the global nodal rotation angles  $\beta_G^i$  excluding the rigid body rotation angle  $\alpha$ , (Figure 9)

$$\hat{\beta}^i = \beta_G^i - \alpha \quad (6)$$

And the body angle “ $\alpha$ ” is the difference between the current and initial beam angles  $\theta$  and  $\theta_0$  at the final and initial element configuration, respectively,

$$\alpha = \theta - \theta_0 \quad (7)$$

The angles  $\theta$  and  $\theta_0$  are defined as

$$\theta_0 = \text{atan2}(z_2 - z_1, x_2 - x_1) \quad (8)$$

$$\theta = \text{atan2}\left[\left[\left(z_2 + w_G^2\right) - \left(z_1 + w_G^1\right)\right], \left[\left(x_2 + u_{0G}^2\right) - \left(x_1 + u_{0G}^1\right)\right]\right] \quad (9)$$

### 2.4.3 Beam Element with High Order Polynomial for Temperature Prediction

In this section the formulation of a two node beam finite element is described regarding the assumed displacement and temperature fields.

For the development of the beam FE, kinematic assumptions have been made for the displacement and temperature fields through the thickness ( $h$ ) of the cross section. The first-order shear deformation theory (FSDT) was implemented in the beam section for calculating the displacement field. According to this theory the beam element can undergo extension along x-axis, bending in z direction and constant shear in the x-z plane (Figure 10). The temperature field is approximated by a 6<sup>th</sup> order polynomial along the height of the cross section.

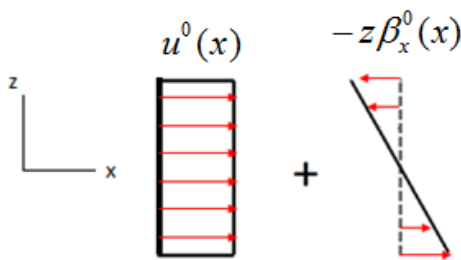


Figure 10: Assumed displacement field through thickness of a beam section

The following equations calculate the displacement and the temperature field on the beam cross-section:

$$u(x, z) = u^0(x) - \beta_x^0(x) \frac{\zeta h}{2} \quad (10)$$

$$w(x, z) = w^0(x) \quad (11)$$

$$T(\tilde{x}, \zeta) = T_0(\tilde{x}) + T_1(\tilde{x}) \frac{\zeta h}{2} + T_2(\tilde{x})(1 - \zeta^2) + T_3(\tilde{x})(\zeta^3 - \zeta) + T_4(\tilde{x})\zeta^4 + T_5(\tilde{x})\zeta^5 + T_6(\tilde{x})\zeta^6 \quad (12)$$

where,  $u(x, z)$  is the total axial displacement,  $u^0(x)$  is the uniform axial displacement,  $\beta_x^0(x)$  is the angle of rotation of the beam cross section and  $w^0(x)$  is the transverse displacement of the center line of the beam cross section. The combination of the seven components shown in Equation (12), describe the temperature field through the thickness of the beam. In the previous equations,  $h$  is the height of the beam's cross section,  $\zeta = \frac{2z}{h}$  is the non-dimensional thickness variable which takes values from -1 to 1, and superscript 0 refers to the value of each variable at the mid-plane of the section. Taking into account the displacement Equations (10) and (11), the axial strain  $\varepsilon_x$  and the shear strain  $\varepsilon_{xz}$  are given by the following expressions,

$$\varepsilon_x = \frac{\partial u(x, z)}{\partial x} = \frac{du^0(x)}{dx} - \frac{d\beta_x^0(x)}{dx} \frac{\zeta h}{2} = \varepsilon_x^0(x) - \frac{d\beta_x^0(x)}{dx} \frac{\zeta h}{2} \quad (13)$$

$$\varepsilon_{xz} = \frac{dw^0(x)}{dx} - \beta_x^0(x) \quad (14)$$

In the same manner, using Equation (12) the temperature gradients in x and z directions are given by the following two expressions respectively.

$$\begin{aligned} \frac{\partial T(\tilde{x}, \zeta)}{\partial \tilde{x}} &= \frac{\partial T_0(\tilde{x})}{\partial \tilde{x}} + \frac{\partial T_1(\tilde{x})}{\partial \tilde{x}} \frac{\zeta h}{2} + \frac{\partial T_2(\tilde{x})}{\partial \tilde{x}} (1 - \zeta^2) \\ &+ \frac{\partial T_3(\tilde{x})}{\partial \tilde{x}} (\zeta^3 - \zeta) + \frac{\partial T_4(\tilde{x})}{\partial \tilde{x}} \zeta^4 + \frac{\partial T_5(\tilde{x})}{\partial \tilde{x}} \zeta^5 + \frac{\partial T_6(\tilde{x})}{\partial \tilde{x}} \zeta^6 \end{aligned} \quad (15)$$

$$\begin{aligned} \frac{\partial T(\tilde{x}, \zeta)}{\partial \tilde{z}} &= \frac{\partial T(\tilde{x}, \zeta)}{\partial \zeta} \frac{\partial \zeta}{\partial \tilde{z}} \\ &= \left[ T_1(\tilde{x}) \frac{h}{2} - 2T_2(\tilde{x})\zeta + T_3(\tilde{x})(3\zeta^2 - 1) + 4T_4(\tilde{x})\zeta^3 + 5T_5(\tilde{x})\zeta^4 + 6T_6(\tilde{x})\zeta^5 \right] \frac{2}{h} \end{aligned} \quad (16)$$

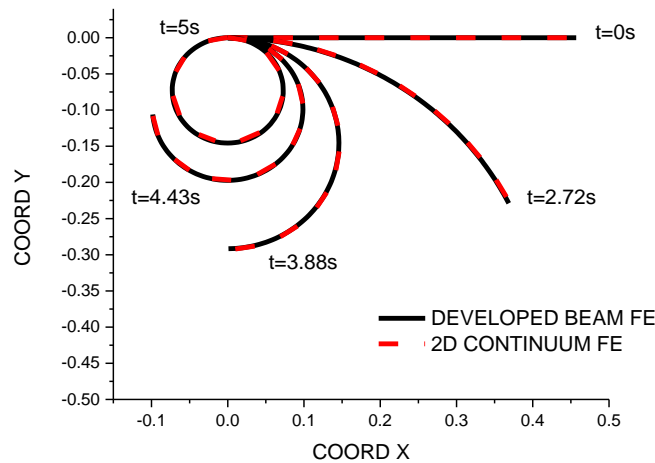
#### 2.4.4 Evaluation of New Capabilities – Validations

The additions to the developed beam finite element increased its accuracy as they enabled it to make better prediction of the temperature profile that affects the response of the actuator during the transformation. Additionally the implementation of the large displacements theory gave the capability to the beam element to predict the large movements of the actuator neglecting the rigid body motion and the effects coming from it on the results regarding the developed stress, strains and transformation percentage. With these enhancements a better exploitation of the actuator capabilities is expected to take place. In this subsection two examples are presented aiming to

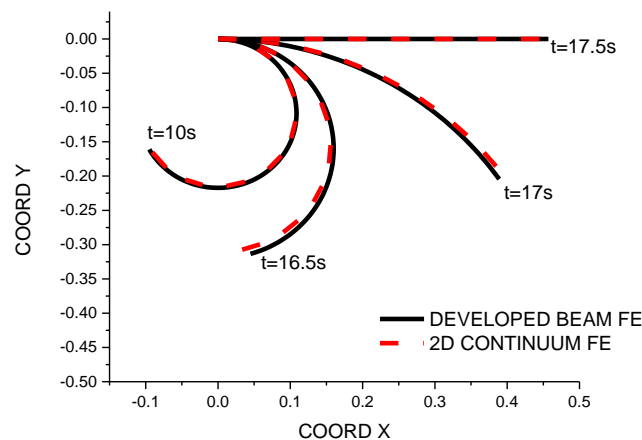
demonstrate the new capabilities and prove the validity of the developed beam element; i) a SMA wire subject to large rotation and ii) a primitive morphing concept analysed considering linear and non linear geometry.

#### 2.4.4.1 SMA Wire Actuator Subject to Large Rotations

In this example a straight cantilever SMA wire with length of 0.45m and a rectangular cross section with dimensions 0.01m x 0.01m subjects to bending under a concentrated linear increasing moment at its free end. The beam is considered to be initially at the austenitic phase and the mechanical loading is applied till the beam wraps to a 360° plane coil. Once the coil has been formed and has partially transformed to martensite, the loading is removed and the beam recovers its elastic strain. After that point a constant Joule heating is applied to the SMA in order to recover the transformation strain and finally the wire restore its initial shape. In Figure 11a snapshots of the SMA deformed shape at five different times,  $t=0.0, 2.72, 3.88, 4.43, 5.0$  secs during the loading phase are presented. The results of the enhanced beam element are correlated with the respective results extracted by a 2D plane stress continuum FE. In Figure 11b the shape of the wire during the unfolding phase is presented. Till 10 secs the wire is recovering the elastic strain while from 10-17.5 sec it recovers the transformation strain due to the applied heating and regains its initial configuration.



a



b

Figure 11: Comparison of the predicted morphing shapes at various time points between the developed beam FE and 2D continuum FE. (a) Folding due to mechanical load; (b) unfolding due to heating.

From the above figures it can be assumed that beam FE presents excellent agreement with the results of a 2D plane stress continuum model that simulates the same problem in much more time, proving the validity of the developed numerical tool. Furthermore the capability to consider large movements of the SMA actuator has been demonstrated.

#### 2.4.4.2 Comparison of Morphing WTB Section Considering Linear and Geometric Non Linear Analyses

The WTB morphing section was foreseen to undergo large displacements/rotations and this was the motivation for the enhancements performed on the already existing numerical tool. In this example a primitive morphing WTB section concept is analysed considering both linear and geometric non linear assumption in order to demonstrate the new capabilities of the enhanced beam FE for the SMA actuators. The concept entails SMA actuators able to move the airfoil both upwards and downwards. Initially the bottom actuators are heated up while the top ones are cooled down resulting in a downwards movement of the airfoil. Following the bottom actuators are being cooled down and the top ones are being heated up leading to an upward movement of the airfoil. In Figure 12 the concept under investigation is presented in both the undeformed configuration and at one of its morphed states.

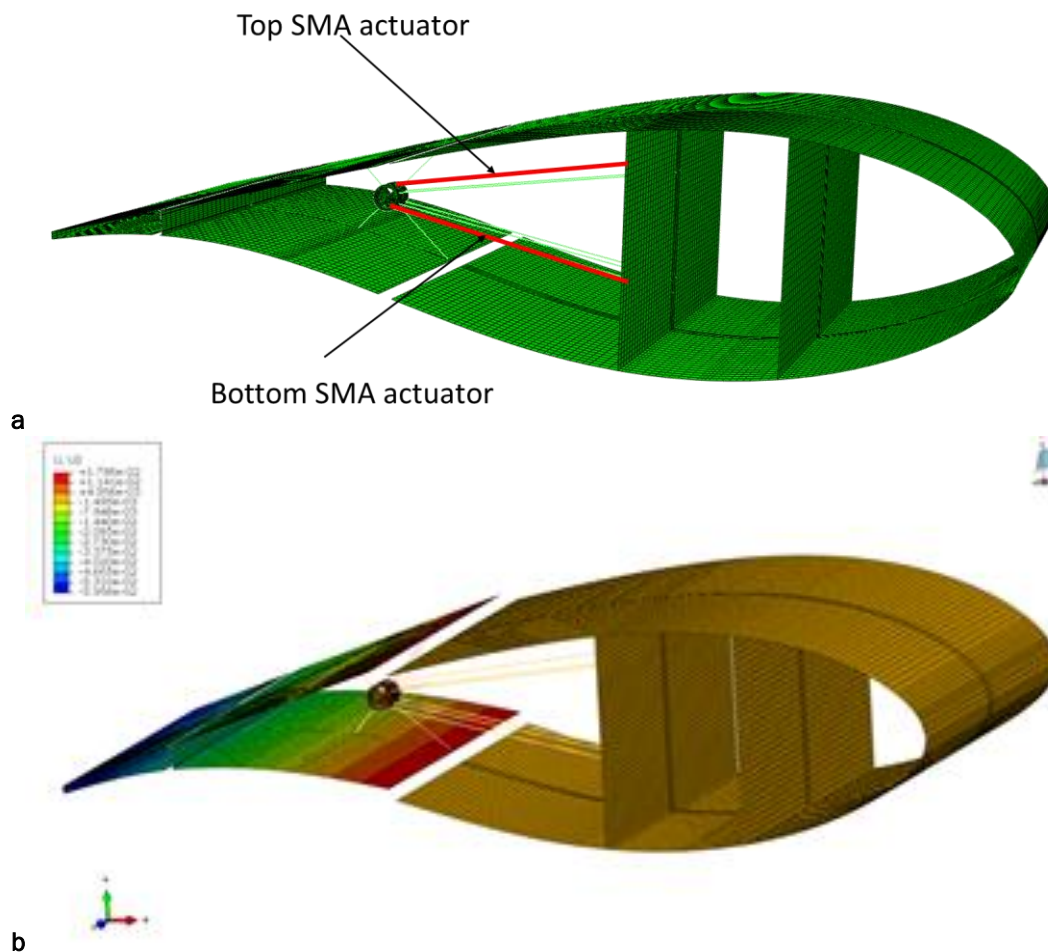


Figure 12: Primitive morphing WTB concept; (a) initial configuration (b) morphed configuration

The change of the actuators temperature was considered as the input load while the response of the morphing WTB section was measured in terms of the actuators martensitic fraction, axial stress of the SMA actuators and the resulted tip displacement of the airfoil as.

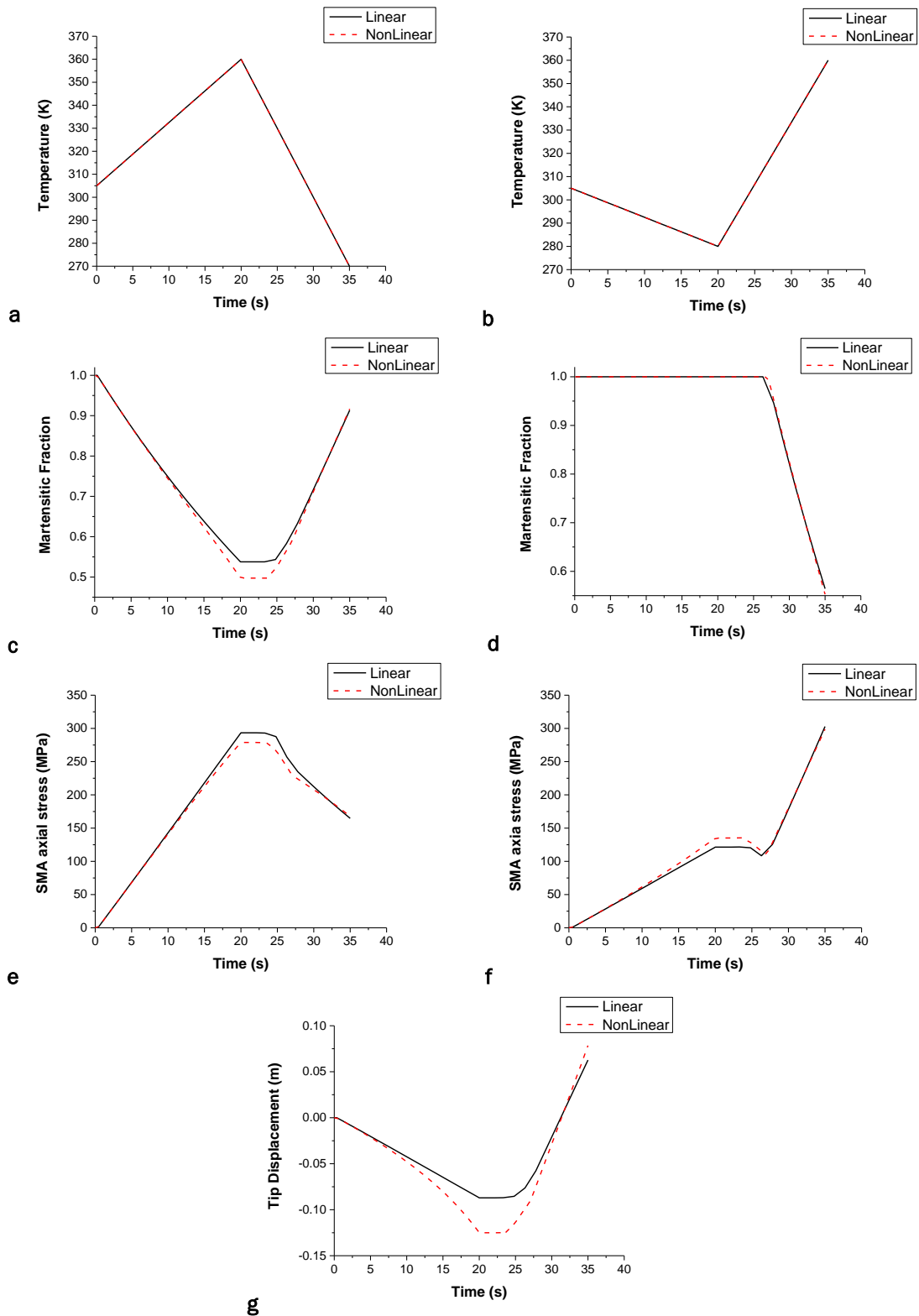


Figure 13: Comparison of results between linear and geometric non linear analyses. (a) Thermal loading of bottom actuators; (b) thermal loading of top actuators; (c) martensitic fraction of bottom actuators; (d) martensitic fraction of top actuators; (e) axial stress of bottom actuators; (f) axial stress of top actuators; (g) tip displacement of the morphing WTB section

From Figure 13 it can be seen that a noticeable difference between the results of the linear and the geometric non linear analyses exist for the most of the individual results. These differences lead to a significant discrepancy between the predicted tip deflection of the linear and the non linear analyses. It must be noted that the deformation of the airfoil defines the extent of morphing each concept can achieve and therefore affects the assessment of each one towards the down-selection of the most promising one.

## 2.5 Morphing Concept

All of the morphing concepts and configurations that are presented in the current work are based on some fundamental assumptions. Each morphing concept was considered as an equivalent trailing edge flap with a centre of rotation and a length that can be expressed as a percentage of the total airfoil 's chord length. As this equivalent flap rotates at an angle  $\beta$  its camber line alters and it leads to a change of lift coefficient. The aforementioned parameters associated with airfoil geometry are graphically illustrated in Figure 14.

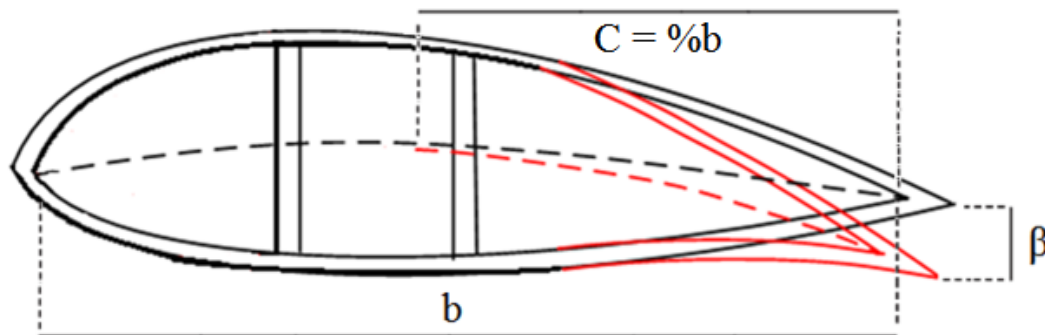


Figure 14: Airfoil parameters

### 2.5.1 Specifications

This section constitutes a brief summary of the specifications that have been taken into consideration in order to assess the proposed morphing concepts, presented in the following sections. NTUA has provided charts that relate the percentage of chordal moving length represented by the flap and angular rotation  $\beta$  with the variation of coefficient of lift at a given reduced angular velocity ( $k$ ) of the blade and a known angle of attack (a.o.a.). In these charts reduced angular velocity varies from 0.02 to 0.1 by an increment of 0.01 and a.o.a. is set to either  $0^\circ$  or  $4^\circ$ . For example a chart where  $k=0.09$  and a.o.a. are equal to  $0^\circ$  is shown in Figure 15. It is clear that a certain variation in coefficient of lift can be achieved by different combinations of flap length and angular rotation  $\beta$ . For example a  $\Delta C_L$  equal to 0.1 can be achieved either by a flap with length equal to 30 % of chord length that rotates at  $1.2^\circ$  or a flap with length of 10% of chord length that rotates at  $2.3^\circ$ . It can be interpreted that the larger the length of the flap is, the lower the demanded angular rotation will be (red and green cycle of Figure 15). Moreover, if a certain flap length is considered, for example 30% of chord length, and a high angular rotation, for instance  $5^\circ$ , can be achieved then the variation in lift coefficient may have a wider variety of values, e.g. from 0.05 to 0.3 (red and blue circles of Figure 15). If the goal is to maximize the morphing capabilities of the airfoil then maximum  $\Delta C_L$  must be achieved. Thus through the assessment of the presented models the most promising will be those which can achieve the maximum variation in coefficient of lift while satisfying some other crucial specification parameters.

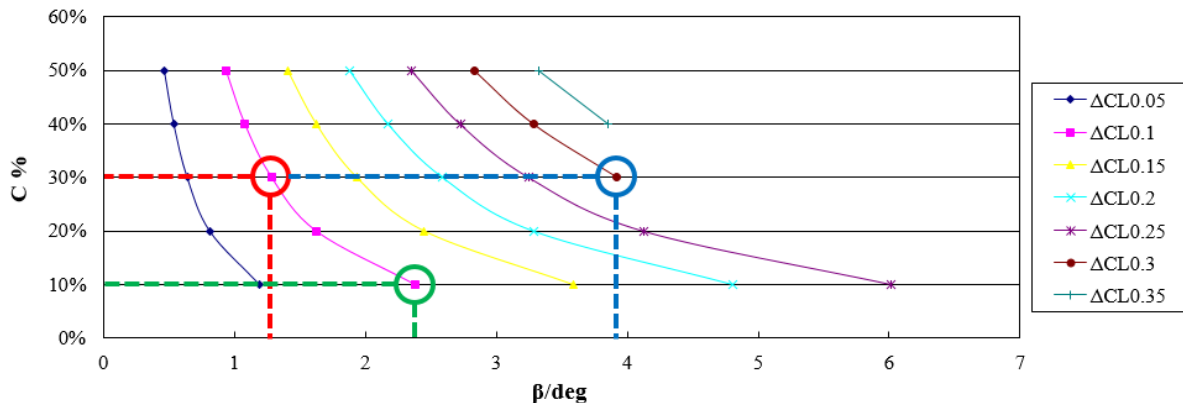


Figure 15: Chart relating percentage of chord length and angular rotation  $\beta$  to variations of coefficient of lift (Courtesy of NTUA)

## 2.6 Preliminary Investigation of Morphing Configurations

In this section the various morphing concepts that have been examined are presented. The study initially focuses, as a preliminary step, on the design and implementation of internal truss structures that provide support for the SMA wire actuators. Trusses are chosen because of the flexibility they offer to achieve a large variety of different configurations. As a result, the key aspects that drive actuators' performance and response of the overall structure can be derived. The results provided by the preliminary study are taken into consideration in the design of morphing mechanism concepts that operate on the principles suggested during this analysis. The morphing mechanisms are assessed afterwards and the most promising concept is selected. Moreover, the selected concept is considered, modelled and its response is numerically simulated under absence of aerodynamic load to prove its morphing capabilities. Finally, aerodynamic loads are taken into consideration to check the response of the morphing mechanism and make any changes in the structure, if needed, to achieve both the proper required stiffness to sustain aerodynamics loads and provide adequate morphing capabilities.

### 2.6.1 Implementation of Internal Truss Structure

The first approach includes the implementation of a truss structure between web B and web C and, in some cases, between web C and Tail V of the airfoil while skin remains intact as well as the rest of the original airfoil structure. All the concepts presented can be divided into three categories depending on their functional principle. The first category uses a complex truss structure to support the SMA wire actuators in different positions and angles inside the airfoil in order to evaluate the effect these parameters have on the bending response of the structure. The second category's models consist of a number of trusses arranged at a "steering rack" configuration to check the effectiveness of elementary mechanism in airfoil's bending. Both the first and second category have antagonistic SMA wire actuators to make it possible to control both the upwards and the downwards bending of the airfoil. On the contrary, models of the third category have only one actuator meaning that bending of the airfoil is controlled only in one direction, while the retracting phase is primarily driven by the elastic response of skin structure and secondarily by the cooling rate of the actuator. In order to distinguish each different concept, a code will be introduced in the form of CXvY, where C stands for concept, X is the number of concept group so it has values of 1, 2 or 3, v stands for version and Y is a number assigned to each different version of the concept.

Consequently, for assessing each concept a finite element model was created. In every model the structure of the original airfoil was modeled as a thin slice of the total blade's length which was connected through shear box with the rest of the structure while the airfoil portion from web B to

tail V was considered independent as a separate part. This admission was made in order to neglect the effects of the third dimension on the stiffness and the general response of the structure. Also it was considered that the movement required to morph the airfoil was a counter clock wise rotation of the trailing edge. Thus, in cases where antagonistic actuators are utilized, the proper set of them will be activated. In most models the calculation of chord's mobile length is not obvious because there is no specific rotation center. For this reason, the calculation of the percentage of chord's mobile length was based on certain assumptions. First of all, the coordinates of chords end at trailing edge at initial and final position are known and can be defined as two sets of coordinates in form  $(x_{c0}, y_{c0}, z_{c0})$  and  $(x_{cd}, y_{cd}, z_{cd})$  respectively. The coordinates at original and deformed position are presented in Figure 16. After the coordinates of the aforementioned points are specified then the coordinates of the point on the lower surface that was translated 5 mm at vertical direction are calculated. With coordinates  $(x_5, y_5, z_5)$  of this point known the calculation of the point  $(x_p, y_p, z_p)$  follows. The point with coordinates  $(x_p, y_p, z_p)$  is addressed as the rotation center of the bending airfoil and the distance between this point and chord's end is the mobile length of the chord. If this length is expressed as a percentage of chords total length then an approximation of the percentage of mobile length of the chord is calculated.

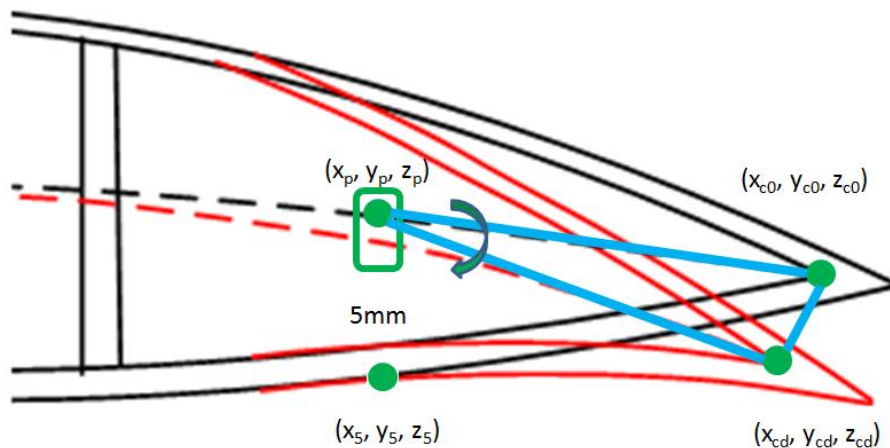


**Figure 16: Schematic representation of required data for calculation of mobile chord length and angular rotation  $\beta$  (Courtesy of NTUA)**

Finite element modelling of the concepts was realized using 8-node shell finite elements with shape functions of quadratic geometric order, 6 degrees of freedom per node and reduced integration while the modelling of the shape memory alloy material properties was performed via the specialty 2D thermomechanical coupled beam finite element combined with the already developed user material subroutine. The elements of the truss structure were modelled with 2-node truss elements with shape functions of linear geometric order. After the description of the finite elements used to model the structure and its components the predefined conditions and the loads will be described. The temperature of the environment as well as the initial temperature of the actuators was set to 310.0 K. It is assumed that there are no initial stresses developed. Thermal load is considered in form of electrical power provided to the proper set to actuators to raise their temperature to 350.0 K and activate them (triggering the reverse transformation). During transformation SMA actuators develop stress and due to their connection with the truss structure they transmit forces and the airfoil changes its shape.

The variables measured to assess the effectiveness of the morphing state are the vertical displacement and angular rotation of trailing edge's tip, the stress developed on the actuators and the airfoil skin and the martensitic volume fraction of the actuators. It should be noted that the radius of the SMA wires was set also as a design variable (varying from 0.5 mm to 3 mm) to examine its effect on the response of the morphing structure. Furthermore, the effect of the implementation of the truss structure regarding the variation in stiffness will be addressed by

loading with a concentrated force at the trailing edge of the airfoil at direction vertical to the chord both the original structure and the structure with the implemented truss elements.

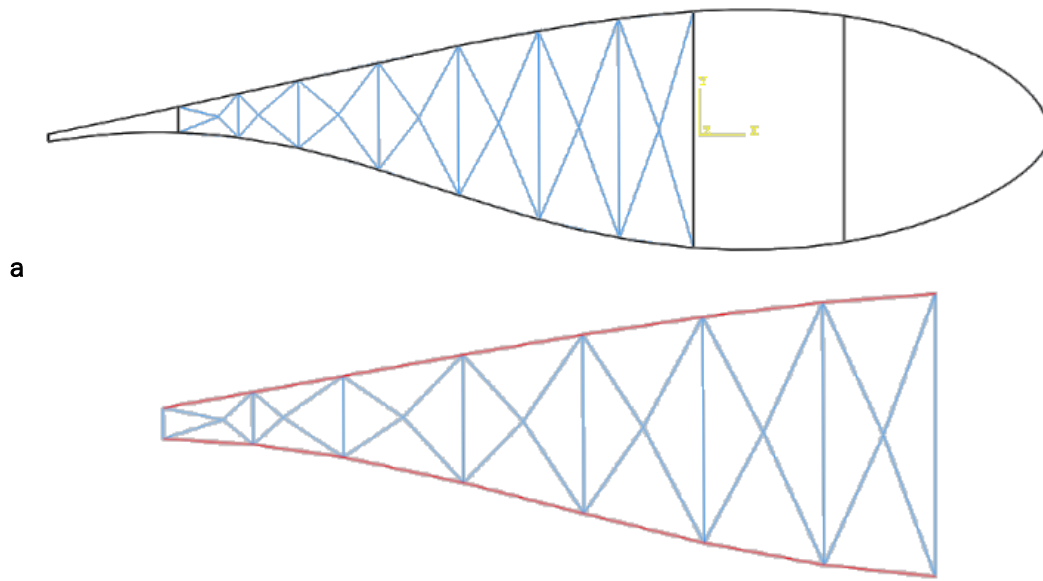
In the following section the most promising concepts from each category will be briefly presented in a paragraph followed by two pictures where the implementation of the truss structure into the airfoil and the position of SMA wire actuators will be illustrated. In the pictures where the truss structure and the SMA actuators are presented the actuators will be always highlighted with red colour. It should be noted though that in figures where the activated actuators are highlighted the chosen colour is also red so the reader should be aware of the notation in these two different cases. After the presentation of each concept details, a summary of the numerical results follows. The concepts that were also studied but not as promising as the ones presented are summarized in Appendix A.

#### *2.6.1.1 Concept Category 1: Antagonistic Actuators Placed in Various Positions*

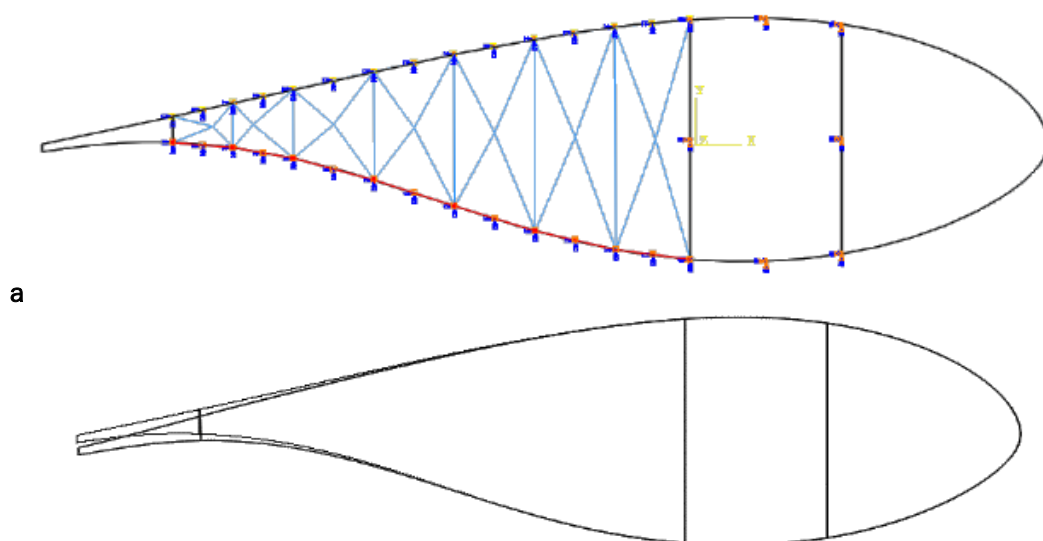
The first category contains those models which utilize a main truss structure on which antagonistic SMA wire actuators are attached and provide the capability of lowering the stiffness of the original airfoil structure due to the fact that stiffness is amplified by the truss elements. The models of this category have relatively complex truss structures because they are designed for addressing the effect different configurations of SMA wire actuators have on bending of the airfoil structure. The length of the wires, their angle in respect of the chord, the way they are connected either to the truss support structure or between each other and the interaction of the implemented elements with the original structure provide vital feedback for further design and optimization of the morphing structure. Ten models have been designed, modelled and numerically simulated under predefined conditions. Here the two most promising models are presented and their results are summarized. The reader can see the complete preliminary analysis based on this concept in Appendix A.

Model C1v0

In this model the SMA wire actuators are located almost tangential to airfoil skin. Successive wires have common support points and wires near the upper surface operate in an antagonistic manner with the wires near the lower surface. This feature can morph the airfoil both upwards and downwards.



**b** Figure 17: Model C1v0 (a) Implementation of morphing structure and (b) truss structure with the SMA actuators



**b** Figure 18: Model C1v0 (a) SMA actuators activated and (b) the undeformed and deformed airfoil in real scale for  $r = 0.003 \text{ m}$

**Table 1: Model C1v0 Effect of SMA wire radius on structural stiffness**

<b>Radius of SMA Wire Actuators</b>		<b>Vertical Displacement</b>
<b>ID</b>	<b>Assigned Value [m]</b>	<b>Value [m]</b>
r <sub>1</sub>	0.0005	-3.6304E-02
r <sub>2</sub>	0.001	-3.4259E-02
r <sub>3</sub>	0.0015	-3.1579E-02
r <sub>4</sub>	0.002	-2.8826E-02
r <sub>5</sub>	0.0025	-2.6320E-02
r <sub>6</sub>	0.003	-2.4179E-02

**Table 2: Model C1v0 Numerical results of lower SMA wire actuators activation**

<b>Radius of SMA Wire Actuators</b>		<b>Percent of Chord Length</b>	<b>Angle <math>\beta</math></b>	<b>MVF</b>	<b>Maximum Stress (Actuators)</b>	<b>Maximum Stress (Composites)</b>
<b>ID</b>	<b>[m]</b>	<b>[%]</b>	<b>[°]</b>		<b>[Pa]</b>	<b>[Pa]</b>
r <sub>1</sub>	0.0005	0	0.000	0.7540	2.6274E+08	1.7758E+06
r <sub>2</sub>	0.001	10	1.481	0.7429	2.6118E+08	6.7059E+06
r <sub>3</sub>	0.0015	20	1.356	0.7262	2.5878E+08	1.3840E+07
r <sub>4</sub>	0.002	30	1.533	0.7049	2.5575E+08	2.3543E+07
r <sub>5</sub>	0.0025	30	1.802	0.6805	2.5226E+08	3.2316E+07
r <sub>6</sub>	0.003	40	2.101	0.6540	2.4846E+08	3.8472E+07

**Table 3: Model C1v0 Predicted  $C_L$  variation for each case study**

<b>Radius of SMA Wire Actuators</b>		<b><math>\Delta C_L</math></b>	
<b>ID</b>	<b>[m]</b>	<b>for a.o.a. 0°</b>	<b>for a.o.a. 4°</b>
r <sub>1</sub>	0.0005	-	-
r <sub>2</sub>	0.001	0.05 up to k = 0.1	0.05 up to k = 0.1
r <sub>3</sub>	0.0015	0.1 up to k = 0.02	0.05 up to k = 0.1
r <sub>4</sub>	0.002	0.1 up to k = 0.1	0.1 up to k = 0.1
r <sub>5</sub>	0.0025	0.15 up to k = 0.07	0.15 up to k = 0.05
r <sub>6</sub>	0.003	0.2 up to k = 0.08	0.2 up to k = 0.07

#### Model C1v4b

This is an alternative of model C1v4 with truss support structure and actuators placed also between web C and tail V.

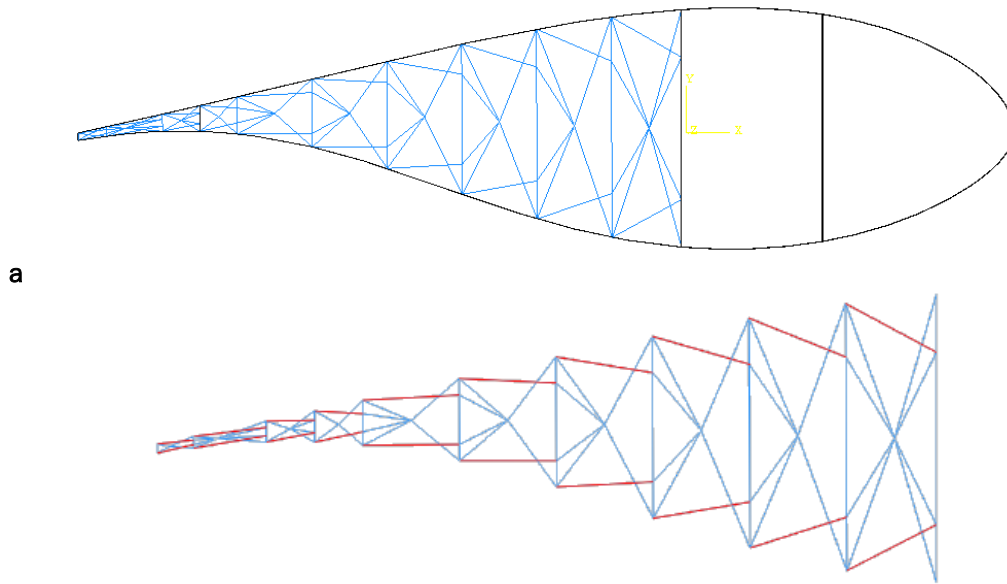


Figure 19: Model C1v4b (a) Implementation of morphing structure and (b) truss structure with the SMA actuators

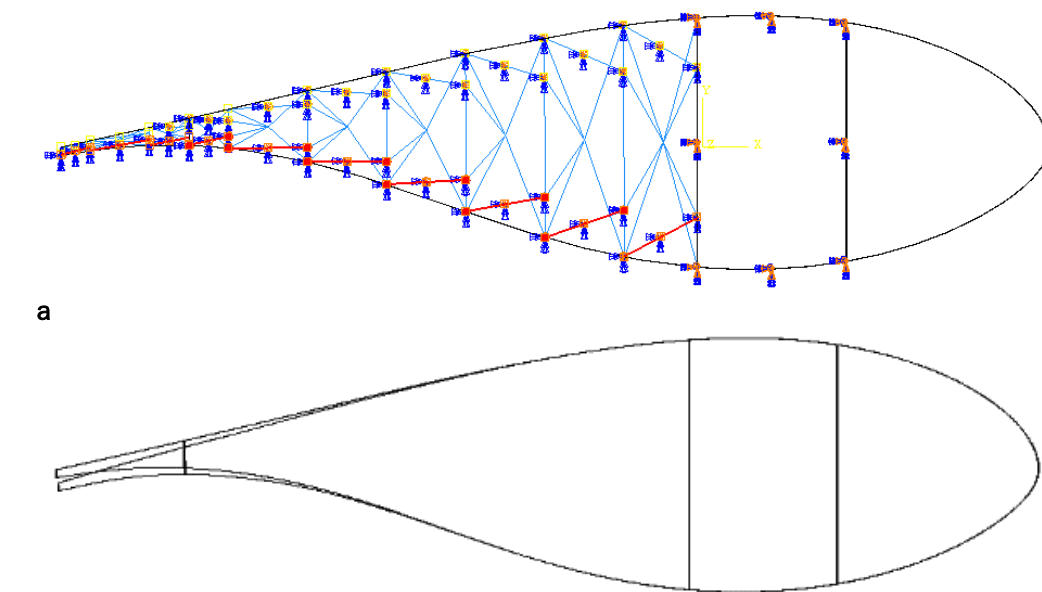


Figure 20: Model C1v4b (a) SMA actuators activated and (b) the undeformed and deformed airfoil in real scale for  $r = 0.003$  m

Table 4: Model C1v4b Effect of SMA wire radius on structural stiffness

Radius of SMA Wire Actuators		Vertical Displacement
ID	Assigned Value [m]	Value [m]
r <sub>1</sub>	0.0005	-1.2912E-02
r <sub>2</sub>	0.001	-1.2374E-02
r <sub>3</sub>	0.0015	-1.1600E-02
r <sub>4</sub>	0.002	-1.0710E-02
r <sub>5</sub>	0.0025	-9.8013E-03
r <sub>6</sub>	0.003	-8.9353E-03

Table 5: Model C1v4b Numerical results of lower SMA wire actuators activation

Radius of SMA Wire Actuators		Percent of Chord Length	Angle $\beta$	MVF	Maximum Stress (Actuators)	Maximum Stress (Composites)
ID	[m]	[%]	[°]		[Pa]	[Pa]
r <sub>1</sub>	0.0005	0	0.000	0.7566	2.6311E+08	2.1533E+06
r <sub>2</sub>	0.001	0	13.314	0.7533	2.6264E+08	8.4484E+06
r <sub>3</sub>	0.0015	10	1.472	0.7481	2.6190E+08	1.8440E+07
r <sub>4</sub>	0.002	20	1.519	0.7410	2.6089E+08	3.1518E+07
r <sub>5</sub>	0.0025	30	1.899	0.7323	2.5965E+08	4.7034E+07
r <sub>6</sub>	0.003	30	2.242	0.7221	2.5821E+08	6.4381E+07

Table 6: Model C1v4b Predicted  $C_L$  variation for each case study

Radius of SMA Wire Actuators		$\Delta C_L$	
ID	[m]	for a.o.a. 0°	for a.o.a. 4°
r <sub>1</sub>	0.0005	-	-
r <sub>2</sub>	0.001	-	-
r <sub>3</sub>	0.0015	0.05 up to k = 0.1	0.05 up to k = 0.1
r <sub>4</sub>	0.002	0.1 up to k = 0.07	0.1 up to k = 0.05
r <sub>5</sub>	0.0025	0.15 up to k = 0.09	0.15 up to k = 0.08
r <sub>6</sub>	0.003	0.2 up to k = 0.03	0.2 up to k = 0.01

### Summary of Interpretation of Analyses Results

In order to address the most effective models of this concept a summary table of the most promising models according to each criterion is created and the model or the models that meet most of the criteria are chosen. According to Table 7 the most promising model is C1v04b followed by C1v0 which are the models presented above.

Table 7: Summary of most promising models of concept category 1 according to specified criteria

Larger Chord Length with Morphing Ability	Angular Rotation $\beta$	Maximum Developed Stress on SMA Wires	Martensitic Volume Fraction $\xi$
C1v00	C1v00	C1v00	C1v03
C1v00b	C1v01b	C1v00b	C1v03b
C1v04	C1v04b	C1v02b	C1v04b
C1v04b		C1v04b	C1v05b
C1v05			
C1v05b			

The selected models are able to achieve satisfying variation in coefficient of lift for a variety of operational conditions (as implied by  $k$  and a.o.a.) due to the combination of portion of chord length with morphing capability and rotational angle. Furthermore, the configurations of the truss elements support the actuators in positions to both bend the airfoil and achieve low variation of martensitic volume fraction which is essential for the fast initiation of reverse transformation to return to initial position. Additionally, the loads imposed by the actuators of these models result in lower developed stresses on airfoil composite structure. Developed stresses in composite structure is a very important parameter because part of this structure should remain intact to provide continuity among morphing section and rest of the blade.

### 2.6.1.2 Concept Category 2: Antagonistic Actuators in Steering Rack Configuration

The second category includes a truss structure that consists of substructures having a layout similar to the one of a steering rack. A simple steering rack structure actuated by SMA wires is presented in Figure 21. The red and green lines represent antagonistic SMA actuator pairs. If the green pair of actuators is activated, moving parts of the structure will rotate around the black axes illustrated with black dashed lines according to the direction implied by the green arrows. Similarly, if the red pair of actuators is activated the structure's moving parts will be rotated according to the direction pointed by the red arrows.

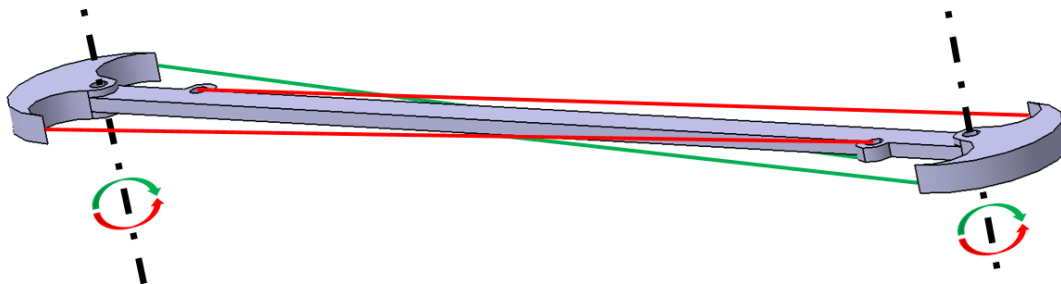
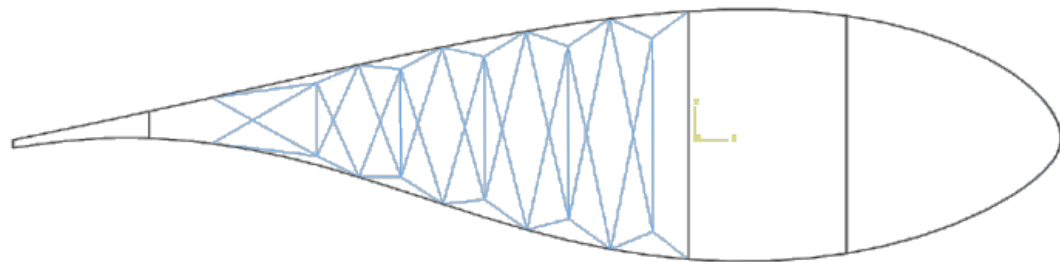


Figure 21: Schematic representation of a steering rack layout

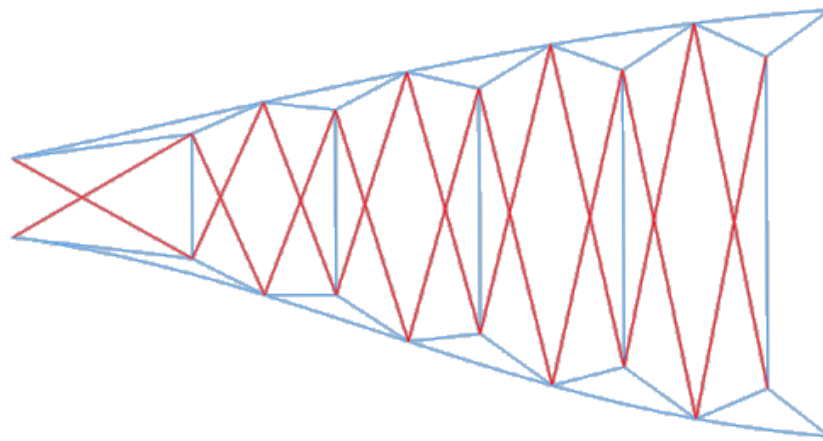
For this category four different truss structure configurations have been considered. After the numerical simulation of the models created, the most promising of the aforementioned four configurations is presented in the following page. The rest of the models with the results that accompany this study are provided in Appendix A.

Model C2v0

The current model utilizes antagonistic SMA wire actuators in a form of multiple steering racks one next to another to morph the airfoil structure. In this model the airfoil skin that shapes the trailing panels is the same as the one of the original airfoil.

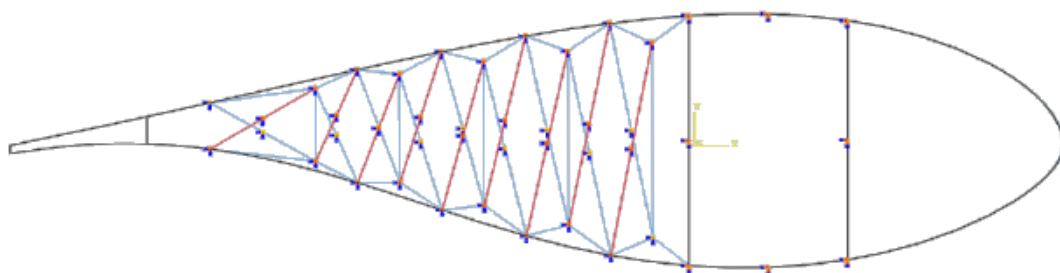


a

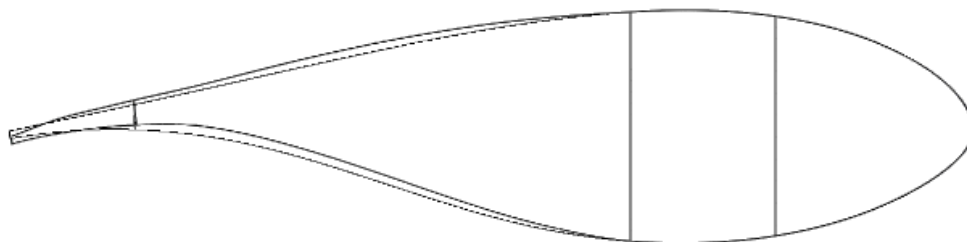


b

Figure 22: Model C2v0 (a) Implementation of morphing structure and (b) truss structure with the sma actuators



a



b

Figure 23: Model C2v0 (a) SMA Actuators Activated and (b) The Undeformed and Deformed Airfoil in Real Scale for  $r = 0.003$  m

Table 8: Model C2v0 Effect of SMA wire radius on structural stiffness

Radius of SMA Wire Actuators		Vertical Displacement
ID	Assigned Value [m]	Value [m]
r <sub>1</sub>	0.0005	-1.5619E-02
r <sub>2</sub>	0.001	-1.2731E-02
r <sub>3</sub>	0.0015	-1.1886E-02
r <sub>4</sub>	0.002	-1.1540E-02
r <sub>5</sub>	0.0025	-1.1365E-02
r <sub>6</sub>	0.003	-1.1264E-02

Table 9: Model C2v0 Numerical results of lower sma wire actuators activation

Radius of SMA Wire Actuators		Percent of Chord Length	Angle $\beta$	MVF	Maximum Stress (Actuators)	Maximum Stress (Composites)
ID	[m]	[%]	[°]		[Pa]	[Pa]
r <sub>1</sub>	0.0005	50	0.392	0.7349	2.6003E+08	1.8765E+07
r <sub>2</sub>	0.001	60	0.395	0.6858	2.5302E+08	5.8068E+07
r <sub>3</sub>	0.0015	60	0.408	0.6355	2.4582E+08	9.5941E+07
r <sub>4</sub>	0.002	60	0.434	0.5928	2.3967E+08	1.2514E+08
r <sub>5</sub>	0.0025	60	0.466	0.5566	2.3443E+08	1.4658E+08
r <sub>6</sub>	0.003	60	0.478	0.5249	2.2982E+08	1.6256E+08

Table 10: Model C2v0 Predicted  $C_L$  variation for each case study

Radius of SMA Wire Actuators		$\Delta C_L$	
ID	[m]	for a.o.a. 0°	for a.o.a. 4°
r <sub>1</sub>	0.0005	0.05 up to k = 0.02	-
r <sub>2</sub>	0.001	0.05 up to k = 0.02	-
r <sub>3</sub>	0.0015	0.05 up to k = 0.03	0.05 up to k = 0.02
r <sub>4</sub>	0.002	0.05 up to k = 0.06	0.05 up to k = 0.05
r <sub>5</sub>	0.0025	0.05 up to k = 0.1	0.05 up to k = 0.08
r <sub>6</sub>	0.003	0.05 up to k = 0.1	0.05 up to k = 0.1

In order to identify the model with the most promising results a table containing the best models according to each different criterion is formed. Table 11 summarizes the criteria and the eligible models. The model that meet the most of the required specifications is model C2v0, but the produced results prove that although the models of this concept achieve a high percentage of chord length with moving ability, the combination with a small angular rotation is insufficient for morphing purposes.

**Table 11: Summary of most promising models of concept category 2 according to specified criteria**

Larger Chord Length with Morphing Ability	Angular Rotation $\beta$	Maximum Developed Stress on SMA Wires	Martensitic Volume Fraction $\xi$
C2v01	C2v00	C2v00	C2v00
C2v02	C2v00b	C2v00b	C2v01
			C2v02

The models of this concept category are able to move larger portion of the chord's length compared to those of concept 1. This outcome is based on the different functional principle. Concept 2 models have multiple steering racks placed perpendicularly to the chord and next to each other. Each steering rack uses wires of larger length thus the transformation strain produced leads to larger movement because the same strain leads to larger displacement if the wire at the initial state is longer. Unlikely to the high percentage of chord length with mobility, the angular rotation achieved is lower compared to the results of models of concept 1. Also the developed stresses on both actuators and composite parts are increased, in some cases more than an order of magnitude. Furthermore, results of model C2v0 and C2v0b prove that altering connection between airfoil parts and separation of skin to different portions does not have a significant impact on airfoil's morphing performance due to the fact that the truss support structure maintains or even reinforces stiffness of the overall structure. The most interesting outcome from this concept models is the effectiveness of using multiple antagonistic actuators in form of an equivalent mechanism distributed along the chord of the airfoil.

### 2.6.1.3 Concept Category 3: Single SMA Wire Actuator with Large Leverage

Finally, models forming the last category take advantage of a large lever provided for the SMA wire actuator to bend the airfoil to one direction. It is assumed that the models of this concept do not need an antagonistic wire and that adequate cooling of the SMA actuator can return the airfoil to its initial position. The truss structures involved in the models of this concept are simpler in comparison with the concept 1 and concept 2 and can be easily tuned. Results provided by the following models simulation runs are essential to prove the effectiveness of a single actuator vs. antagonistic actuators. In the following pages, the two most promising models are presented while the rest of the models are presented in Appendix A along with the detailed results analysis.

**Model C3v1**

Is an alternative of the model C3v0, but here the distance of the right point supporting SMA wire actuator from the upper aerodynamic surface is set to be 60 % of the distance between the aerodynamic surfaces.

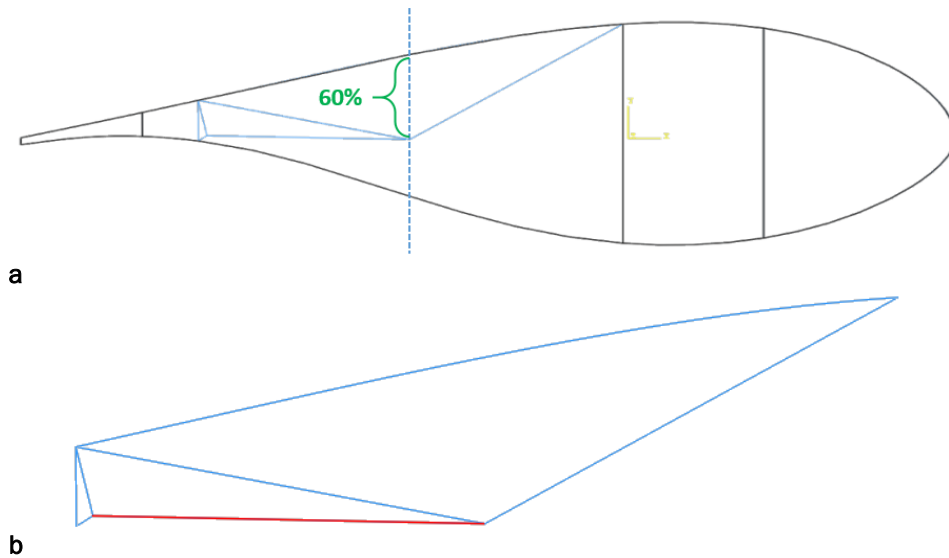


**Figure 24: Model C3v1 (a) Implementation of morphing structure and (b) truss structure with the SMA actuators**

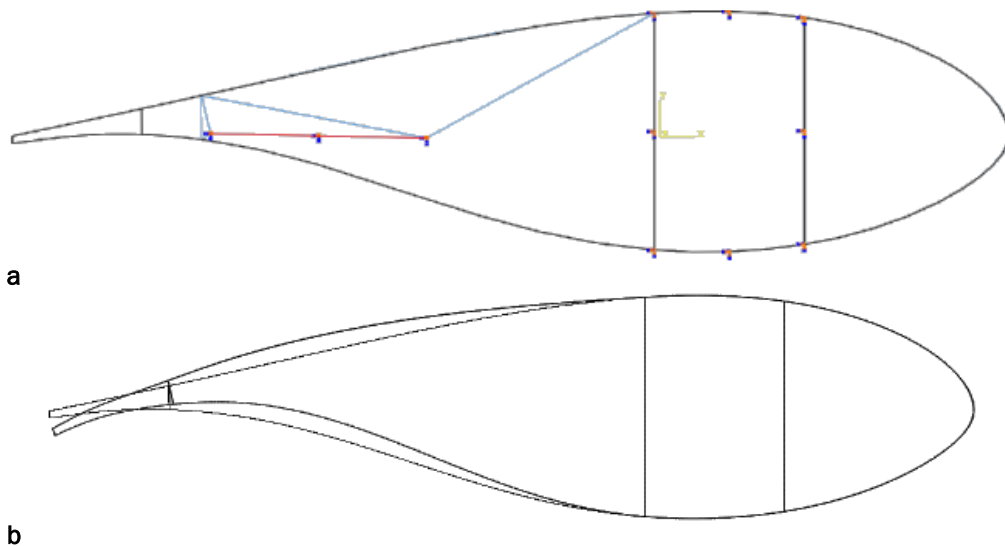


**Figure 25: Model C3v1 (a) SMA actuators activated and (b) the undeformed and deformed airfoil in real scale for  $r = 0.003$  m**

**Table 12: Model C3v1 Effect of SMA wire radius on structural stiffness**

Radius of SMA Wire Actuators		Vertical Displacement
ID	Assigned Value [m]	Value [m]
r <sub>1</sub>	0.0005	-3.0293E-02
r <sub>2</sub>	0.001	-2.2841E-02
r <sub>3</sub>	0.0015	-1.9258E-02
r <sub>4</sub>	0.002	-1.7542E-02
r <sub>5</sub>	0.0025	-1.6631E-02
r <sub>6</sub>	0.003	-1.6100E-02

**Table 13: Model C3v1 Numerical results of lower SMA wire actuators activation**

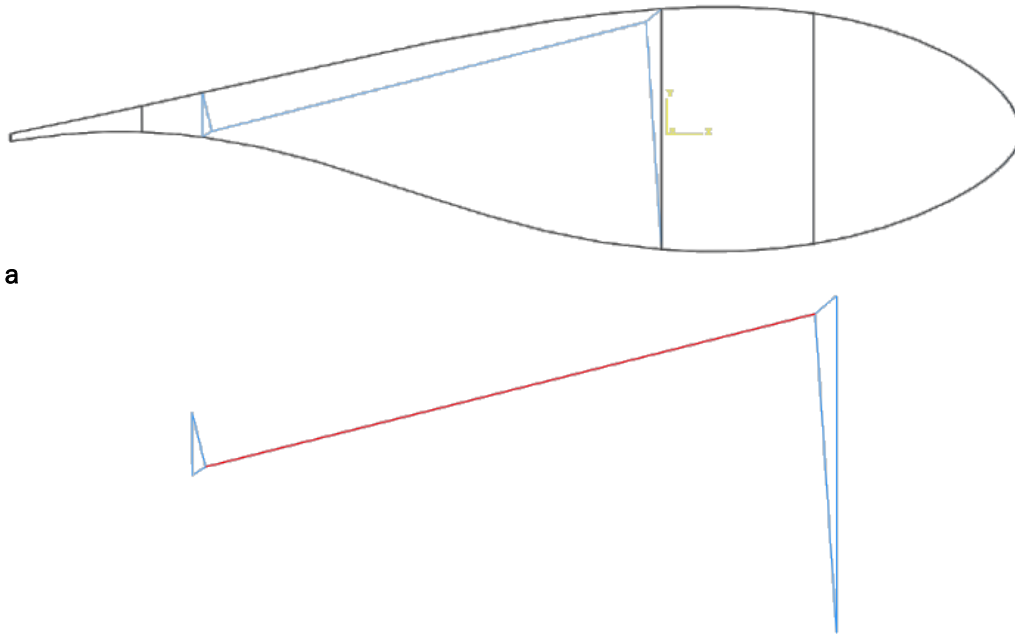
Radius of SMA Wire Actuators		Percent of Chord Length	Angle $\beta$	MVF	Maximum Stress (Actuators)	Maximum Stress (Composites)
ID	[m]	[%]	[°]		[Pa]	[Pa]
r <sub>1</sub>	0.0005	40	0.336	0.6576	2.4898E+08	2.9450E+07
r <sub>2</sub>	0.001	50	0.904	0.4091	2.1286E+08	1.0071E+08
r <sub>3</sub>	0.0015	60	1.544	0.1192	1.6940E+08	1.8033E+08
r <sub>4</sub>	0.002	60	1.827	0.0000	1.1399E+08	2.1572E+08
r <sub>5</sub>	0.0025	60	1.860	0.0000	7.4327E+07	2.1979E+08
r <sub>6</sub>	0.003	60	1.878	0.0001	5.2150E+07	2.2206E+08

**Table 14: Model C3v1 Predicted  $C_L$  variation for each case study**

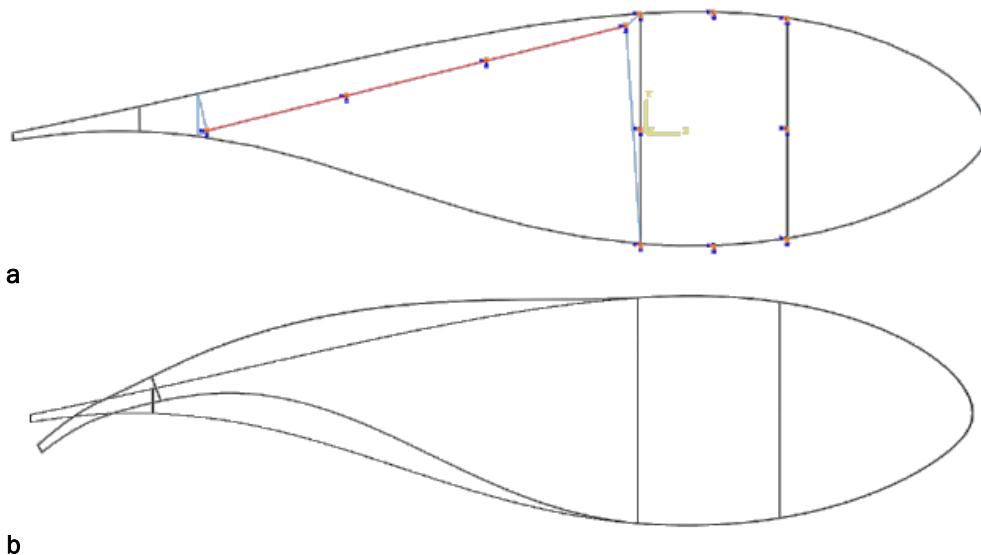
Radius of SMA Wire Actuators		$\Delta C_L$	
ID	[m]	for a.o.a. 0°	for a.o.a. 4°
r <sub>1</sub>	0.0005	-	-
r <sub>2</sub>	0.001	0.1 up to k = 0.08	0.1 up to k = 0.07
r <sub>3</sub>	0.0015	0.15 up to k = 0.1	0.15 up to k = 0.1
r <sub>4</sub>	0.002	0.2 up to k = 0.09	0.2 up to k = 0.07
r <sub>5</sub>	0.0025	0.2 up to k = 0.1	0.2 up to k = 0.08
r <sub>6</sub>	0.003	0.2 up to k = 0.1	0.25 up to k = 0.08

#### Model C3v4

In comparison with model C3v3, this one has a reverted support near web B, meaning that instead of being near lower aerodynamic surface, the support point of the right end of the actuator is near upper aerodynamic surface. Thus the actuator is placed in a diagonal orientation.



**b**  
**Figure 26: Model C3v4 (a) Implementation of morphing structure and (b) truss structure with the SMA actuators**



**b**  
**Figure 27: Model C3v4 (a) SMA actuators activated and (b) the undeformed and deformed airfoil in real scale for  $r = 0.003$  m**

Table 15: Model C3v4 Effect of SMA wire radius on structural stiffness

Radius of SMA Wire Actuators		Vertical Displacement
ID	Assigned Value [m]	Value [m]
r <sub>1</sub>	0.0005	-3.8957E-02
r <sub>2</sub>	0.001	-3.4010E-02
r <sub>3</sub>	0.0015	-3.0710E-02
r <sub>4</sub>	0.002	-2.8815E-02
r <sub>5</sub>	0.0025	-2.7707E-02
r <sub>6</sub>	0.003	-2.7025E-02

Table 16: Model C3v4 Numerical results of lower SMA wire actuators activation

Radius of SMA Wire Actuators		Percent of Chord Length	Angle $\beta$	MVF	Maximum Stress (Actuators)	Maximum Stress (Composites)
ID	[m]	[%]	[°]		[Pa]	[Pa]
r <sub>1</sub>	0.0005	40	0.305	0.7048	2.5574E+08	2.9843E+07
r <sub>2</sub>	0.001	50	0.886	0.5611	2.3507E+08	1.0973E+08
r <sub>3</sub>	0.0015	60	1.663	0.3639	2.0617E+08	2.1654E+08
r <sub>4</sub>	0.002	60	2.459	0.1544	1.7475E+08	3.2629E+08
r <sub>5</sub>	0.0025	60	3.044	0.0001	1.3947E+08	4.0691E+08
r <sub>6</sub>	0.003	60	3.103	0.0001	9.8754E+07	4.1488E+08

Table 17: Model C3v4 Predicted  $C_L$  variation for each case study

Radius of SMA Wire Actuators		$\Delta C_L$	
ID	[m]	for a.o.a. 0°	for a.o.a. 4°
r <sub>1</sub>	0.0005	-	-
r <sub>2</sub>	0.001	0.1 up to k = 0.07	0.1 up to k = 0.06
r <sub>3</sub>	0.0015	0.2 up to k = 0.04	0.2 up to k = 0.03
r <sub>4</sub>	0.002	0.3 up to k = 0.04	0.3 up to k = 0.02
r <sub>5</sub>	0.0025	0.35 up to k = 0.06	0.35 up to k = 0.04
r <sub>6</sub>	0.003	0.35 up to k = 0.07	0.35 up to k = 0.05

In the following table (Table 18) the most promising models of this concept for each one of the criteria studied are summarized. The models that are most consistent with the specified criteria are models C3v1 and C3v4. Models of this concept category proved that even using one SMA wire actuator is possible to morph the airfoil. Although this means a simpler support structure with less additional weight and parts it also mean that retracting phase is difficult to control and adequate cooling of the actuator must be ensured. Furthermore, the low number of truss elements used does not entail that the added elements do not increase drastically the stiffness of the overall structure.

Table 18: Summary of most promising models of concept category 3 according to specified criteria

Larger Chord Length with Morphing Ability	Angular Rotation $\beta$	Maximum Developed Stress on SMA Wires	Martensitic Volume Fraction $\xi$
C3v01	C3v00	C3v00	C3v03
C3v02	C3v01	C3v01	C3v04
C3v04	C3v04	C3v02	C3v05

At this point it should be noted that the limited results produced by the aforementioned model concepts are mainly driven by the fact that a structure has been implemented in the original airfoil without any changes regarding materials, connection joints etc. A simple way to increase the capabilities of the most promising models is to study the effect a modification of the joints of the airfoil on its response when the actuator is activated. For example if model C3v4 is considered and the proper pin joints are placed near connections of web C with tail A, the result in the deformed shape when using an actuator with 0.5 mm radius is shown in Figure 28. The morphed airfoil is shaped more easily because it operates as a mechanism with moving parts, but in order to be effective a further study must take place.

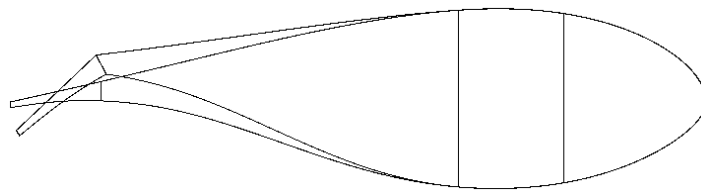


Figure 28: Deformed shape of model c3v4 after alternation of joints

### **Summary of Results**

The structural response of each morphing concept entailing SMA actuators and a support truss structure has been investigated. Models belonging in the category of concept 1 have proved that the use of successive actuators in an antagonistic configuration result in an effective angular rotation while the developed stresses on both the actuators and the composite structure have remained in low levels. However this concept category fails to provide mobility of a larger portion of the chord length. The disadvantage of concept 1 models is overcome by concept 2 models which can achieve mobility of a large portion of chord length. The developed stresses on composite structure are higher while the developed stresses on SMA actuators are of the same level. The main disadvantage of concept 2 is that the large length of the chord that is able to move is not accompanied by an adequate angular rotation in order to achieve the required variation of lift coefficient. Finally, models of concept 3 proved that only one actuator placed on a proper simple support structure can lead to movement of a large portion of chord length with an adequate angular rotation, but without an antagonistic actuator the retracting phase cannot be controlled. Furthermore, the simplicity of the support structure does not lead necessarily to small variation in overall structural stiffness. Thus, the support structure must be implemented in a more continuous manner with original airfoil and combined with direct changes in joints between both the structural parts of the airfoil and the implemented structure with the airfoil parts. In the next section the conclusions derived from the above concepts are going to be taken into consideration and provide information for the design of morphing mechanisms.

## **2.7 Implementation of Morphing Mechanism**

As it is proved from the previous section, a morphing mechanism with slotted skin or altered joints between structural parts can be more efficient. The following mechanism concepts consist of Shape Memory Alloy actuators and parts of a mechanism. All the mechanism parts are initially modelled using properties of aluminium 2024 which is stiff and is widely used for aerospace applications. Use of this material is considered only at initial numerical simulations whereas in future study will be replaced with foam to lower the weight of the structure. For simulation purposes the inertial effects of the structure were neglected as well as the aerodynamic loads acting on the airfoil. The purpose of the following part of the study is to address the most promising mechanism concept regarding the kinematics behaviour and structural response when actuators are operating.

### 2.7.1 Morphing Mechanism Concept 1a and 1b

This concept has two similar versions which utilize a mechanism implemented between web B and web C and a SMA wire actuator, as shown in Figure 29 A and Figure 30 A. Concept 1a consists of one immobile part ( $P_a$ ) which is shaped to hold rod  $r_a$  and have two curved surfaces with specific geometry. The one curved surface is the path that rod  $r_a$  follows when actuator is activated. Rod  $r_a$  carries part  $P_c$  which is connected with lower aerodynamic surface of the skin and slides on the curved path formed on  $P_a$  because of the slotted edge between part  $P_a$  and  $P_c$  (red circle with arrow pointer). When part  $P_c$  moves rods  $r_b$ ,  $r_c$  and  $r_d$  transfer motion to part  $P_b$  and the airfoil is morphed. The upper surface of part  $P_a$  which is close to the upper aerodynamic surface is shaped in such a way to hold and shape the skin during morphing in order to retain a continuous aerodynamic surface. Concept 1b is designed in a similar way. The difference lies in the replacement of the rods and parts  $P_b$  and  $P_c$  with a single part noted as  $P_b$  in Figure 30 A. The lower aerodynamic surface is slotted at the position of the red circle pointed with the red arrow. Part  $P_b$  is tied with lower aerodynamic surface while it is also connected with upper aerodynamic surface through a pin joint indicated by the upper left circle in Figure 30 A. The shape of upper surface of part  $P_b$  is properly designed in order to shape the airfoil skin in a manner that it creates a continuous and smooth aerodynamic surface.

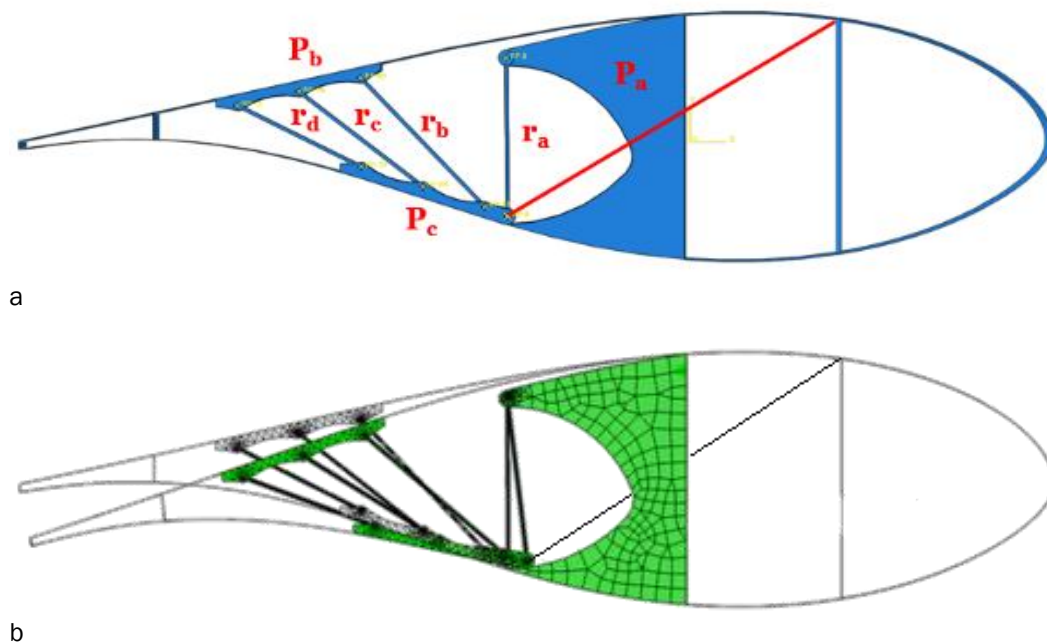
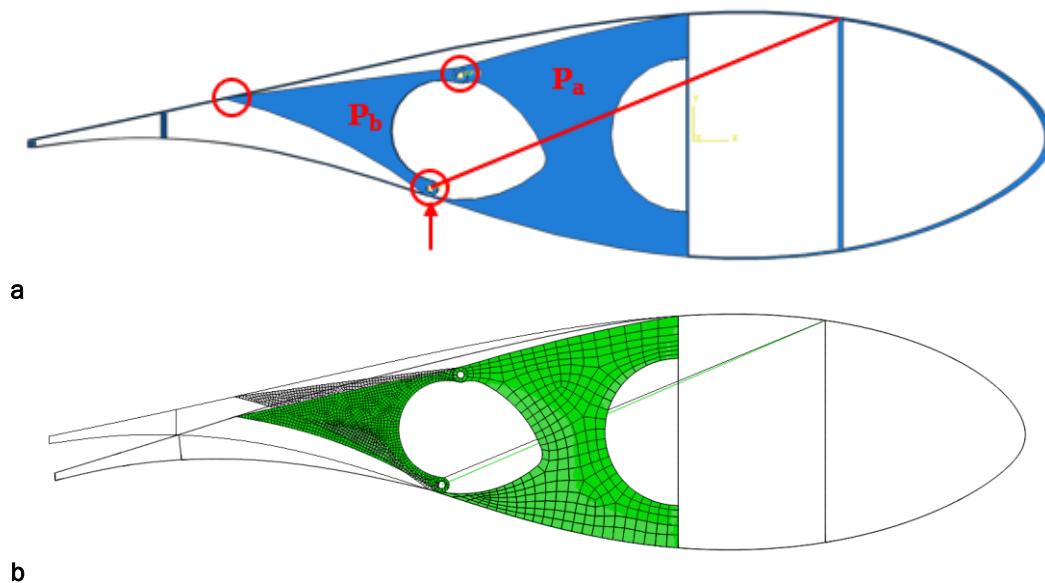


Figure 29: Morphing Mechanism Concept 1a (a) Overall configuration and (b) Morphing state during activation of SMA wire actuators



**Figure 30: Morphing mechanism concept 1b (a) Overall configuration and (b) Morphing state during activation of SMA wire actuators**

The response of concept 1 mechanisms was simulated using SMA wire actuators with a 0.5 mm radius and the deformed structure is presented in Figure 29 B and Figure 30 B, respectively. The angular rotation the first mechanism version has achieved is  $14^\circ$  and the portion of the chord length that was able to move was over 40% while the second version of the mechanism was rotated about  $10^\circ$  and the portion of the chord length with morphing capability was almost 40%. The results regarding the maximum developed stresses on the SMA wire actuators and composite parts of the airfoil were 15 MPa and 4 MPa respectively for version a and 22 MPa and 2.5 MPa respectively for version b of the mechanism concept. Preserving the upper aerodynamic surface, deflection of original position to the maximum provided angle as well as the control of overall stiffness by adjusting the position of the mechanism parts are the main advantages of this concept. The produced results indicate that version b of the mechanism concept is more stiff which can be explained by the fact that part  $P_B$  is a solid part while in version a this part is in form of rods that bridge upper and lower surfaces and transfer motion. The main disadvantages of this concept include the disability of upper surface to provide enough bias load to retract the initial position, the lack of control for the retracting phase, the difficulty to control the centre of rotation and the requirement of power in order to maintain the undeformed configuration during aerodynamic loading of the skin. Furthermore, addressing the centre of rotation of the mechanism is challenging because its position varies due to the elastic deformation of the skin.

### 2.7.2 Morphing Mechanism Concept 2

For this concept antagonistic SMA wire actuators are considered. The main mechanism consists of two discrete parts that are connected through a pin joint. First part is noted as “Case” in Figure 31 A, it is immobile and is attached rigidly on web B of the airfoil. Inside the case there are two antagonistic SMA wire actuators that are arranged in an “X” configuration and have one of their end pinned at the moving part of the mechanism. The moving part and the actuators are presented in Figure 31 B where the SMA wires are highlighted with red colour. The branches of moving part are carefully shaped in order to provide continuous aerodynamic surfaces at any angular rotation. Moreover, moving part’s branches and trailing edge are connected with pinned joints that allow a rotation of few degrees between those parts in order to achieve more possible morph shapes. Although the shapes of the parts are designed to provide smooth surfaces during activation of actuators and subsequent rotation of the mechanism, there are two slots, one on the upper and one on the lower surface that need to be bridged in order to maintain the aerodynamic

surfaces. Bridging of those slots may be performed either by an elastomeric skin or by another flexible material.

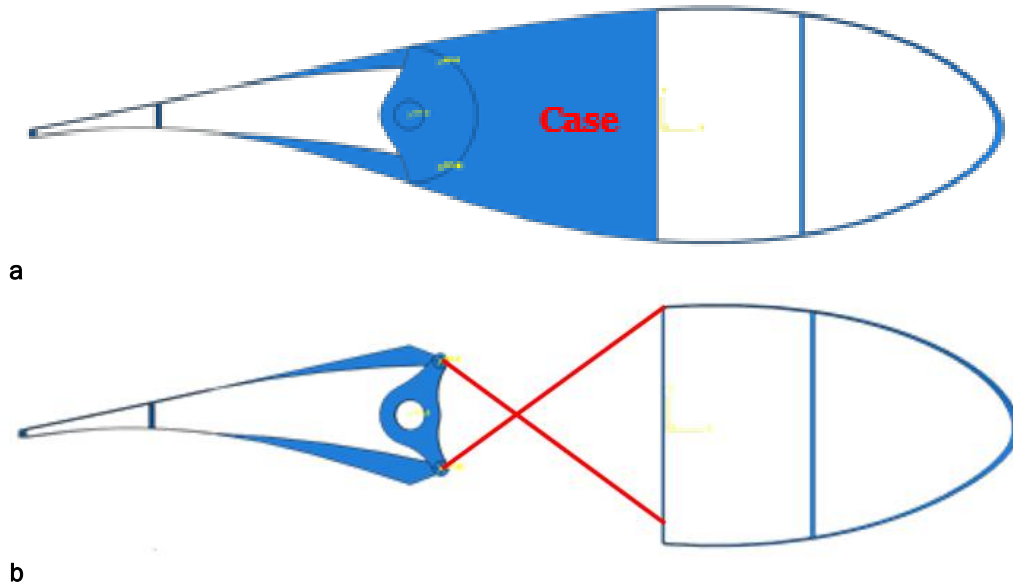


**Figure 31: Morphing mechanism concept 2 (a) Overall configuration and (b) The morphing mechanism without the “case” part**

This mechanism concept has the main advantage of being deflected from its initial position in both upwards and downwards because of the antagonistic actuators implied. Centre of rotation is known and can be adjusted according to the design and analysis specifications. Significant drawback is the difficulty in manufacturing and the complexity in the design and control of the pin joints that connect the moving part of the mechanism with the trailing edge. The lack of precise control when high aerodynamic loads act on airfoil’s surfaces might lead to unstable response of the flap. In Figure 32 the deformed body of the airfoil is presented after the activation of the SMA actuator responsible for moving the mechanism downwards. The maximum developed stress on the actuators was approximately 202 MPa while the rotational angle was calculated to 16° and portion of the chord with moving capability was calculated at about 40%.

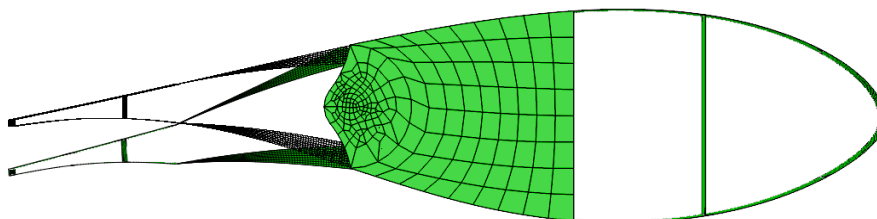


**Figure 32: Morphing mechanism 2 deformed body of the structure after SMA actuators activation**

### 2.7.3 Morphing Mechanism Concept 3

The concept presented here is similar with the mechanism concept 2 regarding the actuators configuration and the assembly between an immobile part and the flap of the mechanism. Except of the two main parts of the mechanism there are also two parts that are used to bridge the slots indicated with red arrows in Figure 33 A. These parts are presented more clearly in Figure 33 B where their ends are highlighted with the red circle indicators. Each cap has its right end connected through pin joints with the “case” of the mechanism while its left end is in contact with the moving part of the mechanism. If the moving part is rotated, for example, counter clock wise

then the upper cap is pushed upwards. In order the lower cap to follow the motion of the flap and preserve contact between them a twist spring is embedded in pin support. Similarly, a twist spring is embedded in pin support of the upper cap to preserve contact between cap and flap when flap rotates clock wise.

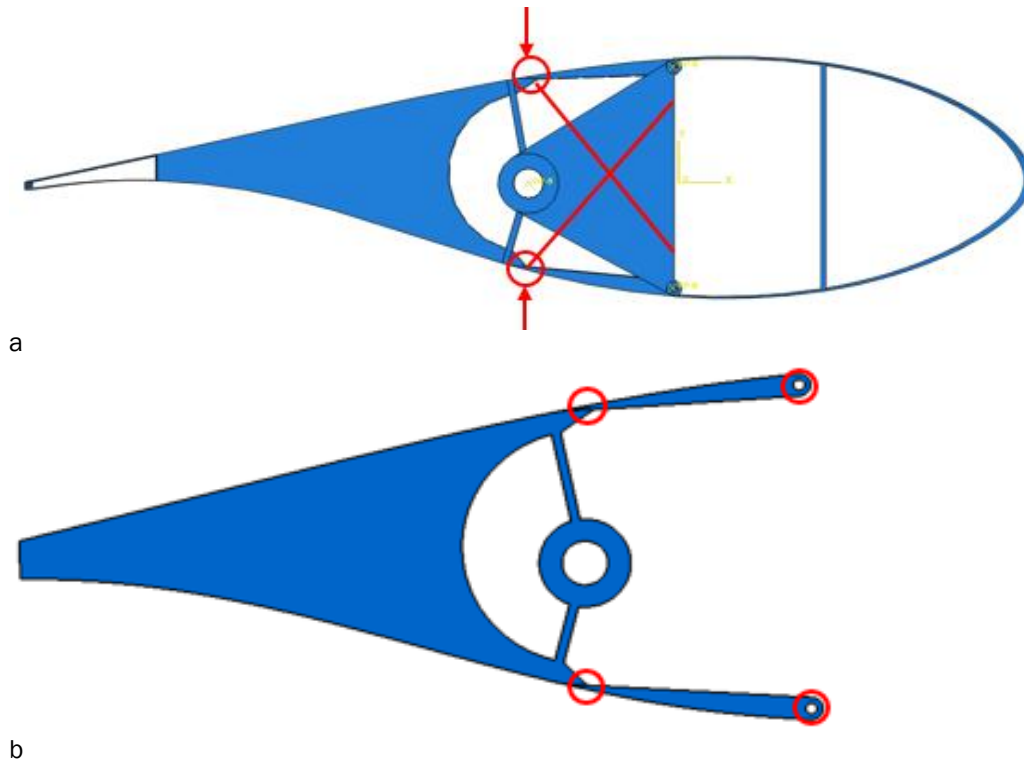


**Figure 33: Morphing mechanism concept 3 (a) Overall configuration and (b) the flap part with bridging caps**

In this concept category, the aerodynamic surfaces are preserved. Though the slots located in various locations of the skin allow the upwards and downward movement of the morphing trailing edge. Additionally this concept provides a known centre of rotation that can be adjusted to address the required specifications. However the realization of this concept is envisioned to be difficult due to the complexity of the shape of the caps and the flap. Furthermore, the contact between moving parts lead to friction forces that might cause wear to the mechanism surfaces. Finally, the mechanism is more of a flap than a morphing concept thus is not suitable to be considered for further study, thus there are no numerical results regarding its response.

#### 2.7.4 Morphing Mechanism Concept 4

The morphing mechanism of this concept was optimized through the design and testing of different versions. It is oriented in providing distributed moving parts along the camber line in order to achieve various morphing shapes. The main concept is based on the results of the preliminary study with implementation of truss support elements for the SMA wire actuators. The configuration of the first version (4a) of the mechanism parts and the SMA actuators is presented in Figure 34 A. Actuators are antagonistic and bridge mechanism part  $P_1$  attached to web B with the mechanism part  $P_5$  attached to web C. Each actuator passes through channels of the mechanism parts  $P_2$ ,  $P_3$  and  $P_4$ . Between each successive pair of mechanism parts there is a pin joint that allows rotation between them. When an actuator, for example the one near lower surface, is activated the airfoil bends in the respective direction as shown in Figure 34 B. The main disadvantage of this version is that due to the shape of the parts  $P_2$ ,  $P_3$  and  $P_4$  and their pin joints the actuator wires cannot transfer effectively the force generated from transformation.

Moreover, the use of only one actuator for each movement (upwards or downwards) does not provide enough control to rotate each part individually.

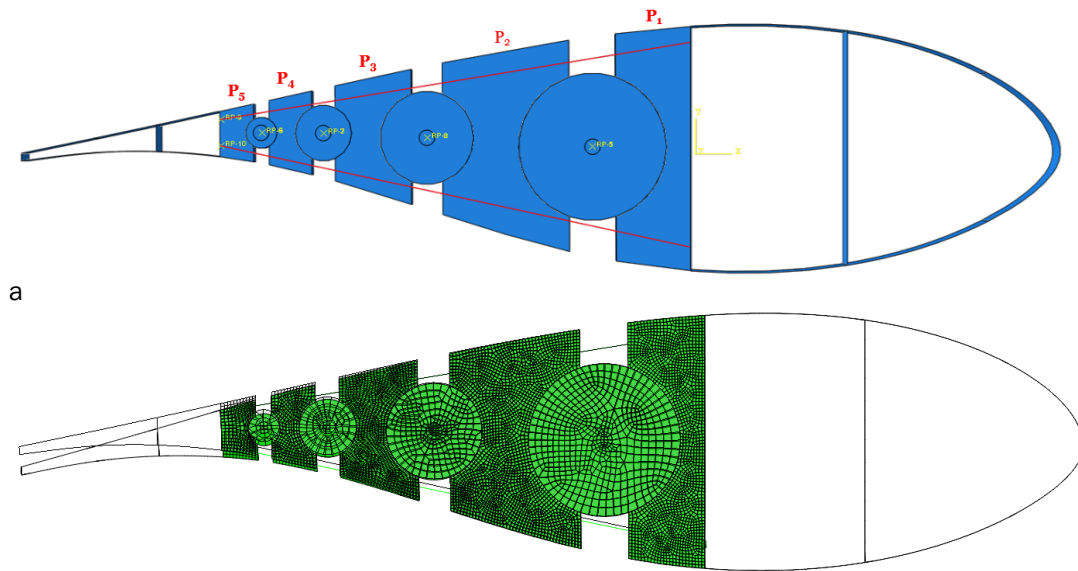


**Figure 34: Morphing mechanism concept 4 (a) Overall configuration and (b) morphing state during activation of SMA wire actuators**

Because of the difficulties observed in first version an updated design of the mechanism was created and considered as version b. The general layout remained the same but the pins were downsized and the mechanism parts shaped in a more efficient way. Also the SMA wire actuators were placed as antagonistic pairs for each one of the mechanism parts in order to provide advanced control of the airfoil morphing shape. In Figure 35 A the general layout of the morphing mechanism is presented with the actuators highlighted with red color while in Figure 35 B the morphed state is shown. Considering that the simulation of mechanism response was performed for the same conditions in case of version a and version b of the mechanism the difference in response is more than obvious. By heating lower actuators from their initial temperature of 310 K to a temperature of 350 K, simulations of version a exhibited a rotation of 6.5° combined with movement of 20% of chord length while numerical results of model of version b proved rotational angle of 20° with movement capability of 40% of chord length. Furthermore, the maximum developed stress on the actuators of version a was 345 MPa which is above the specification defined in the previous sections while the same stress for version b was 248 MPa. Consequently, version b of the concept 4 is indeed an optimized version with improved capabilities. An additional advantage of this version is that the centers of rotation of the mechanism parts are known because each one of them can rotate independently from the others. Also the SMA actuator pairs can control the stiffness of the structure by proper adjustment of their geometrical characteristics. The only drawback of this version is the complexity of the mechanism regarding the large number of moving parts and the number of actuators involved.

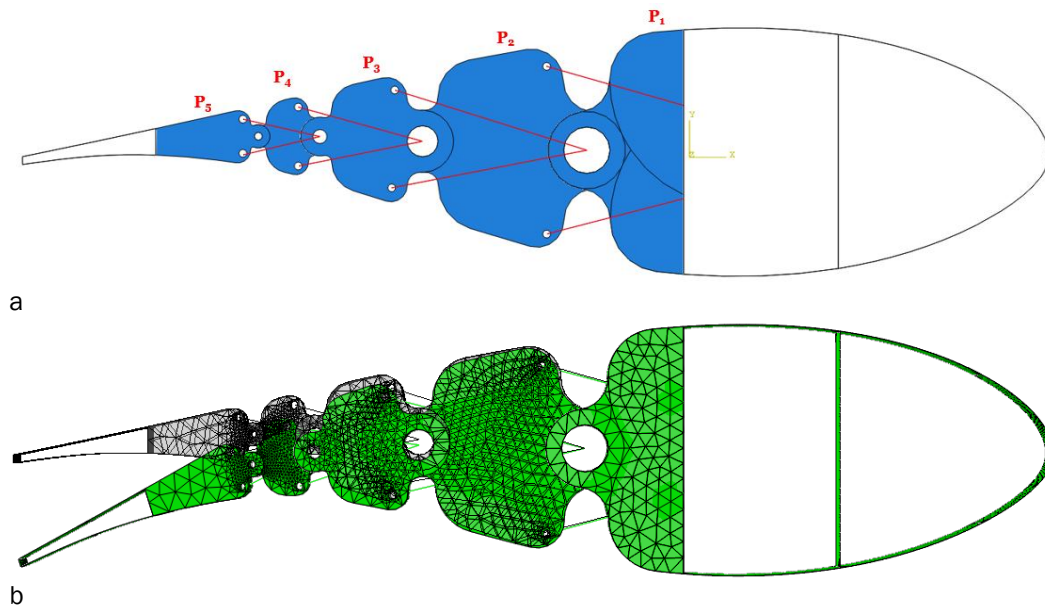


Figure 35: Morphing mechanism concept 4b (a) overall configuration and (b) morphing state during activation of SMA wire actuators

## 2.8 Downselected Morphing Mechanism

The complexity of the mechanism is a vital issue for the feasibility of the morphing concept, thus the version b of the concept mechanism was further improved regarding the simplification of the configuration of the moving parts and SMA wire actuator pairs. The final version of the downselected mechanism configuration is presented in Figure 36. In this configuration the mechanism consists of four rigid parts, three with moving capability and one immobile. The immobile part is fixed on web B of the original airfoil structure while the other parts are pinned with each other and restrained by the SMA wire actuators that are indicated with red colour. The positions of the pin joints are placed on the camber line of the original airfoil geometry.

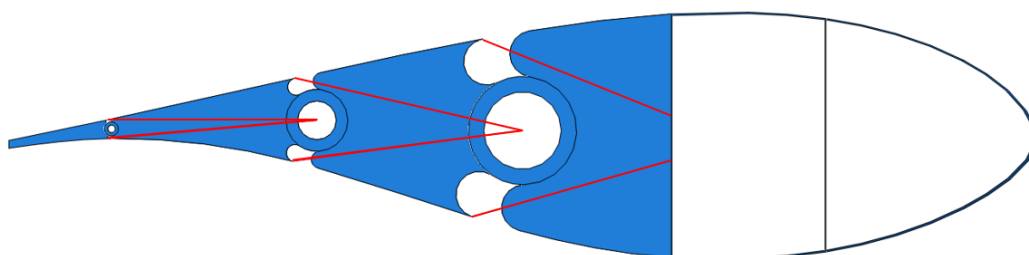
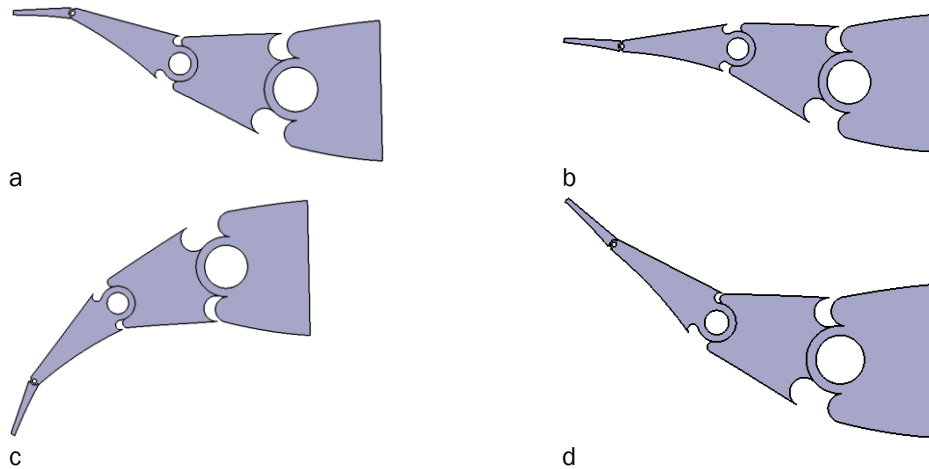


Figure 36: Morphing mechanism concept 4c

Each one of the moving parts of the mechanism structure can move independently, thus there can exist numerous combinations that can satisfy a wide variety of morphing shapes. In Figure 37 few of the mechanism morphing capabilities are presented. The only limitation for mechanism movement comes from the position of the SMA wire actuators which are restricted to move inside the boundaries of the aerodynamic surfaces. It must be noted that this mechanism concept requires large slots on the skin to provide the required space for the moving parts to rotate and move to the desired positions.



**Figure 37: Kinematic capabilities and morphing functionality of the mechanism**

The capabilities of the morphing mechanism combined with the excellent numerical results that prove maximum developed stresses in SMA wire actuators under 240 MPa lead to the approval of this version of the concept as the optimum among the cases studied. In Table 19 the specifications used to assess the different concepts are summarized and the values from the numerical simulations are presented.

**Table 19: Specifications comparison of morphing concepts**

Concept	Complexity	Chord Length Activated [%]	Angular Rotation [°]	Stress (Actuators) [MPa]	Stress (Composites) [MPa]	Martensitic Volume Fraction	$\Delta C_L$
1a	High	40	14	15	4	0.99	0.35
1b	Average	40	10	22	2.5	0.99	0.35
2	Low	40	16	202	0	0.35	0.35
3	High	N/A	N/A	N/A	N/A	N/A	N/A
4a	High	20	6.5	345	0	0.01	0.25
4b	Average	40	20	248	0	0.57	0.35
4c	Low	10	13.35	239	0	0.49	0.25
4c	Low	30	8.25	239	0	0.49	0.30
4c	Low	50	6.25	239	0	0.49	0.40

Among the designed and modelled morphing mechanism concepts, the selected concept provides the largest variation in coefficient of lift when all the mechanism parts are activated and 50% of chord length moves. The maximum angular rotation of the tip of the trailing edge is 6.25° when the lower set of actuators is activated and heated up to 350 K (initial temperature: 310 K). As mentioned above, the developed stress on the actuators is below 240 MPa and the martensitic volume fraction is approximately 0.5 regardless of the moving part under the specific activation conditions (initial value of MVF = 0.2). The developed stress is much higher than the value of morphing mechanism concepts 1a and 1b. This can be explained by the fact that the aforementioned concepts do not have antagonistic actuators and as a result cannot provide both upwards and downwards movement of the mechanism. Hence, the selected concept is considered superior. Moreover, it provides known centre of rotation for each moving part and every centre is located on the camber line of the airfoil, so the morphing shape is more continuous.

## 2.9 Numerical Simulations of the Downselected Concept

### 2.9.1 Morphing without Aerodynamic Pressure Loads

In this section the response of the selected morphing mechanism under extreme operation requirements will be presented, assessed and discussed. As it was mentioned in previous sections, the morphing mechanism has the capability of moving 10, 30 and 50 % of airfoil chord length both upwards and downwards as independent equivalent flaps or combined. For simplicity reasons, the numerical simulations performed are focused on moving independently each of the three moving parts in order to address the effect of their activation separately. Thus there are three cases that are investigated, one for each independent moving part. For every case the initial temperature of the SMA wire actuators is set to 310 K and heat is provided during their activation until their temperature reaches 600 K (almost doubled). The maximum temperature value is selected way above the  $A_f$  temperature to ensure that the actuator will present the maximum available transformation strain and consequently the maximum actuation force. Thus the martensitic volume fraction for the undeformed shape and initial configuration is set equal to 1. Finally, the radius of all the wire actuators is set to 2.5 mm and the total time for the simulation run was defined to be 60 seconds (1 minute).

#### 2.9.1.1 Case 1: Morphing Mechanism at 10% of Chord Length Activated

Starting with morphing mechanism part representing 10% of chord length, the maximum deflection in downwards and upwards movement is presented in Figure 38 A and Figure 38 B respectively.

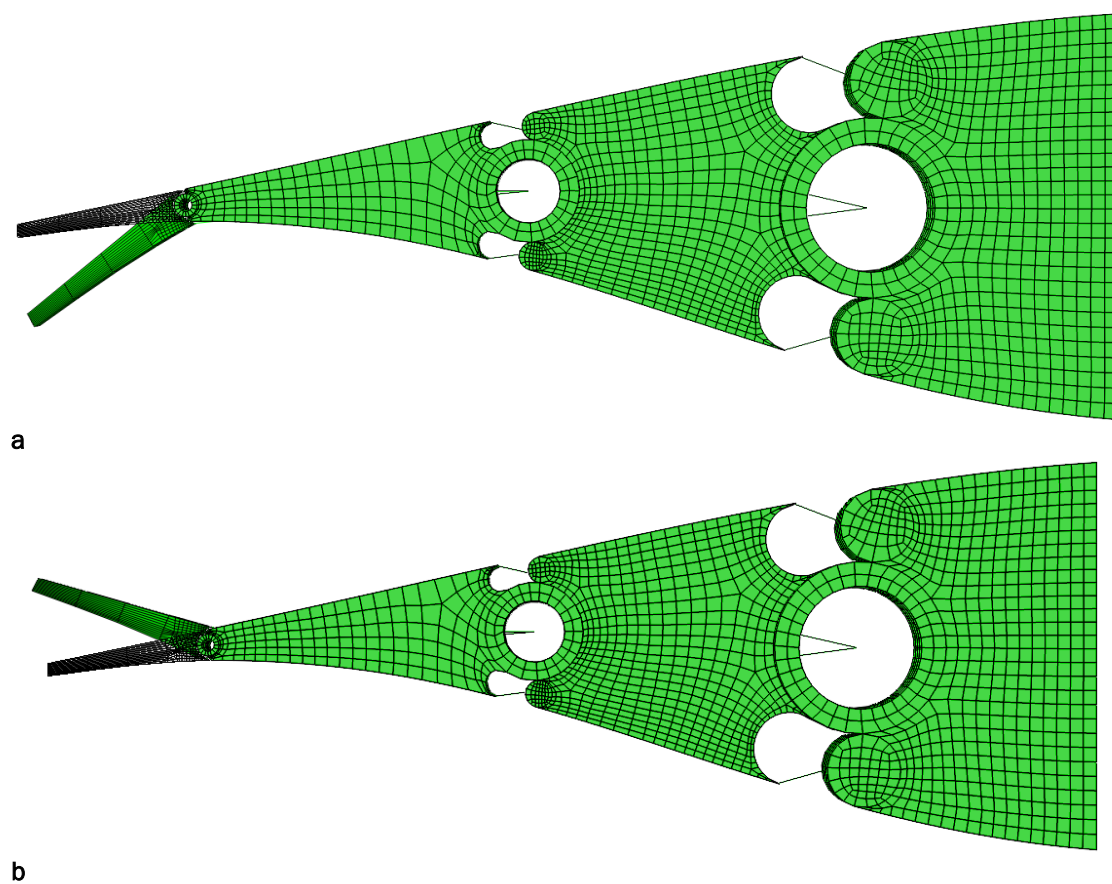


**Figure 38: Morphing mechanism at 10% of chord length activated for (a) downwards and (b) upwards movement**

The maximum angular rotation achieved is  $27.5^\circ$  in both directions and the required time for that movement is approximately 17 seconds for the downwards and 20 seconds for the upwards movement (Figure 39). Although this is an acceptable result it cannot be assessed without considering the developed stress on the actuators, their temperature and their martensitic volume fraction.

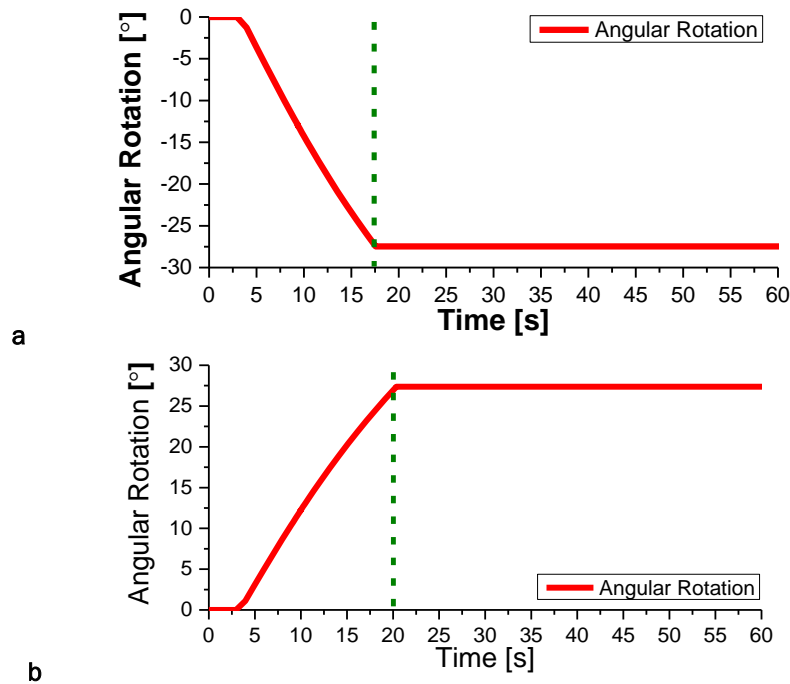


Figure 39: Angular rotation of morphing mechanism with 10% of chord length activated for (a) downwards and (b) upwards movement

In Figure 40 the maximum developed stress on the SMA wire actuators is presented for both cases. At 17 seconds the developed stress on upper actuator (antagonistic) is 570 MPa during downwards movement, while in upwards movement the maximum stress developed on the same actuator is 640 MPa. Of course this values exceed the specification of 240 MPa. The time point when the developed stress reaches the critical value of 240 MPa can be extracted from Figure 40 A and Figure 40 B and the respective angular rotation of the morphing mechanism can be derived. This will provide the maximum angular rotation for the maximum allowed developed stress. For downwards movement the predefined stress value is achieved at 7.5 seconds while for upwards movement at 9 seconds. Consequently, from Figure 39, the maximum angular rotation permitted for downwards movement is  $5^\circ$  while for upwards movement is  $7^\circ$ .

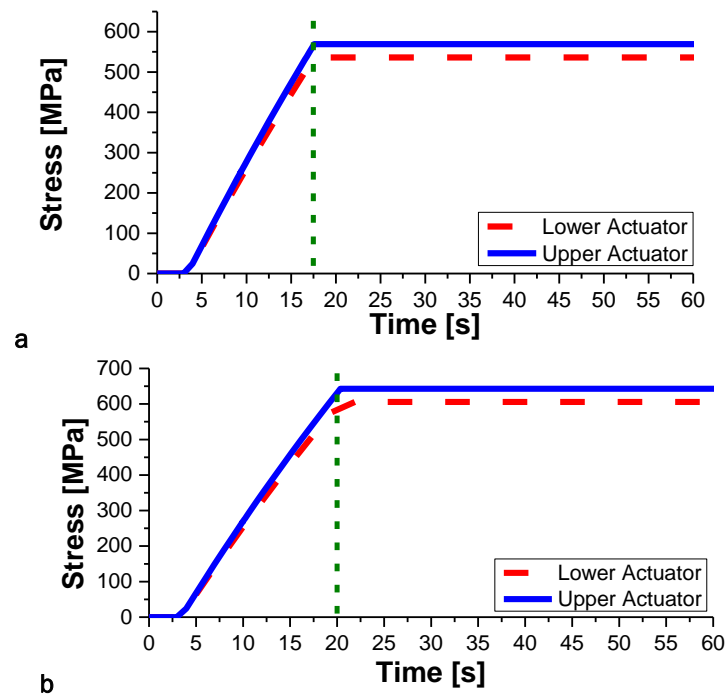
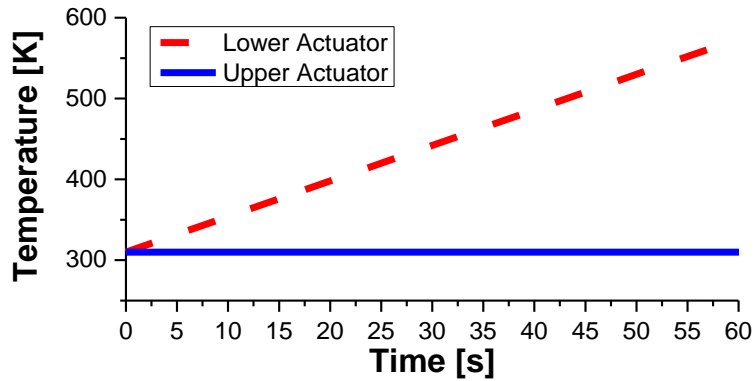
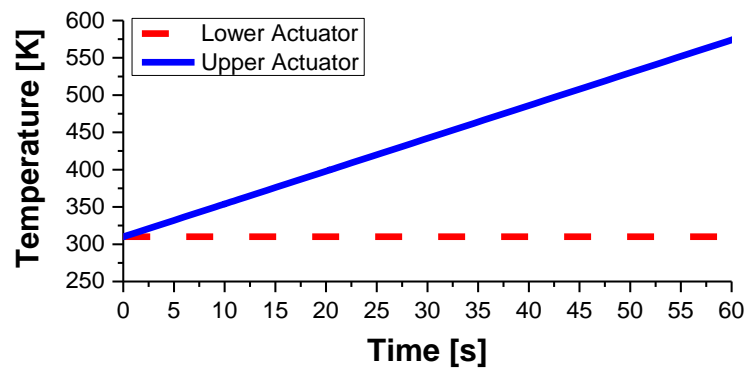


Figure 40: Developed stress on actuators of morphing mechanism with 10% of chord length activated for (a) downwards and (b) upwards movement

For the selected times the maximum temperature can be derived from Figure 41 A and Figure 41 B. For downwards movement, the lower SMA actuator temperature is 345 K while for upwards movement the upper SMA actuator temperature is approximately 351 K. It must be noted that during numerical simulation only the activated actuator is considered to be heated, thus actuators that are not activated have constant temperature. This is confirmed in Figure 41 A where upper the actuator keeps a constant temperature while in Figure 41 B the lower actuator is on constant temperature.



a



b

Figure 41: Temperature of actuators of morphing mechanism with 10% of chord length activated for (a) downwards and (b) upwards movement

During the activation of the SMA wire actuators one actuator is heated and transformed providing actuation force, while the antagonistic actuator resists to mechanism movement and due to that a reaction force is generated. As it can be seen in Figure 42 A and Figure 42 B, the antagonistic actuators in both downwards and upwards movement do not exhibit a change in their martensitic volume fraction, which means that they are not transformed during the operation although they are mechanically loaded. This can be explained by the fact that their temperature remains relative low compared to the temperature of the activated actuator. While the developed stress increases and temperature remain low the transformation cannot initialize.

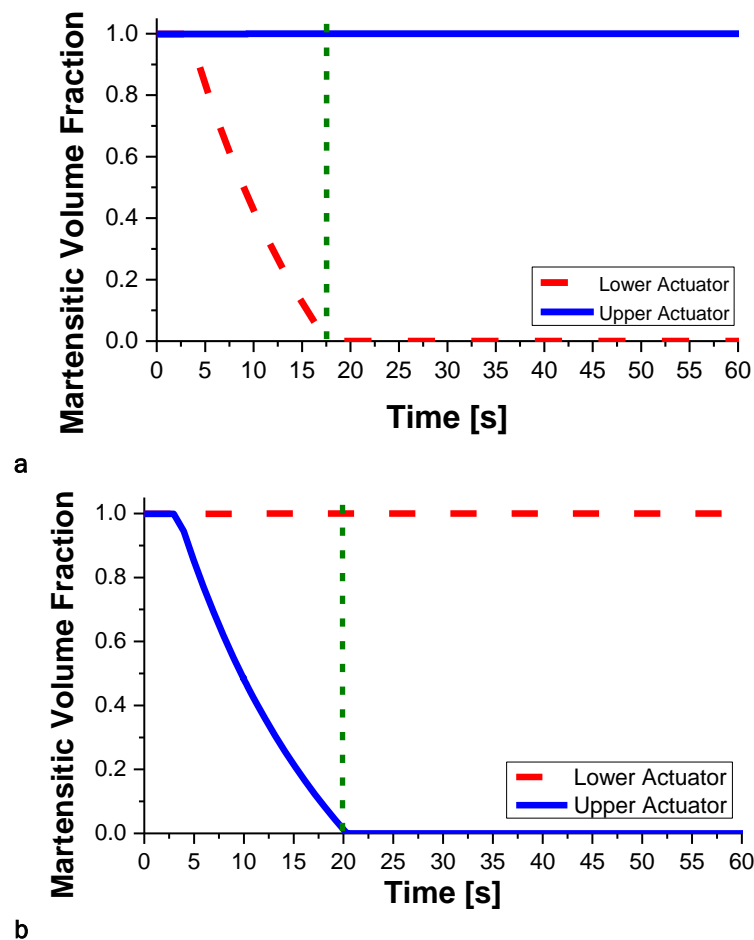


Figure 42: Martensitic volume fraction of actuators of morphing mechanism with 10% of chord length activated for (a) downwards and (b) upwards movement

In Figure 43 the morphing capabilities of the mechanism are expressed in form of  $C_L$  variation using the diagram provided by NTUA for maximum  $k$  and a.o.a. The horizontal dashed lines indicate the moving length of the flap as a percentage of the chord length. The two vertical dashed lines indicate the limitations regarding the angular rotation  $\beta$  for each movement (upwards and downwards). During downwards movement  $\Delta C_L$  can reach 0.2 while in upwards movement the value of 0.25 can be reached. The results indicate that when 10% of the chord length is moved the morphing state achieved can satisfy all the required  $C_L$  variations in upwards direction which prove the effectiveness of the mechanism design.

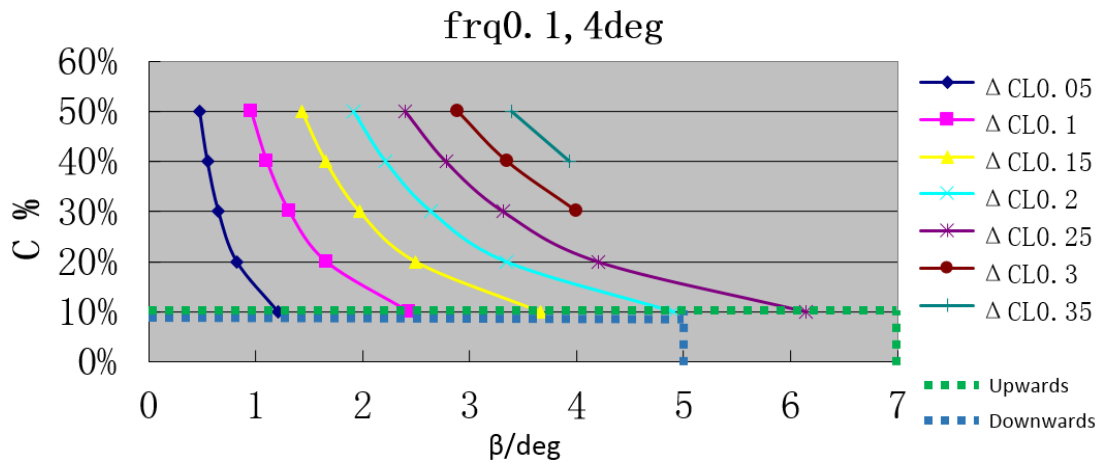


Figure 43: Effect of morphing of 10% of chord length on the variation of  $c_1$

Continuing the morphing mechanism part corresponding to 30% of chord length will be activated and the numerical results of the simulation runs will be presented. In Figure 44 A and Figure 44 B the downwards and upwards morphed shape is presented after activating lower and upper actuator respectively.

#### 2.9.1.2 Case 2: Morphing Mechanism at 30% of Chord Length Activated



Figure 44: Morphing mechanism at 30% of chord length activated for (a) downwards and (b) upwards movement

In this case the maximum angular rotation for downwards movement is achieved at 17.5 seconds while for the upwards movement at 20 seconds as shown in Figure 45 A and Figure 45 B respectively. The maximum angular rotation values are  $-8.3^\circ$  and  $+8.3^\circ$  for the two different directions.

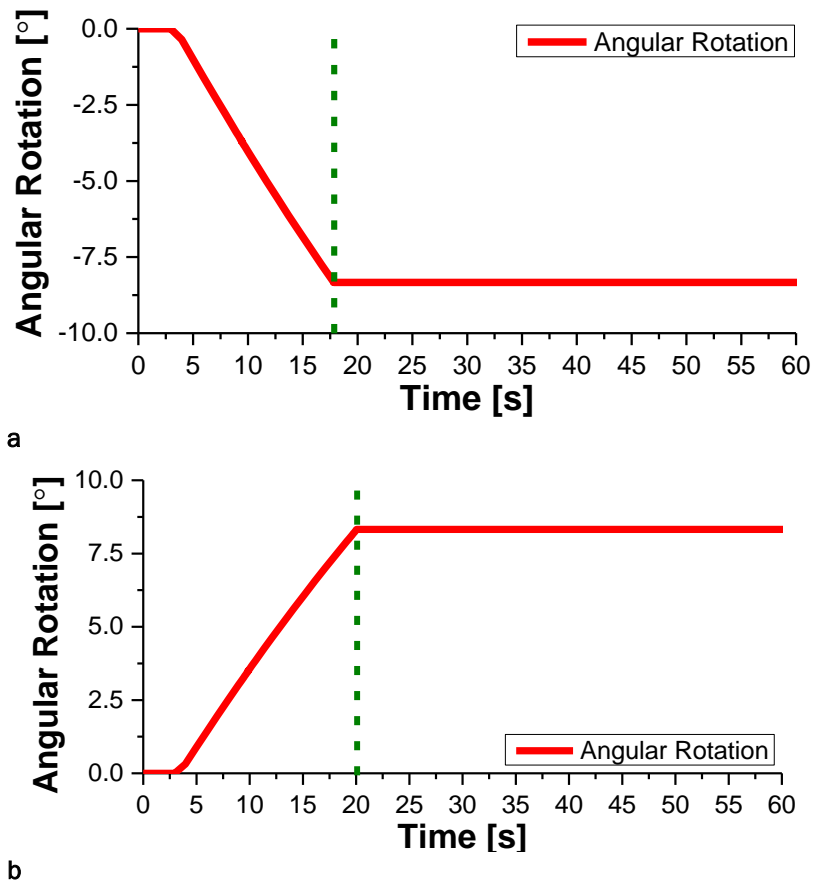


**Figure 45: Angular rotation of morphing mechanism with 30% of chord length activated for (a) downwards and (b) upwards movement**

The stress developed on actuators during each simulation run are presented in Figure 46 where it can be seen that for downwards movement the upper SMA wire actuator develops stress over 550 MPa while the same actuator in upwards movement develops stress of approximately 630 MPa. Again these values are much higher than the stress limit of 240 MPa. The maximum permitted value for developed stress is located at 8 seconds for downwards and at 9 seconds for upwards movement.

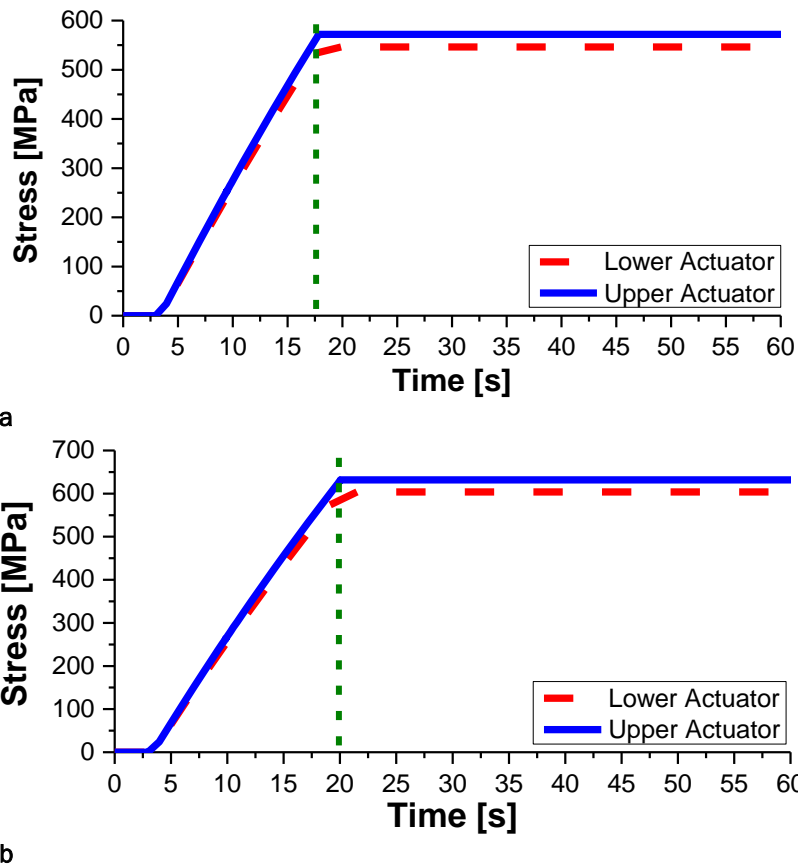
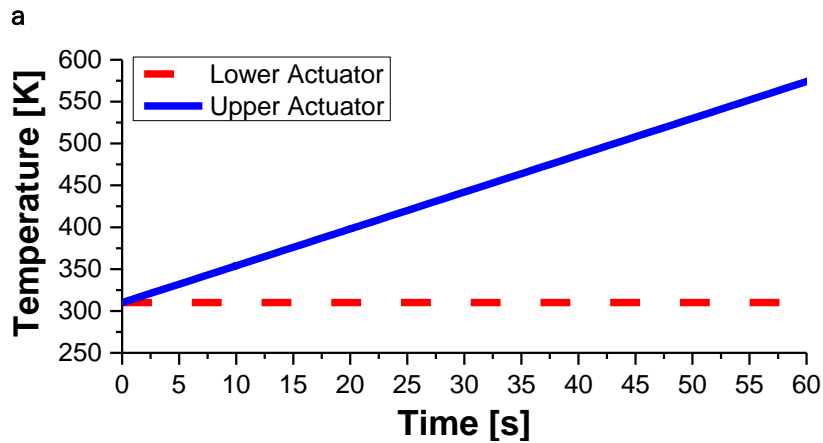
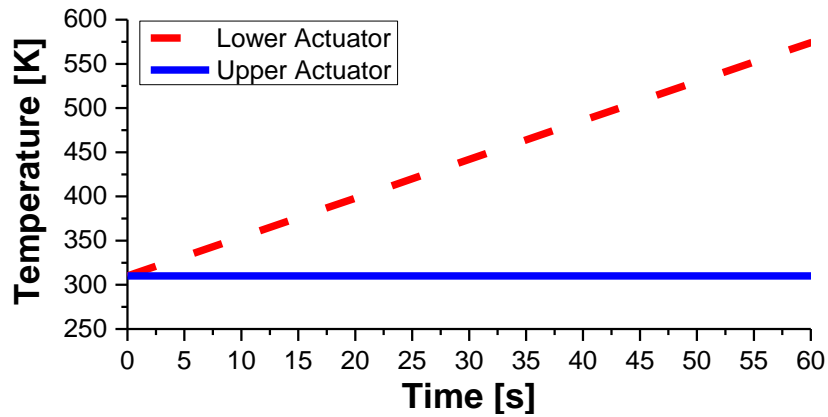


Figure 46: Developed stress on actuators of morphing mechanism with 30% of chord length activated for (a) downwards and (b) upwards movement

Considering the actuators developed stress, the maximum allowable angular rotation of the morphing mechanism is  $-3.5^\circ$  and  $+3.6^\circ$  in downwards and upwards direction respectively. The maximum temperature for the activated actuator in each case is 352 K for rotating the mechanism counter clockwise (lower actuator activated) and 360 K for rotating the mechanism clockwise (upper actuator activated). The variation of actuators temperature during the numerical simulations is presented in Figure 47 A and Figure 47 B for each activated movement direction.



**Figure 47: Temperature of actuators of morphing mechanism with 30% of chord length activated for (a) downwards and (b) upwards movement**

Figure 48 A and Figure 48 B show that when the maximum angular rotation is achieved the active actuators have developed the maximum transformation strain as at 17.5 and 20 seconds the martensitic volume fraction of these actuators is zero. This mean that there is no more martensite in the material so there is no more transformation strain to be recovered.

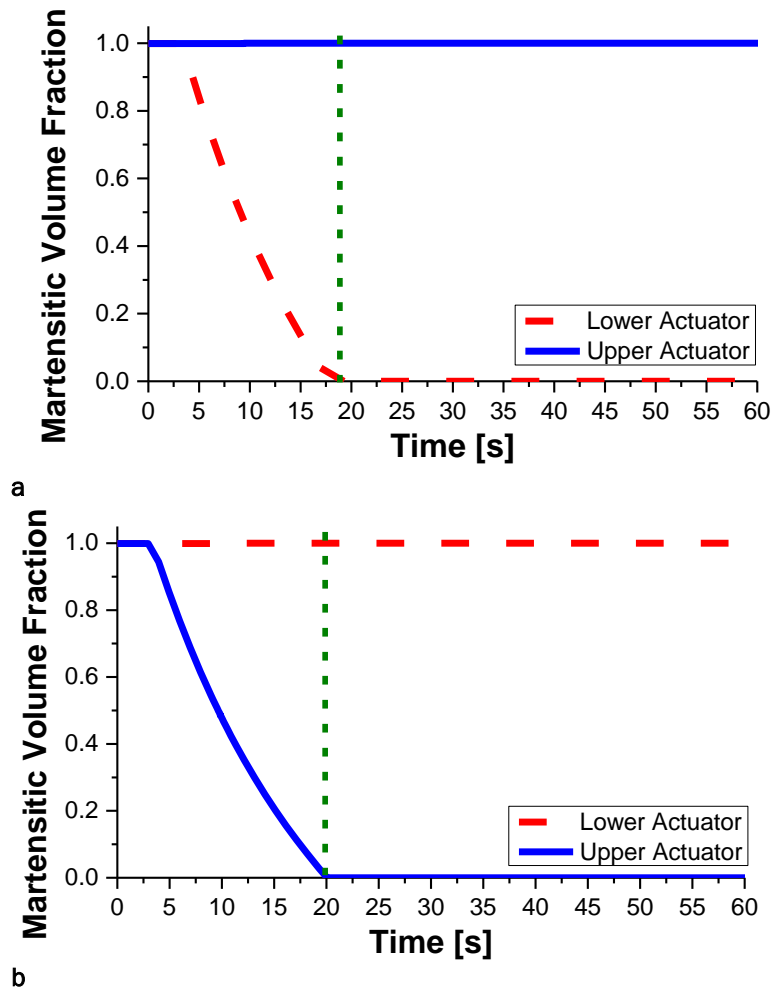


Figure 48: Martensitic volume fraction of actuators of morphing mechanism with 30% of chord length activated for (a) downwards and (b) upwards movement

Having the capabilities of the moving part of the mechanism representing 30% of chord length addressed, the assessment of this case is completed by proving the morphing capabilities of the structure. In Figure 49 the curves of variation of the lift coefficient are plotted with respect to the percentage of chord length with moving capability and the angular rotation of the mechanism. The diagram is considered under the assumption that reduced frequency  $k$  equals 0.1 and angle of attack is  $4^\circ$ . The value of  $C$  is 30% and is stated by the horizontal dashed lines. Upwards and downwards movement of the mechanism flap is  $3.6^\circ$  and  $3.5^\circ$ , which means that these values are almost the same. Thus, in Figure 49 they are represented by two vertical dashed lines so close to each other to define the region of the diagram where  $C_l$  can vary. Based on the results the maximum variation in coefficient of lift is 0.25 which is near the result achieved by rotating the part of the mechanism that represents 10% of chord length.

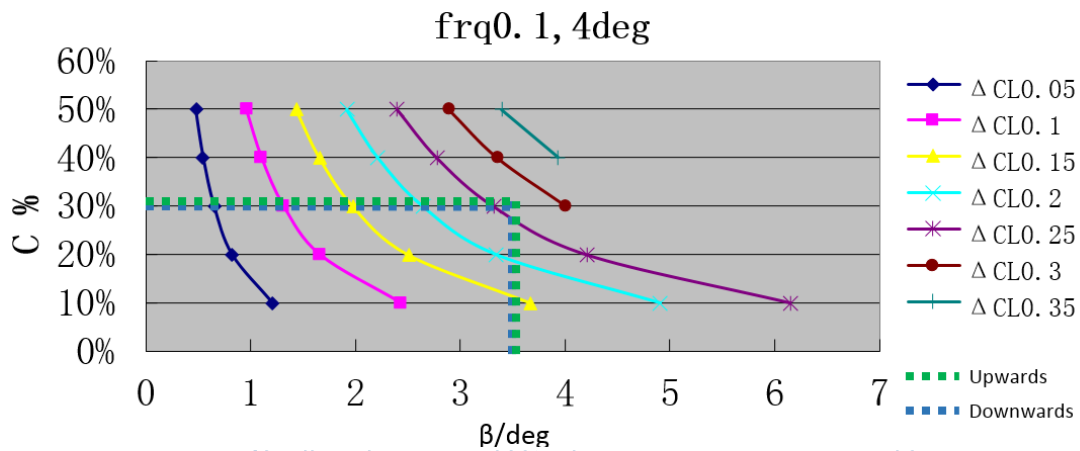


Figure 49: Effect of morphing of 30% of chord length on the variation of  $C_l$

### 2.9.1.3 Case 3: Morphing Mechanism at 50% of Chord Length Activated

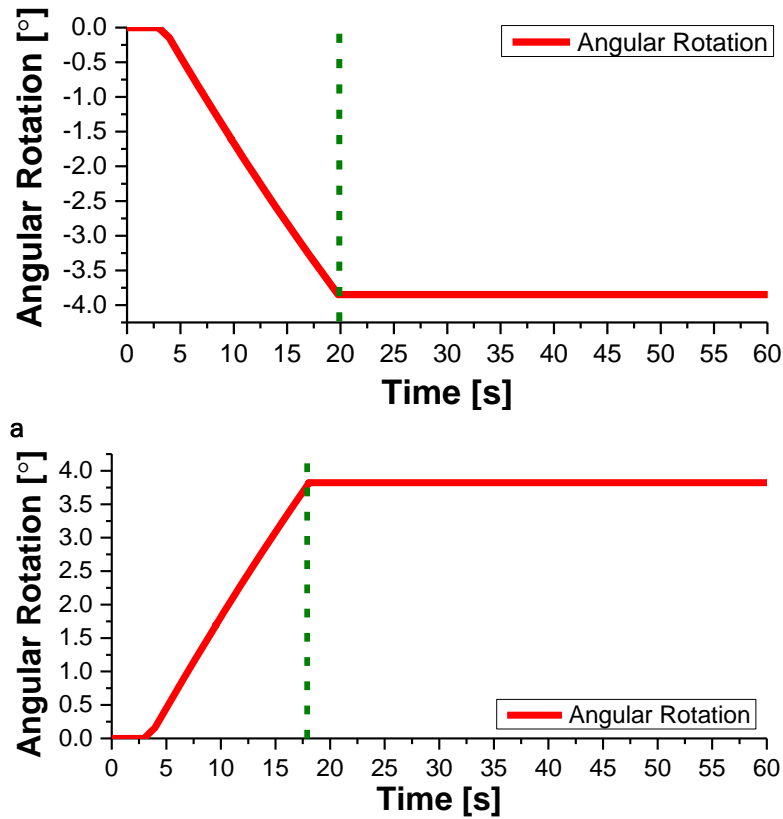
The last case involves the activation of the antagonistic pair of SMA wire actuators that are responsible for moving 50% of chord length. Figure 50 A presents the maximum deflection position in downwards movement while in Figure 50 B the respective position for upwards movement is presented.



Figure 50: Morphing Mechanism at 50% of chord length activated for (a) downwards and (b) upwards movement

In the morphed state presented in Figure 50 A and Figure 50 B the angular rotation of the mechanism around the centre of rotation defined by the pin at 50% of chord length is approximately  $3.9^\circ$  for the downwards and  $3.8^\circ$  for the upwards movement. As it can be seen in

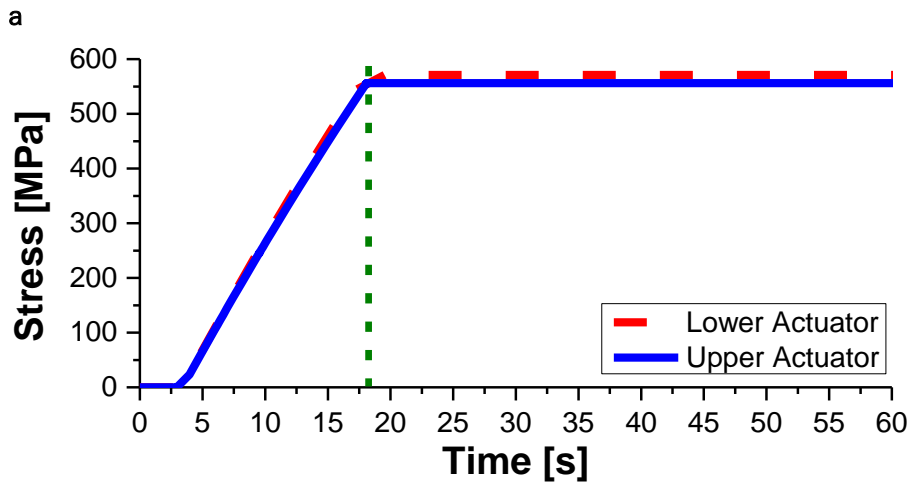
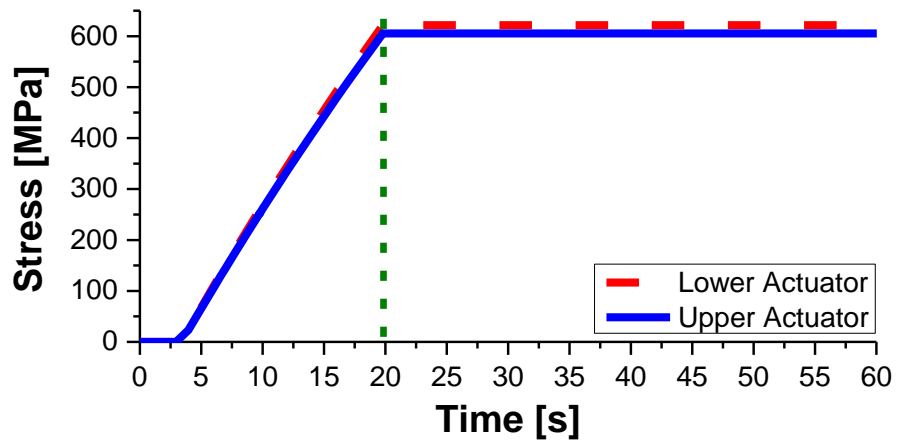
Figure 51 A and B these values are reached at 20 and 17.5 seconds of the numerical simulation time and are preserved till the end of the simulation run.



b

Figure 51: Angular rotation of morphing mechanism with 50% of chord length activated for (a) downwards and (b) upwards movement

The maximum angular rotation that the morphing mechanism can achieve is limited by the maximum allowable stress that has been specified at 240 MPa. The maximum angular rotation values mentioned above correspond to 622 MPa and 571 MPa for the lower SMA wire actuator during counter clockwise and clockwise rotation of the mechanism respectively. From Figure 52 A the maximum stress of 240 MPa is located for the lower SMA actuator at 9.5 seconds while in Figure 52 B this stress limit is reached at 9 seconds. At the selected times the angular rotation that the morphing mechanism exhibits is 1.8 ° and 1.6 ° for downwards and upwards direction respectively.



**b**  
 Figure 52: Developed stress on actuators of morphing mechanism with 50% of chord length activated for (a) downwards and (b) upwards movement

When the aforementioned stress limit is reached the temperature for the lower actuator during its activation (Figure 53 A) is 353 K while the temperature of the upper actuator when it is activated is 348 K approximately. This mean that during the downwards movement the variation in temperature is 43 K whereas in upwards movement the temperature variation is 38 K.

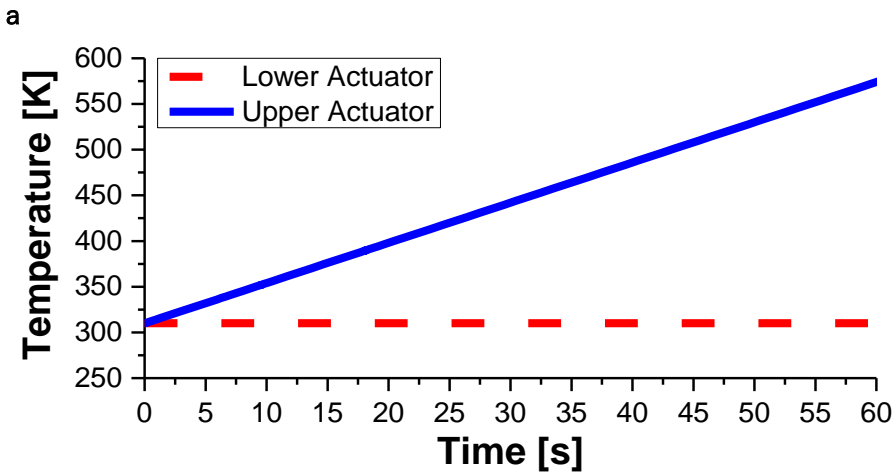
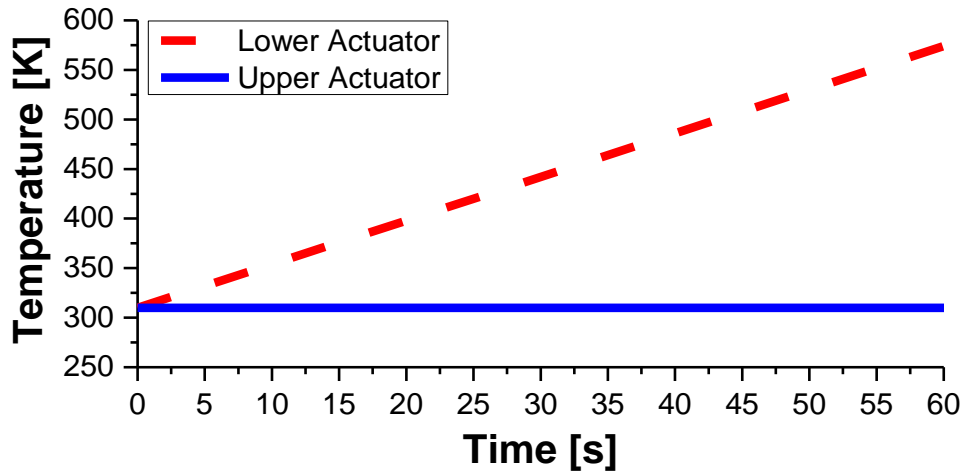


**Figure 53:** Temperature of actuators of morphing mechanism with 50% of chord length activated for (a) downwards and (b) upwards movement

The thermomechanical loading of the actuators (combination of heat with the developed stress) lead to changes in the martensitic volume fraction in their material. As can be seen in Figure 54a and Figure 54b, the martensitic volume fraction of the activated actuator changes while the martensitic volume fraction of the antagonistic actuator is maintained constant. As it has been mentioned before, the antagonistic actuator is kept in a constant temperature relatively lower in comparison with the temperature of the activated one. When the developed stress increases the transformation temperature limits increase also. Thus in any case the antagonistic actuator is elastically loaded without being transformed, so its martensitic volume fraction remains constant and equal to the initial value.

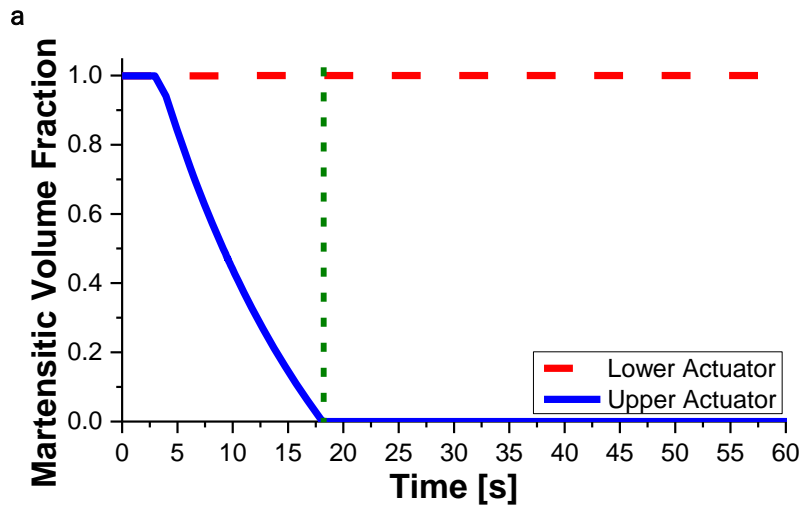
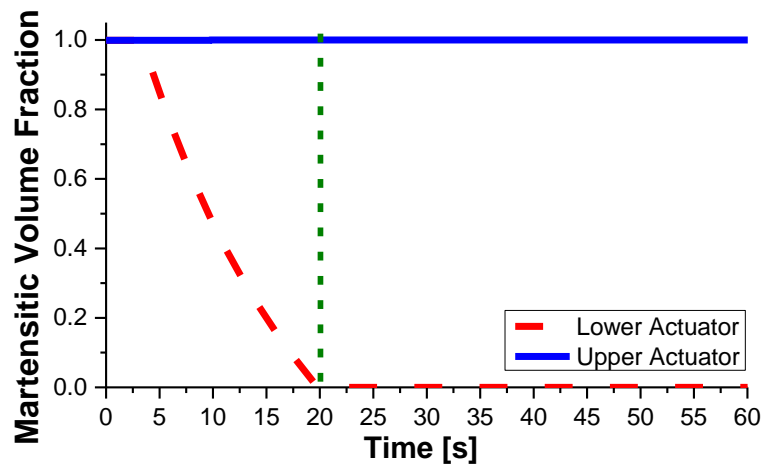


**Figure 54: Martensitic volume fraction of actuators of morphing mechanism with 50% of chord length activated for (a) downwards and (b) upwards movement**

The results discussed above lead to a certain morphing state that can be related to a change in airfoil's coefficient of lift. In Figure 55 the horizontal dashed lines indicate the percentage of chord that has moving capability and for this case is 50%. The two vertical dashed lines stand for the maximum achieved angle during counter clockwise and clockwise rotation of the mechanism (upwards and downwards movement). In both directions the maximum  $\Delta C_L$  achieved is 0.15, as both dashed lines include the upper point of the yellow curve that represent this value.

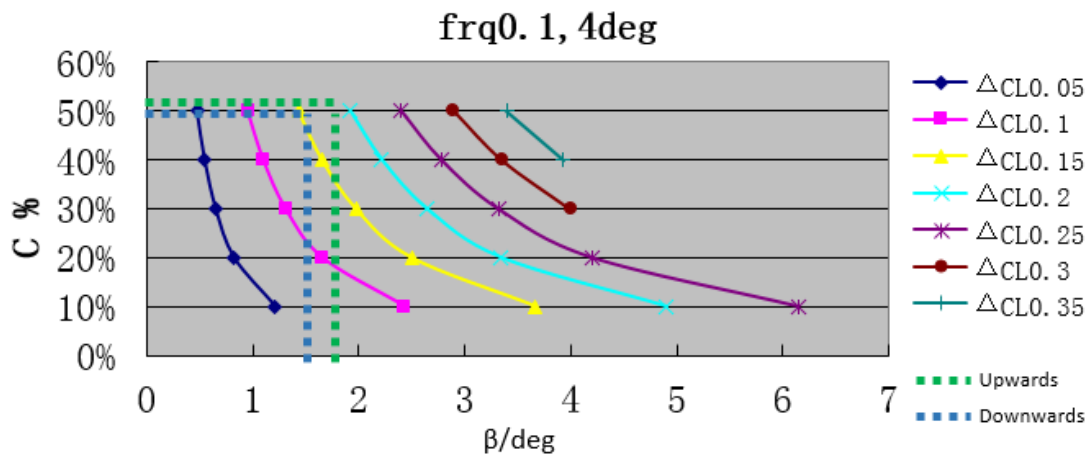


Figure 55: Effect of morphing of 50% of chord length on the variation of  $c_l$

The variation in coefficient of lift that this part of the mechanism can achieve is lower when compared to the capabilities of the other two mechanism parts at 10% and 30% of chord length, although the diameter of the SMA wire actuators is the same as well as the thermal loading conditions. The variation of lift that each moving part of the morphing mechanism can independently achieve is summarized in Figure 56 where negative values of angular rotation indicate downwards movement while positive values of angular rotation indicate upwards movement.

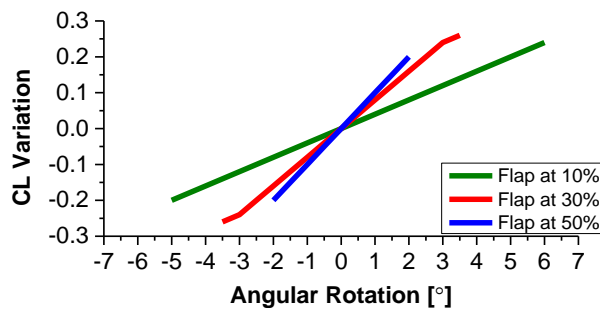


Figure 56:  $C_L$  Variation with respect of angular rotation for each morphing mechanism flap

#### 2.9.1.4 Summary of Results

In the three cases presented above, each part of the articulated morphing mechanism was considered as an independent equivalent flap mechanism located at 10, 30 and 50 % of chord length. Under this assumption two numerical simulation runs were performed for each case: one for the counter clockwise (downwards) and one for the clockwise (upwards) rotation of the morphing mechanism. At the end of each simulation run the rotational angle, the developed stress of the actuators, the temperature and the martensitic volume fraction of the actuators were plotted with respect to the time in order to assess the results.

For all morphing mechanism parts and for both movements (upwards and downwards) the results of the developed stress indicate that in the case that the total transformation strain is recovered, meaning that martensitic volume fraction initially equals 1 and at the end of simulation equals 0, the stress value will be greater than the specification limit of 240 MPa. This criterion leads to a limit of the allowable maximum rotation the mechanism can achieve. Although this limit compromises the performance capabilities of the mechanism in regards of movement, provides certain conditions to ensure actuators smooth operation, because they can be activated under

smaller mechanical load and with less provided heat (smaller temperature difference). Furthermore, from the figures that give variation of  $C_L$  and are provided by NTUA, it is shown that the independent movement of each mechanism can provide a morphing state that leads to changes in coefficient of lift. Highest potential is shown by morphing mechanism that represents 10% of chord length, which can achieve a variation of  $C_L$  equal to 0.25 during upwards movement and 0.2 during downwards movement. Mechanism at 30% of chord length can provide variation of  $C_L$  up to 0.25 during both upwards and downwards movement while morphing mechanism part at 50% of chord length is more confined and can achieve  $\Delta C_L$  equal to 0.15 for both morphing directions.

It must be noted that the position of the SMA wire actuators for the selected morphing mechanism has been derived based on the results of the preliminary analysis with the implementation of truss structures in the morphing concepts. Once the initial configuration was defined, afterwards it was improved by trial and error method in order to enhance the leverage of each actuator to provide increased momentum. At the same time, during this procedure it was also taken into consideration the improvement of the kinematic response of the rotating part. The key variable in this process is the radius of the pin where two successive mechanism parts are connected. The SMA wire actuators are considered to be pinned on the radius of the major pin between the two mechanism parts. So in order to maximize the rotational angle  $\theta$ , radius needs to be decreased as indicated by equation (17), while in order to maximize momentum, radius needs to be increased as indicated by equation (18). The aforementioned parameters are contradicting and for the purposes of the present study were addressed by trial and error but in order to find the optimum solution, a separate study need to be performed.

$$s = r \cdot \theta \Rightarrow \theta = \frac{s}{r} \quad (17)$$

$$M = F \cdot r \quad (18)$$

## 2.10 Consideration of Steady Pressure Loads on Morphing Mechanism

Till this point the study has focused on the structural design of the morphing mechanism for the trailing edge of the airfoil neglecting the effect of aerodynamic load on the airfoil during operation. NTUA has provided data for the distribution of pressure coefficient ( $C_p$ ) for each airfoil section throughout the length of the blade. From the pressure coefficient the pressure distribution on the airfoil can be calculated using the following equation:

$$\text{Pressure} - 101325 = C_p \frac{\rho_{\text{air}}}{2} \omega^2 \quad (19)$$

where

$$\omega^2 = (\omega \cdot R)^2 + v_{\text{wind}}^2 \quad (20)$$

In the above equations the rotational velocity of the blade is denoted as  $\omega$ ,  $f$  stands for the rotational frequency of the blade and is equal to 0.16 Hz,  $R$  denotes the position of the airfoil under investigation from the root of the blade,  $v_{\text{wind}}$  is the velocity of the wind which equals 10 m/s and  $\rho_{\text{air}}$  is the density of the air which is considered to be 1.2 kg/m<sup>3</sup>. Figure 57 provides a schematic representation of the distribution of aerodynamic pressure (in terms of absolute pressure – atmospheric pressure is not considered) on airfoil's aerodynamic surfaces.

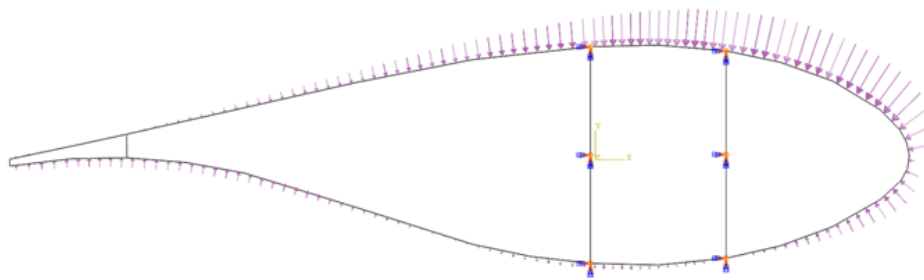


Figure 57: Pressure Distribution around the Airfoil of Interest

With the pressure distribution known, a 2.5D finite element model of the original airfoil structure was created and numerical simulation was performed to predict its response when nominal operational aerodynamic loads act on it. Figure 58 A presents the distribution of vertical displacements (Y direction) on the airfoil structure while Figure 58 B represent the angular rotation around Z axis. The maximum values are located on leading edge panels and upper trailing edge panel where the value of the displacement is about 1.8 mm while maximum von Mises stress was 20 MPa. The region that concerns the present study is the skin portion from web B to trailing edge tip because this is the region where the morphing mechanism will be embedded. Especially the trailing edge tip which in this numerical analysis was rotated at about  $0.2^\circ$  around Z axis.

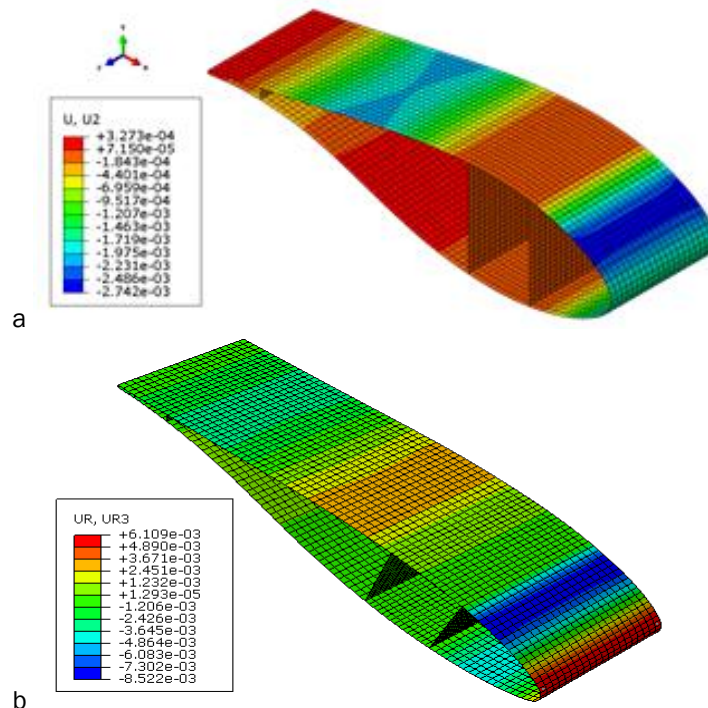


Figure 58: (a) Vertical displacement and (b) angular rotation around z axis of the original airfoil under operational aerodynamic loads

The numerical results of the original airfoil FE model set a reference state regarding the structural stiffness and the distribution of the displacements and consequently the strains. After the baseline was set, the application of pressure load was considered for the airfoil structure with the implemented morphing mechanism. In Figure 59 the pressure field is schematically plotted around the airfoil and morphing mechanism.

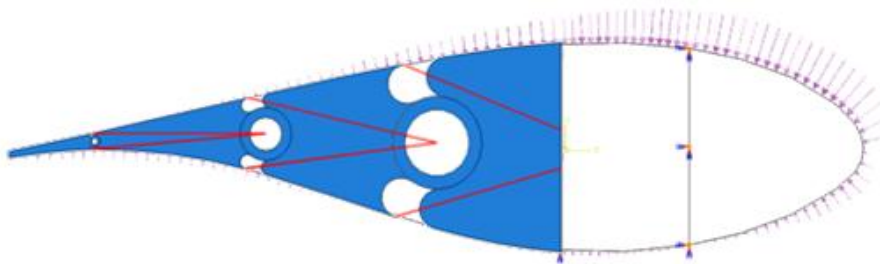


Figure 59: Pressure distribution around airfoil structure and morphing mechanism

SMA wire actuators consist the components that provide the stiffness for the morphing mechanism structure because between the moving and the immobile parts of the mechanism there are only pin joints. The effect of aerodynamic loading is initially assessed. The radius of the SMA wire actuators was set to 1 mm and the pressure load was applied to the mechanism part that represents 10% of the chord length. A single part was selected for pressure application in order to focus on the effect it has on that part without complicating the study with the whole mechanism response. The resulting tip displacement was 0.517 m which is much greater than the amplitude of the displacement of the original airfoil structure under the same load. Figure 60 presents the deformed body of the mechanism after the application of aerodynamic pressure at part representing 10% of chord's length. The angular rotation of the tip in this state was found to be  $15^\circ$ .

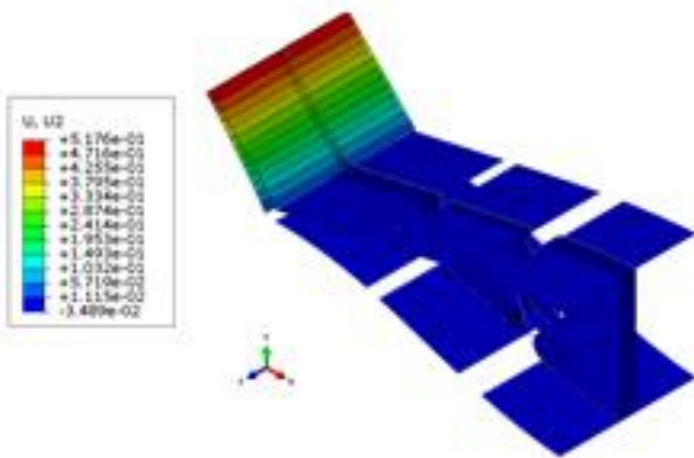
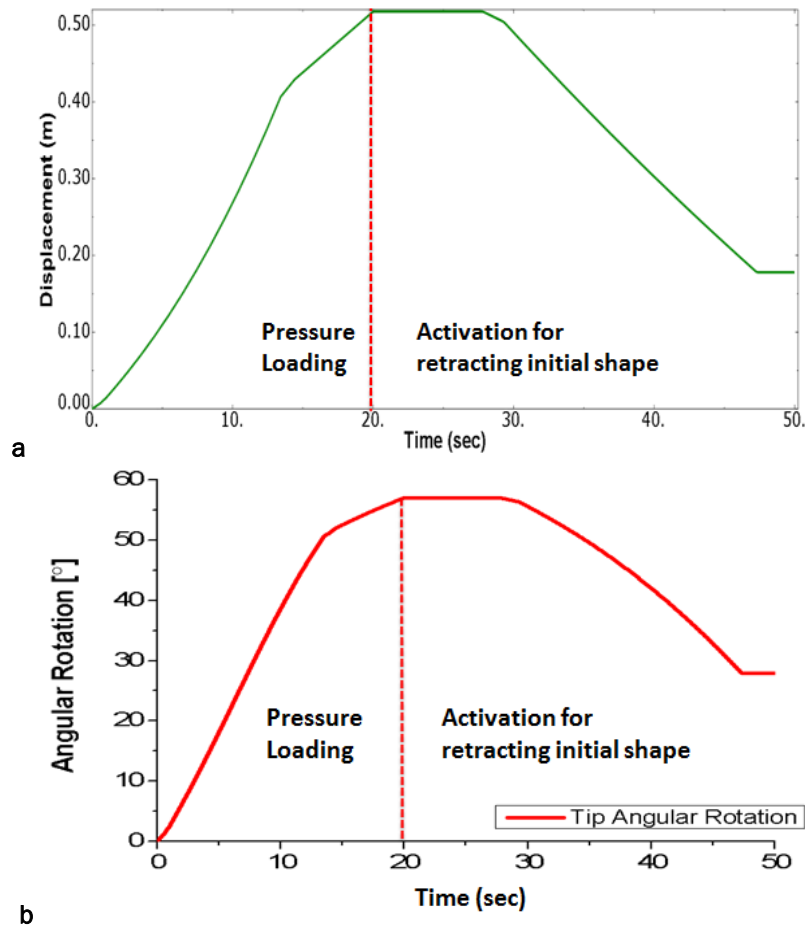


Figure 60: Deformed body of the mechanism under aerodynamic pressure effect

### 2.10.1 Compensation of Structural Stiffness Under Aerodynamic Loading

The numerical results of the previous section prove that modifications for the morphing mechanism in order to be able to withstand the operational aerodynamic loads without changing its shape and retain its structural integrity are required. The first approach was to activate lower SMA wire actuator to bend the mechanism downwards and counterbalance the initial movement caused by aerodynamic pressure. In Figure 61 the response of the tip of the flap regarding its vertical displacement is presented with respect to the analysis time. Pressure load is applied linearly from the beginning of the analysis till 20 seconds. At time of 20 seconds lower SMA wire actuator is activated and remains activated till the end of the analysis at 50 seconds. During this time the flap retracts and at the time point  $t=48$  seconds is stabilized to a position that has a vertical displacement of approximately 0.17 m, which is far from returning to its initial position.



**Figure 61: Morphing mechanism (a) vertical displacement and (b) angular rotation of tip end with respect of analysis time under aerodynamic loading and subsequent activation of lower SMA wire actuator**

The flap mechanism is not able to return to its initial position because there is no more available transformation strain for the actuator to provide as it can be seen in Figure 62 where martensitic volume fraction of the lower actuator is presented with respect to analysis time. From analysis start till time of 20 seconds pressure load forces lower SMA wire actuator to transform from its initial state of 20% to 100% martensite. When the actuator is activated and its temperature is being elevated it starts transforming back to austenite but at about 48 seconds becomes fully austenite and there is not any transformation strain left to be recovered.

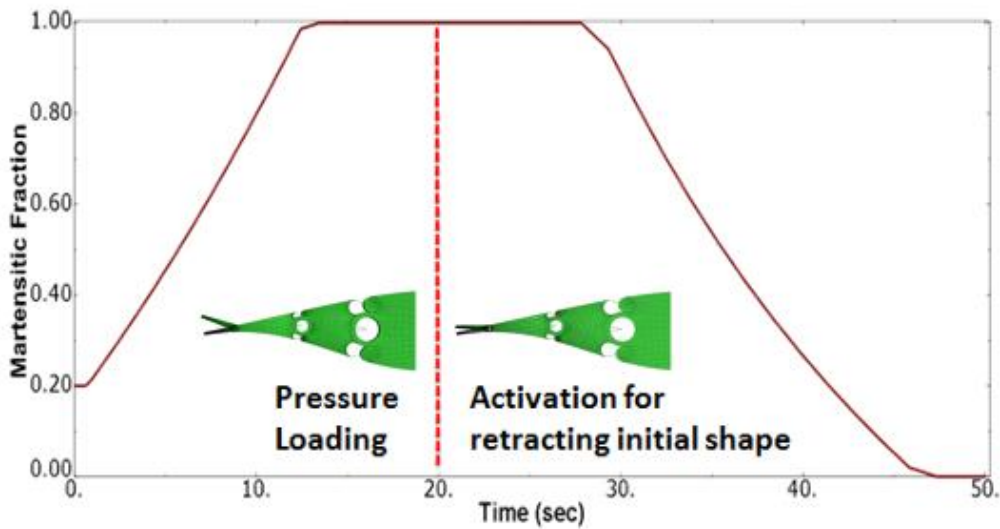


Figure 62: Martensitic volume fraction of the SMA actuator vs. analysis time with morphing mechanism under aerodynamic loading and subsequent activation of lower SMA wire actuator

Furthermore, from Figure 63 which presents the variation of stress of the lower SMA wire actuator of the flap with respect of analysis time, it is clear that the developed stress in the actuator has order of magnitude of GPa. The high stress developed in the lower actuator is above 1 GPa when aerodynamic pressure is fully applied and increases more when actuator is activated till its amplitude is doubled at the end of the analysis.

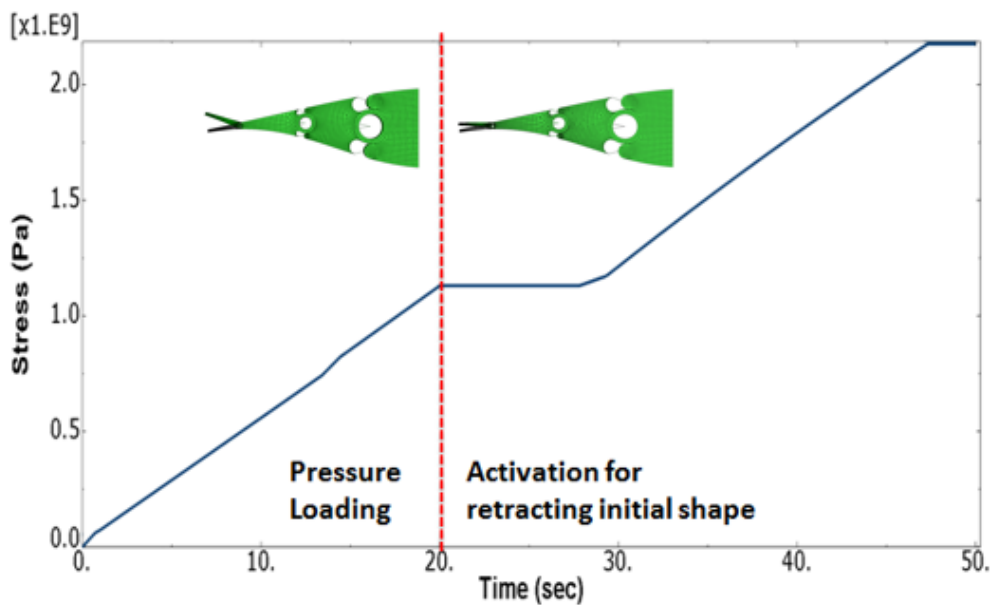


Figure 63: Stress developed on lower SMA wire actuator vs. Analysis time with morphing mechanism under aerodynamic loading and subsequent activation of lower SMA wire actuator

The above numerical results show that the morphing mechanism structure is too flexible to sustain pressure created by aerodynamic loads during operational state and SMA wire actuators provide inadequate forces to morph the flap to its initial state and certainly not enough to morph it to the desired position. Consequently, resizing of the SMA wire actuators is required.

A number of different diameters for both the upper and the lower actuator of the morphing flap mechanism representing 10% of chord's length were examined. The resulting radius of 0.017m for the upper actuator and that of 0.025 m for the lower actuator were found adequate to maintain the structural stiffness of the mechanism. Numerical results of simulation runs performed considering the aforementioned sizes of the actuators proved an angular rotation of 0.06° for the tip of the trailing edge. In Figure 64 the angular rotation of morphing mechanism tip around Z axis is presented with respect to analysis time. From this diagram the ability of the morphing mechanism to retain its initial position during aerodynamic loading is confirmed. Also the movement capability of the morphing flap in both directions is confirmed. From 20<sup>th</sup> till 50<sup>th</sup> second the lower actuator is activated and the flap is rotated at -4°. In the time period from 50 to 80 seconds the upper actuator is activated while the lower one is deactivated resulting in a morphing flap rotation of +4°.

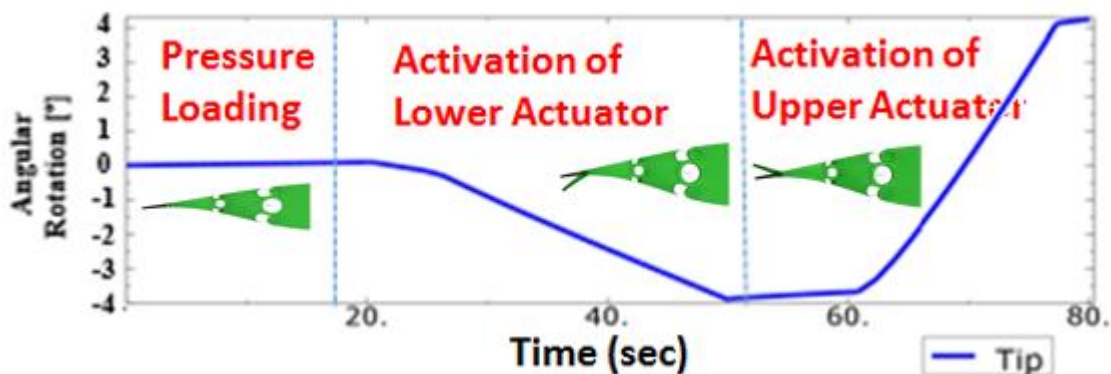


Figure 64: Angular rotation of trailing edge's tip around z axis with morphing mechanism under aerodynamic loading and subsequent activation of SMA wire actuators

Figure 65 shows a diagram of the martensitic volume fraction of the SMA wire actuators with respect to analysis time. In the first 20 seconds pressure load is applied and the martensitic volume fraction retain its initial value for both actuators. From 20<sup>th</sup> to 50<sup>th</sup> second the lower actuator is activated thus reverse transformation takes place. The antagonistic upper actuator develops stress by the reaction forces exerted due to the retraction of the lower actuator and rotation of the flap. Thus forward transformation takes place for the upper actuator. From 50<sup>th</sup> to 80<sup>th</sup> second upper actuator is activated (heated) while lower actuator is cooling down through natural convection conditions. Because of the low cooling rate and forces implied by lower actuator, upper actuator is rapidly transformed so its martensitic volume fraction drops from 0.4 to 0. In the meantime lower actuator's martensitic volume fraction increases from 0.1 to 0.25 because of the cooling and initialization of reverse transformation.

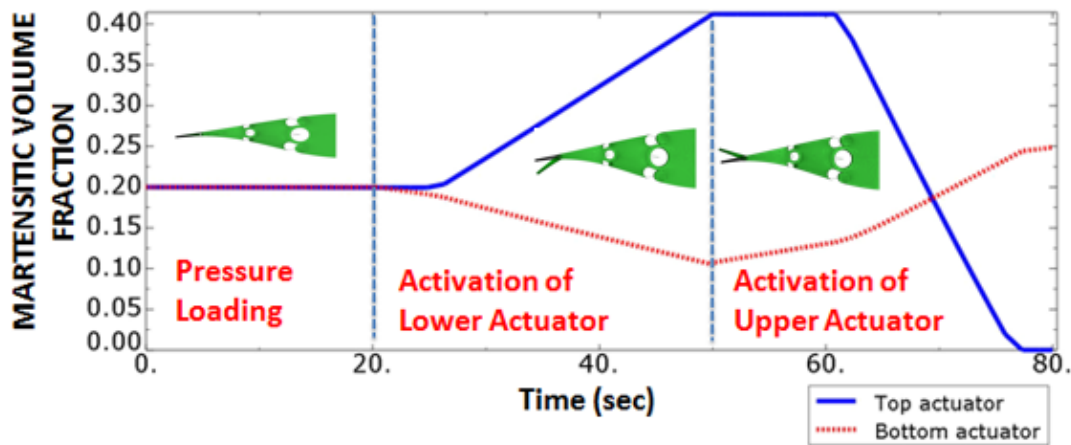


Figure 65: Martensitic volume fraction of SMA actuators vs. analysis time with morphing mechanism under aerodynamic loading and subsequent activation of SMA wire actuators

In Figure 66 the variation of the developed stresses on SMA wire actuators are presented with respect to analysis time. When the structure is loaded with aerodynamic pressure the actuators seem to develop infinitesimal stresses. On 20<sup>th</sup> second lower actuator is activated and both actuators develop small stresses because lower actuator retracts and subsequently rotates the morphing mechanism and upper actuator antagonizes this motion. Developed stresses increase more after 60<sup>th</sup> second when the upper actuator has already been activated. Low cooling rate of lower actuator does not provide the required conditions to initiate its transformation, thus its reaction to the movement imposed by the upper actuator increases dramatically.

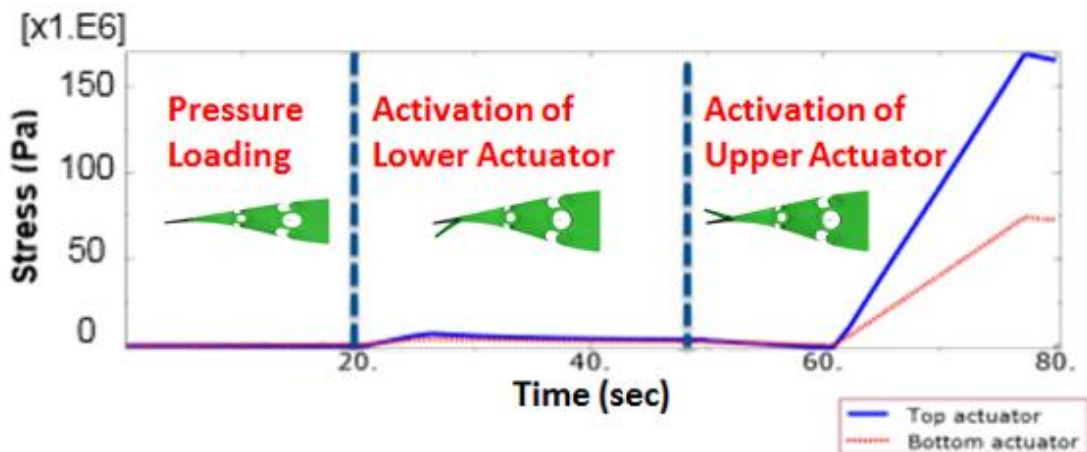


Figure 66: Actuators stress vs. analysis time with morphing mechanism under aerodynamic loading and subsequent activation of SMA wire actuators

### 2.10.2 Investigation of Morphing prior to Aerodynamic Pressure Loading application

In this section the solution of morphing the airfoil prior to the application of aerodynamic loading is investigated. For the numerical simulation of this model the diameter of the SMA wires was 4mm for the upper actuator and 6mm for the lower actuator. Lower actuator's dimensions are considered to be increased in comparison with the upper actuator because net aerodynamic force acting on the flap mechanism tend to rotate the flap clock wise, thus lower actuator need to provide the required stiffness. Figure 67 A present the morphing mechanism part representing 10% of chord length while it is activated prior to aerodynamic loading while Figure 67 B shows the

airfoil in its original shape which is achieved by the effect aerodynamic loads have on the rotation of the morphing mechanism flap.

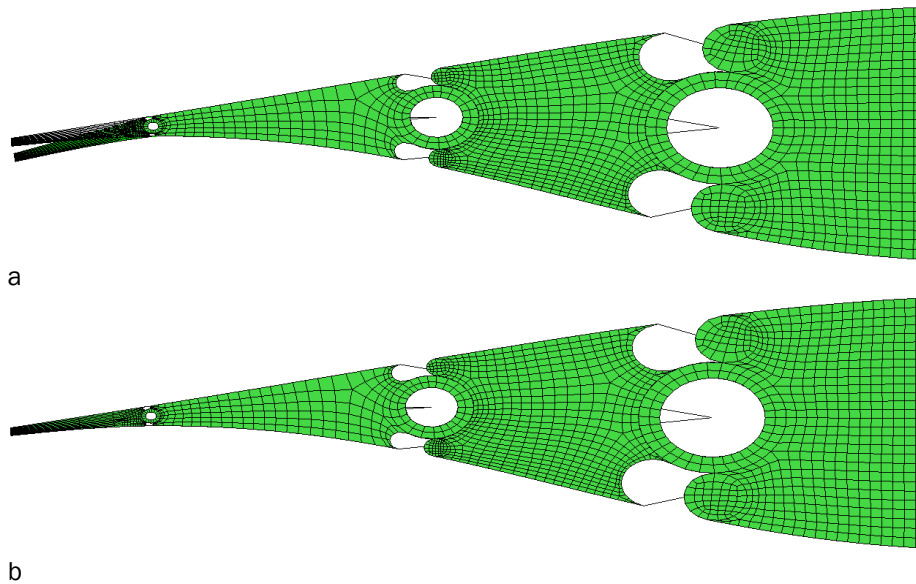


Figure 67: Morphing mechanism (a) deflected prior to aerodynamic loading and (b) after aerodynamic loads are applied

In Figure 68 the angular rotation of the morphing mechanism flap representing 10% of chord length is plotted with respect of analysis time. From 0 till 30<sup>th</sup> second the lower SMA wire actuator is activated in order to rotate the flap to the proper direction. After it reaches that position, aerodynamic pressure is applied and forces the flap to stabilize in a position that forms the initial shape of the airfoil. During aerodynamic loading the lower SMA wire actuator remains activated meaning that Joule heating is applied in a constant rate. After the initial shape position is achieved more electrical power is provided to the lower actuator, in order to rotate the flap of the morphing mechanism to an angle of  $-4^{\circ}$ . The extra power provided to lower actuator begins at 50 seconds and stops at 80 seconds. From 80 seconds and for a period of 30 seconds, upper actuator is activated while lower actuator is cooling down in order to rotate the flap to an angle of  $+4^{\circ}$ .

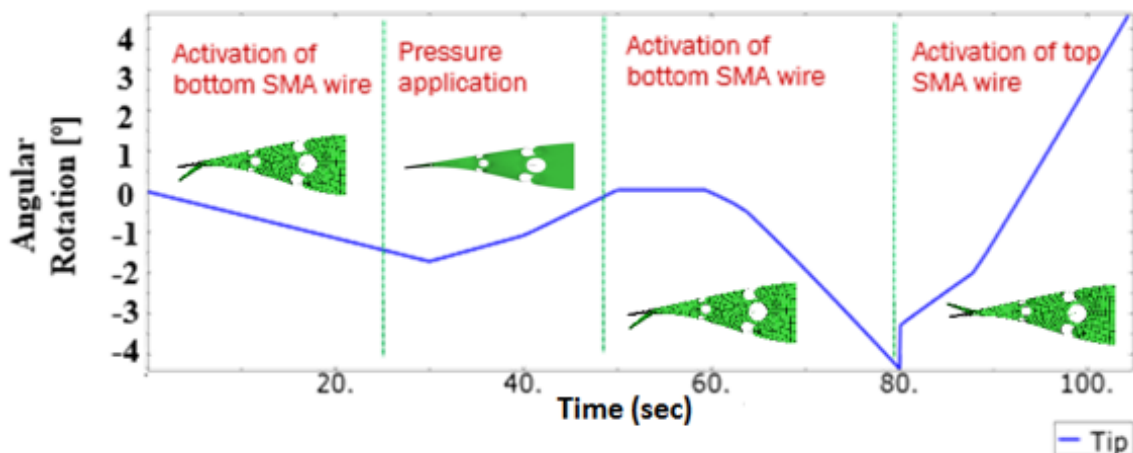


Figure 68: Angular rotation of the morphing mechanism when activated prior to aerodynamic loading vs. analysis time

Although morphing mechanism seems to respond effectively to the morphing requirements the predicted stresses on the actuators and their martensitic volume fraction needs to be studied in order to assess the concept feasibility. In Figure 69 the developed stress for each SMA wire actuator is presented with respect to analysis time. From 0 till 30 second, the lower actuator is activated to rotate the morphing mechanism counter clock wise. Till 30<sup>th</sup> second upper actuator's stress is increasing with a larger rate than the stress developed in the lower actuator because upper actuator antagonizes lower and it is elastically loaded. In 30<sup>th</sup> second the developed stress of the upper actuator reaches a peak and from that time till 50<sup>th</sup> second it is reduced because of the applied aerodynamic pressure. During this time period lower actuator remains activated with a constant amount of power but aerodynamic loads exceed the force implied by the transformation and rotate the flap till it reaches original airfoil shape. At the time the flap reaches this position, the developed stress of upper actuator is zero while lower actuator is activated to sustain aerodynamic loading. From 50 till 80 seconds, where power is supplied to the lower actuator the developed stress increases as well as the stress of upper SMA wire actuators because it antagonizes the rotation of the flap. Finally, from 80 till 110 second the upper actuator is activated while the lower remain activated but with reduced supplied power. Therefore the developed stress in both actuators decreases until 88<sup>th</sup> second. The reduction of the developed stresses is expected because when power provided to lower actuator decreases, aerodynamic pressure tends to rotate the morphing flap mechanism in a clock wise manner, so load on both actuators decreases as the lower one is cooling down and the upper starts to get heated. After 88<sup>th</sup> second the developed stresses start to increase again because upper SMA actuator tends to continue to rotate the mechanism clock wise but the antagonistic actuator reacts in this movement because is elastically loaded. Developed stresses throughout this procedure remain under the design specification level which was set to 270 MPa proving the feasibility of the concept.

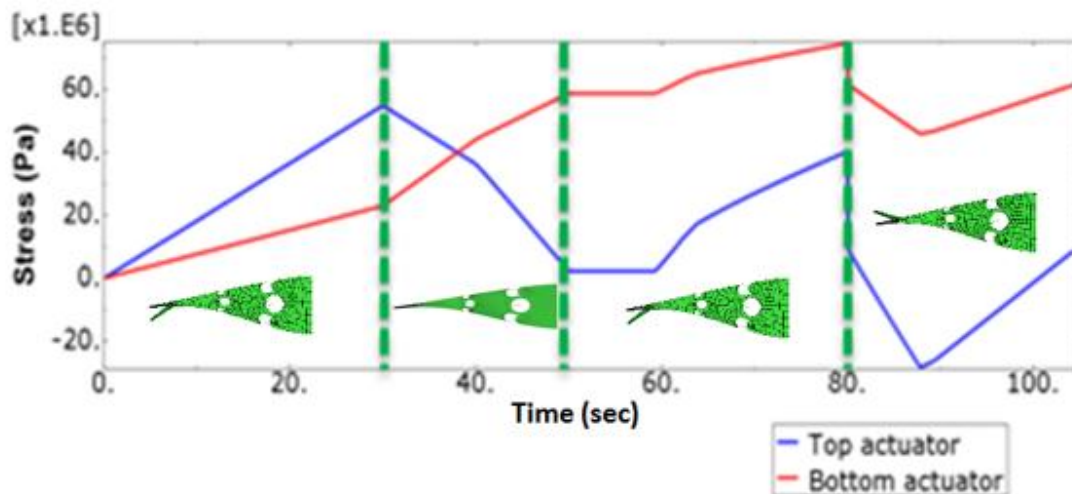


Figure 69: SMA wire actuators developed stress in case of morphing mechanism activated prior to aerodynamic loading and then morphed to predefined positions vs. analysis time

Finally, in Figure 70 the variation of the SMA wire actuators martensitic volume fraction is presented with respect of analysis time. Both actuators have their martensitic volume fraction set at 0.2 at their initial state. As power is supplied to the lower actuator and it gets heated his temperature rises and reverse transformation is initiated meaning that martensite begins to turn into austenite. Due to the transformation till 30<sup>th</sup> second lower actuator's martensitic volume fraction decreases while upper actuators remain constant as the developed stress is not enough to initialize the forward transformation. During aerodynamic load application (30<sup>th</sup> to 50<sup>th</sup> second) upper actuator is practically unloaded while lower actuator is stressed because it tries to sustain

the load developed by aerodynamic pressure. The mechanical loading combined with the constant power provided lead to the stabilization of the transformation of lower actuator till 42<sup>nd</sup> second where martensitic volume fraction slightly increases. From 50<sup>th</sup> second till 80<sup>th</sup> second lower actuator is provided with increased power to rotate the morphing mechanism counter clock wise so its martensitic volume fraction decreases as the actuator transforms from martensite to austenite. Upper actuator's martensitic volume fraction remain stable until approximately 70<sup>th</sup> second, but after that it begins to increase because the developed stress due to the antagonistic configuration initializes forwards transformation. After 80<sup>th</sup> second and till the end of the numerical simulation, upper actuator is activated while power provided to lower actuator is decreased in order to rotate the morphing mechanism clock wise. During this procedure the martensitic volume fraction of the lower actuator increases rapidly. On the contrary provided heat to upper SMA actuator causes the initialization of reverse transformation thus martensite is transformed to austenite and martensitic volume fraction decreases with time.

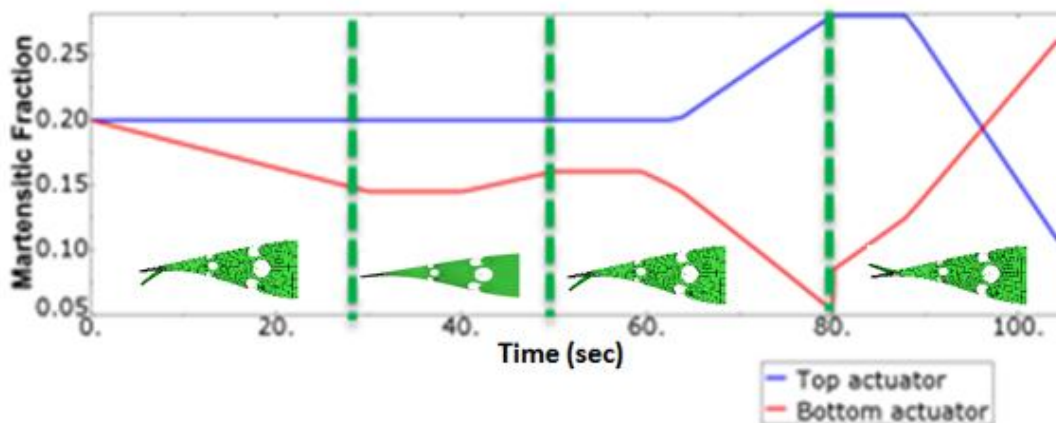


Figure 70: SMA wire actuators martensitic volume fraction in case of morphing mechanism activated prior to aerodynamic loading and then morphed to predefined positions vs. analysis time

Consequently, this final concept utilizes smaller actuator dimensions (smaller cross sectional areas) as the diameter of the SMA wires is 4mm for the upper actuator and 6mm for the lower actuator, while it provides the forces required to morph the mechanism to the prescribed configurations. The dimensions of the actuators for the morphing mechanism part at 10% of chord length and the initial value of their martensitic volume fraction (MVF) are summarized in Table 20. Furthermore the actuator stresses are reasonable and way below the specification set, thus its structural response has been proved sufficient as it sustains the aerodynamic loads and it deforms the flap with 10% of chord length to the desired configuration without being overstressed.

Table 20: Actuator dimensions for the morphing mechanism part at 10% of chord length

Actuator	Length [m]	Diameter [m]	Initial MVF
Upper	0.680	0.004	0.2
Lower	0.675	0.006	0.2

In Figure 71 the horizontal red dashed line states the percent of chord length with morphing capability and the vertical red dashed line states the maximum angular rotation this mechanism achieves under the specified conditions of the numerical simulation. The target angular rotation of 4° in both upwards and downwards direction produces a variation in coefficient of lift which is 0.15. This value is adequate for normal operational conditions but can be increased if more heat is applied to the actuators to enhance their performance.

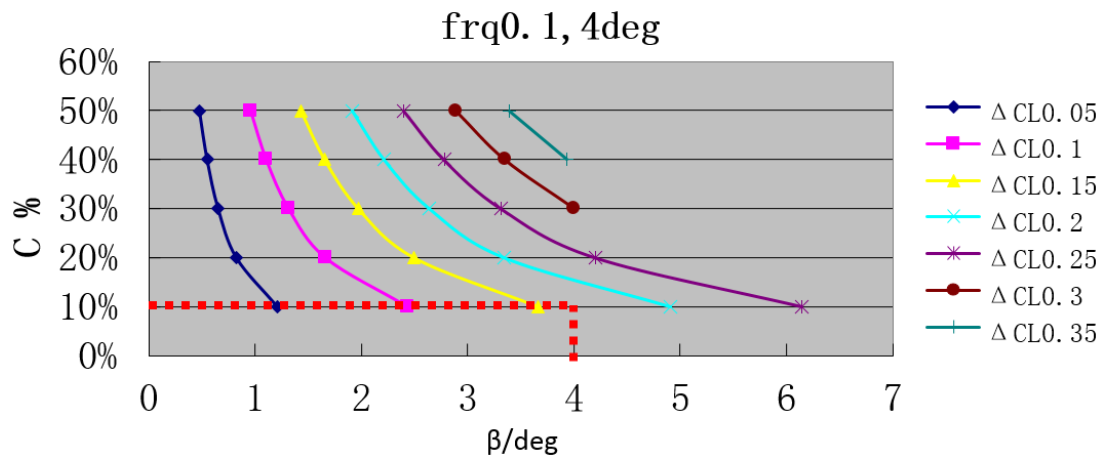


Figure 71: Variation of  $C_i$  capability during morphing state

### 2.11 Selection of Skin Material

To bridge the gaps created from the slots that exist between mechanism parts, a proper skin material structure must be considered. An extended literature review has been performed to address a suitable airfoil skin material or concept in order to both bridge the slotted gaps and provide a continuous skin surface that would sustain aerodynamics loads and be easily morphed. The aforementioned requirements are contradictory because aerodynamic loads are out of plane whereas the stretching loads implied by movement of mechanism parts are in plane. Consequently, the skin material selected should provide enough out of plane stiffness and in plane flexibility.

The first solution considered was the use of cellular materials such as honeycomb structures that either are anisotropic or can be pressure adaptive. Anisotropic cellular materials have elastic response that depends on the direction of load. Pressure adaptive cellular materials “recognize” the applied pressure on their surfaces and respond to a predefined way. In Figure 72 a pressure adaptive cellular structure is presented schematically. When the mechanism parts move the cellular structure is stretched as small black arrows indicate. Because of the stretching cell are deformed and increase their volume as they expand like bold black arrow show in Figure 72. The described expansion of the cellular structure increases its stiffness in the out of plane direction. The main advantage of these materials is their adaption to various geometries but their response is difficult to control and require extensive study and to design them properly.

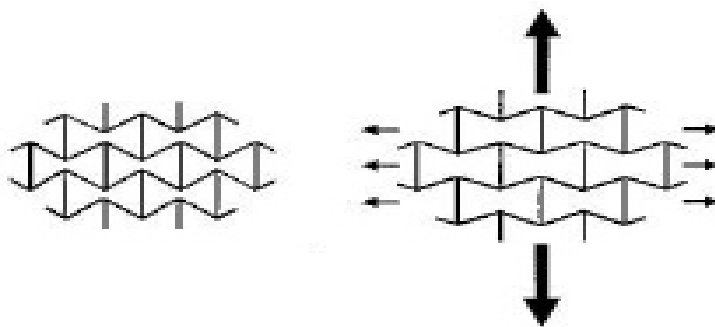


Figure 72: Response of an adaptive cellular material when loaded

Another possible alternative for skin material is the use of elastomeric matrix composite materials that have flexible rubber matrix and are reinforced by stiff rods wrapped with fabric as shown in Figure 73. This composite structure can be easily integrated with airfoil original skin and can

provide the required in plane flexibility. The challenge that this concept requires is the design of the composite in order to have the desired mechanical properties. Moreover, the flexibility of the elastomeric matrix is compromised by the stiff elements that are inserted in order to increase the stiffness in out of plane direction. Design requires different strain amplitude in perpendicular directions which is very challenging and is difficult to model and test.

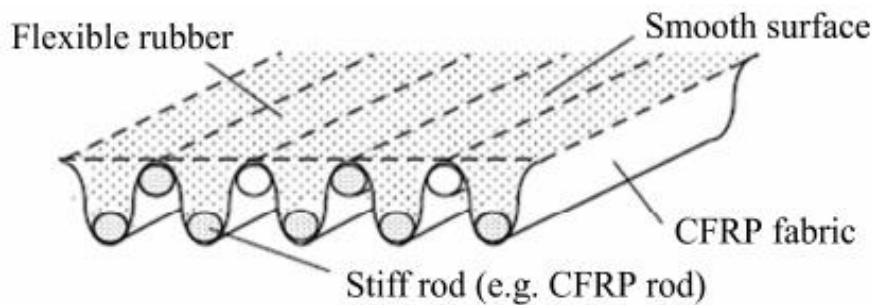


Figure 73: Schematic representation of an elastomeric matrix composite

A morphing skin solution that can be considered for this morphing concept is the use of air pressure to inflate a highly flexible elastomeric skin that is wrapped around the morphing mechanism. The concept is presented schematically in Figure 74. The section of the blade where morphing mechanism is implemented needs to be dry sealed and the mechanism must be separated from the rest of the blade as a totally enclosed structure. When the SMA actuators are activated and the mechanism morphs the airfoil proper channels near the slots of the mechanism open in order to let air inflate properly the elastomeric skin in order to create a continuous aerodynamic surface which is fully compatible with the mechanism movement. Although this concept might seem ideal, it requires careful design and many modifications in both original airfoil and morphing mechanism structure increasing significantly the complexity of the concept and therefore rendering it unfeasible.

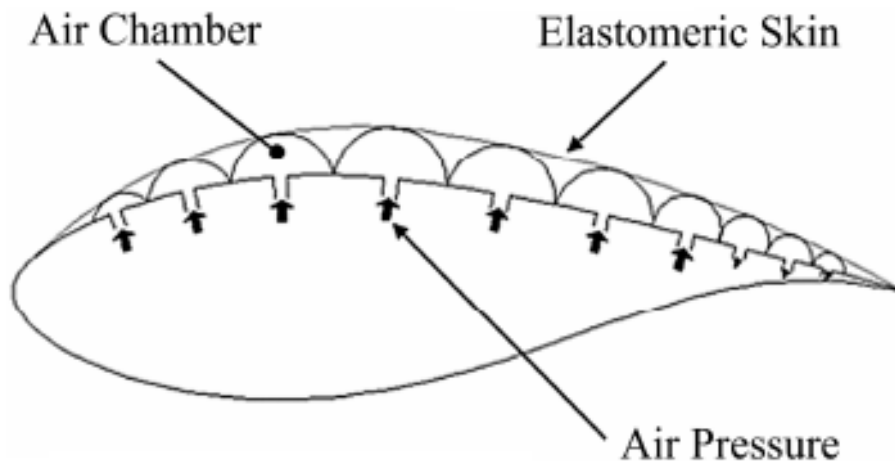
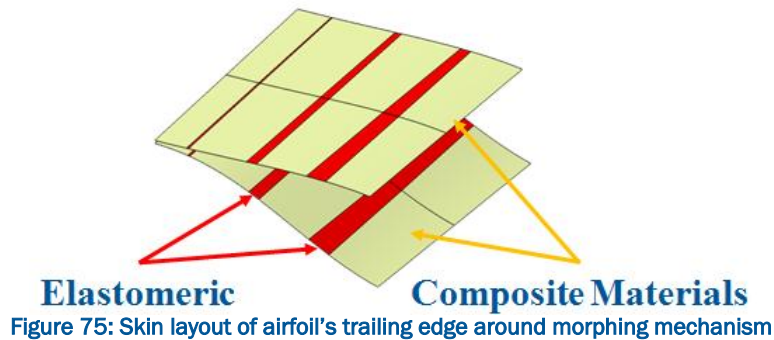


Figure 74: Representation of layout of an airfoil with inflatable skin

The skin material selected is a flexible elastomer that can be easily shaped during the movements of the rotating mechanism parts. Elastomeric skin can be easily embedded and tied with the composite materials that constitute the airfoil skin. It will provide a smooth aerodynamic surface when under stretch but it will not be as ideal when compressed. This drawback can be neglected for the purposes of the present study.



## 2.12 Conclusions and Recommendations

In the preceding paragraphs the work conducted and the steps followed towards the development of a new morphing concept for the wind turbine blade section based on Shape Memory Alloy actuators has been described. The additions performed in the developed numerical tool for SMA actuators in order to increase its accuracy and enhance its capabilities for the prediction of their morphing function were described. Various primitive morphing concepts based on SMA actuators have been examined to reveal the fundamental operational principles and give the design guidelines to be followed towards the development of the final concept. The most promising concept has been further investigated to assess its structural integrity under aerodynamic and actuation loads. The numerical simulations have proved the successful development of the morphing concept, as it meets the morphing requirements and reaches the desired morphed configuration without overstressing any of its components.

### Conclusions:

The presented morphing concept solution has been based on Shape Memory Alloy actuators in order to provide the required forces to deflect the structure to the desired configuration. It comprises the first part of the morphing section design and development for active fatigue load alleviation. As the structural response of the morphing concept has been simulated, optimized and proved to be feasible additional tasks have been accomplished in order to further expand and/or demonstrate the functionality and promote the technology readiness level (TRL) of the proposed morphing section concept.

The prediction of time response as well as the estimation of power requirements of the proposed concept have already been examined based on the downselected morphing concept in the framework of INN WIND.Eu project under Task 2.3. Results of this study can be found in deliverable D2.31. Fatigue life estimation of SMA actuators, manufacturing issues and experimental tests of a reduced scale prototype have been planned to be addressed in Task 2.2 of INN WIND.Eu project under the deliverable D2.24 entitled “Manufactured and laboratory tested scaled blades and parts of the blade” which is due month 46. Additionally, multidisciplinary assessment of both structural and aerodynamic phenomena on the morphing airfoil is planned to take place under task 2.3 in order to further prove the plausibility of the concept and to measure its effect on the primary goal of this effort, the active load alleviation of the wind turbine blade.

### Issues and considerations to be addressed inside the INN WIND.EU framework:

- Prediction of time response of the structure (completed in WP2.3, D2.31)
- Estimation of power requirements for the concept function (completed in WP2, D2.31)
- Experimental characterization of SMA fatigue life (planned in WP2.2, D2.24)
- Manufacturing aspects of the proposed concept (planned in WP2.2, D2.24)
- Reduced scale prototype manufacturing and morphing functionality tests (planned in WP2.2, D2.24)

Effect of thermal loading of SMAs on the composite parts of the airfoil (planned in WP2.2, D2.24)  
Simulation of fluid structure interaction between the morphing section and the surrounding flow conditions will be performed in collaboration with NTUA (planned in WP2.3, D2.32)  
Integration of the morphing concept to the wind turbine blade and numerical prediction of the morphing concept effect on the load alleviation in collaboration with NTUA (planned in WP2.3)

**Cost issues:**

In order to implement the proposed solution presented in the previous sections a few modifications and additions to the structure of the wind turbine blade section need to be done. These alterations will cause additional manufacturing as well as operating costs of the morphing WTB section on top of the respective costs of the conventional blade structure. Few aspects are envisioned to affect the cost of the morphing WTB section;

- Cost of SMA wire actuators and required links to the blade structure
- Realization of the mechanisms and supportive structure
- Cost of wiring required for heating of actuators
- Cost of energy to heat the actuators through Joule effect, cost to cool them quickly
- Maintenance costs regarding actuator issues
- Cost of the controller used to define the position of the morphing section

Based on this remarks a more extensive cost analysis study should take place in order to assess the cost efficiency of the proposed concept and especially to evaluate if the benefits due to fatigue load alleviation can compensate the increased manufacturing and operational cost of the morphing WTB section based on SMA actuators.

### 3 STRUCTURAL INVESTIGATIONS PERFORMED OF A MORPHING FLAP DESIGNED FOR LONG FATIGUE LIFE

The present section includes the efforts performed by University of Bristol (UBRISTOL) regarding the morphing flap using an elastomer of zero Poisson ratio and the structural issues involved in the application on wind turbine blades. The work has been conducted within the INN WIND.EU projects.

#### 3.1 State of the art and motivation

The INN WIND.EU project [25] aims at designing 20 megawatt (MW) wind turbines; consequently new approaches to load control are required. Significant load reduction was demonstrated in recent research [3], [20], [21], [26] by actively adapting the blade profile at any span-wise location in response to the wind environment. These so called ‘smart rotor controls’ are often active surfaces distributed along the blade and controlled by measured quantities, able to locally adjust the blade profile and quickly reduce the loads in real-time. A number of concepts have been investigated and reported by several laboratories and many articles can be found in the literature, including those of Buhl et al. and Anderson et al. [26], [27], [28]. Variable geometry ‘morphing’ structures are in essence ideal candidates for smart rotor concepts for their adaptive load carrying capability, reduced actuation cost and aerodynamic efficiency. In this report, the design and analysis of an active morphing flap is presented as part of the WP2 “Lightweight Rotor” Task D2.23 “New Morphing Blade Section Designs” of the INN WIND.EU project. Emphasis is given to the structural aspect of the flap, actuation is achieved using off the shelf components. The reader is referred to review articles by Straub [29] and Chopra [30], Hulskamp [31] or Thill et al. [32] for more details on smart actuation.

Historically, morphing devices on rotary structures were first investigated for helicopters, mainly to minimise noise and vibrations. Straub and Chopra reviewed several ideas for load control including pitch, twist, camber and moveable control surfaces [29], [30] from the extensive experience gained during the past 20 years. The concepts and results are of great interest for wind turbine smart control applications and should be considered when developing new designs for wind turbines; although differences exist between helicopter and wind turbine applications. As such, operating parameters differ between the two: helicopter blades are subjected to higher rotational speeds, frequencies, centrifugal forces and aerodynamic forces whereas wind turbines are larger, more cost-driven and not so weight or vibration critical. In both applications, maintenance must be as low as possible and face similar challenges in predicting and understanding the unsteady aerodynamic loads and performance, dynamic stresses and aeroelastic response of the blade. While helicopter blades see highly periodic aerodynamic loads, wind turbine blades are subjected to complicated effects like wind shear, turbulence, tower shadow and the wake of other turbines.

Focus has been mainly given to adaptive trailing edge devices due to their reduced mass and complexity, low aeroacoustic noise and low drag compared to conventional mechanical flaps. Several demonstrators were manufactured and were able to prove the load reduction potential of trailing edge devices [9], [28], [33]-[39].

The proof of concept presented by Daynes et al. [9], [36], [37] demonstrated that a morphing flap is a feasible option for a wind turbine blade. Using commercially available materials, the flap was able to deflect  $\pm 5^\circ$  at 0.45Hz under aerodynamic loading (Reynolds number equal to  $5.4 \times 10^6$ ). The present research extends the work by Daynes et al. on the morphing trailing edge device by investigating the reliability of the structure. While the fundamental design is kept, the concept is adapted to the INN WIND reference wind turbine in a first instance. Several modifications are made to the system presented by Daynes et al. The reliability of the structure is then investigated by fatigue testing separate subcomponents of flap before testing the entire structure.

### 3.2 Brief description of the concept

The external geometry of the morphing flap is extracted from the reference 10MW DTU wind turbine. The flap is positioned at a 75% radial position along the blade, thus its contour follows the FFA-W-3-241 profile with a chord equal to 3.34m. The aerodynamic loading is calculated considering the following conditions:

- the wind turbine speed of rotation is 1rad/s
- the free stream air speed is 25m/s
- the induction factor is approximated to 2/3
- the blade pitch angle is zero

The above conditions yield a wind speed of 69m/s and a local angle of attack of  $14^\circ$  at the morphing flap section. It is deduced that the Mach number is  $M \sim 0.2$  and the Reynolds number is  $Re \sim 15 \cdot 10^6$  at this radial location. It is worth noting that the aerodynamic panel code X-Foil [43] is used for the aerodynamic part of this study. It is found that the coefficient of lift is  $C_l = 1.975$  under the above mentioned atmospheric conditions. The aim of the morphing flap is to reduce by 25% the  $C_l$  in the same aerodynamic conditions. The requirements for reduced actuation power and system complexity are also key design factors. The structure selected for the morphing flap is composed of a carbon fibre reinforced plastic (CFRP) suction skin covering an anisotropic core material (honeycomb). A low Young's modulus material (polyurethane foam) is applied to the pressure side of the flap, enabling large bending deformations with reduced actuation force. This solution also provides air/water tightness to the structure. A push-pull rod is used to enforce bending of the flap. The rod is attached to the tip of the flap at one end, to the actuator at the other end and is guided through the core with eyelets. A hard wearing material (ceramic) could be used for the eyelet to reduce friction and increase working life. A schematic view of the flap is shown in Figure 76.

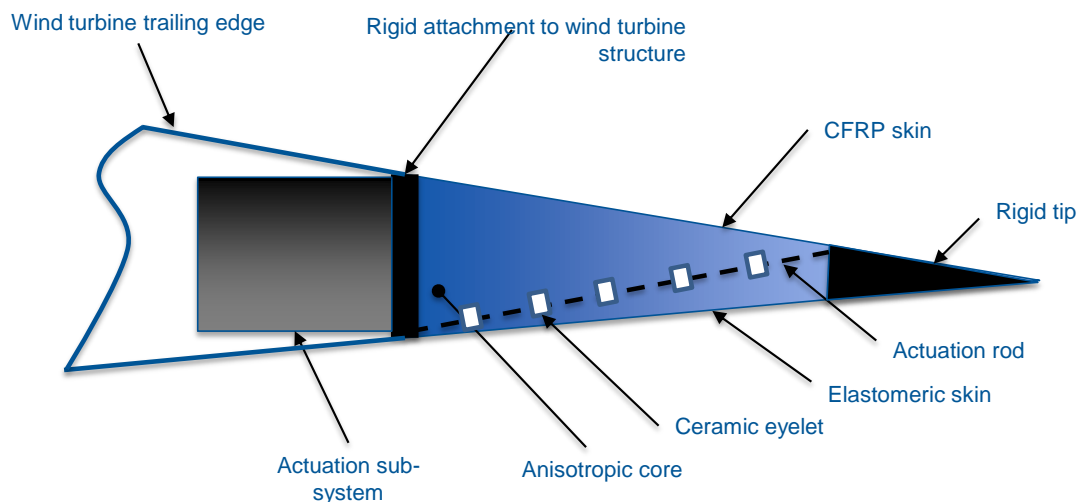


Figure 76. Schematic view of the morphing flap concept.

To reduce the design space of the flap, the effect of key parameters on the flap response is investigated with a sensitivity study. Those design parameters are the size of the rigid tip and the size of the flap, taken from the rigid attachment to the wind turbine. The size of the flap is expressed relative to the chord of the blade section whereas the size of the tip is given relative to the flap size. The flap size is varied between 0.1 to 0.3 in 0.1 increments and the tip size is set between 0.15 to 0.45 in 0.15 increments. The material properties for the CFRP / elastomeric

skins as well as the properties of the core are given in Table 21. It is worth noting that those materials correspond to widely used, commercially available, materials.

**Table 21. Mechanical properties of the materials employed for the morphing flap.**

Material	$E_1$ (GPa)	$E_2$ (GPa)	$E_3$ (GPa)	$\nu_{12}$ (-)	$\nu_{13}$ (-)	$\nu_{23}$ (-)	$G_{12}$ (GPa)	$G_{13}$ (GPa)	$G_{23}$ (GPa)	thickness (mm)
SE70 HE200	137	7.81	7.81	0.29	-	-	4	4	2.69	0.2
Poly urethane foam	$0.6 \times 10^{-3}$	$0.6 \times 10^{-3}$	$0.6 \times 10^{-3}$	0.3	0.3	0.3	$0.23 \times 10^{-3}$	$0.23 \times 10^{-3}$	$0.23 \times 10^{-3}$	-
Honeycomb (3mm cells)	$0.9 \times 10^{-3}$	$100 \times 10^{-3}$	2.5	$\sim 0$	$\sim 0$	$\sim 0$	$50 \times 10^{-3}$	$50 \times 10^{-3}$	$1.25 \times 10^{-3}$	-

### 3.3 Design and analysis of a morphing flap

#### 3.3.1 Influence of flap size and tip size

##### 3.3.1.1 Fluid structure interaction tool

In order to run the several sensitivity studies, a Fluid Structure Interaction (FSI) tool was designed. The program, written in Matlab [44], manages the results given by the structure solver Abaqus [45] and the aerodynamic pressure distribution computed by X-Foil; as shown by the diagram in Figure 77. In the first step, no aerodynamic pressure or actuator displacement is applied to the analysis run with Abaqus. This initial step provides the un-deformed mesh of the flap in a load free condition. The contour of the mesh is then sent to X-Foil to compute the pressure distribution and coefficients of lift and drag. Those values are the reference values; against which the load alleviation of the flap will be compared. In the second Abaqus analysis, the actuator displacement is provided, yielding the deformed shape of the flap in a load free condition. The deformed contour of the flap is then passed to X-Foil for aerodynamic calculations. At this point of the simulation, a conditional statement checks the last two values of the coefficient of lifts computed. If the difference between the values is above a defined threshold, an Abaqus input file is produced with the latest pressure distribution given by X-Foil. The smaller the threshold, the longer the analysis as the number of loops between Abaqus and X-Foil is increased. It was found that the value of 0.05 yields accurate results yet fast analyses.

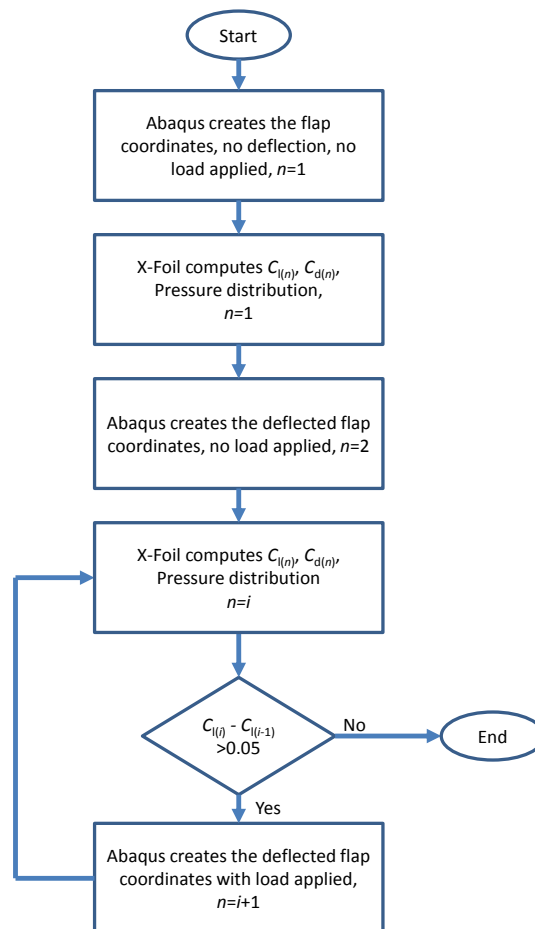


Figure 77. Diagram showing the Matlab FSI loop

It is worth noting that the Abaqus model only requires the flap section whereas X-Foil needs the entire aerofoil. The two different meshes are managed by a Matlab script; which refines the mesh at the trailing edge for the Abaqus input file and defines the aerofoil outer shape for X-Foil.

### 3.3.1.2 Sensitivity studies

The sensitivity studies were carried out by incorporating the FSI script inside loops varying the size of the tip and the size of the flap. Different properties for the flap were monitored and are shown in Figure 78a to d for three actuation displacements:  $U = 10\text{mm}$ ,  $U = 12.5\text{mm}$  and  $U = 15\text{mm}$ . The x-axis of the plots corresponds to the chord-wise size of the flap, expressed as a fraction of the aerofoil chord. Calculations are made for the ratio: 0.1; 0.2 and 0.3. The size of the tip is expressed as a fraction of the flap size and is equal to 0.15, 0.3 and 0.45. Figure 78a shows the difference of coefficient of lift between the non-actuated state and the actuated, stable shape of the morphing flap, i.e. once the aeroelastic script has converged. Figure 78b presents the variation between the coefficient of lift of the deflected flap in a load free condition and the coefficient of lift of the deflected flap in the stable, loaded condition. The 100% mark means the two values are identical, i.e. there is no residual bending of the flap caused by the aerodynamic loading. Figure 78c shows the force applied to the rod to actuate the flap in a load free condition. Contrarily to a mechanical flap, the morphing flap has an inherent structural stiffness that the actuator must fight, even in a load free environment. Figure 78d plots the evolution of the total force required to actuate the flap under aerodynamic loading.

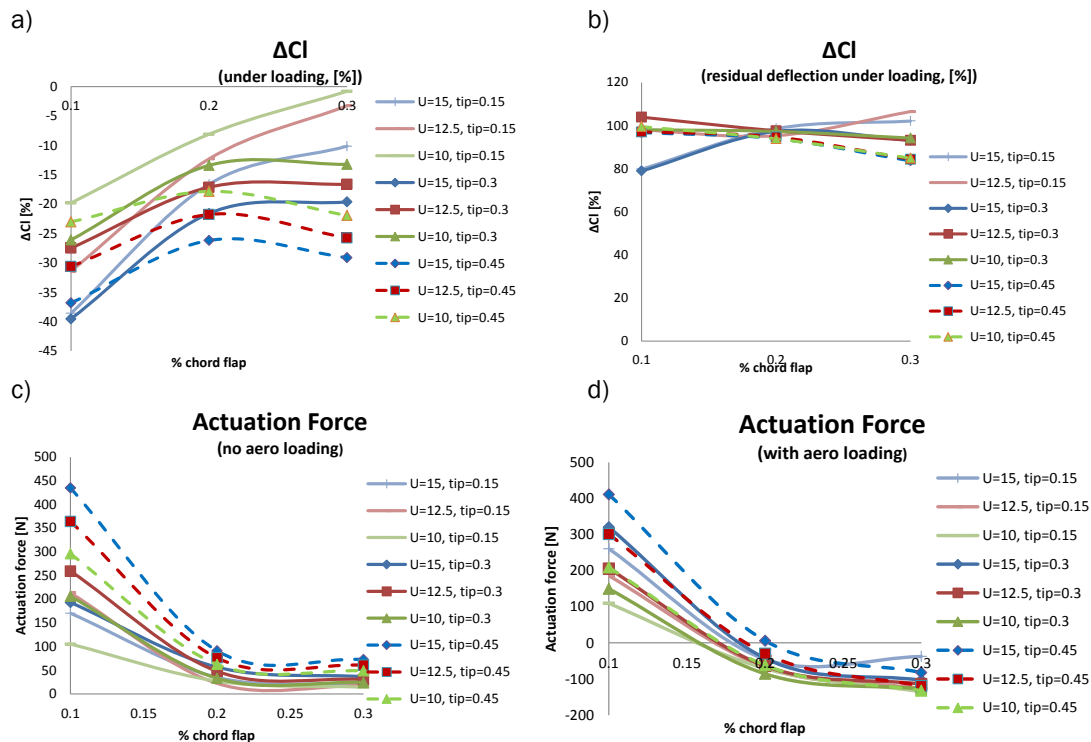


Figure 78. Influence of the flap size and rigid tip size for three actuator displacements. a) Global change in coefficient of lift. b) Residual change of coefficient of lift. c) Load free actuation force. d) Total actuation force.

A careful analysis of the data set shows that a flap having a 20% chord with a rigid tip of 45% presents the best compromise between actuation requirements, change of coefficient of lift and residual bending deformation under loading. The above properties can be found on the plot of Figure 78a to d for the set of dashed line at the x-coordinate  $x = 0.2$ .

### 3.4 Design of a reduced scale morphing flap

As a proof of concept, a reduced scale demonstrator was manufactured at the University of Bristol. The reduction in scale was driven by the potential wind tunnel test of the demonstrator; hence the scale of the demonstrator fixed at 1:2.1. The profile of the aerofoil remains the FF-A-W-3-241; but the chord is now 1590mm. Keeping the 20% chord flap, the morphing flap is 318mm in chord with a maximum height of 75.5mm at the interface with the rigid body of the blade. The span of the flap is limited to 250mm for manufacturing purposes. Larger prototypes would be difficult to handle by ourselves and any machining would need to be outsourced; hence the limitation in span.

The same study as in §2.2.2 was carried out to find the optimum tip size, to achieve the best compromise in terms of flap deflection for a given actuation displacement and to lower the actuation power. This was done under the aerodynamic loading the flap would be subjected to in our wind tunnel, i.e. a wind flow of  $60\text{m}\cdot\text{s}^{-1}$ . No angle of attack was added to the current simulation. As a result, the rigid tip size was reduced to 30% of the flap chord to reduce actuation power, yet without increasing the aeroelastic deflections. The maximum actuation load was found to be 250N. The position of the rod attachment to the tip was also tailored to achieve a smooth curvature of the suction side of the flap, see next sections.

A CAD model of the reduced scale demonstrator is shown in Figure 79. As per a full scale flap, it consists of a CFRP skin, a rigid tip, a honeycomb core covered with flexible foam and an actuation

rod attached to the tip. The attachment of the flap to the wind turbine is made via a rigid spar, through which the actuation rod travels. It is envisaged that the actuator is an electrical linear cylinder for the fast reaction time and ease of integration it can offer; however the selection, integration and command of the actuator itself are not covered in this study.

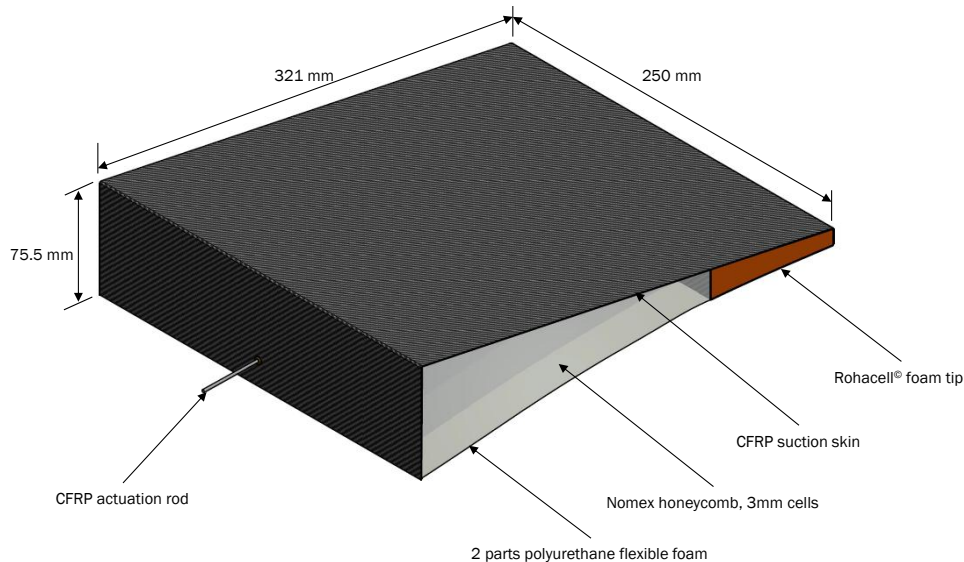


**Figure 79. CAD representation of the morphing flap and detail of the main components**

The next sections detail the design of the key components of the flap. Emphasis is given to the methods in order to enable reproduction and/or scaling up of the manufacturing processes.

### 3.4.1 Morphing skin design

Previous experience in manufacturing morphing skins made of a sheet of silicone rubber bonded to honeycomb cells highlighted the low bond strength between the two components, leading to regions of skin peeling off under aerodynamic pressure. This issue is addressed here by developing a new morphing skin using low stiffness polyurethane “soft” foam instead.

The low bond strength observed between the silicone skin and the honeycomb cells originates from the small area of bond provided. Indeed, in this instance, only the edges of the honeycomb cells are in contact with the skin. To palliate this outcome, one needs to wet the inside surfaces of the honeycomb cells. This could be achieved by increasing the thickness of the silicone skin; however this adversely increases the actuation power. The use of a lower Young’s modulus material is therefore required, keeping in mind the necessity to maximise the wetted surface of the honeycomb cells.

The material chosen is a flexible polyurethane foam from Polycraft [46] made by mixing two chemicals: a polyol and an isocyanate. This enables us to “grow” the foam inside the honeycomb, as illustrated in Figure 80. By actually making the foam in-situ, the bond between the foam and the honeycomb wall cells is immediately made and ensures greater pull strength compared to the silicon skin solution. It is worth noting that this manufacturing method requires the honeycomb cells to remain open; as otherwise the foam cannot grow due to the increasing pressure of the air trapped inside the cells. In the course of manufacturing samples for characterisation, it was also noticed that the growth rate and quality of the foam inside the honeycomb cells is highly dependent on the ambient temperature and the ratio between the two components constituting the polyurethane chemical system; while the quality of the skin was highly sensitive to the release agent applied to the mould and the time spend mixing the chemicals. Note that the short pot life

of the polyurethane foam could actually be an issue in terms of mass production, as this leaves little time to pour the liquid mixture in the cast and to place the honeycomb over it. Figure 81 show few of the samples of morphing skin produced where different mixing ratios and release agents were used. It was found that increasing the amount of isocyanate improved the skin quality: the foam grew uniformly and the cell size remained small and constant over the entire surface of the skin. This also increased the curing time and the stiffness of the foam. A series of tests was therefore carried out to find the optimum mixing ratio between the two chemicals constituting the polyurethane system. It was found that a mixing ratio of 2 parts of polyol to 1.125 part of isocyanate (in weight), instead of the 2:1 specified by the supplier, the foam produced had uniformly distributed small cells and an increased working time, enabling the manufacture of a skin of large dimensions. It was noticed however that some area of foam presented open cells. This in terms reduces the aerodynamic properties of the aerofoil and increases the risk of water ingress and dirt accumulation on the surface of the aerofoil. The use of different release agents, instead of using a release film, was therefore investigated. A PTFE (silicon) spray was tried but adversely increased the size of the foam cells by reacting with the polyurethane chemicals. Finally, a uniform distribution of cells across the entire area of the sample was achieved using wax as release agent, as shown in the far right photograph in Figure 81. In average, the foam grew ~10mm inside the honeycomb cells. A thinner skin would be suitable in terms of pull-off strength, as explained later; however handling a small amount of foam would make the manufacture impracticable.

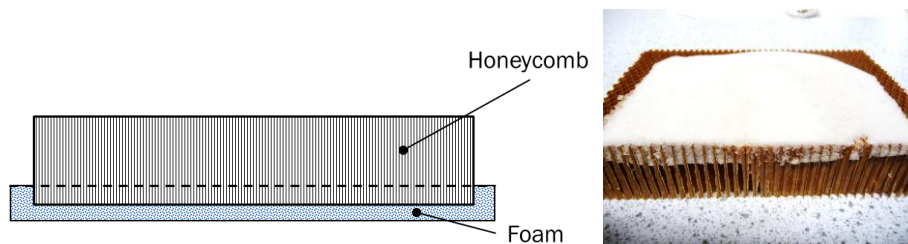


**Figure 80. Schematic view of the morphing skin and photograph of the through thickness foam growth in the honeycomb cells.**



**Figure 81. Photographs of different morphing skin samples. One can notice the increasing quality of the surface of the foam. From left to right: 2:1 polyol to isocyanate mixing ratio / no release agent; 2:1.5 polyol to isocyanate mixing ratio / no release agent; 2:1.125 polyol to isocyanate mixing ratio / silicon release agent; 2:1.125 polyol to isocyanate mixing ratio / wax release agent.**

The foam elastic properties were first tested in a tensile test, see results in Figure 82. Dog bone shaped samples were casted and trimmed to comply with ASTM D3574 part E. The thickness of the samples was 11 mm and the test speed was set at 500mm/min. The Young's modulus was averaged at 500Pa and used in the FE analysis of the flap. Interestingly, one can notice the peak in Young's modulus for small strains (<4%). This repeatable effect could not be explained by the authors at the time of publication of this report.

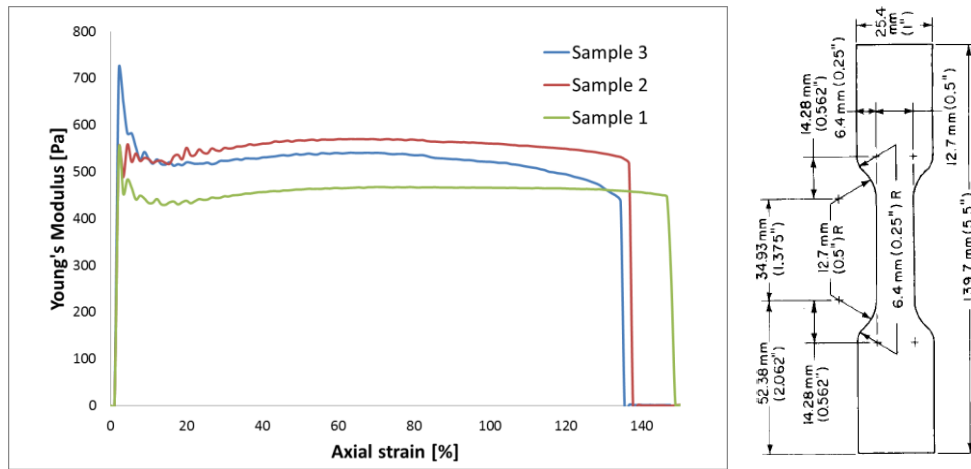


**Figure 82.** Tensile test results on three samples of Polyfoam flexible polyurethane foam, the shape of the samples is given by the ASTM D3574 part E, as shown on the right.

The tensile strength of the interface between the foam and the honeycomb cells is a crucial feature to ensure flap integrity. An experiment, inspired by the ISO 4624 (pull-off adhesion testing of coatings), was therefore carried out to evaluate this property. It consisted of a sample of morphing core bonded to a thick aluminium base on one side and to a test dolly on the other side, see Figure 83. The adhesive used to bond the test dolly to the foam and the honeycomb to the base is the two components epoxy resin AS89.1 and AW89.1 from Elantas [47]. The tensile test result shows two stages (see Figure 84): first, for vertical displacements < 4mm, the foam is elastically elongated and there is no failure of the foam or of the bond between the foam and the honeycomb, as shown by the picture in Figure 84. Then, for vertical displacements > 4mm, the reduction in adhesion force denotes the failure of the foam, as seen in the photograph of Figure 83.

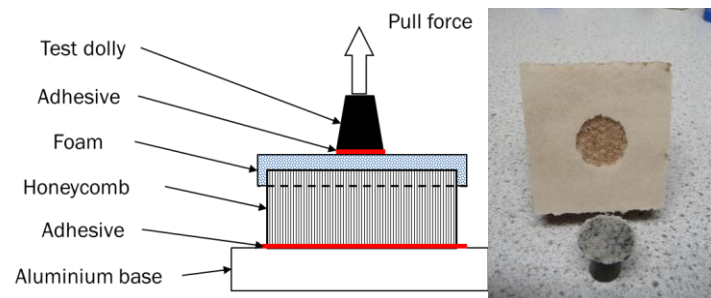


**Figure 83.** Pull-off adhesion test of the morphing skin and test apparatus.

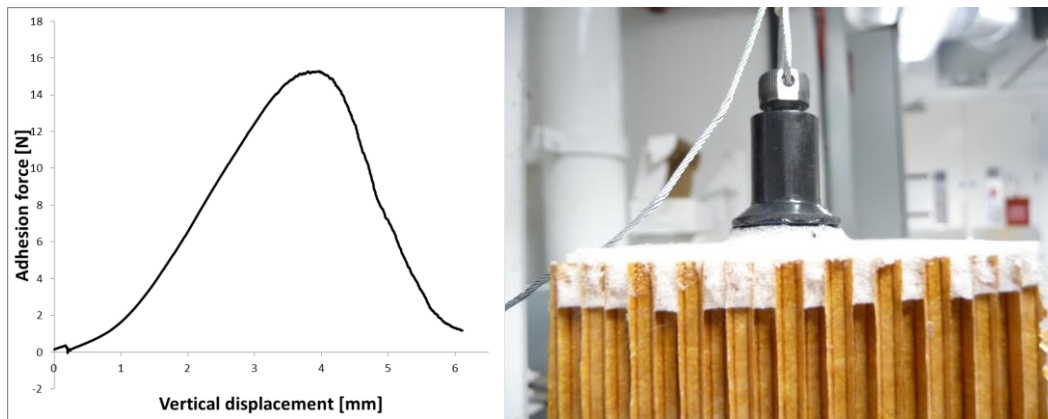


**Figure 84.** Left: Result of the pull-off test carried out with a  $\varnothing 20\text{mm}$  dolly bonded with Elantas epoxy resin system [47] on a sample of morphing skin. Right: Photograph of the pull-off test in the elastic deformations phase.

Converting to pressure the maximum value of 16N found with the pull-off adhesion test, the morphing skin can withstand a maximum of  $\sim 50 \times 10^3 \text{ Pa}$  before failing. This is compared to the 1600Pa of dynamic air pressure found with X-foil; yielding a safety factor of  $\sim 31$ .

### 3.4.2 Zero Poisson's ratio honeycomb core

In order to keep the flap profile constant along its span, the honeycomb core needs to offer a single curvature in the chord-wise direction. This is in contradiction with the well-known anti-clastic curvature developed by conventional honeycomb, like the Nomex core used in this demonstrator. Note that several concepts were investigated to solve this issue and can be found in the literature [48], [49], [50] but none of them can easily and cheaply be mass produced. It was therefore chosen to slice the core into narrow strips of 22mm in order to obtain the desired single curvature surface of the pressure side, as was done in ref [37]. Note that for the manufacture of the flap, the block of honeycomb was grooved and not sliced in order to ease the handling of the material. As such, 5mm of honeycomb was left at the boundary with the CFRP skin, as shown in the drawing in Figure 85. A bending test was also carried out to quantify the influence on the stiffness of the honeycomb of the added foam skin. Slices of morphing core were therefore tested in bending and the results compared to the conventional Nomex core. As shown in Figure 86, the added skin has a negligible impact on the stiffness of the core for the range of deflections the demonstrator will undergo. The honeycomb modulus in the direction perpendicular to the ribbon was approximated to 0.9MPa, slightly higher than the value on the experimental curve, to account for the restraint provided by the remaining 5mm of material.

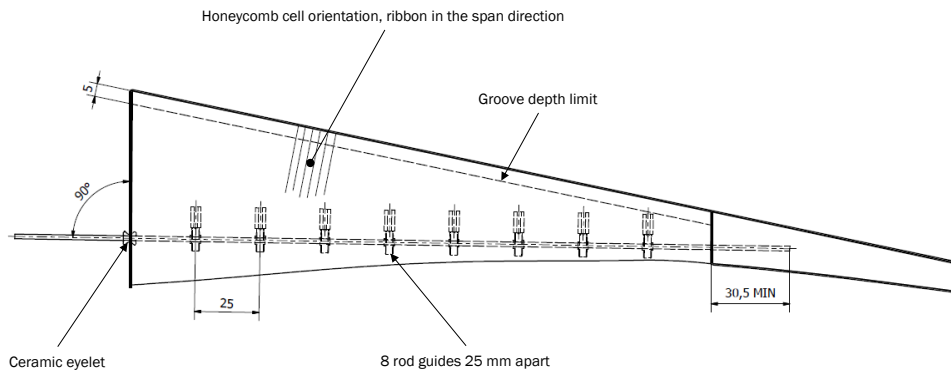


**Figure 85.** Side view showing the actuation rod guides, the honeycomb cell direction, details of the actuation rod bond and the groove depth limit.

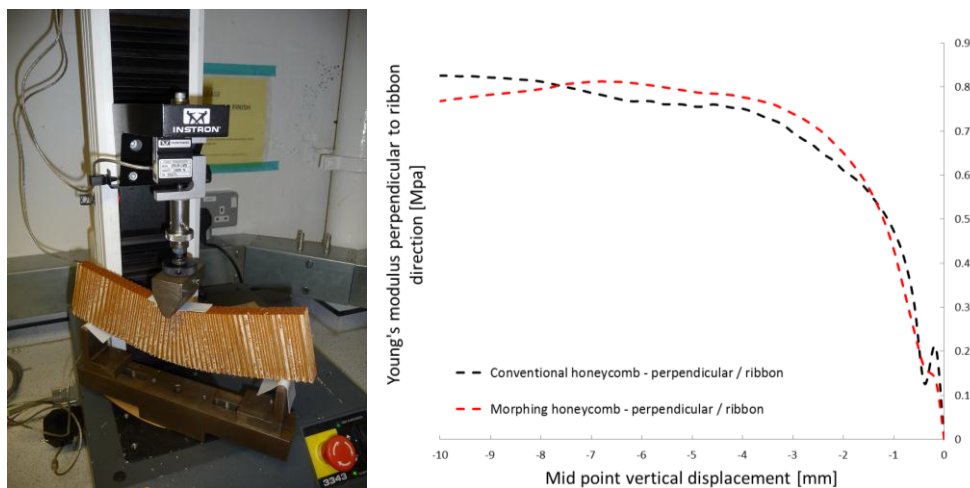


**Figure 86.** Photograph of the honeycomb bending test and comparison between the morphing core and the conventional core properties. Note that results of the Young's modulus are shown only in the direction perpendicular to the ribbon's direction to match the direction the honeycomb is used in the morphing flap.

### 3.4.3 Actuator rod attachment and guides

The tensile strength of the bonds at both ends of the actuation rod was tested. A simple tensile test reproducing the configuration of the attachments was therefore carried out, as shown in Figure 87. The fixed end of the rod was inserted and bonded to the foam core used in the tip of the demonstrator while the moving end of the rod was bonded to a metal pin to reproduce the attachment to the actuator. Both ends were impregnated with the two components epoxy resin from Elantas over a length of 20mm, as shown by the right hand side photograph in Figure 87. It can be seen on the same picture that the failure is caused by the breaking of the foam, not of the resin. The wetted area by the resin in the tip of the flap is thus critical in achieving the maximum load of 250N required to morph the flap. Note that in the final design of the flap, the bonded length of carbon rod was increased to 50mm at both ends of the rod to ensure adequate stress transfer through the bond.

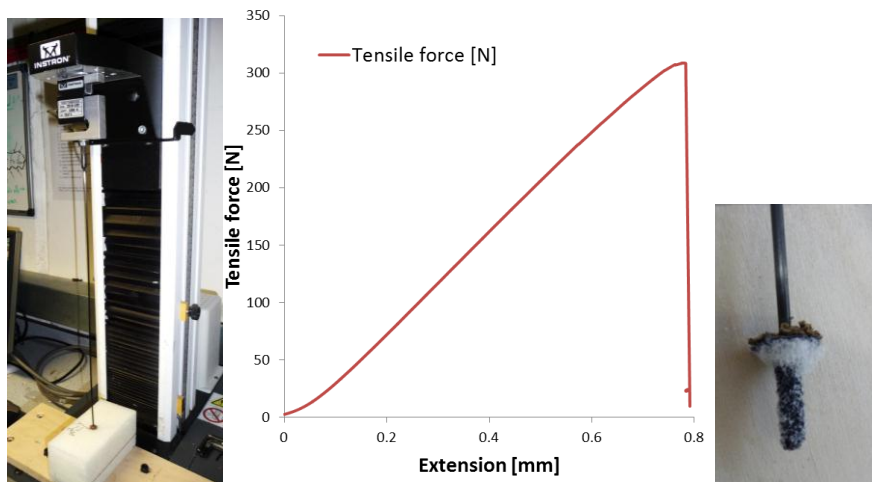


Figure 87. Tensile test of the actuation rod attachment points

### 3.5 Manufacture of a reduced scale morphing flap

The manufacture was decomposed into several stages: first, the carbon skin was manufactured, which included the rigid foam tip. Second, the honeycomb was prepared: grooves were made with a circular saw to achieve the near zero Poisson's ratio, the pressure side was then milled to match the FFAW3241 profile, the rod ends were bonded to the honeycomb before the foam skin was casted on the pressure side. Finally, the honeycomb and the actuation rod were bonded to the carbon skin. The next sections detail the manufacture of each component to allow for future manufacture of demonstrators.

#### 3.5.1 CFRP skin manufacture

A female mould was made out of MDF to reduce cost and lead time for the manufacture of the CFRP suction skin. It was also chosen to make the suction skin, the tip and the rigid spar in a single entity to avoid bonding several individual pieces together. To maximise compliance of the skin, the lay-up was  $[90\ 0\ 90]$ , with the zero degree aligned with the chord axis of the flap. Additional plies were inserted at the flap spar, resulting in a  $[90\ 0\ 45\ 90\ -45\ 0\ -45\ 90\ 45\ 0\ 90]$  lay-up to provide a stiff anchor for later testing. A low temperature CFRP, the SE70 HEC200 from Gurit [51], was selected to enable the cure of the composite using the MDF mould. This also enabled us to include the rigid foam (Evonik Rohacell® IG foam, as used in helicopter blade D nose) in the tip of the flap, as otherwise a dummy mould would be required in this location. Figure 88 shows the lay-up of the CFRP plies; the entire mould bagged up and vacuumed; the finished, cured, part out of the mould. Note that the recommended 8hrs cure cycle at 80°C of the carbon prepreg could be reduced by employing a higher temperature resin system into an aluminium mould, as long as the rigid foam melting temperature is not reached (130°C according to Rohacell).

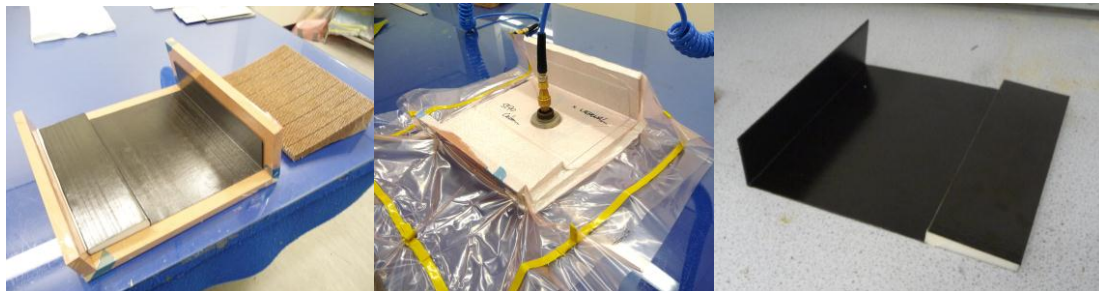


**Figure 88.** The CFRP skin required the manufacture of a mould. The CFRP plies were laid in the mould and wrapped around the rigid foam tip. Note that a tool plate was used where the vacuum valve was positioned in order to achieve a smooth surface. The same was also achieved on the pressure side of the rigid tip by placing several layers of bagging material. A vacuum bag enclosed the entire mould.

### 3.5.2 Morphing core manufacture

As mentioned earlier, the honeycomb core was first machined to the shape of the FFAW3241 profile then the foam was casted on the pressure side; finally the part was bonded to the CFRP skin. Note that the core is perpendicular to the CFRP skin for manufacture purposes: the suction side of the flap being flat, it provides a perfect reference plane to handle and machine the other faces of the core. Furthermore, to increase the accuracy of the cuts and ease the handling of the core, face sheets of 2mm plywood were temporarily bonded to the top and bottom surfaces of the honeycomb block with double sided tape. The block of core material was also cut wider to allow for a finer cut at the exact width at the final step of the manufacture.

The machining of the core employed conventional tools. First, the angled leading and trailing edges cuts were made with a circular saw. Grooves were then created in the chord direction of the flap to obtain the zero Poisson's ratio effect. It is worth noting that contrarily to the previous work by Daynes [37], the core was not sliced through its entire thickness; as otherwise the core would not have any structural rigidity for the next manufacturing steps. Instead, 5mm of honeycomb were left on the suction side, see Figure 85. This was also achieved with a circular saw. Again, the plywood face sheets enabled straight, regular and parallel cuts by providing additional in-plane stiffness.

To reduce the amount of core to be milled, the curvature of the pressure side was approximately cut using a band saw with a diamond tooth blade. The exact curvature was milled using a 3 axis CNC milling machine equipped with a conventional  $\varnothing$  5mm cutter rotating at 5000 rpm. For it, the block of core was temporarily bonded to a tool plate with double sided tape. Initial trials using a ball cutter, as would be used on "conventional" material, proved to be unsuccessful. Although using a conventional cutter did not produce the exact profile, the small size of the cutter made the deviation minimal. The rigid Rohacell block of foam was machined at the same time by positioning the two components as they would be in the flap. Again, double side tape was employed to secure the foam into place. It was noticed that the milling direction and depth of each pass were crucial for the cutter to remove neatly the material: passes of 3mm deep were set up with the cutter going from the trailing edge block of foam "up" to the spar following the FFAW3241 profile. The finished parts are shown in Figure 89.

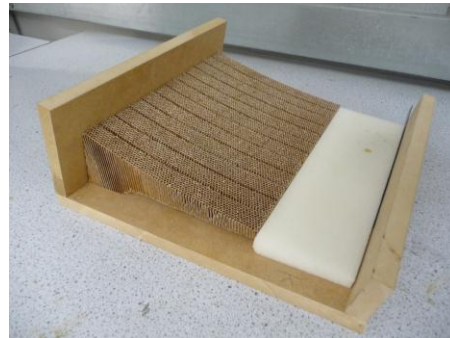


**Figure 89. Milled honeycomb core and rigid foam inside the MDF mould used for the CFRP skin.**

Before the foam was casted, the actuation rod guides were bonded at regular intervals of 25 mm in the core, see Figure 90. The rotational degrees of freedom given by those components enable the actuation rod to follow the deformations of the flap without stress concentrations. However, those components are not designed to accept a sliding rod oscillating through their central hole, thus the fatigue life of the entire system could be compromised. This would require further experiments or the development of a bespoke component. The rod ends are bonded to the Nomex core with the two components Elantas epoxy resin [47]. For it, the core was sliced in two along the mid-span; enabling easy access to the guide positions. Note that the central olives of the rod ends were first coated with silicon to avoid the polyurethane foam from jamming the parts once in-situ. Silicone was also applied to the actuation rod for the same reason.



**Figure 90. Photograph detailing the rod ends inserted in the honeycomb core before the foam skin is applied.**

The last step in the manufacture of the morphing core was the moulding of the foam onto the pressure side of the core. A female mould of the pressure side surface was made out of plywood then waxed to enable easy de-moulding. The mixed chemical system of polyurethane foam was poured onto the mould, quickly spread before the block of honeycomb was positioned over it. Gages of the right thickness were used on the sides of the mould to ensure the skin had a constant thickness over the entire area. The actuation rod was set through the guides during this operation, so the foam would grow around it; hence the importance of the silicon coat on the rod to enable an easy de-moulding. Unfortunately, the foam didn't grow uniformly over a  $\sim 1\text{cm}^2$ , resulting in an open patch, as seen in Figure 91. To the knowledge of the authors, better

manufacturing technics and carefully selected polyurethane foam could prevent this type of incident; thus this shouldn't be considered as a show stopper for the present technology.

### 3.5.3 Morphing flap assembly

The final step in the manufacture of the flap was the bonding of the morphing core to the CFRP skin and the bonding of the actuation rod to the rigid flap tip. The CFRP surface was first sand blasted to improve bond strength while the honeycomb face was acetone cleaned. The CFRP surface was coated with a ~0.5mm thick layer of two component epoxy resin [47]. Attention was given to filling the hole in the flap tip with resin using a syringe to ensure appropriate bonding between the actuation rod and the tip. The same care applied to the bond between the actuation rod and the metallic fitting at the end of the rod. Furthermore, any gap between the morphing core and the flap tip was filled with epoxy resin to achieve a smooth surface. Finally, the flap was cut to the exact span using a band saw with a diamond tooth blade, resulting in the demonstrator shown in Figure 91.



**Figure 91.** Morphing flap demonstrator seen with the pressure side upwards. For unknown reasons, bubbles gathered on the surface of the morphing skin at the time the foam was casted, resulting in a ~1cm<sup>2</sup> patch of uncovered honeycomb, as seen on the right hand bottom corner of the skin.

### 3.6 Morphing flap tests

Static tests were performed to compare the data provided by the FE analysis, the FSI analysis results and the demonstrator. The bending stiffness of the flap was first tested in order to verify the honeycomb material properties. As such, a simple bending test of a 13mm thick slice of flap was performed as seen on the left of Figure 92. The total displacement controlled by the tensile test machine was  $\pm 50$ mm. As shown on the right hand side of Figure 92, the deflected shapes are in agreement with the FE analysis. The force required to bend the flap are shown in the graph of Figure 93. Again, for both downward and upward deflections, the results are in agreement.

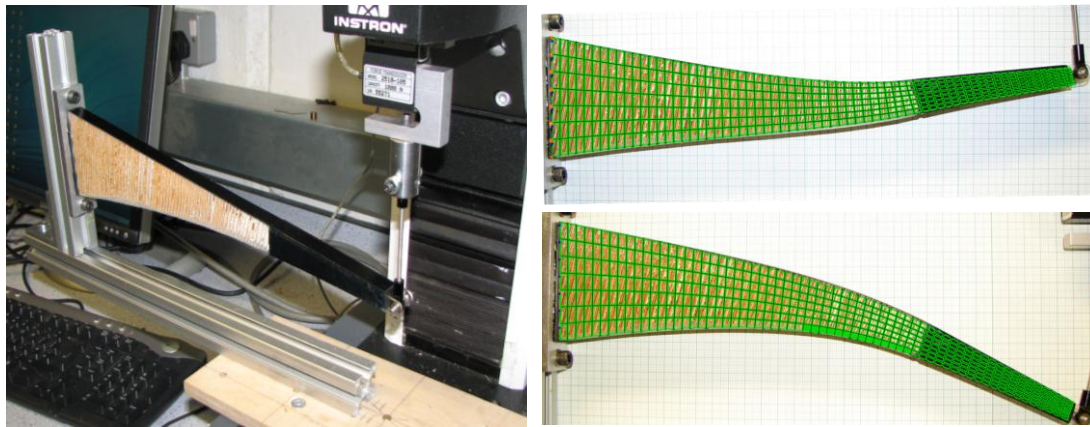


Figure 92. Left: Bending test of a 13mm thick slice of morphing flap. Right: the FEM deflected shapes (green mesh) were superposed on the photographs of the deformed demonstrator for deflections of  $\pm 50$  mm.

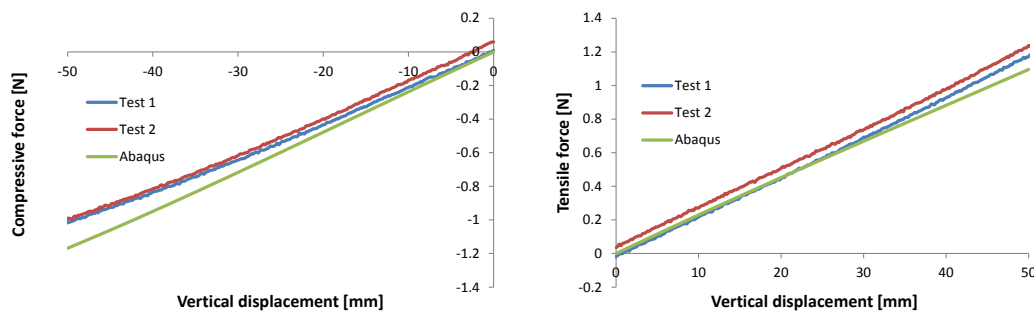


Figure 93. Comparison of the tip forces given by the FEM and the experiment for both downward and upward deflections.

A test rig was manufactured to test the morphing flap, as shown in Figure 94. The displacement controlled test was performed using a 10kN Instron tensile machine equipped with a 1000N load cell. A vertical, upward, 10mm displacement was first imposed to the actuation rod, resulting in the deflected shape seen in Figure 94. The force displacement property of the flap is illustrated in Figure 95. The friction between the actuation rod and the foam skin could noticeably affect the force-displacement results, although the rod was coated with silicone before assembly. This theory is supported by the relaxation of the maximum force required to morph the flap. Indeed, while a maximum force of 270N was noted when the test machine reached the 10mm displacement mark, the load reduced to 264N within seconds of the end of the test (see Figure 94). This is coherent with the viscoelastic properties of foams and applies here due to the friction with the actuation rod. Figure 96 compares the deformed shape of the demonstrator (dashed line) to the FEM deformed mesh. Agreement in terms of vertical displacement is found at the tip; however differences can be seen in terms of flap angle. The FEM predicted a maximum flap angle of  $20^\circ$  for the 10mm rod displacement; however in Figure 96, a difference of  $2.5^\circ$  was found; thus the aerodynamic properties predicted by the FSI model would not be matched. A refinement of the FEM would be required, in particular the modelling of the attachment of the rod onto the rigid tip.

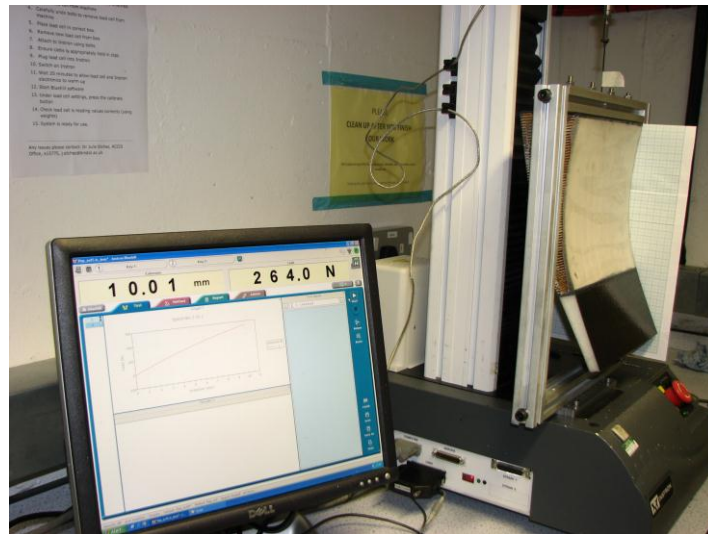


Figure 94. Bespoke rig mounted on the Instron 10kN tensile test machine at the University of Bristol and deflected shape of the flap under a 10mm upward displacement of the actuation rod. As seen on the computer screen, the load dropped from 270N at the end of the test to 264N after resting for a few seconds

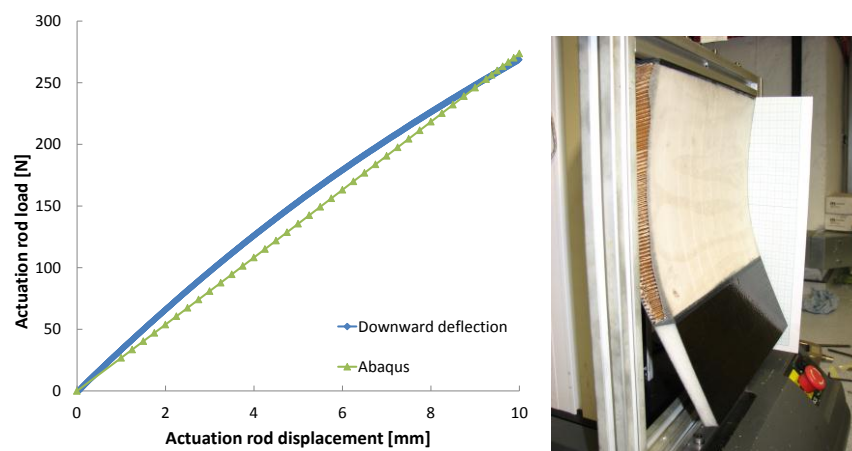
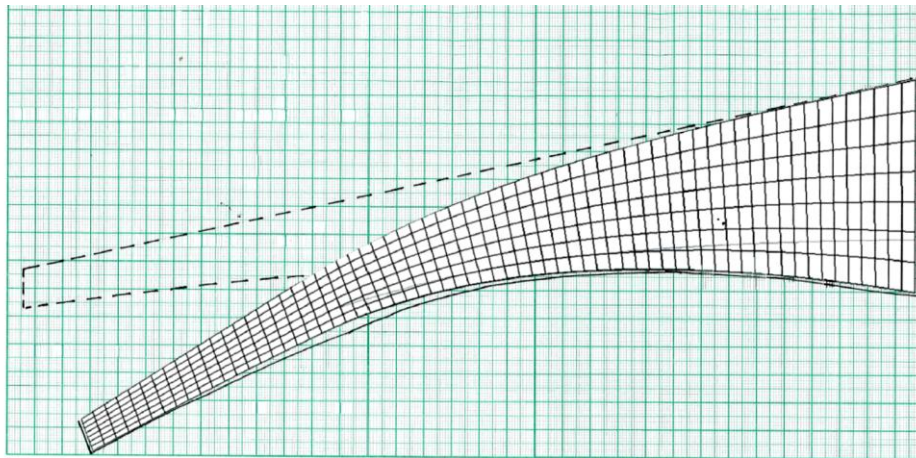
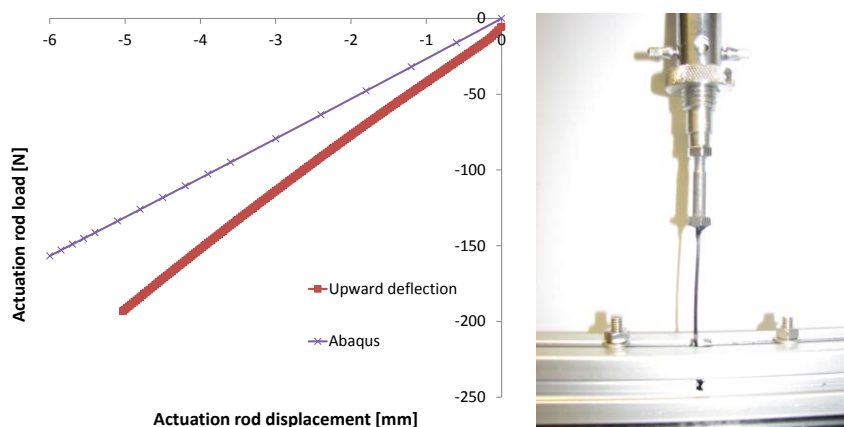


Figure 95. Left: Force-displacement property of the morphing flap for downward tip deformations. Right: Deformed shape of the flap under 10mm actuation displacement.



**Figure 96. Comparison between the FEM and demonstrator deformed shapes for a 10mm actuation rod displacement.**

In a second test, a 10mm vertical, downward, displacement was imposed to the actuation rod. It was noticed however that the rod buckled under the load at a displacement of ~6mm; thus the test was stopped, see photograph in Figure 97. The force-displacement curve is shown in Figure 97. The difference between the two curves is believed to originate from the friction between the ceramic eyelet guiding the rod into the flap and the carbon rod itself. Indeed, it was noticed that the cross-head of the tensile test machine was not perfectly aligned with the actuation rod. This drastically lowered the buckling load the rod can withstand; meaning buckling started nearly at the beginning of the test. As a consequence, the rod deformed in an “S” shaped; which interfered with the eyelet and increased drastically the friction between the two components. Due to time constraints, the actuation rod could not be shortened and the test re-ran. From the FEM results of the downward tip deflection simulations, the authors are confident the upward tip deflection force found with the FEM are realistic and could be used for actuator sizing purposes. Because of the buckling issue encountered, the deformed shape of the flap for upward tip deflections was not recorded in this study.



**Figure 97. Left: Force displacement curve for upward tip deflections. Right: buckling of the actuation rod, resulting in the rod passing through the ceramic eyelet with great friction.**

### 3.7 Conclusions and recommendations

With the growth in size of wind turbine blades, it has become difficult to rely upon passive power control, as was the case in the past, leading modern wind turbines to use sophisticated control systems, ensuring both safe and optimal operating conditions under a variety of atmospheric conditions. To enable further growth in size, wind turbines require yet another advance in load control. As larger rotors experience more pronounced structural and fatigue loading, particularly in turbulent winds, shape morphing brings possible structural solutions. The load reduction potential has already been shown in helicopters, where numerous concepts and experiments have been carried out. In the wind turbine area, numerical simulations and prototypes demonstrated the benefits of blade morphing.

This section investigated the design of a morphing flap for the DTU 10MW wind turbine. It detailed the design assumptions and the reasons for the technical solution developed. Focus was given to the manufacturability and the life time of the flap. As such, a novel morphing skin, using polyurethane foam, was developed. Each step of the manufacture was detailed to enable the concept to be further explored.

The next steps into this research would include the wind tunnel testing of the flap, fatigue testing at a component and system levels before testing the flap onto a rotating rig.

## 4 NEW MORPHING BLADE SECTIONS INVOLVING INNOVATIVE MECHANISM

The work described in this section was performed by DTU in the frame of InnWind.Eu workpackage WP2. The innovative morphing mechanism described refers to the use of active flaps and how these can be incorporated in the structural design. The structural consequences are studied and the pros and cons are highlighted.

### 4.1 State of the art and motivation

One of the innovative concepts explored in INNWIND project is the use of active flaps for load control [34], [52]. In the past decade at DTU the design of such a system has been explored and it is oriented towards flexible elastomer morphing trailing edge geometry, activated by pressure fluid, referred to as Controllable Rubber Trailing Edge Flap (CRTEF) [53].

In order to deliver an aeroelastic design of a smart blade for WP1, the aeroelastic optimization of a 10MW wind turbine smart blade equipped with active trailing edge flaps is carried out and reported in INNWIND deliverable 1.24 [54]. In [54] the structural design is based on a beam model and the linear finite element cross sectional tool BECAS. Here the structural consequences of such a design are studied in more details using non-linear finite element analysis.

The concept of integrating active flaps in a blade design is illustrated in Figure 98, where the blade is designed without a trailing edge over the whole span going from flatback airfoils on the inner part to an outboard part where active and passive morphing trailing edges (flaps) should be mounted. A trailing edge web is inserted to compensate for the missing trailing edge, and to be used as attachment point for the flap modules as implemented in the INDUFLAP project flap prototypes, Figure 99. The DTU 10MW Reference Wind Turbine blade design [1] is considered as the baseline case.

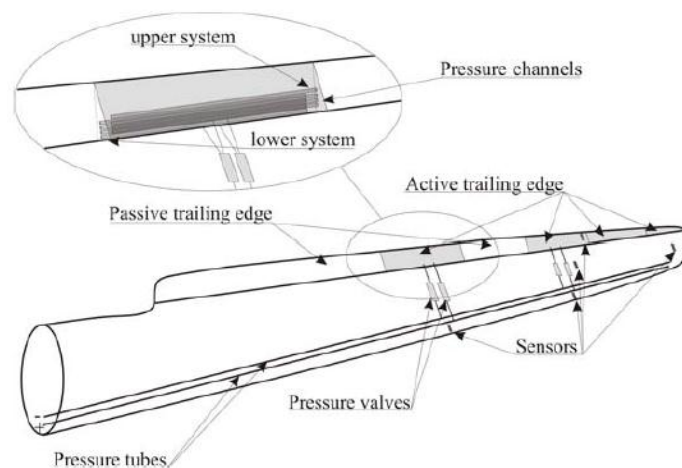


Figure 98 - Concept of integrated active flaps in a blade design. [54]



Figure 99 - Integration of the flap system in a blade section structure in the Induflap project [52].

#### 4.2 Brief description of the concept

The idea described in the following is to truncate the airfoil sections at the trailing edge as shown in Figure 100. This design idea is somewhat different from that of the INDUFLAP project flap prototypes as shown in Figure 99. In this sense the active flaps are not part of the structure and will not contribute to the global stiffness or mass of the blade nor carry any global loads.

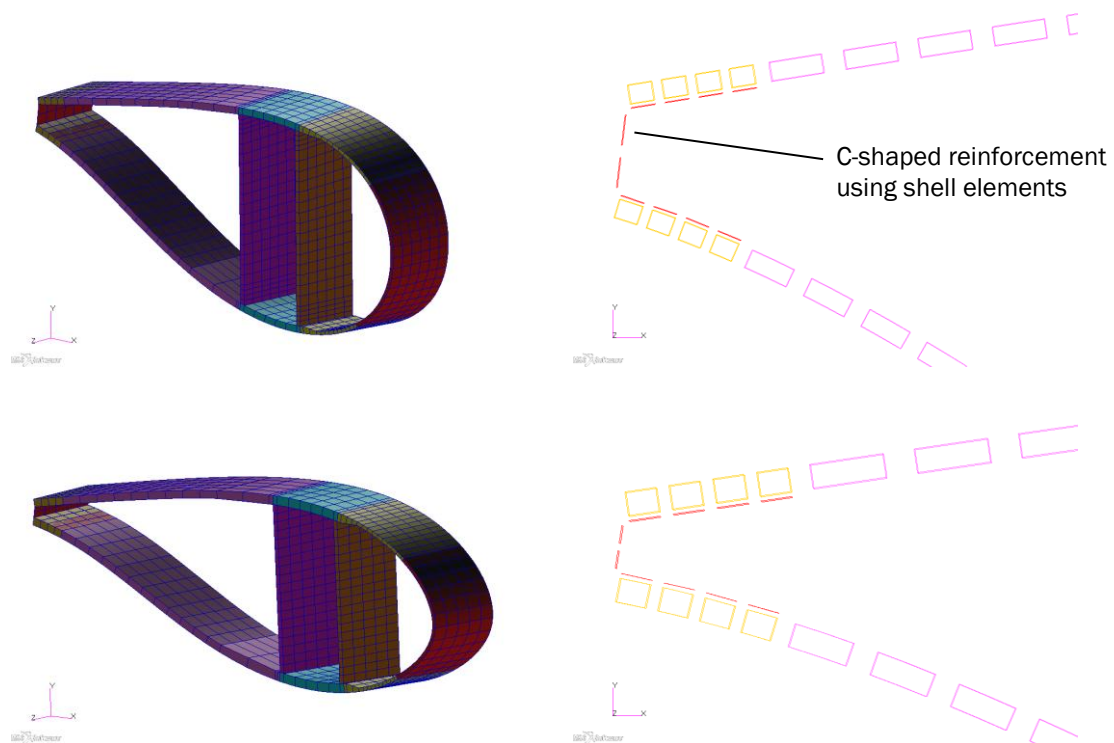


Figure 100 - The truncated airfoil design.

## 4.3 Analysis of the concept

### 4.3.1 Software used

The blades were modeled using the commercial finite element package MSC.Patran (version 2014). Based on input data available for the benchmark [1], the model was generated by utilizing Risø-DTU's in-house software Blade Modeling Tool (BMT). MSC.Marc was applied as the solver in all analyses.

As 20-noded layered continuum elements were used to model the blade structure, as a volume representation of the geometry was required. This geometry was generated using BMT together with MSC.Patran. All 101 cross-sections from the input data were applied in the modeling scheme, which describes the outer geometry of the blade. The curves defining these cross-sections were offset according to the layup definition in order to represent the thickness of the laminates. Finally, the individual cross-sections were connected by spline curves and interpolation surfaces to obtain a volume representation of the blade. This approach results in solids which vary in thickness between cross sections. This differs slightly from the input data, as these are constant between cross sections.

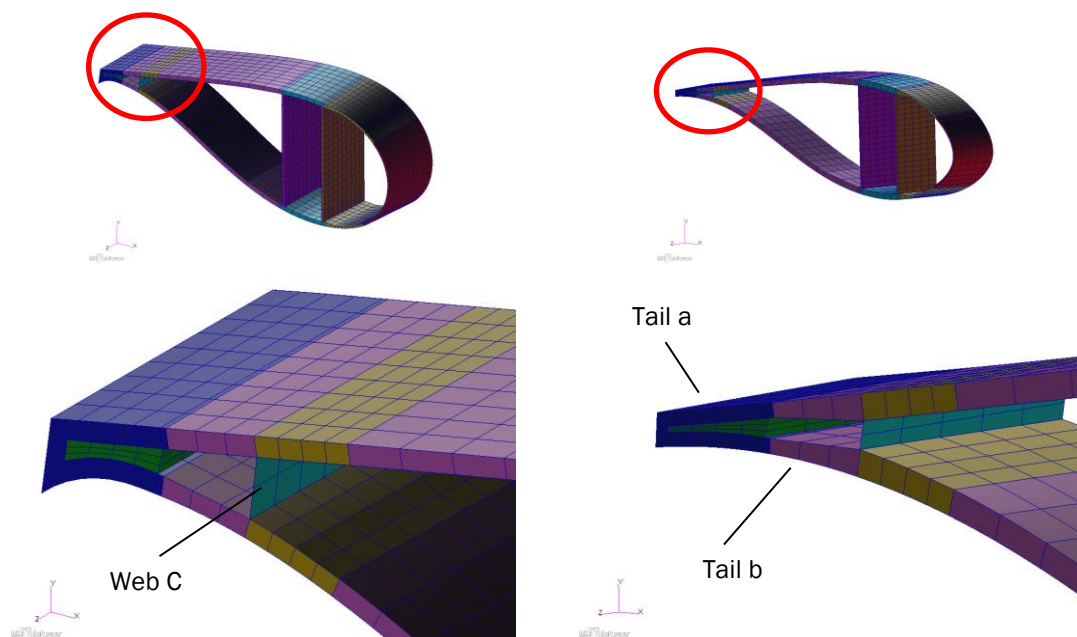


Figure 101 – Definition of web C, tail a and tail b.

The process described in the previous paragraph was handled automatically by BMT, which utilizes 60 regions/solids to assign the different properties. Variations in thickness between regions results in tapered solids, which requires some assumptions of how to interpret the input data, as these do not include this level of information. It is noted that for some cross sections there is an overlap of materials for the part of the blade called tail b (see Figure 101). To avoid this overlapping the core thickness in the layup for tail b has been modified. The skins thicknesses are unchanged and therefore the effect on global response is assumed minor.

A custom-made script was used to model the small shear web (web C) in the trailing edge of the reference blade (see Figure 101). This is modeled with 8-noded layered shell elements applying a thick shell formulation.

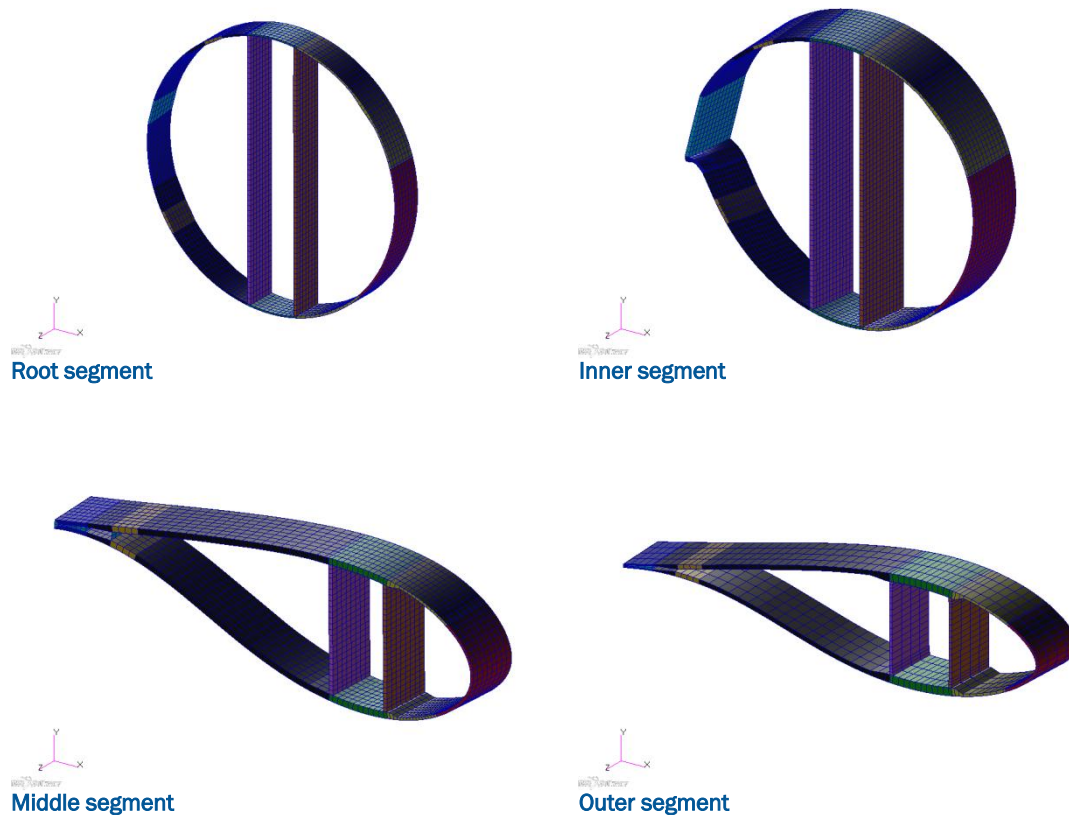


Figure 102 – 4 cross sections along the span of the reference blade.

#### 4.3.2 Two modified versions of the reference blade

The reference blade and the two modified blade versions are identical from the root up till radial position 21.8m. From radial position 21.8m and outward the two modified blade models deviate in trailing edge region of the blade.

**Blade without shear web C:** The difference between this blade and the reference model is that the small shear web which starts in radial position 21.8m and runs all the way to the tip is removed. Otherwise the two models are identical.

**Blade with truncated airfoil:** The trailing edge of the blade and the small shear web (web C) is removed from radial position 21.8m and all the way to the tip of the blade and replaced with a new reinforcement of trailing edge. The new reinforcement consist of a c-shaped profile, which is mounted insight the cut trailing edge. The layup of this reinforcement is approximately 2 times the layup of the original trailing edge (tail a), see Figure 101. Furthermore it is assumed that this profile is glued to the insight of the opened trailing edge on the pressure and suction side of the sandwich panels. This adhesive bound is assumed to be 5mm thick. The c-profiled reinforcement is modelled with shell elements. See Figure 100 for the resulting finite element mesh.

#### 4.3.3 Modelling details and mesh

The composite layup was modeled with 15-25 plies though the thickness via BMT and composite properties were assigned to layered 20-noded continuum elements. The models are densely meshed and it has approximately 100.000 layered 20-noded continuum elements and 8-noded

shell elements are applied to model the small shear web and the new reinforcement of the trailing edge.

The loads were applied via MPC-element (Multi Point Constrains) of the type RBE 3, which is a linear interpolation element which doesn't constrain the cross section. The master node was located in the center of the load carrying box and connected to the nodes associated to the two caps (see Figure 103).

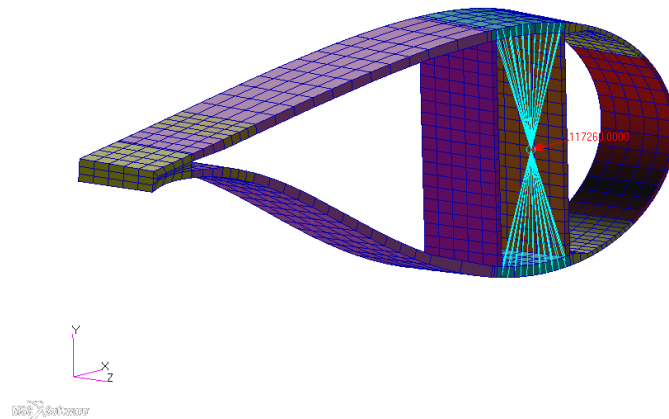


Figure 103 – Cross section with MPC-elements shown.

#### 4.3.4 Load cases

As this study mainly focuses on the structural response of the trailing edge region of the blade the leading-towards-trailing edgewise load cases (LTT) were taken from [1] and subjected to the three models applied in this study. The moment distribution was converted into 6 point loads which were applied to the model along the span of the blade. Furthermore, this load case was transformed into two new off axis load configurations by rotating the point loads by +/- 30 deg. See Figure 104.

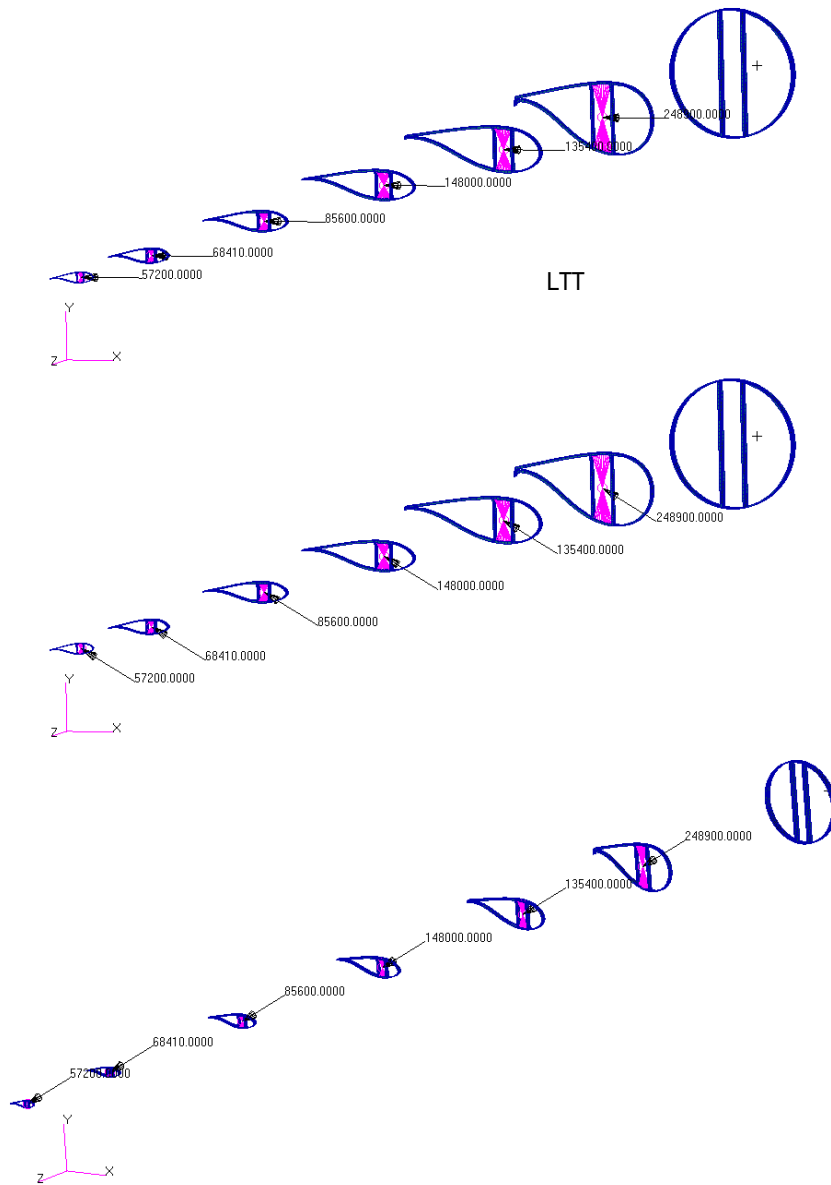


Figure 104 – The 3 load cases used in the study.

#### 4.3.5 Simulations

The models are used for computing the following responses:

- Tip displacement
- Natural Frequencies (Modal analysis)
- Non-linear Buckling analyses

The displacements reported in these studies were computed via non-linear geometric analysis.

The modal analyses were performed applying the Lanczos method in MSC.Marc.

Non-linear buckling analyses include the geometric nonlinear effects, which a wind turbine blade is subjected to under extreme loading. The following eigenvalue problem was solved by applying the Lanczos method in MSC.Marc.

$$(\mathbf{K} + \lambda \cdot \Delta\mathbf{K}_G(\Delta\mathbf{u}, \mathbf{u}, \Delta\sigma)) \cdot \boldsymbol{\Phi} = 0 \quad P_{\text{buckling}} = P_{\text{start}} + \lambda \cdot \Delta P \quad (21)$$

$\mathbf{K}$  is the material stiffness matrix,  $\lambda$  is the eigenvalue and  $\boldsymbol{\Phi}$  is the eigenvector. The geometric stiffness matrix  $\Delta\mathbf{K}_G$  is assumed to be a linear function of the load increment  $\Delta P$  and is based on the stress and displacement state change at the start of the last increment.  $P_{\text{start}}$  is the load applied at the start of the increment prior to the buckling analyses and  $\lambda$  is the value obtained by the power sweep method. For  $\lambda$  equal to unity the critical buckling load is obtained

### 4.3.6 Results

#### 4.3.6.1 Global blade properties

Mass properties for the reference blade:

Overall mass of blade: 42341 kg.

Location of centre of gravity of blade: x: -0.130 (m), y: 0.040 (m), z: 28.47 (m)

Mass properties for the blade without shear web C:

Overall mass of blade: 42212kg.

Location of centre of gravity of blade: x: -0.122(m), y: 0.040(m), z: 28.43(m)

Mass properties for the Blade with truncated airfoil:

Overall mass of blade: 42325kg.

Location of centre of gravity of blade: x: -0.105(m), y: 0.040(m), z: 28.48 (m)

#### 4.3.6.2 Natural frequencies and mode shapes for the three models

Natural frequencies and modes shapes for the three models are reported in Table 22 below.

**Table 22 - Natural frequencies for the three models**

Mode (#)	Ref. model	Model without web C	Truncated airfoil model
1	0.616 1 <sup>st</sup> Flapwise	0.618 1 <sup>st</sup> Flapwise	0.613 1 <sup>st</sup> Flapwise
2	0.953 1 <sup>st</sup> Edgewise	0.951 1 <sup>st</sup> Edgewise	0.898 1 <sup>st</sup> Edgewise
3	1.77 2 <sup>nd</sup> Flapwise	1.78 2 <sup>nd</sup> Flapwise	1.76 2 <sup>nd</sup> Flapwise
4	2.87 2 <sup>nd</sup> Edgewise	2.86 2 <sup>nd</sup> Edgewise	2.70 2 <sup>nd</sup> Edgewise
5	3.62 3 <sup>rd</sup> Flapwise	3.63 3 <sup>rd</sup> Flapwise	3.60 3 <sup>rd</sup> Flapwise
6	5.78 combined mode flapwise, edgewise and torsion	5.77 combined mode flapwise, edgewise and torsion	5.55 combined mode flapwise, edgewise and torsion
7	6.06 1 <sup>st</sup> Torsion	6.04 1 <sup>st</sup> Torsion	6.05 combined mode flapwise, edgewise and torsion

Comments to natural frequencies

The main difference between the natural frequencies from the analyses of the 3 models are observed for the first edgewise mode where the truncated airfoil model has a lower natural frequency, which is caused by the lower edgewise stiffness. The higher modes shapes vary a great

deal especially the 7 mode, which for the ref. model and the model without web C is a clear torsional mode, while the response for truncated airfoil model is more complicated, as the 7 mode for this model consist of both flapwise, edgewise and torsional response.

#### 4.3.6.3 Global tip displacements for the three models

The global tip displacements found for the three models when subjected to the three load cases applied in this study are reported in Table 23 below.

**Table 23 - Tip displacement for the three models subjected to the three different load cases**

Load case	Ref. Model			Model without web C			Truncated airfoil model		
	x [m]	y [m]	mag [m]	x [m]	y [m]	mag [m]	x [m]	y [m]	mag [m]
LTT	-2.62	-0.50	2.67	-2.66	-0.50	2.70	-2.99	-0.59	3.05
LTT 30 deg	-2.02	3.09	3.69	-2.06	3.09	3.71	-2.30	3.02	3.80
LTT -30 deg	-2.54	-4.04	4.76	-2.56	-4.02	4.78	-2.90	-4.10	5.02

#### 4.3.6.4 Load carrying capacity computed via non-linear buckling analysis

Presented below in Table 24 is the resistance toward buckling for the three models.

**Table 24 - Resistance toward buckling**

Load case	Ref. model	Model without web C	Truncated airfoil model
LTT	2.43	1.63	2.93
LTT 30 deg	2.60	1.87	3.27
LTT -30 deg	2.42	1.89	3.34

The design without the third web is closest to the most common modern blade designs of the three models in this study. It is clear that the third web is added in the 10MW reference wind turbine blade design in order to reduce buckling problems in the trailing edge region. It is however interesting to note that the truncated airfoil design have even higher buckling resistance.

Table 25 - Buckling analysis for the ref. model when subjected to the LTT load case.

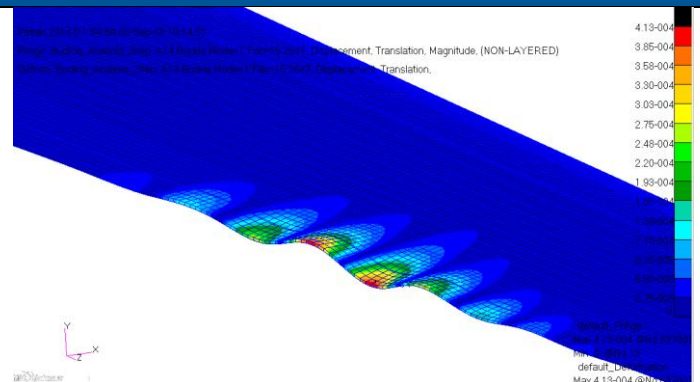
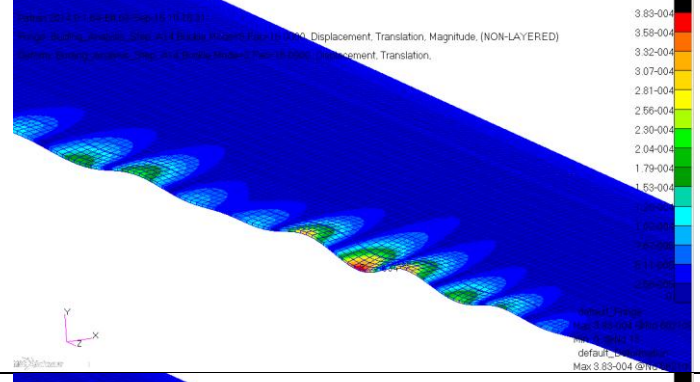
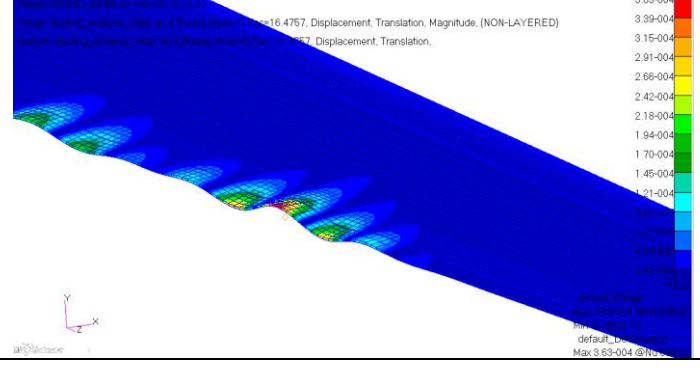
Mode (#)	Buckling factor	Buckling mode	Description/ comments
1	2.43	 <p>Max 4.13e-04 3.85e-04 3.58e-04 3.30e-04 3.03e-04 2.75e-04 2.48e-04 2.20e-04 1.93e-04 1.65e-04 1.38e-04 1.10e-04 8.25e-05 5.50e-05 2.75e-05 0</p>	Location : Radial position R=59m, Buckling of trailing edge and panels
2	2.50	 <p>3.83e-04 3.58e-04 3.32e-04 3.07e-04 2.81e-04 2.56e-04 2.30e-04 2.04e-04 1.79e-04 1.53e-04 1.27e-04 1.01e-04 7.50e-05 4.90e-05 2.30e-05 0</p>	Location : Radial position R=63m, Buckling of trailing edge and panels
3	2.55	 <p>3.63e-04 3.39e-04 3.15e-04 2.91e-04 2.66e-04 2.42e-04 2.18e-04 1.94e-04 1.70e-04 1.45e-04 1.21e-04 9.70e-05 7.25e-05 4.80e-05 2.35e-05 0</p>	Location : Radial position R=67m, Buckling of trailing edge and panels

Table 26 - Buckling analysis for the no web C model when subjected to the LTT load case.

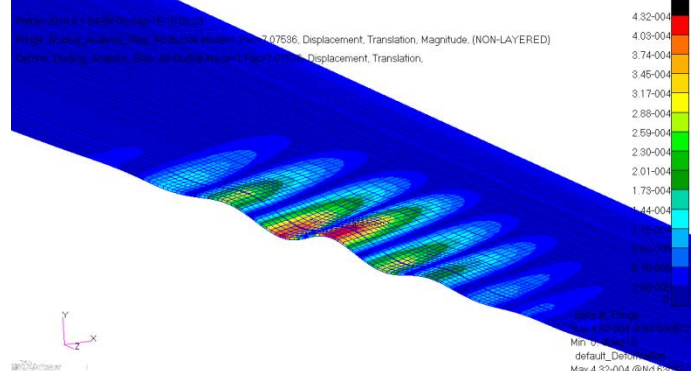
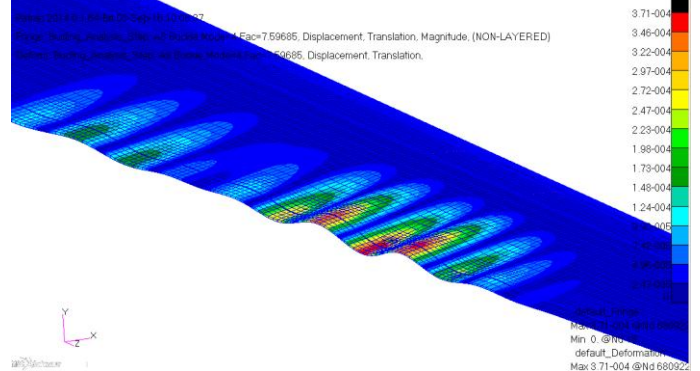
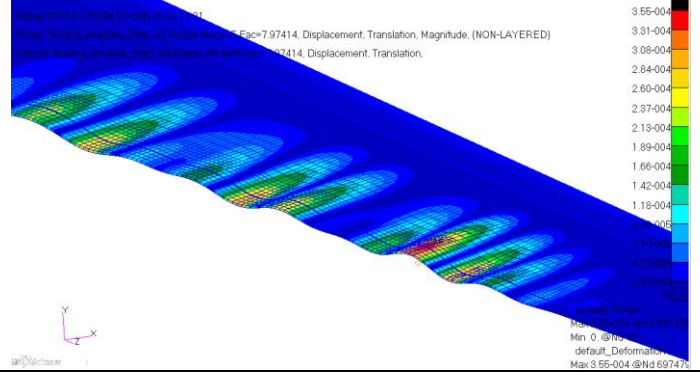
Mode (#)	Buckling factor	Buckling mode	Description/ comments
1	1.61		Location : Radial position R=59m, Buckling of trailing edge and panels
2	1.66		Location : Radial position R=65m, Buckling of trailing edge and panels
3	1.70		Location : Radial position R=67m, Buckling of trailing edge and panels

Table 27 - Buckling analysis for the truncated airfoil model when subjected to the LTT load case.

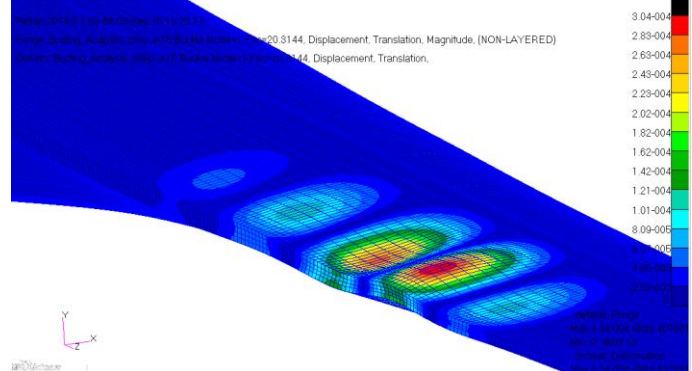
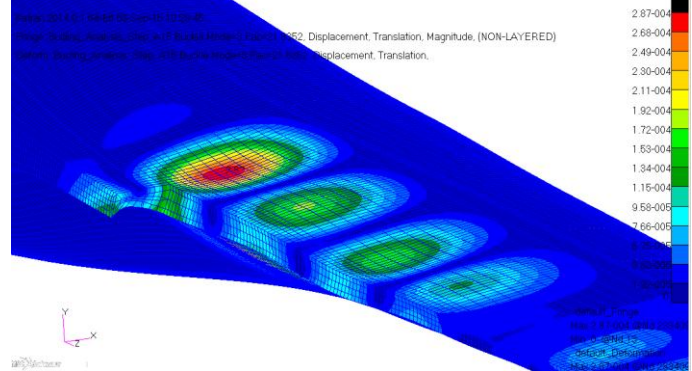
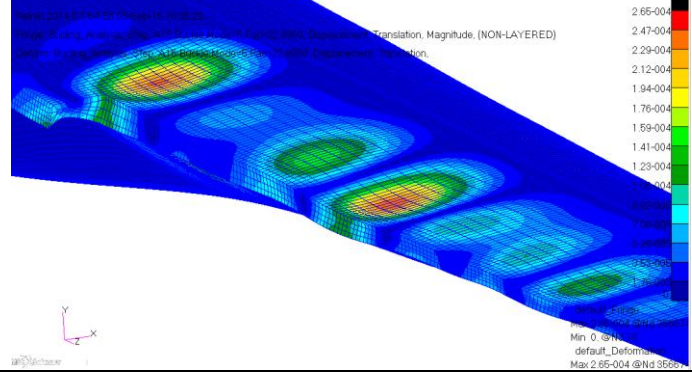
Mode (#)	Buckling factor	Buckling mode	Description/ comments
1	2.93		Location : Radial position R=32m, Buckling of trailing edge and panels
2	3.01		Location : Radial position R=22m, Buckling of trailing edge and panels
3	3.19		Location : Radial position R=27m, Buckling of trailing edge and panels

Table 28 - Buckling analysis for the Ref. model when subjected to the LTT 30 deg load case.

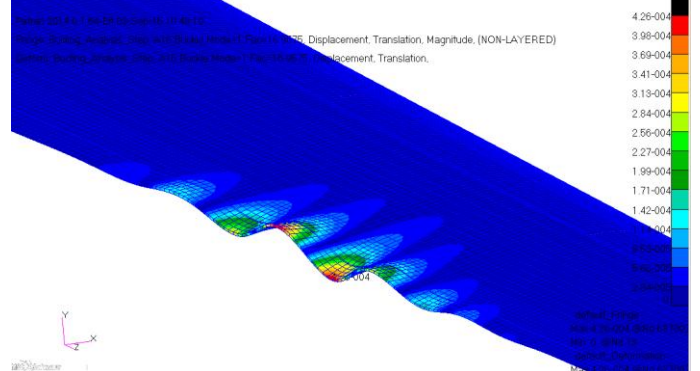
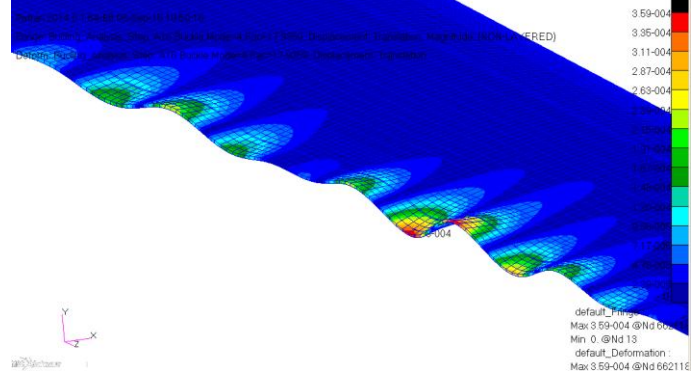
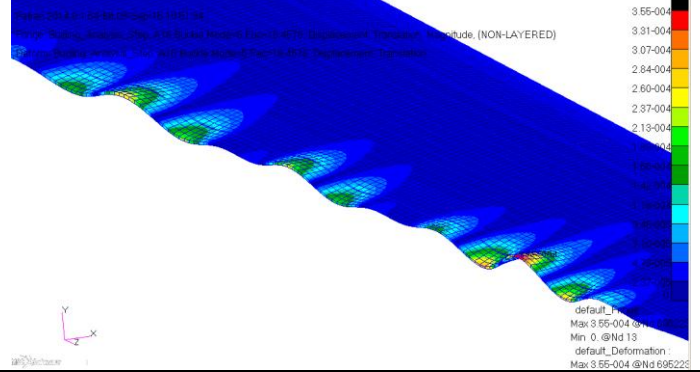
Mode (#)	Buckling factor	Buckling mode	Description/ comments
1	2.60	 <p>Max: 4.26e-04 @Nd 662116            Edge Buckling Analysis: Displacement, Translation, Magnitude, (NON-LAYERED)            default_Buckling_Analysis: Displacement, Translation, Magnitude, (NON-LAYERED)</p>	Location : Radial position R=60m, Buckling of trailing edge and panels
2	2.69	 <p>Max: 3.59e-04 @Nd 662116            Edge Buckling Analysis: Displacement, Translation, Magnitude, (NON-LAYERED)            default_Buckling_Analysis: Displacement, Translation, Magnitude, (NON-LAYERED)</p>	Location : Radial position R=64m, Buckling of trailing edge and panels
3	2.75	 <p>Max: 3.55e-04 @Nd 662116            Edge Buckling Analysis: Displacement, Translation, Magnitude, (NON-LAYERED)            default_Buckling_Analysis: Displacement, Translation, Magnitude, (NON-LAYERED)</p>	Location : Radial position R=67m, Buckling of trailing edge and panels

Table 29 - Buckling analysis for the no web C model when subjected to the LTT 30 deg load case.

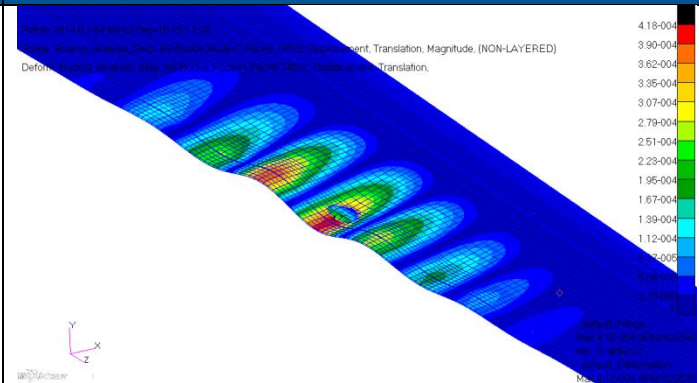
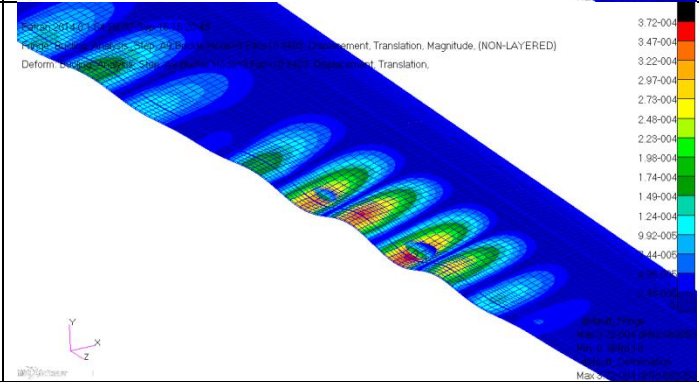
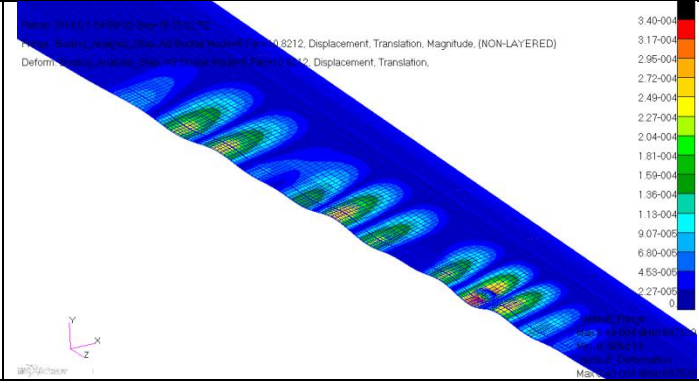
Mode (#)	Buckling factor	Buckling mode	Description/ comments
1	1.87	 <p>Mode: 0141144 Buckling over 18.7102 Hz            FEM: Buckling Analysis, Map, 40 Buckling Modes, 1000 Displacement, Translation, Magnitude, (NON-LAYERED)            Deform: Buckling Analysis, Map, 40 Buckling Modes, 1000 Displacement, Translation.</p>	Location : Radial position R=60m, Buckling of trailing edge and panels
2	1.93	 <p>Mode: 0141144 Buckling over 18.7102 Hz            FEM: Buckling Analysis, Map, 40 Buckling Modes, 1000 Displacement, Translation, Magnitude, (NON-LAYERED)            Deform: Buckling Analysis, Map, 40 Buckling Modes, 1000 Displacement, Translation.</p>	Location : Radial position R=65m, Buckling of trailing edge and panels
3	1.98	 <p>Mode: 0141144 Buckling over 18.7102 Hz            FEM: Buckling Analysis, Map, 40 Buckling Modes, 1000 Displacement, Translation, Magnitude, (NON-LAYERED)            Deform: Buckling Analysis, Map, 40 Buckling Modes, 1000 Displacement, Translation.</p>	Location : Radial position R=68m, Buckling of trailing edge and panels

Table 30 - Buckling analysis for the truncated airfoil model when subjected to the LTT 30 deg load case.

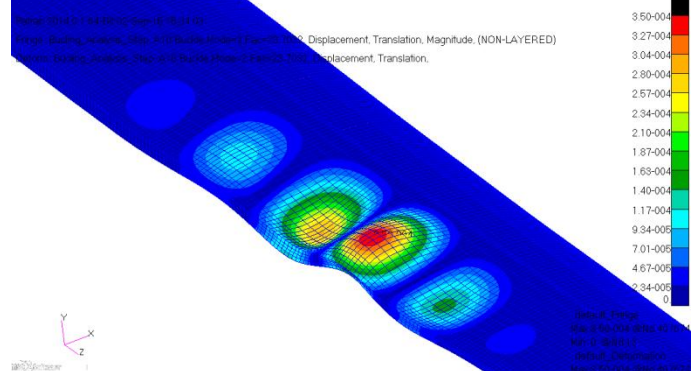
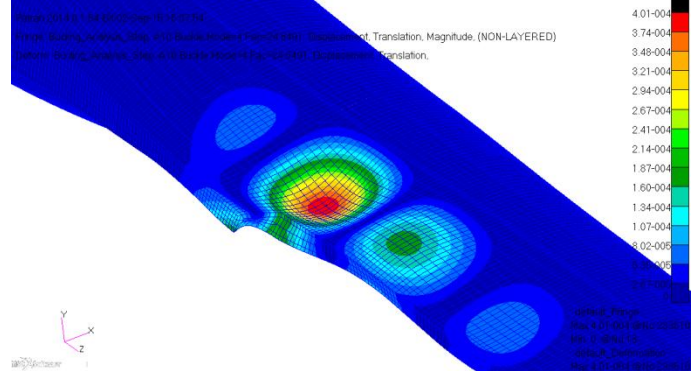
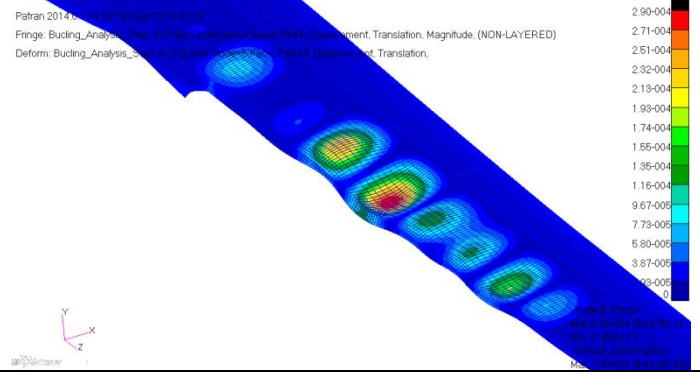
Mode (#)	Buckling factor	Buckling mode	Description/ comments
1	3.27	 <p>Patran 2014: C:\patran\over\1614119 Fringe: Bucleing_Analysis_2014_1614119\Buckling_Mode1\1614119_Displacement, Translation, Magnitude (NON-LAYERED) Deform: Bucleing_Analysis_2014_1614119\Buckling_Mode1\1614119_Displacement, Translation.</p>	Location : Radial position R=38m, Buckling of trailing edge and panels
2	3.37	 <p>Patran 2014: C:\patran\over\1614119 Fringe: Bucleing_Analysis_2014_1614119\Buckling_Mode2\1614119_Displacement, Translation, Magnitude (NON-LAYERED) Deform: Bucleing_Analysis_2014_1614119\Buckling_Mode2\1614119_Displacement, Translation.</p>	Location : Radial position R=22m, Buckling of trailing edge and panels
3	3.57	 <p>Patran 2014: C:\patran\over\1614119 Fringe: Bucleing_Analysis_2014_1614119\Buckling_Mode3\1614119_Displacement, Translation, Magnitude (NON-LAYERED) Deform: Bucleing_Analysis_2014_1614119\Buckling_Mode3\1614119_Displacement, Translation.</p>	Location : Radial position R=32m, Buckling of trailing edge and panels

Table 31 - Buckling analysis for the Ref. model when subjected to the LTT -30 deg load case

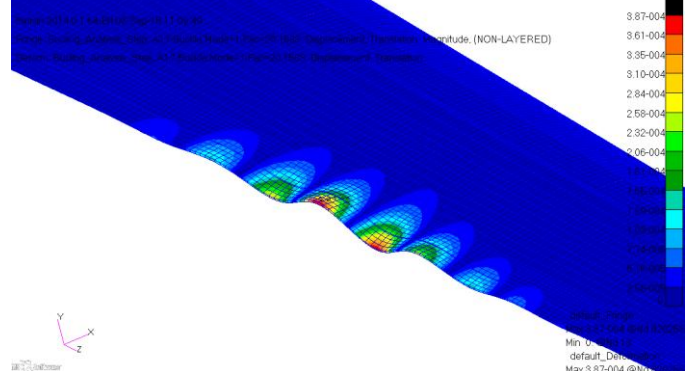
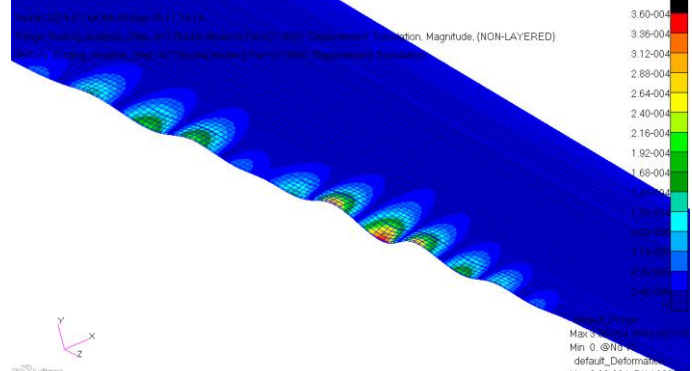
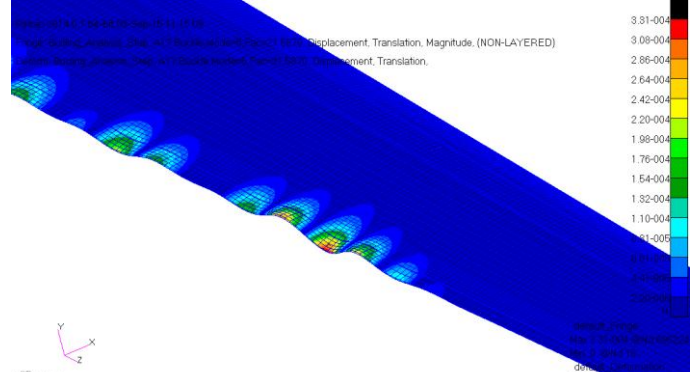
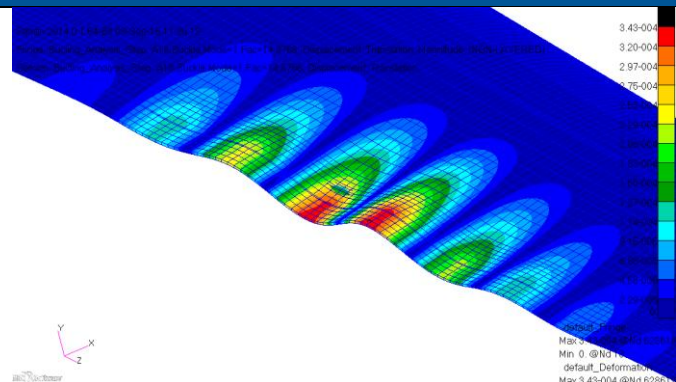
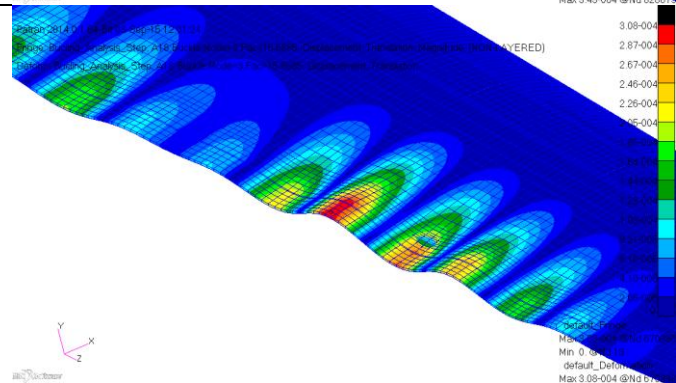
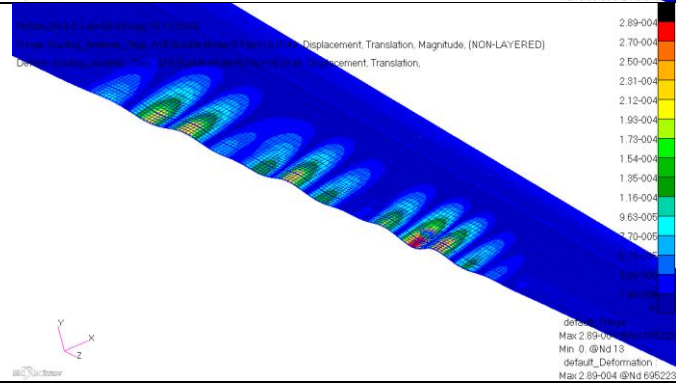
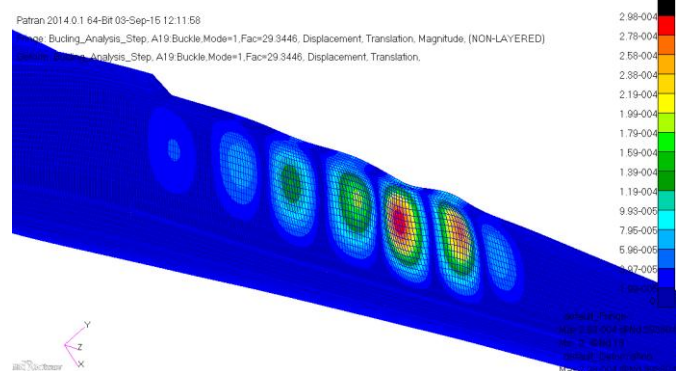
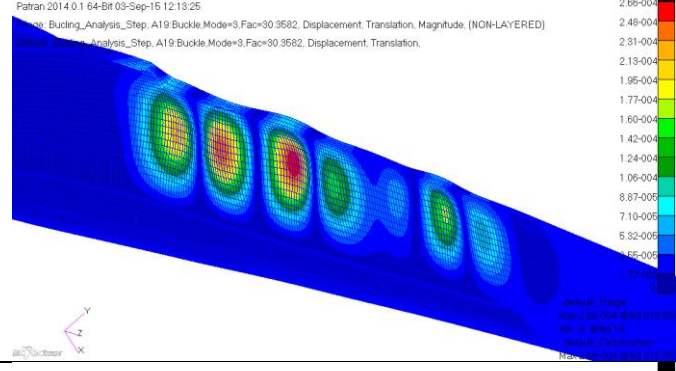
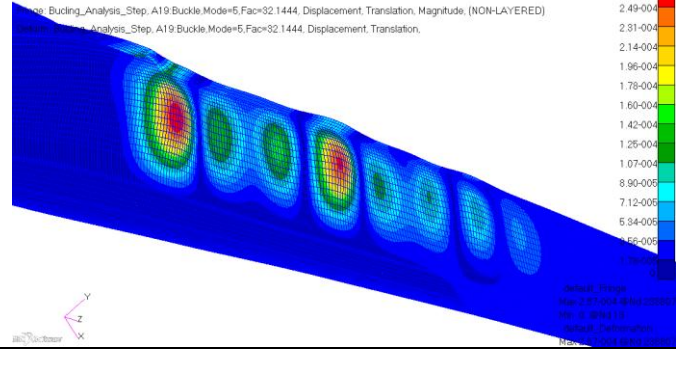
Mode (#)	Buckling factor	Buckling mode	Description/ comments
1	2.42		Location : Radial position R=58m, Buckling of trailing edge and panels
2	2.51		Location : Radial position R=63m, Buckling of trailing edge and panels
3	2.56		Location : Radial position R=67m, Buckling of trailing edge and panels

Table 32 - Buckling analysis for the no web C model when subjected to the LTT -30 deg load case

Mode (#)	Buckling factor	Buckling mode	Description/ comments
1	1.89		Location : Radial position R=59m, Buckling of trailing edge and panels
2	1.96		Location : Radial position R=64m, Buckling of trailing edge and panels
3	2.00		Location : Radial position R=67m, Buckling of trailing edge and panels

**Table 33 - Buckling analysis for the truncated airfoil model when subjected to the LTT -30 deg load case**

Mode (#)	Buckling factor	Buckling mode	Description/ comments
1	3.34	 <p>Patran 2014.0.1 64-Bit 03-Sep-15 12:11:58            Buckling_Analysis_Step, A19 Buckle.Mode=1, Fac=29.3446, Displacement, Translation, Magnitude, (NON-LAYERED)            Buckling_Analysis_Step, A19 Buckle.Mode=1, Fac=29.3446, Displacement, Translation.</p>	Location : Radial position R=36m, Buckling of trailing edge and panels
2	3.44	 <p>Patran 2014.0.1 64-Bit 03-Sep-15 12:13:25            Buckling_Analysis_Step, A19 Buckle.Mode=3, Fac=30.3582, Displacement, Translation, Magnitude, (NON-LAYERED)            Buckling_Analysis_Step, A19 Buckle.Mode=3, Fac=30.3582, Displacement, Translation.</p>	Location : Radial position R=29m, Buckling of trailing edge and panels
3	3.61	 <p>Patran 2014.0.1 64-Bit 03-Sep-15 12:14:31            Buckling_Analysis_Step, A19 Buckle.Mode=5, Fac=32.1444, Displacement, Translation, Magnitude, (NON-LAYERED)            Buckling_Analysis_Step, A19 Buckle.Mode=5, Fac=32.1444, Displacement, Translation.</p>	Location : Radial position R=22m, Buckling of trailing edge and panels

#### 4.4 Conclusions and recommendations

It can be concluded that the truncated airfoil section has the highest resistance towards buckling of the three models when subjected to edgewise loading. The buckling resistance for the truncated airfoil section is significantly higher compared to the model with no third shear web (web C). The design without the third web is closest to the most common modern blade designs of the three models in this study. It is clear that the third web is added in the 10MW reference wind turbine blade design in order to reduce buckling problems in the trailing edge region. It is however interesting to note that the truncated airfoil design have even higher buckling resistance.

The overall mass of the three models is very similar but a difference in the x and y-location of the mass centre is observed. The global edgewise stiffness is reduced for the truncated airfoil section, as material is moved closer towards the elastic centre. This lower edgewise stiffness can be observed in both the natural frequencies analysis and the computed tip displacements for the three load cases. The edgewise stiffness is approximately reduced by 14% in this study. The stiffness reduction of course depends on the truncated reinforcement, which can be either higher or lower than utilized in these studies. Furthermore additional reinforcement of the leading edge could also be needed in order to obtain an edgewise stiffness which is more similar to the reference model. It might probably not be profitable to aim at achieving the same edgewise stiffness for a truncated airfoil section design. This will than result in higher strains in the trailing and leading edge, which off course needs to be accorded for in the design process of the blade.

Based on the analysis performed in this study no structural problems are observed for the truncated airfoil section blade. Actually it looks like this design could have some structural benefits. The truncated airfoil blade design is shown to have higher buckling resistance than the reference design. This may lead to reduced blade mass if buckling is driving the design. If the design is driven by material strength then the truncated airfoil blade design may have a somewhat higher mass.

## 5 CONCLUSIONS & NEXT STEPS

Three different implementation solutions of morphing blade sections to accommodate the requirements of smart blades have been investigated within WP2 “Light Rotors” of the INN WIND.EU project. Efforts regarding the structural needs of each alternative and the wind turbine blade component, conducted within Task 2.2 ‘Lightweight Structural design’ have been presented in the current report. These come to support the research performed under Task 2.3 on load alleviation on wind turbine components through active and passive control of the wind turbine system.

The concepts investigated include morphing blade sections achieved through use of Shape Memory Alloys (SMA), use of zero Poisson ratio elastomer, and use of an innovative mechanism. All these concepts need to meet different requirements and set different constraints on the wind turbine structure. Elastic, stiffness and strength analyses were performed and six different structural solutions were investigated.

The first morphing section design presented is using SMA wire actuators for the upward and downward deflection of blade’s trailing edge in order to achieve load alleviation control due to changes of the lift coefficient. The capability of SMA actuators to retract their initial shape after elongation and to apply high induced strains, block stress and high actuation energy density make them suitable for application in wind turbine blade sections where large movements are required and space limitations exist. In order to develop structural solutions for this concept in the frame of INN WIND.EU project, a numerical tool for the prediction of SMA behaviour has been developed. The development of this numerical tool enables the accurate prediction of the response of the SMA under the various thermo-mechanical loads required to morph the blade section. The interaction of the SMA actuators with the remaining elastic parts of the morphing airfoil and the structural response prediction were achieved by implementing the developed numerical tool to a commercial FEM program.

Investigations for four structural solutions were carried out in a section located 66.711m away from blade root in order to include the presence of high velocities of the wind turbine that increase significantly the developed stresses. The first concept consists of a mechanism implemented between WEB B and WEB C of the RWT and a SMA wire actuator, the second one consists of an antagonistic set of actuators arranged in an “X” formation, the third one is the second one expanded with two additional parts to cover the slots in suction and pressure side and the last one comprises of two antagonistic SMA placed in suction and pressure side of the section. Studies on these concepts resulted in a morphing section concept which employs three pairs of SMA attached to four parts, three with moving capabilities and one immobile. Numerical simulations of this morphing concept led to a design able to reach the desired morphed configuration without overstressing of any of its components.

A structural solution for the second morphing section design was proposed by University of Bristol and reported herein. The mechanisms composed of a CFRP suction skin covering an anisotropic core material (honeycomb). Polyurethane foam was applied to the pressure side of the flap while a push-pull rod was used in order to bend the flap. Flap and tip size of the morphing concept was decided by means of a Fluid Structure Interaction tool designed within the project. This numerical tool manages the results given by Abaqus structure solver and aerodynamic pressure distribution computed by X-FOIL. Next step of the study was the design, manufacturing and testing of a reduced scale morphing flap. Performed static tests where upward deflection was applied, revealed that vertical deflections were in good agreement with the FEM simulations in contrast with flap angle where some differences were spotted. Downward deflection test was not successful due to actuator’s elastic instability.

Finally, a structural solution for a wind turbine smart blade equipped with active trailing edge flaps, presented in this report by Technical University of Denmark. The RWT blades were truncated at the trailing edge, where the morphing trailing edges (flaps) should be mounted, and a trailing

edge web was inserted in order to compensate for the missing trailing edge. Strength and buckling analysis as well as stiffness calculations of the truncated airfoil section blade didn't reveal any structural problems. As a matter of fact, the truncated airfoil blade design proved being able to carry higher buckling load than the reference one. On the other hand, a reduction on the edgewise stiffness was observed.

The technology readiness level (TLR) of the three morphing blade solutions ranges from 4-6 for wind turbine system applications. Feasibility studies have been undertaken by looking at the complete system by numerical simulations and dedicated experiments. Through the efforts performed and presented in this report an advance of this level has been achieved.

Regarding the next stage of the required research, for the down-selected structural solution using SMA actuators, experiments on a scaled prototype will further allow assessment of manufacturing requirements. This is planned as the next action within INN WIND.EU Task 2.2. Additionally, multidisciplinary assessment of both structural and aerodynamic phenomena on the morphing airfoil is already foreseen and planned under Task 2.3 in order to further validate the plausibility of the concept and to measure its effect on the primary goal of this effort, the active load alleviation of the wind turbine blade. Furthermore, within Task 2.3 a morphing blade using a special elastomer is planned to be placed on a rotating test-rig in DTU on a 2m blade part which allows both pitching and smart trailing edge control based on inflow sensing.

In conclusion this report gave an overview of, four structural solutions that led to a down-selected concept for further numerical simulations using the SMA technology, a structural solution using a zero Poisson elastomer and structural investigations for a blade with truncated airfoils to equip an innovative mechanism. Part of the obtained results will be used as input for the experimental campaign in Subtask 2.2.3 and for the experiment on the rotating test-rig in Task 2.3. Supplementary studies might be necessary, outside the frame of INN WIND.EU WP2 to assess the cost effectiveness of the proposed solutions.

## 6 REFERENCES

- [1] Bak C, Zahle F, Bitsche R, Kim T, Yde A, Henriksen LC, Andersen PB, Natarajan A, Hansen MH, 2013, "Design and performance of a 10 MW wind turbine", submitted to J. Wind Energy.
- [2] ABAQUS\_6. (2012). User Subroutines Reference Manual. Simulia.
- [3] Bak, C., Gaunaa, M., Andersen, P., Buhl, T., Hansen, P., Clemmensen, K., & Moeller, R. (2007). "Wind tunnel test on wind turbine airfoil with adaptive trailing edge geometry". 45th AIAA Aerospace Sciences Meeting and Exhibit.
- [4] Bak, C., Zahle, F., Bitsche, R. K., Yde, A., Henriksen, L., Natarajan, A., & Hansen, M. (2013). Description of the DTU 10 MW Reference Wind Turbine. DTU.
- [5] Barbarino, S., Ameduri, S., Lecce, L., & Concilio, A. (2009). Wing shape control through an SMA-based device. *Journal of Intelligent Material Systems and Structures*, 283-296.
- [6] Barret, R., Burger, C., & Melian, J. P. (2001). Recent advances in uninhabited aerial vehicle (UAV) flight control with adaptive aerostructures. 4th European Demonstrators Conference. Edinburgh.
- [7] Berg, D., Zayas, J., Lobitz, D., vanDam, C., Chow, R., & Baker, J. (2007). Active aerodynamic load control for wind turbine blades. Proceedings of the 5th Joint ASME/JSME Fluids Engineering Conference, FEDSM2007-37604. San Diego CA.
- [8] Bottasso, C., Croce, A., Riboldi, C., & Salvetti, M. (2014). "Cyclic pitch control for the reduction of ultimate loads on wind turbines". *Journal of Physics: Conference Series*, Volume 524, Issue 1; DOI: 10.1088/1742-6596/524/1/012063.
- [9] Daynes, S., & Weaver, M. P. (2012). "A morphing trailing edge device for a wind turbine". *Journal of Intelligent Material Systems*, 23(6) 691-701; DOI: 10.1177/1045389X12438622.
- [10] Kudva, J., & Carpenter, B. (2000). Smart Wing Program DARPA Technology Interchange Meeting.
- [11] Lagoudas, D., Hartl, D., Chemisky, Y., MacHado, L., & Popov, P. (2012). Constitutive Model for the Numerical Analysis of Phase Transformation in Polycrystalline Shape Memory Alloys. *International Journal of Plasticity*, 32-33, 155-183.
- [12] Mabe, J., Calkins, F., & Butler, G. (2006). Boeing's variable geometry chevron: Morphing aerospace structures for jet noise reduction. Proceedings of SPIE. San Diego, CA.
- [13] Martin, C., Kudva, J., Austin, F., Jardine, A., Scherer, L., Lockyer, A., & Carpenter, B. (1998). Smart materials and structures -smart wing volumes I,II,III, and IV Report AFRL-ML-WP-TR-1999-4162.
- [14] Nam, C., Chattopadhyay, A., & Kim, Y. (2002). Application of shape memory alloy (SMA) spars for aircraft maneuver enhancement. SPIE.
- [15] Ng, B., Palacios, R., Kerrigan, E., Graham, J., & Hesse, H. (2015). "Aerodynamic load control in horizontal axis wind turbines with combined aeroelastic tailoring and trailing-edge flaps". *Wind Energy*, 10.1002/we.1830.
- [16] Qidwai, A. M., & Lagoudas, D. C. (2000). Numerical Implementation of a Shape Memory Alloy Thermomechanical Constitutive Model using Return Mapping Algorithms. *International Journal for Numerical Methods in Engineering*, 47(6), 1123-1168.
- [17] Quintanilla, A., Hulskamp, A., & Bersee, H. (2013). A high rate shape memory alloy actuator for aerodynamic load control on wind turbines. *Journal of Intelligent Material Systems and Structures*, 1834-1845.
- [18] Ruotsalainen, P., Kroneld, P., Nevala, K., Brander, T., Lindroos, T., & Sippola, M. (2009). Shape control of a FRP airfoil structure using SMA-actuators and optical fiber sensors. *Solid State Phenomena*, 196-201.
- [19] Turner, T., Buehrle, R., Cano, R., & Fleming, G. (2006). Modeling fabrication and testing of a SMA hybrid composite jet engine chevron concept. *Journal of Intelligent Material Systems and Structures*, 483-497.
- [20] Wilson DG, Berg DE, Barone MF, Berg JC, Resor BR, Lobitz DW (2009). "Active aerodynamic blade control design for load reduction on large wind turbines". European Wind Energy Conference & Exhibition.

- [21] Zayas, J., van Dam, C., Chow, R., Baker, J., & Mayda, E. (2006). "Active aerodynamic load control for wind turbine blades". European Wind Energy Conference & Exhibition (EWEC).
- [22] Zhu, P., Brinson, L., Peraza-Hernandes, E., Hartl, D., & Stebner, A. ( 16-18 September, 2013). Comparison of Three-Dimensional Shape Memory Alloy Constitutive Models: Finite Element Analysis of Actuation and Superelastic Responses of a Shape Memory Alloy tube. ASME Conference on Smart Materials, Adaptive Structures and Intelligent Systems. Snowbird, Utah, USA: ASME
- [23] UpWind.[Online]. Available: <http://www.upwind.eu/>. (Accessed December 2012).
- [24] Vestas, Lecture on wind turbine blade structures and material, 2012. p. 56.
- [25] InnWind.[Online]. Available: <http://www.innwind.eu/>. (Accessed March 2013).
- [26] Buhl T, Bak C, Gaunaa M, Andersen PB. Load alleviation through adaptive trailing edge control surfaces: ADAPWING overview. European Wind Energy Conference & Exhibition (EWEC), Milan, Italy, 7-10 May 2007.
- [27] Andersen PB, Gaunaa M, Bak C, Buhl T. Load alleviation on wind turbine blades using variable airfoil geometry. European Wind Energy Conference & Exhibition (EWEC), Athens, Greece, 27 February - 2 March 2006.
- [28] Bak C, Gaunaa M, Buhl T, Hansen P, Clemmensen K. Wind tunnel test on airfoil Risø-B1-18 with an Active Trailing Edge Flap. *Wind Energy* 2009; 13: 207-219. DOI: 10.1002/we.369.
- [29] Straub FK. A feasibility study of using smart materials for rotor control. *Smart Materials and Structures* 1996; 5: 1-10. DOI:10.1088/0964-1726/5/1/002.
- [30] Chopra I. Review of state of art of smart structures and integrated systems. *AIAA journal* 2002; 40: 2145-2187. DOI:10.2514/2.1561.
- [31] Hulskamp A. Inventory of actuators and first order evaluation of 2 actuators and structural concepts. Delft University of Technology, 2007. Upwind Work Package 1B3, deliverable 3, [http://www.upwind.eu/media/858/Upwind%20D\\_1B3\\_3%20-%20Inventory%20of%20actuators%20and%20first%20order%20evaluation%20of%20%20actuators%20and%20structural%20concepts.pdf](http://www.upwind.eu/media/858/Upwind%20D_1B3_3%20-%20Inventory%20of%20actuators%20and%20first%20order%20evaluation%20of%20%20actuators%20and%20structural%20concepts.pdf)
- [32] Thill C, Etches JA, Bond IP, Potter KD, Weaver PM. Morphing skins. *The Aeronautical Journal* 2008; 112: 117-139.
- [33] Barlas TK, van Kuik GAM. Aeroelastic modelling and comparison of advanced active flap control concepts for load reduction on the Upwind 5MW wind turbine. European Wind Energy Conference & Exhibition (EWEC), Marseille, France, 16-19 March 2009.
- [34] Barlas TK, van Kuik GAM. Review of state of the art in smart rotor control research for wind turbines. *Progress in Aerospace Sciences* 2010; 46: 1-27. DOI:10.1016/j.paerosci.2009.08.002
- [35] Barlas TK, van Wingerden JW, Hulskamp A, van Kuik G. Closed-loop control wind tunnel tests on an adaptive wind turbine blade for load reduction. 46th AIAA Aerospace Sciences Meeting and Exhibit, Reno, Nevada, USA, 7 - 10 January 2008.
- [36] Daynes S, Weaver PM. A shape adaptive airfoil for a wind turbine blade. SPIE Smart Structures/NDE, San Diego, California, USA, 6 -10 March 2011.
- [37] Daynes S, Weaver PM. Design and testing of a deformable wind turbine blade control surface. *Smart Materials and Structures* 2012; 21: 1-10. DOI:10.1088/0964-1726/21/10/105019.
- [38] Madsen HA, Andersen PB, Andersen TL, Bak C, Buhl T. The potentials of the controllable rubber trailing edge flap (CRTEF). European Wind Energy Conference & Exhibition (EWEC), Warsaw, Poland, 20-23 April 2010.
- [39] van Wingerden JW, Hulskamp AW, Barlas T, Marrant B, Van Kuik GAM, Molenaar DP, Verhaegen M. On the proof of concept of a 'smart' wind turbine rotor blade for load alleviation. *Wind Energy* 2008; 11: 265-280. DOI: 10.1002/we.264.
- [40] Brondsted P, Holmes JW, Sorensen BF. Wind rotor blade materials technology. *European sustainable energy review* 2008; 36-41.
- [41] Williams A, *Strutural Analysis: In Theory and Practice*, Butterworth-Heinemann: Burlington, MA, USA, 2009. Chapter 4; Conjugate beam methods, p. 203.
- [42] Barlas T, Hulskamp A, Bak C, Lutz T, Apinaniz SA. Requirements for Smart rotors. UpWind, 2008. WP1B3 - Deliverable 13,

- [http://www.upwind.eu/media/882/UpWind%20D\\_1B3\\_13%20Requirements%20for%20Smart%20Rotors%20-%20v%202.5%20-%20All%20contributions.pdf](http://www.upwind.eu/media/882/UpWind%20D_1B3_13%20Requirements%20for%20Smart%20Rotors%20-%20v%202.5%20-%20All%20contributions.pdf)
- [43] X-Foil. 2008, Massachusetts Institute of Technology. <http://web.mit.edu/drela/Public/web/xfoil/>
  - [44] MATLAB, R2009a. 2009, The MathWorks.
  - [45] ABAQUS/CAE. 2008, Simulia. <http://www.simulia.com/>
  - [46] Polycraft, Poly soft foam data sheet, 2014, Polycraft.
  - [47] Elantas, Elantas AS89.1 & AW89.1, 2014, Elantas.
  - [48] Bornengo D, Scarpa F, Remillat C. Evaluation of hexagonal chiral structure for morphing airfoil concept. Proceedings of the Institution of Mechanical Engineers, Part G: Journal of Aerospace Engineering 2005; 219: 185-192. DOI:10.1243/095441005X30216
  - [49] Olympio KR, Gandhi, F. Flexible Skins for Morphing Aircraft Using Cellular Honeycomb Cores. Journal of Intelligent Material Systems and Structures 2009; 21: 1719-1735. DOI:10.1177/1045389X09350331.
  - [50] Olympio KR, Gandhi F. Zero-Cellular Honeycomb Flexible Skins for One-Dimensional Wing Morphing. 48th AIAA/ASME/ASCE/AHS/ASC Structures, Structural Dynamics & Materials Conference, Honolulu, Hawaii, USA, 23 - 26 April 2007.
  - [51] Gurit, SE 70 LOW TEMPERATURE CURE HIGH TOUGHNESS EPOXY PREPREG SYSTEM, 2014, Gurit
  - [52] Bergami, L., Adaptive Trailing Edge Flaps for Active Load Alleviation in a Smart Rotor Configuration, PhD thesis, DTU Wind Energy, 2013.
  - [53] Madsen, H. A. et al., Towards an industrial manufactured morphing trailing edge flap system for wind turbines, Proceedings of EWEC 2014, Barcelona, Spain, 2014.
  - [54] Chaviaropoulos et al., InnWind.EU Deliverable D1.24, 2015

## Appendix A:

### Morphing Truss Configurations Considered in Preliminary Analysis

In this Appendix section all the truss structure configurations for the support of the SMA wire actuators for every concept category are presented. Each configuration is followed by the results that numerical simulations have produced. When the models of each category are presented a summary of the results of the category is provided in order to help the reader follow the procedure for the selection of the most promising concepts of the category. Furthermore, the results for each criterion considered are both presented in common diagrams for the models of each category and discussed in order to get the most of the information about the configurations examined.

**Concept Category 1**

**Model C1v0b**

The model presented here is based on the same functional principle with model C1v0, although the difference lies in the placement of an internal truss structure between web C and tail V of the airfoil structure. This variation of the model is introduced in order to study the effect of using actuators to morph this region. In Figure 105 the internal truss structure layout is presented.

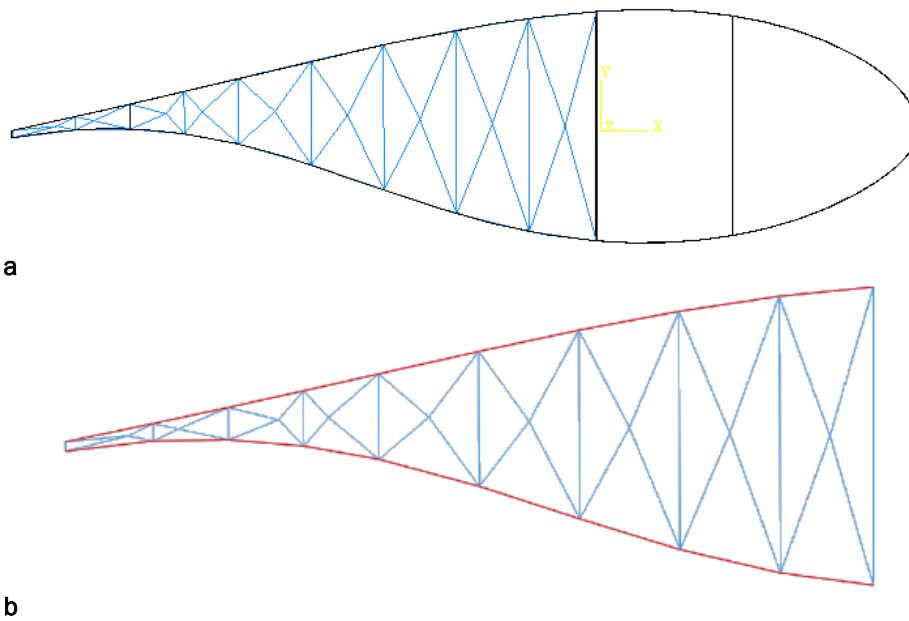


**Figure 105: Model c1v0b (a) implementation of morphing structure and (b) truss structure with the SMA actuators**

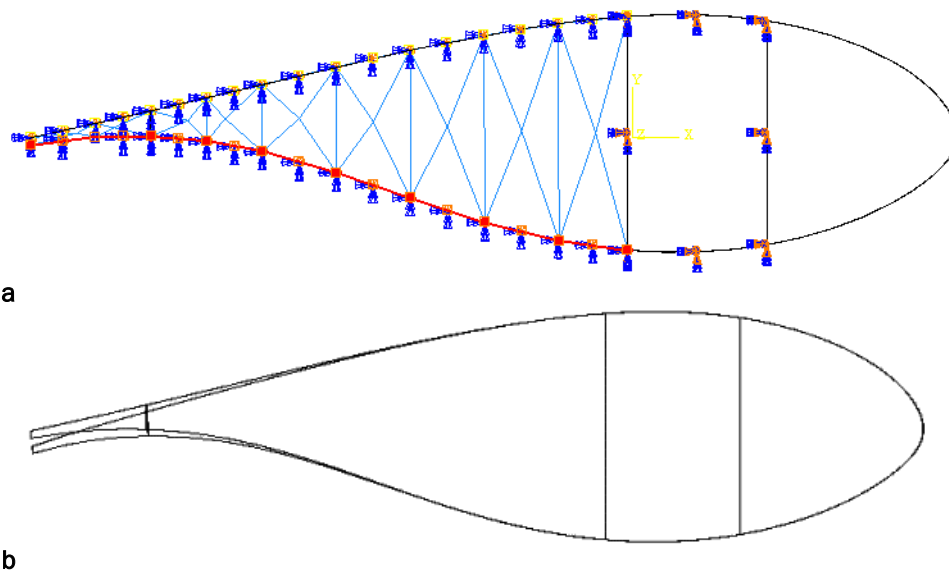


**Figure 106: Model C1v0b (a) SMA actuators activated and (b) the undeformed and deformed airfoil in real scale for  $r = 0.003$  m**

Table 34: Model C1v0b effect of SMA wire radius on structural stiffness

Radius of SMA Wire Actuators		Vertical Displacement
ID	Assigned Value [m]	Value [m]
r <sub>1</sub>	0.0005	-2.8204E-02
r <sub>2</sub>	0.001	-2.6090E-02
r <sub>3</sub>	0.0015	-2.3232E-02
r <sub>4</sub>	0.002	-2.0186E-02
r <sub>5</sub>	0.0025	-1.7311E-02
r <sub>6</sub>	0.003	-1.4771E-02

Table 35: Model C1v0b numerical results of lower sma wire actuators activation

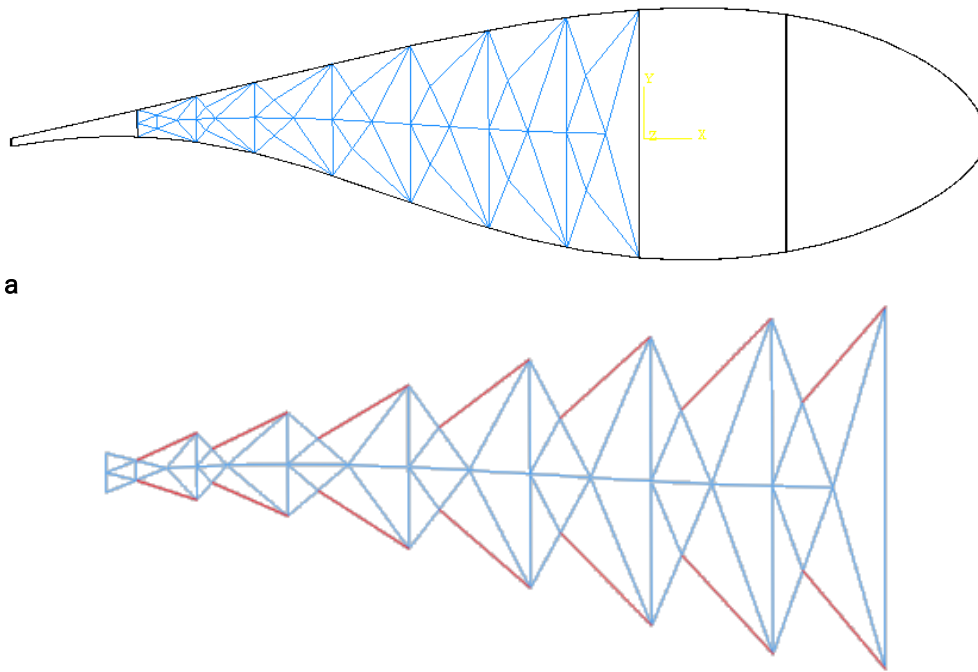
Radius of SMA Wire Actuators		Percent of Chord Length	Angle $\beta$	MVF	Maximum Stress (Actuators)	Maximum Stress (Composites)
ID	[m]	[%]	[°]		[Pa]	[Pa]
r <sub>1</sub>	0.0005	0	0.000	0.7556	2.6297E+08	3.1294E+06
r <sub>2</sub>	0.001	10	2.036	0.7491	2.6205E+08	1.4198E+07
r <sub>3</sub>	0.0015	20	1.605	0.7390	2.6060E+08	3.0710E+07
r <sub>4</sub>	0.002	30	1.836	0.7258	2.5872E+08	5.1775E+07
r <sub>5</sub>	0.0025	30	2.177	0.7103	2.5652E+08	7.5836E+07
r <sub>6</sub>	0.003	40	2.555	0.6933	2.5410E+08	1.0141E+08

Table 36: Model C1v0b predicted  $c_l$  variation for each case study

Radius of SMA Wire Actuators		$\Delta C_L$	
ID	[m]	for a.o.a. 0°	for a.o.a. 4°
r <sub>1</sub>	0.0005	-	-
r <sub>2</sub>	0.001	0.1 up to k = 0.02	0.1 up to k = 0.02
r <sub>3</sub>	0.0015	0.1 up to k = 0.1	0.1 up to k = 0.08
r <sub>4</sub>	0.002	0.15 up to k = 0.08	0.15 up to k = 0.06
r <sub>5</sub>	0.0025	0.2 up to k = 0.02	0.15 up to k = 0.1
r <sub>6</sub>	0.003	0.25 up to k = 0.07	0.25 up to k = 0.05

### Model C1v1

Here the SMA wire actuators are placed with inclination in relation to the previous models. The actuators layout is similar to a fish bone having one of their ends near the skin while the other is placed in a greater distance. The position was specified in order to have good leverage and a near 90° angle between actuator and support truss elements to transfer the biggest portion of the produced force.



**Figure 107: Model C1v1 (a) Implementation of morphing structure and (b) truss structure with the SMA actuators**

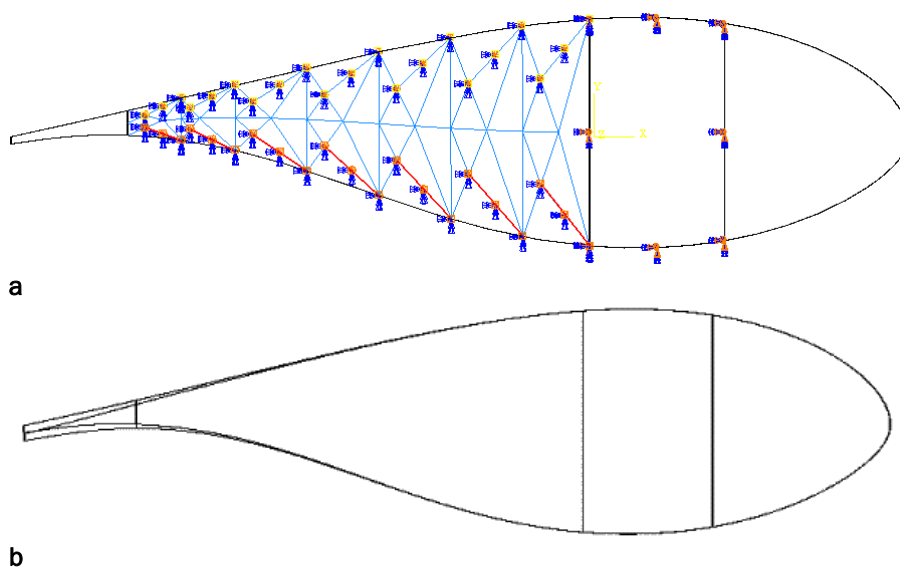


**Figure 108: Model C1v1 (a) SMA actuators activated and (b) the undeformed and deformed airfoil in real scale for  $r = 0.003$  m**

Table 37: Model C1v1 Effect of SMA wire radius on structural stiffness

Radius of SMA Wire Actuators		Vertical Displacement
ID	Assigned Value [m]	Value [m]
r <sub>1</sub>	0.0005	-3.6686E-02
r <sub>2</sub>	0.001	-3.5646E-02
r <sub>3</sub>	0.0015	-3.4189E-02
r <sub>4</sub>	0.002	-3.2556E-02
r <sub>5</sub>	0.0025	-3.0920E-02
r <sub>6</sub>	0.003	-2.9378E-02

Table 38: Model C1v1 Numerical results of lower SMA wire actuators activation

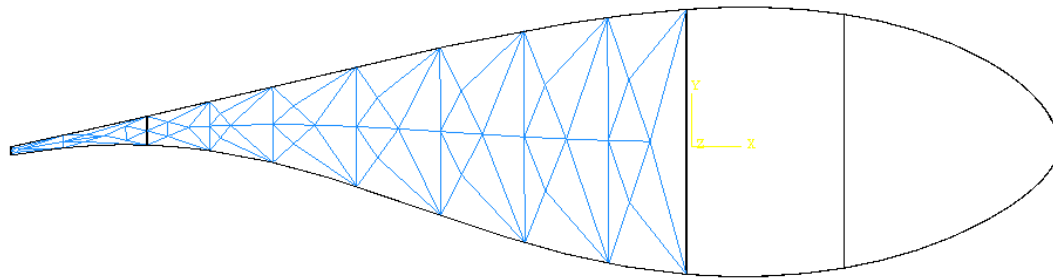
Radius of SMA Wire Actuators		Percent of Chord Length	Angle $\beta$	MVF	Maximum Stress (Actuators)	Maximum Stress (Composites)
ID	[m]	[%]	[°]		[Pa]	[Pa]
r <sub>1</sub>	0.0005	0	0.000	0.7559	2.6301E+08	1.2180E+06
r <sub>2</sub>	0.001	0	0.000	0.7509	2.6230E+08	4.6738E+06
r <sub>3</sub>	0.0015	10	1.338	0.7429	2.6116E+08	9.8647E+06
r <sub>4</sub>	0.002	20	1.452	0.7320	2.5962E+08	1.6188E+07
r <sub>5</sub>	0.0025	20	1.596	0.7189	2.5774E+08	2.3118E+07
r <sub>6</sub>	0.003	30	1.777	0.7038	2.5560E+08	3.0284E+07

Table 39: Model C1v1 Predicted  $C_L$  variation for each case study

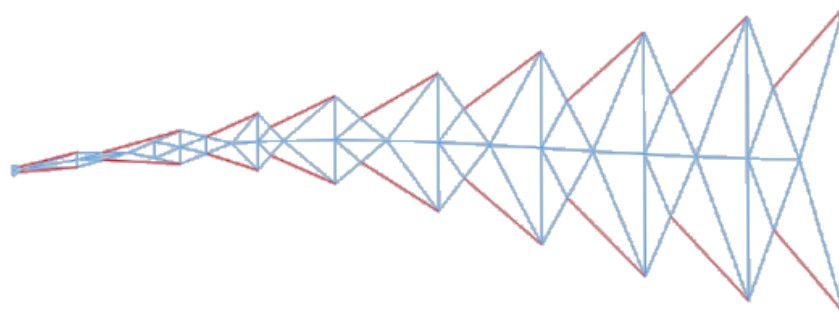
Radius of SMA Wire Actuators		$\Delta C_L$	
ID	[m]	for a.o.a. 0°	for a.o.a. 4°
r <sub>1</sub>	0.0005	-	-
r <sub>2</sub>	0.001	-	-
r <sub>3</sub>	0.0015	0.05 up to k = 0.1	0.05 up to k = 0.1
r <sub>4</sub>	0.002	0.1 up to k = 0.05	0.1 up to k = 0.03
r <sub>5</sub>	0.0025	0.1 up to k = 0.09	0.1 up to k = 0.07
r <sub>6</sub>	0.003	0.15 up to k = 0.06	0.15 up to k = 0.04

Model C1v1b

This concept is a variation of model C1v1 with an addition of truss structure between web C and tail V.

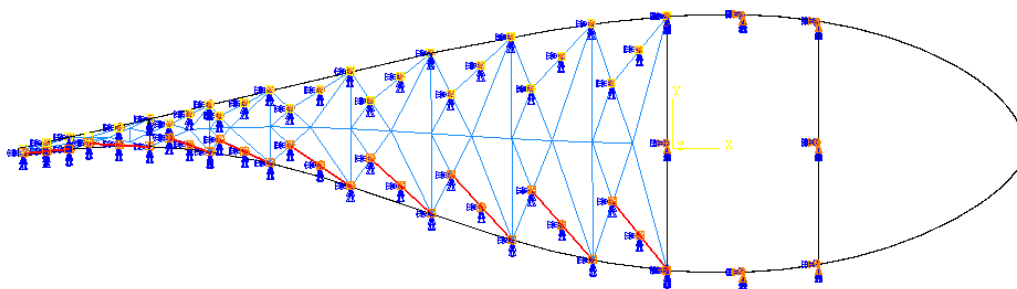


a

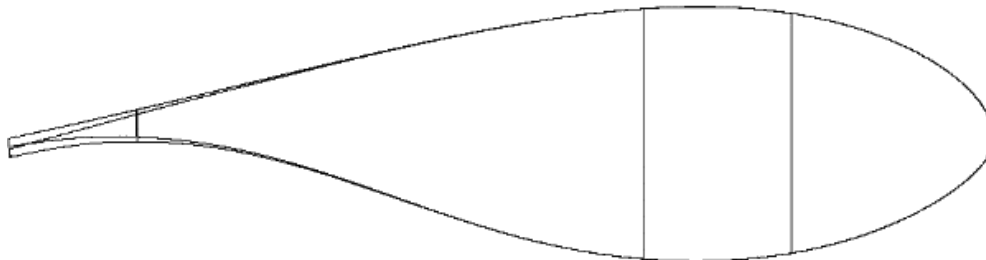


b

Figure 109: Model C1v1b (a) Implementation of morphing structure and (b) truss structure with the sma actuators



a



b

Figure 110: Model C1v1b (a) SMA actuators activated and (b) the undeformed and deformed airfoil in real scale for  $r = 0.003$  m

Table 40: Model C1v1b Effect of SMA wire radius on structural stiffness

Radius of SMA Wire Actuators		Vertical Displacement
ID	Assigned Value [m]	Value [m]
r <sub>1</sub>	0.0005	-1.3804E-02
r <sub>2</sub>	0.001	-1.3272E-02
r <sub>3</sub>	0.0015	-1.2504E-02
r <sub>4</sub>	0.002	-1.1614E-02
r <sub>5</sub>	0.0025	-1.0694E-02
r <sub>6</sub>	0.003	-9.8038E-03

Table 41: Model C1v1b Numerical results of lower sma wire actuators activation

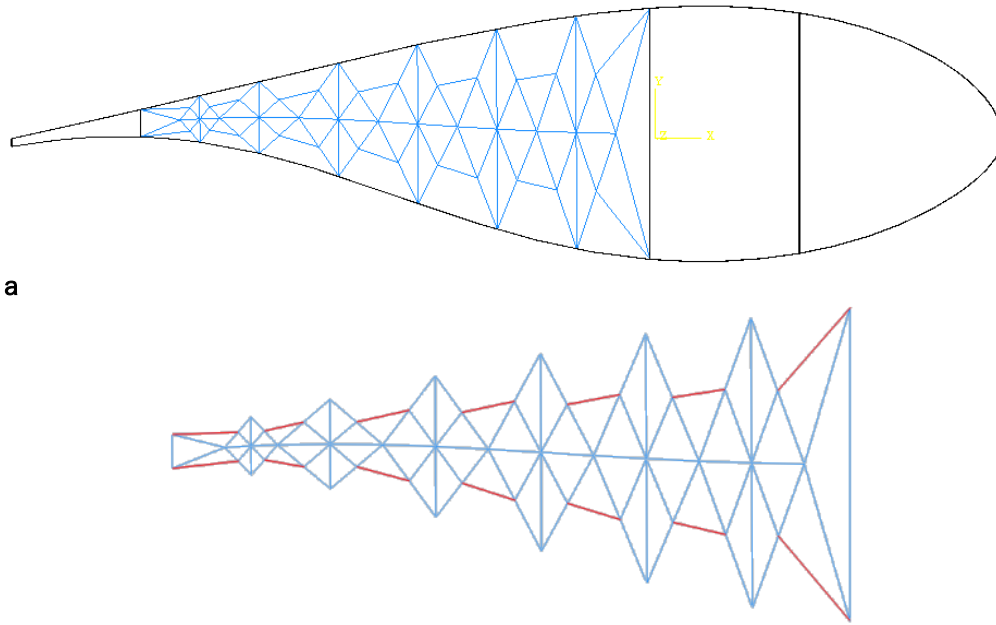
Radius of SMA Wire Actuators		Percent of Chord Length	Angle $\beta$	MVF	Maximum Stress (Actuators)	Maximum Stress (Composites)
ID	[m]	[%]	[°]		[Pa]	[Pa]
r <sub>1</sub>	0.0005	0	0.000	0.7564	2.6308E+08	3.6459E+06
r <sub>2</sub>	0.001	0	0.000	0.7526	2.6254E+08	1.4568E+07
r <sub>3</sub>	0.0015	10	1.672	0.7463	2.6164E+08	3.2720E+07
r <sub>4</sub>	0.002	20	1.700	0.7374	2.6038E+08	5.8037E+07
r <sub>5</sub>	0.0025	20	1.881	0.7259	2.5874E+08	9.0433E+07
r <sub>6</sub>	0.003	30	2.109	0.7118	2.5674E+08	1.2980E+08

Table 42: Model C1v1b Predicted  $C_L$  variation for each case study

Radius of SMA Wire Actuators		$\Delta C_L$	
ID	[m]	for a.o.a. 0°	for a.o.a. 4°
r <sub>1</sub>	0.0005	-	-
r <sub>2</sub>	0.001	-	-
r <sub>3</sub>	0.0015	0.05 up to k = 0.1	0.05 up to k = 0.1
r <sub>4</sub>	0.002	0.1 up to k = 0.1	0.1 up to k = 0.1
r <sub>5</sub>	0.0025	0.1 up to k = 0.1	0.1 up to k = 0.1
r <sub>6</sub>	0.003	0.15 up to k = 0.1	0.15 up to k = 0.1

### Model C1v2

The model presented here has the SMA wire actuators placed away from the skin in order to assess their effectiveness of this layout.



**Figure 111: Model C1v2 (a) Implementation of morphing structure and (b) truss structure with the sma actuators**

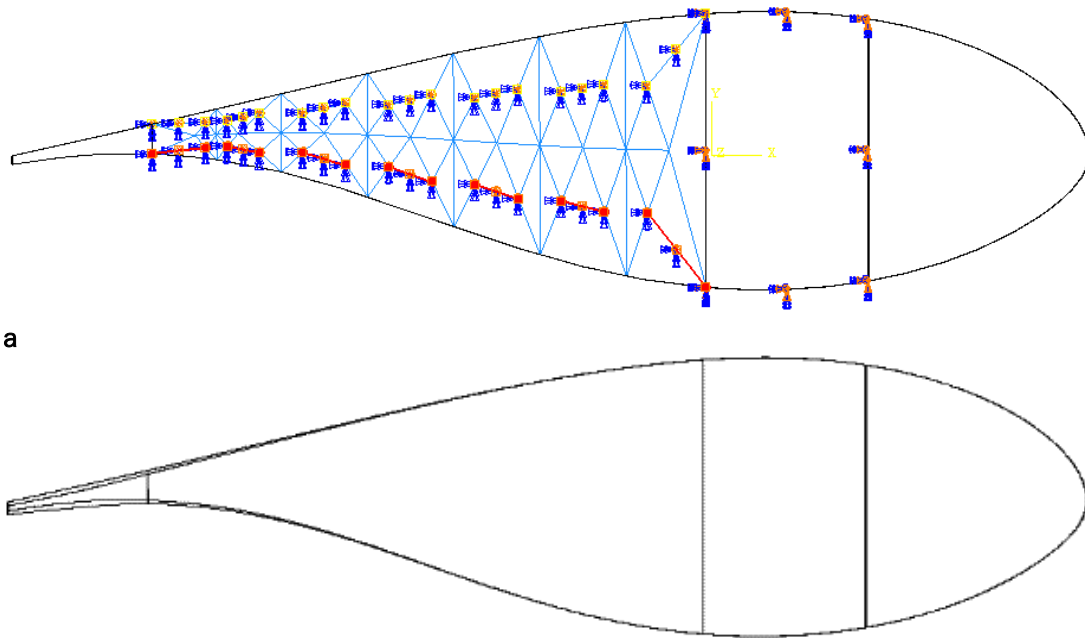


**Figure 112: Model C1v2 (a) SMA actuators activated and (b) the undeformed and deformed airfoil in real scale for  $r = 0.003$  m**

**Table 43: Model C1v2 Effect of SMA wire radius on structural stiffness**

Radius of SMA Wire Actuators		Vertical Displacement
ID	Assigned Value [m]	Value [m]
r <sub>1</sub>	0.0005	-1.4773E-02
r <sub>2</sub>	0.001	-1.4462E-02
r <sub>3</sub>	0.0015	-1.4011E-02
r <sub>4</sub>	0.002	-1.3485E-02
r <sub>5</sub>	0.0025	-1.2940E-02
r <sub>6</sub>	0.003	-1.2414E-02

**Table 44: Model C1v2 Numerical Results of lower sma wire actuators activation**

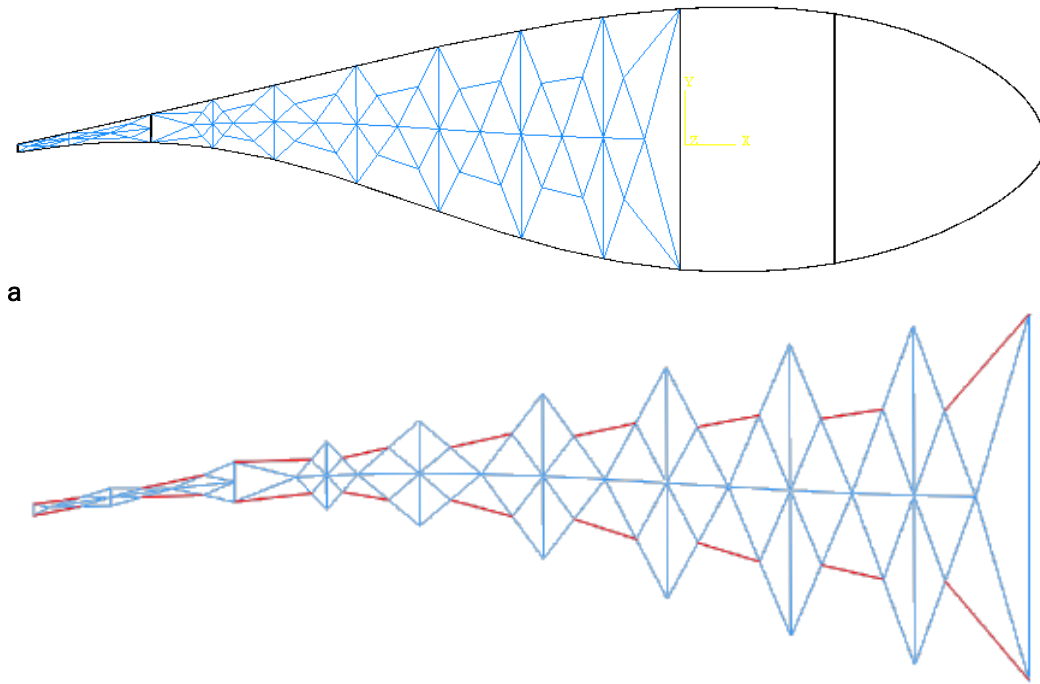
Radius of SMA Wire Actuators		Percent of Chord Length	Angle $\beta$	MVF	Maximum Stress (Actuators)	Maximum Stress (Composites)
ID	[m]	[%]	[°]		[Pa]	[Pa]
r <sub>1</sub>	0.0005	0	0.000	0.7559	2.6301E+08	3.7067E+06
r <sub>2</sub>	0.001	0	0.000	0.7509	2.6230E+08	1.4633E+07
r <sub>3</sub>	0.0015	0	0.000	0.7430	2.6117E+08	3.2242E+07
r <sub>4</sub>	0.002	10	0.781	0.7326	2.5970E+08	3.2242E+07
r <sub>5</sub>	0.0025	20	0.799	0.7205	2.5797E+08	8.4363E+07
r <sub>6</sub>	0.003	20	0.842	0.7069	2.5604E+08	1.1719E+08

**Table 45: Model C1v2 Predicted  $C_L$  variation for each case study**

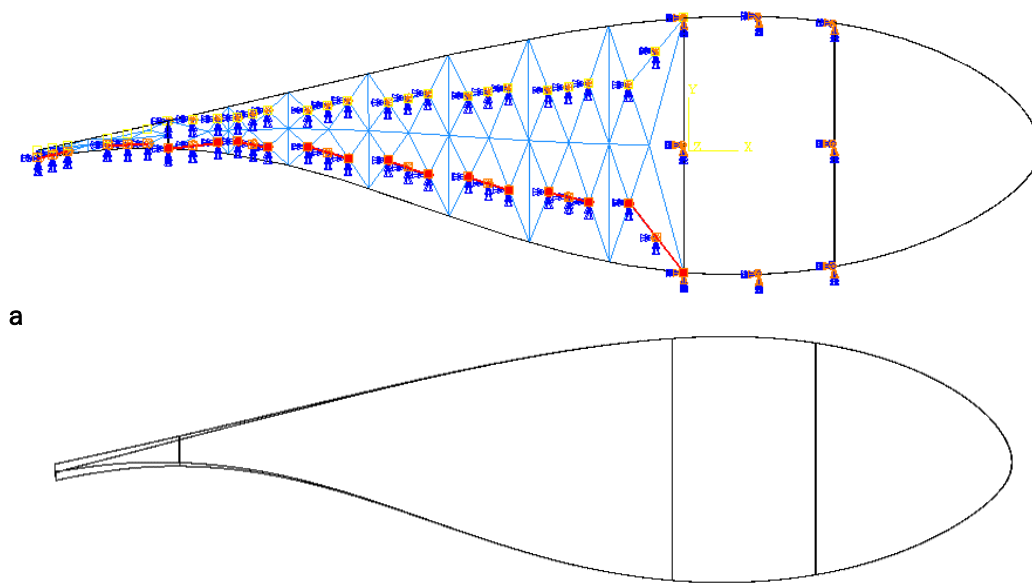
Radius of SMA Wire Actuators		$\Delta C_L$	
ID	[m]	for a.o.a. 0°	for a.o.a. 4°
r <sub>1</sub>	0.0005	-	-
r <sub>2</sub>	0.001	-	-
r <sub>3</sub>	0.0015	-	-
r <sub>4</sub>	0.002	-	-
r <sub>5</sub>	0.0025	0.05 up to k = 0.1	0.05 up to k = 0.08
r <sub>6</sub>	0.003	0.05 up to k = 0.1	0.05 up to k = 0.1

Model C1v2b

This is alternative of the previous model with truss structure addition between web C and tail V.



**b**  
Figure 113: Model C1v2b (a) Implementation of morphing structure and (b) truss structure with the SMA actuators



**b**  
Figure 114: Model C1v2b A. SMA actuators activated and b. the undeformed and deformed airfoil in real scale for  $r = 0.003$  m

Table 46: Model C1v2b Effect of SMA wire radius on structural stiffness

Radius of SMA Wire Actuators		Vertical Displacement
ID	Assigned Value [m]	Value [m]
r <sub>1</sub>	0.0005	-1.3805E-02
r <sub>2</sub>	0.001	-1.3273E-02
r <sub>3</sub>	0.0015	-1.2499E-02
r <sub>4</sub>	0.002	-1.1601E-02
r <sub>5</sub>	0.0025	-1.0675E-02
r <sub>6</sub>	0.003	-9.7869E-03

Table 47: Model C1v2b Numerical results of lower SMA wire actuators activation

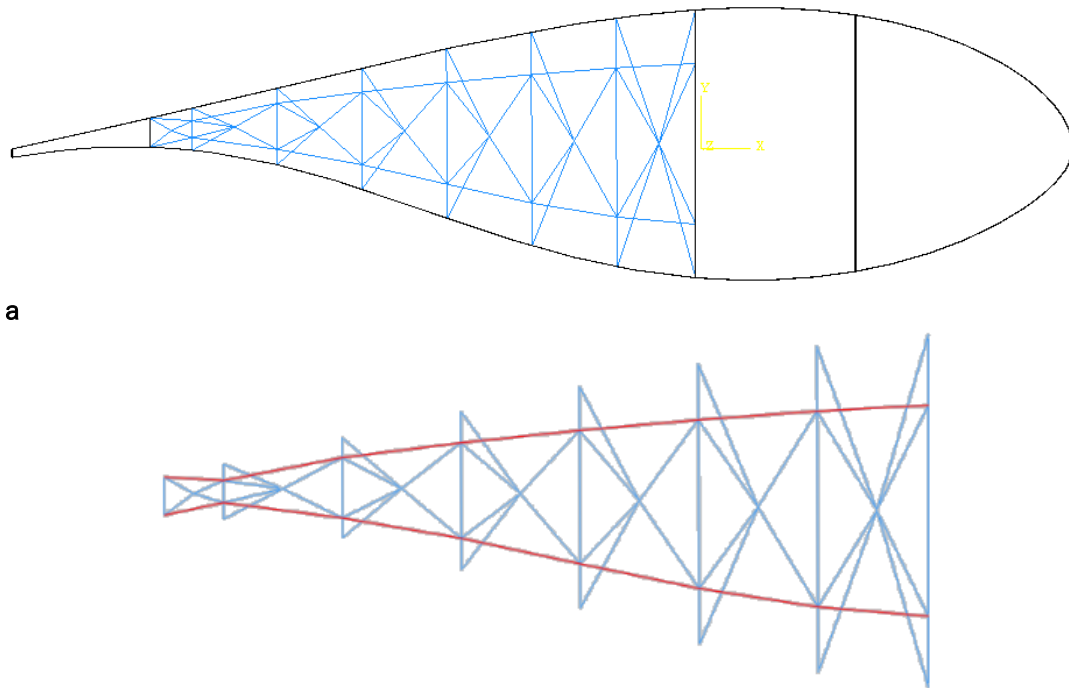
Radius of SMA Wire Actuators		Percent of Chord Length	Angle $\beta$	MVF	Maximum Stress (Actuators)	Maximum Stress (Composites)
ID	[m]	[%]	[°]		[Pa]	[Pa]
r <sub>1</sub>	0.0005	0	0.000	0.7564	2.6308E+08	1.3561E+06
r <sub>2</sub>	0.001	0	0.000	0.7461	2.6161E+08	5.1824E+06
r <sub>3</sub>	0.0015	10	1.709	0.7333	2.5980E+08	1.0860E+07
r <sub>4</sub>	0.002	20	1.600	0.7178	2.5759E+08	1.7630E+07
r <sub>5</sub>	0.0025	20	1.766	0.7008	2.5517E+08	2.4805E+07
r <sub>6</sub>	0.003	30	1.931	0.6834	2.5268E+08	3.1876E+07

Table 48: Model C1v2b Predicted  $C_L$  variation for each case study

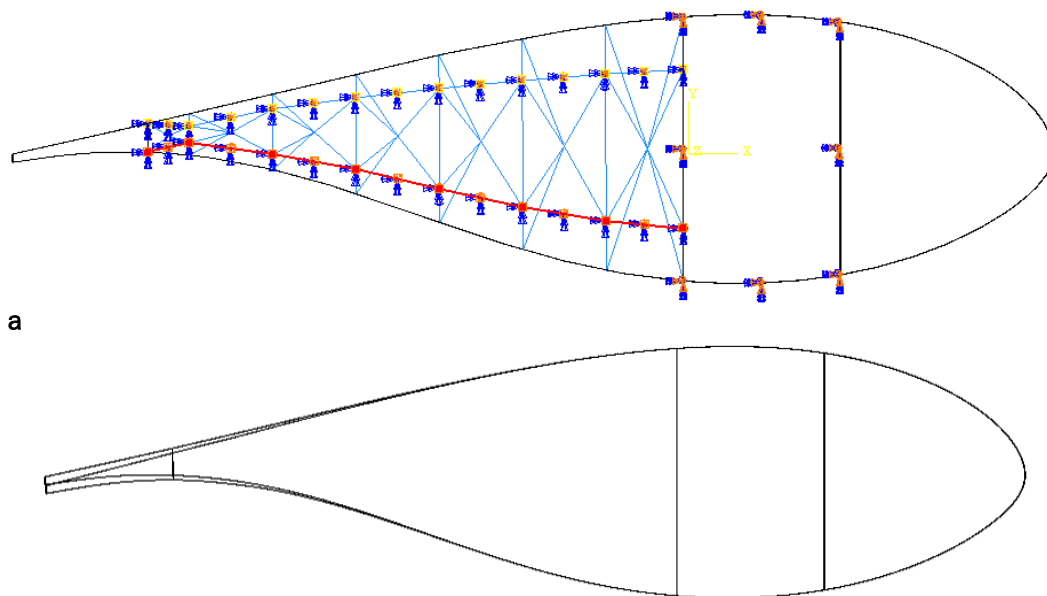
Radius of SMA Wire Actuators		$\Delta C_L$	
ID	[m]	for a.o.a. 0°	for a.o.a. 4°
r <sub>1</sub>	0.0005	-	-
r <sub>2</sub>	0.001	-	-
r <sub>3</sub>	0.0015	0.05 up to k = 0.1	0.05 up to k = 0.1
r <sub>4</sub>	0.002	0.1 up to k = 0.09	0.1 up to k = 0.08
r <sub>5</sub>	0.0025	0.1 up to k = 0.1	0.1 up to k = 0.1
r <sub>6</sub>	0.003	0.15 up to k = 0.1	0.15 up to k = 0.08

**Model C1v3**

This model is a modification of the previous model in terms of SMA wire dimensions and positioning. In this case the wire actuators are attached successively one after another to utilize more effectively the transformation strain that is produced when longer wires are engaged.



**b** Figure 115: Model C1v3 (a) Implementation of morphing structure and (b) truss structure with the SMA actuators



**b** Figure 116: Model C1v3 (a) SMA actuators activated and (b) the undeformed and deformed airfoil in real scale for  $r = 0.003$  m

Table 49: Model C1v3 Effect of SMA wire radius on structural stiffness

Radius of SMA Wire Actuators		Vertical Displacement
ID	Assigned Value [m]	Value [m]
r <sub>1</sub>	0.0005	-3.3562E-02
r <sub>2</sub>	0.001	-3.2805E-02
r <sub>3</sub>	0.0015	-3.1713E-02
r <sub>4</sub>	0.002	-3.0441E-02
r <sub>5</sub>	0.0025	-2.9109E-02
r <sub>6</sub>	0.003	-2.7795E-02

Table 50: Model C1v3 Numerical results of lower SMA wire actuators activation

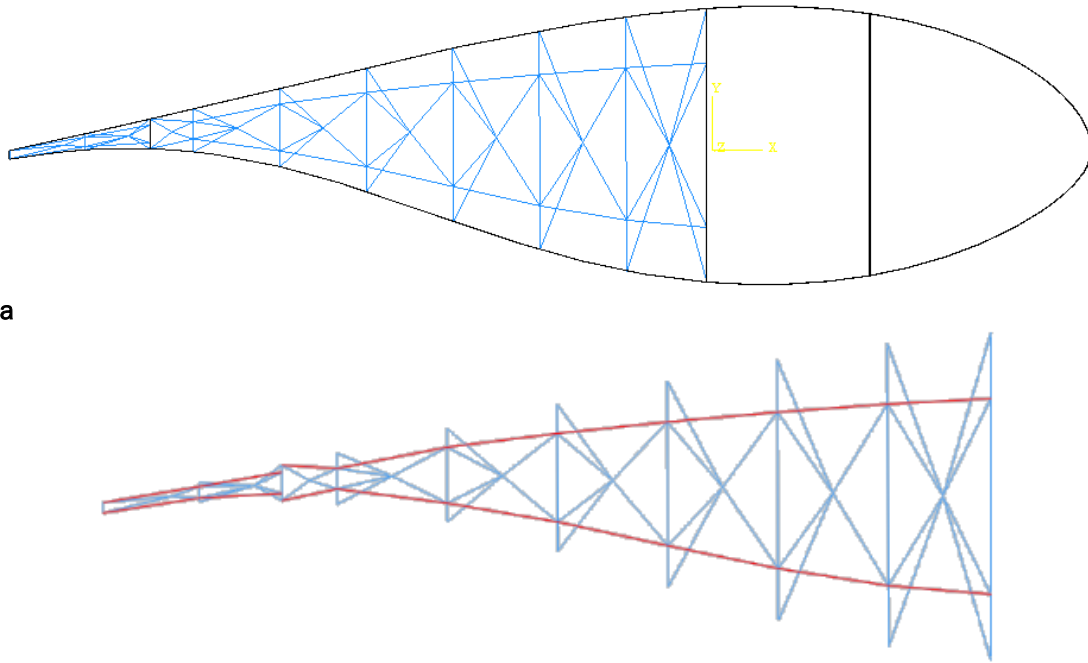
Radius of SMA Wire Actuators		Percent of Chord Length	Angle $\beta$	MVF	Maximum Stress (Actuators)	Maximum Stress (Composites)
ID	[m]	[%]	[°]		[Pa]	[Pa]
r <sub>1</sub>	0.0005	0	0.000	0.7569	2.6315E+08	1.8494E+06
r <sub>2</sub>	0.001	0	0.000	0.7548	2.6285E+08	7.2414E+06
r <sub>3</sub>	0.0015	10	1.389	0.7511	2.6233E+08	1.5761E+07
r <sub>4</sub>	0.002	20	1.167	0.7458	2.6158E+08	2.6856E+07
r <sub>5</sub>	0.0025	30	1.401	0.7389	2.6059E+08	3.9953E+07
r <sub>6</sub>	0.003	30	1.655	0.7304	2.5938E+08	5.4527E+07

Table 51: Model C1v3 Predicted  $\Delta C_L$  variation for each case study

Radius of SMA Wire Actuators		$\Delta C_L$	
ID	[m]	for a.o.a. 0°	for a.o.a. 4°
r <sub>1</sub>	0.0005	-	-
r <sub>2</sub>	0.001	-	-
r <sub>3</sub>	0.0015	0.05 up to k = 0.1	0.05 up to k = 0.1
r <sub>4</sub>	0.002	0.05 up to k = 0.1	0.05 up to k = 0.1
r <sub>5</sub>	0.0025	0.1 up to k = 0.1	0.1 up to k = 0.1
r <sub>6</sub>	0.003	0.15 up to k = 0.03	0.15 up to k = 0.1

#### Model C1v3b

Similar to the models presented before, an expansion of the truss structure and use of actuators is applied between web C and tail V in this model.



**Figure 117: Model C1v3b (a) Implementation of morphing structure and (b) truss structure with the SMA actuators**

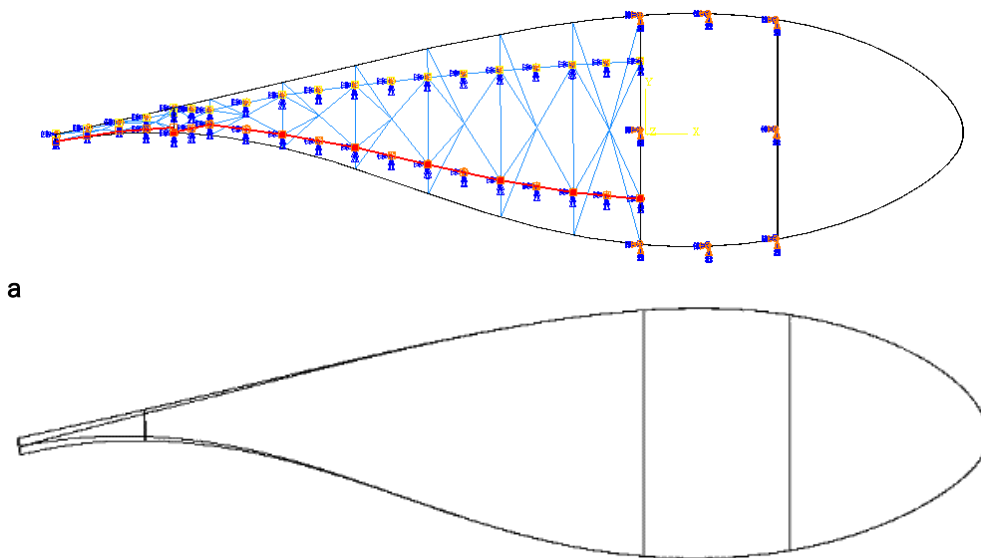


**Figure 118: Model C1v3b (a) SMA actuators activated and (b) the undeformed and deformed airfoil in real scale for  $r = 0.003$  m**

Table 52: Model C1v3b Effect of SMA wire radius on structural stiffness

Radius of SMA Wire Actuators		Vertical Displacement
ID	Assigned Value [m]	Value [m]
r <sub>1</sub>	0.0005	-1.3387E-02
r <sub>2</sub>	0.001	-1.2956E-02
r <sub>3</sub>	0.0015	-1.2335E-02
r <sub>4</sub>	0.002	-1.1611E-02
r <sub>5</sub>	0.0025	-1.0850E-02
r <sub>6</sub>	0.003	-1.0093E-02

Table 53: Model C1v3b Numerical results of lower sma wire actuators activation

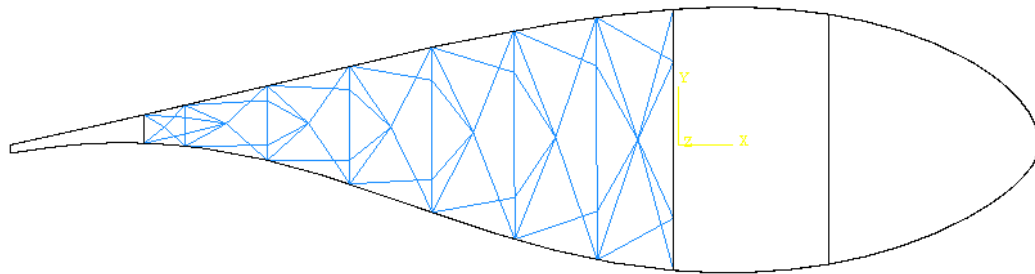
Radius of SMA Wire Actuators		Percent of Chord Length	Angle $\beta$	MVF	Maximum Stress (Actuators)	Maximum Stress (Composites)
ID	[m]	[%]	[°]		[Pa]	[Pa]
r <sub>1</sub>	0.0005	0	0.000	0.7580	2.6330E+08	2.1731E+06
r <sub>2</sub>	0.001	0	0.000	0.7591	2.6346E+08	8.5916E+06
r <sub>3</sub>	0.0015	10	2.061	0.7608	2.6370E+08	1.8965E+07
r <sub>4</sub>	0.002	20	1.333	0.7627	2.6398E+08	3.2843E+07
r <sub>5</sub>	0.0025	20	1.491	0.7647	2.6426E+08	4.9668E+07
r <sub>6</sub>	0.003	30	1.773	0.7666	2.6452E+08	6.8821E+07

Table 54: Model C1v3b Predicted  $C_L$  variation for each case study

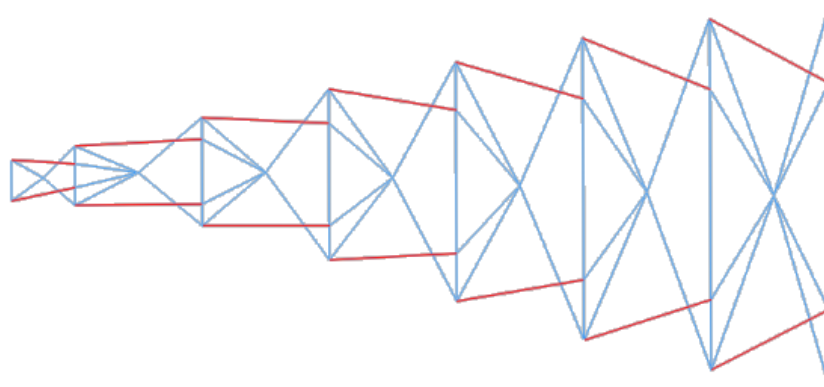
Radius of SMA Wire Actuators		$\Delta C_L$	
ID	[m]	for a.o.a. 0°	for a.o.a. 4°
r <sub>1</sub>	0.0005	-	-
r <sub>2</sub>	0.001	-	-
r <sub>3</sub>	0.0015	0.1 up to k = 0.03	0.1 up to k = 0.03
r <sub>4</sub>	0.002	0.05 up to k = 0.1	0.05 up to k = 0.1
r <sub>5</sub>	0.0025	0.1 up to k = 0.06	0.1 up to k = 0.04
r <sub>6</sub>	0.003	0.15 up to k = 0.06	0.15 up to k = 0.04

#### Model C1v4

In this concept an opposite orientation of the SMA actuators is considered in comparison with model C1v1.

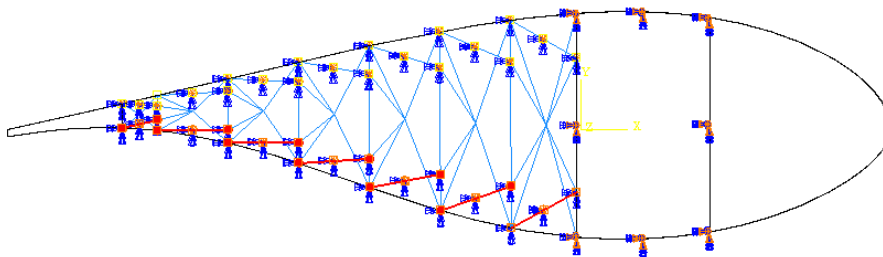


a

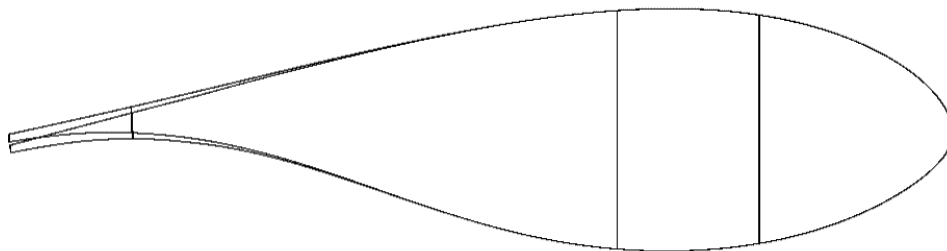


b

Figure 119: Model C1v4 (a) Implementation of morphing structure and (b) truss structure with the sma actuators



a



b

Figure 120: Model C1v4 (a) SMA actuators activated and (b) the undeformed and deformed airfoil in real scale for  $r = 0.003$  m

Table 55: Model C1v4 Effect of SMA wire radius on structural stiffness

Radius of SMA Wire Actuators		Vertical Displacement
ID	Assigned Value [m]	Value [m]
r <sub>1</sub>	0.0005	-1.6730E-02
r <sub>2</sub>	0.001	-1.6258E-02
r <sub>3</sub>	0.0015	-1.5587E-02
r <sub>4</sub>	0.002	-1.4827E-02
r <sub>5</sub>	0.0025	-1.4065E-02
r <sub>6</sub>	0.003	-1.3353E-02

Table 56: Model C1v4 Numerical results of lower sma wire actuators activation

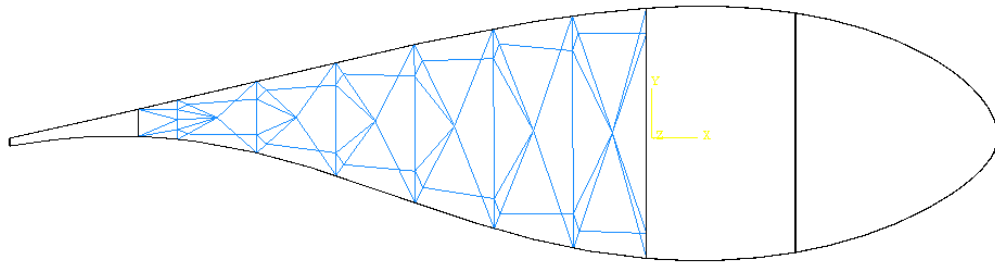
Radius of SMA Wire Actuators		Percent of Chord Length	Angle $\beta$	MVF	Maximum Stress (Actuators)	Maximum Stress (Composites)
ID	[m]	[%]	[°]		[Pa]	[Pa]
r <sub>1</sub>	0.0005	0	0.000	0.7555	2.6294E+08	2.1649E+06
r <sub>2</sub>	0.001	0	0.000	0.7491	2.6204E+08	8.4973E+06
r <sub>3</sub>	0.0015	10	1.240	0.7385	2.6054E+08	1.8559E+07
r <sub>4</sub>	0.002	20	1.273	0.7241	2.5848E+08	3.1751E+07
r <sub>5</sub>	0.0025	30	1.591	0.7059	2.5590E+08	4.7431E+07
r <sub>6</sub>	0.003	30	1.879	0.6844	2.5282E+08	6.4998E+07

Table 57: Model C1v4 Predicted  $C_L$  variation for each case study

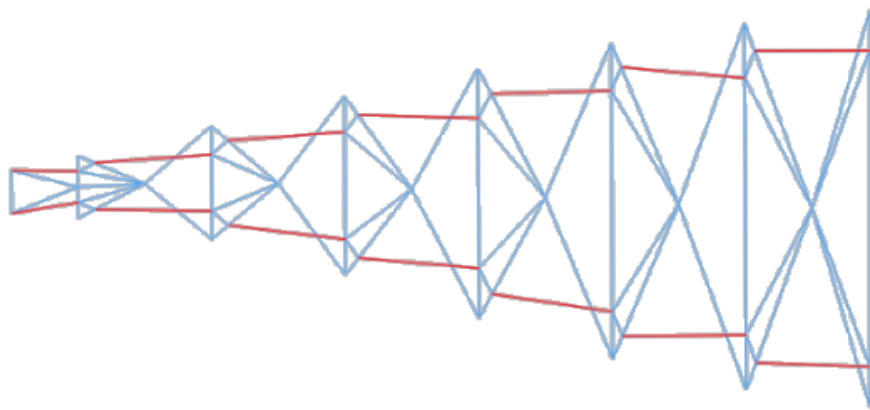
Radius of SMA Wire Actuators		$\Delta C_L$	
ID	[m]	for a.o.a. 0°	for a.o.a. 4°
r <sub>1</sub>	0.0005	-	-
r <sub>2</sub>	0.001	-	-
r <sub>3</sub>	0.0015	0.05 up to k = 0.1	0.05 up to k = 0.1
r <sub>4</sub>	0.002	0.05 up to k = 0.1	0.05 up to k = 0.1
r <sub>5</sub>	0.0025	0.15 up to k = 0.1	0.15 up to k = 0.1
r <sub>6</sub>	0.003	0.15 up to k = 0.09	0.15 up to k = 0.07

#### Model C1v5

The current model utilizes antagonistic SMA wire actuators distant from the airfoil skin and pinned on a truss support structure. For each side the successive actuators are near each other but they have no common support positions.

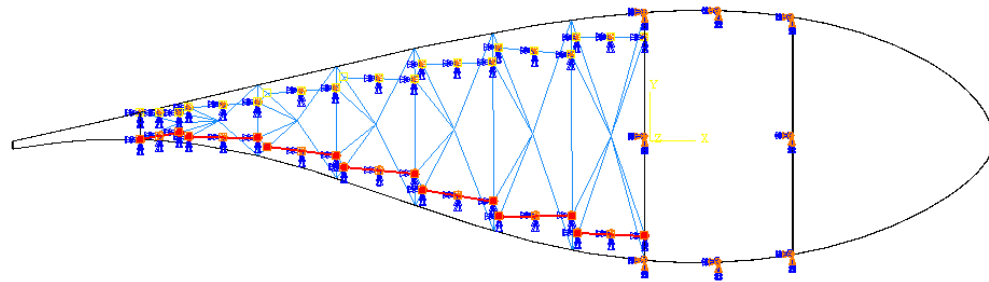


a

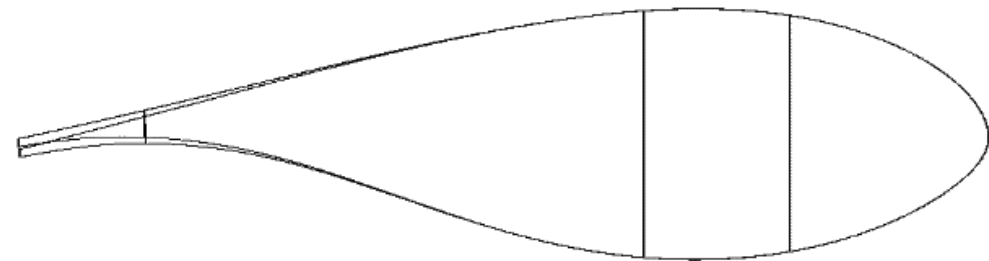


b

Figure 121: Model C1v5 (a) Implementation of morphing structure and (b) truss structure with the SMA actuators



a



b

Figure 122: Model C1v5 A. SMA actuators activated and b. the undeformed and deformed airfoil in real scale for  $r = 0.003$  m

**Table 58: Model C1v5 Effect of SMA wire radius on structural stiffness**

<b>Radius of SMA Wire Actuators</b>		<b>Vertical Displacement</b>
<b>ID</b>	<b>Assigned Value [m]</b>	<b>Value [m]</b>
r <sub>1</sub>	0.0005	-1.7125E-02
r <sub>2</sub>	0.001	-1.6712E-02
r <sub>3</sub>	0.0015	-1.6103E-02
r <sub>4</sub>	0.002	-1.5381E-02
r <sub>5</sub>	0.0025	-1.4622E-02
r <sub>6</sub>	0.003	-1.3880E-02

**Table 59: Model C1v5 Numerical results of lower SMA wire actuators activation**

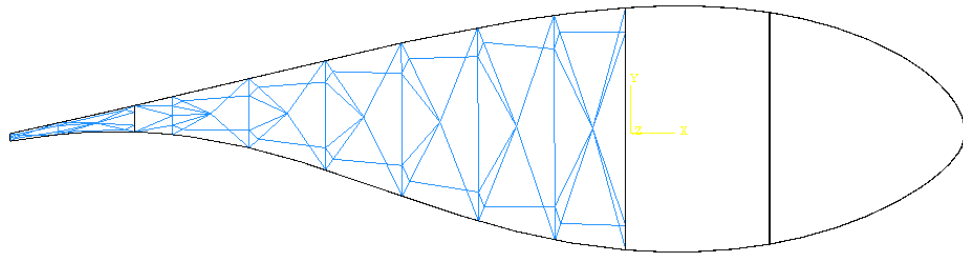
<b>Radius of SMA Wire Actuators</b>		<b>Percent of Chord Length</b>	<b>Angle <math>\beta</math></b>	<b>MVF</b>	<b>Maximum Stress (Actuators)</b>	<b>Maximum Stress (Composites)</b>
<b>ID</b>	<b>[m]</b>	<b>[%]</b>	<b>[°]</b>		<b>[Pa]</b>	<b>[Pa]</b>
r <sub>1</sub>	0.0005	0	0.000	0.7562	2.6305E+08	1.7228E+06
r <sub>2</sub>	0.001	0	0.000	0.7521	2.6247E+08	6.8039E+06
r <sub>3</sub>	0.0015	10	1.162	0.7453	2.6150E+08	1.4998E+07
r <sub>4</sub>	0.002	20	1.173	0.7358	2.6015E+08	2.5945E+07
r <sub>5</sub>	0.0025	30	1.451	0.7237	2.5844E+08	3.9227E+07
r <sub>6</sub>	0.003	30	1.713	0.7092	2.5637E+08	5.4413E+07

**Table 60: Model C1v5 Predicted  $\Delta C_L$  variation for each case study**

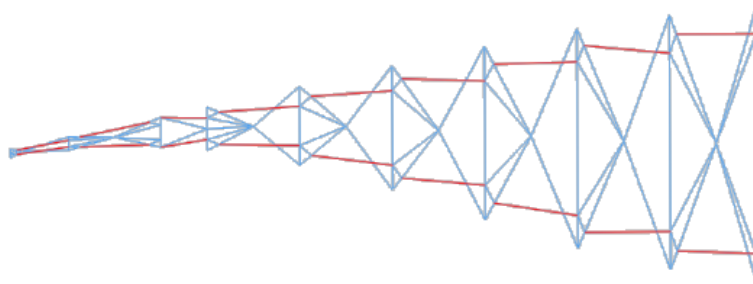
<b>Radius of SMA Wire Actuators</b>		<b><math>\Delta C_L</math></b>	
<b>ID</b>	<b>[m]</b>	<b>for a.o.a. 0°</b>	<b>for a.o.a. 4°</b>
r <sub>1</sub>	0.0005	-	-
r <sub>2</sub>	0.001	-	-
r <sub>3</sub>	0.0015	0.05 up to k = 0.08	0.05 up to k = 0.08
r <sub>4</sub>	0.002	0.05 up to k = 0.1	0.05 up to k = 0.1
r <sub>5</sub>	0.0025	0.1 up to k = 0.05	0.1 up to k = 0.02
r <sub>6</sub>	0.003	0.2 up to k = 0.1	0.1 up to k = 0.1

#### Model C1v5b

This model is the last of this concept category and as rest models noted with “b” is a variation of the previous one with actuators and truss support structure expanded in the region between web C and tail V.

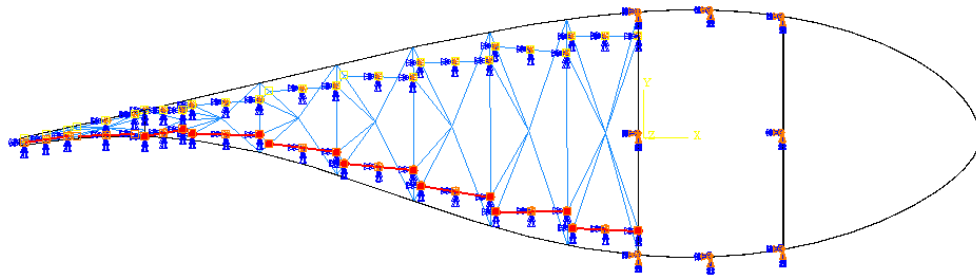


a

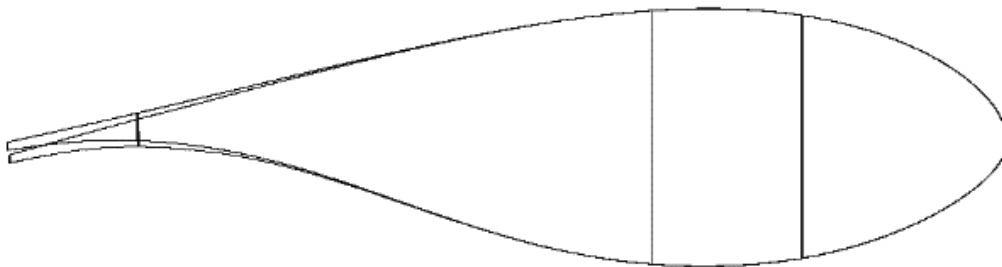


b

Figure 123: Model C1v5b (a) Implementation of morphing structure and (b) truss structure with the sma actuators



a



b

Figure 124: Model C1v5b (a) SMA actuators activated and (b) the undeformed and deformed airfoil in real scale for  $r = 0.003$  m

**Table 61: Model C1v5b Effect of SMA wire radius on structural stiffness**

Radius of SMA Wire Actuators		Vertical Displacement
ID	Assigned Value [m]	Value [m]
r <sub>1</sub>	0.0005	-1.2931E-02
r <sub>2</sub>	0.001	-1.2424E-02
r <sub>3</sub>	0.0015	-1.1675E-02
r <sub>4</sub>	0.002	-1.0788E-02
r <sub>5</sub>	0.0025	-9.8552E-03
r <sub>6</sub>	0.003	-8.9428E-03

**Table 62: Model C1v5b Numerical results of lower sma wire actuators activation**

Radius of SMA Wire Actuators		Percent of Chord Length	Angle $\beta$	MVF	Maximum Stress (Actuators)	Maximum Stress (Composites)
ID	[m]	[%]	[°]		[Pa]	[Pa]
r <sub>1</sub>	0.0005	0	0.000	0.7570	2.6317E+08	1.7162E+06
r <sub>2</sub>	0.001	0	0.000	0.7552	2.6291E+08	6.7745E+06
r <sub>3</sub>	0.0015	10	1.405	0.7521	2.6247E+08	1.4921E+07
r <sub>4</sub>	0.002	20	1.406	0.7476	2.6182E+08	2.5784E+07
r <sub>5</sub>	0.0025	30	1.734	0.7415	2.6097E+08	3.8932E+07
r <sub>6</sub>	0.003	30	2.039	0.7340	2.5989E+08	5.3922E+07

**Table 63: Model C1v5b Predicted  $\Delta C_L$  variation for each case study**

Radius of SMA Wire Actuators		$\Delta C_L$	
ID	[m]	for a.o.a. 0°	for a.o.a. 4°
r <sub>1</sub>	0.0005	-	-
r <sub>2</sub>	0.001	-	-
r <sub>3</sub>	0.0015	0.05 up to k = 0.1	0.05 up to k = 0.08
r <sub>4</sub>	0.002	0.05 up to k = 0.03	0.1 up to k = 0.02
r <sub>5</sub>	0.0025	0.15 up to k = 0.05	0.15 up to k = 0.03
r <sub>6</sub>	0.003	0.15 up to k = 0.1	0.15 up to k = 0.1

### Interpretation of Analyses Results

After presenting the configurations and the results of the simulation for the models of the first concept category, the interpretation of the results follows. All models are assessed in order to select the most effective layouts according to certain predefined criteria. The main target is to achieve the largest variation (ideally between 0.25÷0.30) in coefficient of lift ( $\Delta C_L$ ) with the proper combination of chordal moving length and angular rotation  $\beta$ . Another criterion is the limitation of developed stresses on airfoil structural geometry and SMA wire actuators. For the actuators the limit for stress value is set to 270 MPa. Similarly, the stress level for the composites which constitute airfoil structure was set to 320 MPa. Furthermore, the martensitic volume fraction variation in the SMA wires need to remain as low as possible in order to have a fast return to the initial position. Finally, the change in structural stiffness due to the implementation of the support truss structure inside the airfoil section will be shown. In the following figures results for all the models of this category are summarized.

Figure 125 show the length of the chord with movement ability in respect to the radius of SMA wire actuator utilized for every model of the first concept category. From the diagram, it is obvious that a wire radius of 0.5 mm is unable to bend the airfoil structure. If the radius is increased to 1 mm, then only models C1v0 and C1v0b are able to have a move over 5 % of the chord length

while all the other models remain almost at their initial position. For SMA wires of radius greater than 1.5 mm the chordal moving length increases intensively and in some cases exerts 30%. At this stage of the study, a moving length between 10 and 20 % of the chord length achieved using the minimum possible value of wire radius was considered as the selection variable. Thus models C1v0, C1v0b, C1v4, C1v4b, C1v5 and C1v5b were selected according to this criterion. It should be noted though that out of the six aforementioned models the ones that are substantially chosen are C1v0, C1v4 and C1v5 because the addition of letter “b” in the model name indicates a small variation in the model’s layout which has infinitesimal effect on moving portion of chord’s length.

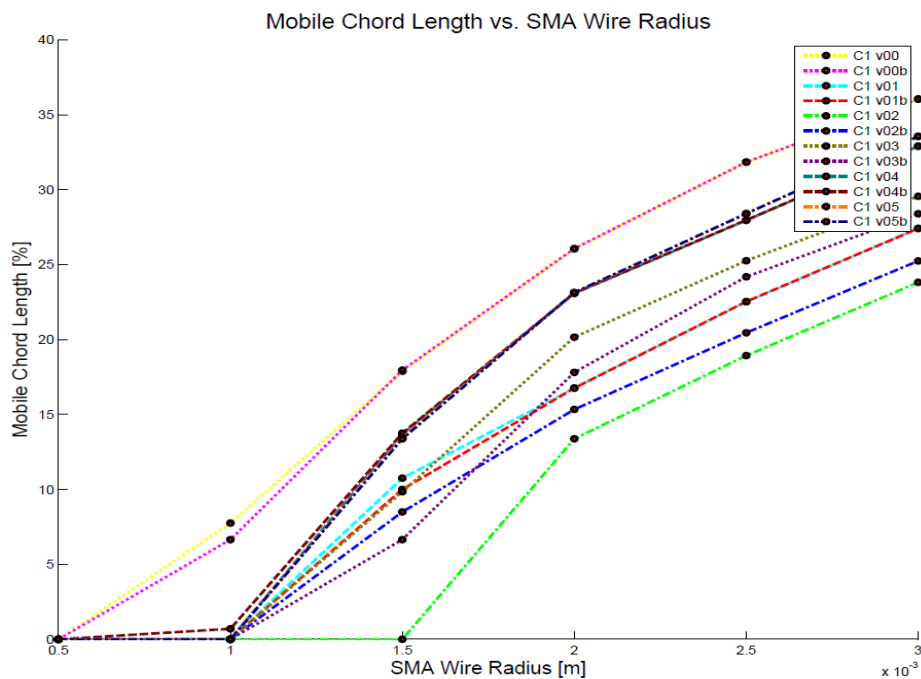


Figure 125: Concept 1 models chord length with morphing capability vs. SMA wire radius for each model

In order to get a better insight of the response of the selected models, Figure 126 is created. This figure states clearly that expanding the truss structure and adding actuators between web C and Tail V does not change the moving length of the chord, as it is expected. The expansion of the truss structure is added in a region which is after the main actuators structure, thus it helps achieve a better angular rotation (as it is presented later on) but it does not affect the moving length of the chord.

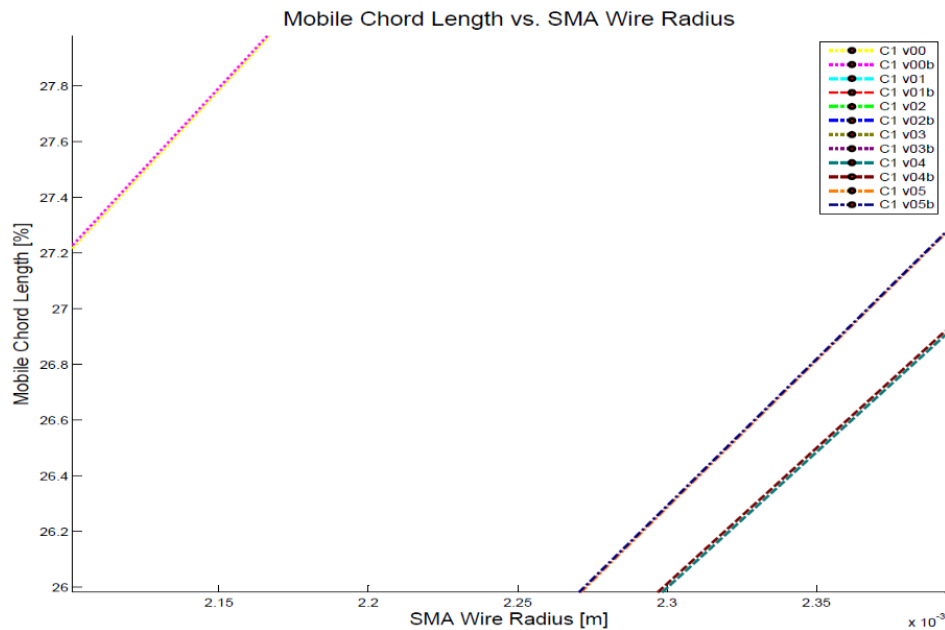


Figure 126: Concept 1 models zoomed region of Figure 125

In Figure 127 the angular rotation  $\beta$  of the (equivalent) flap is presented in respect to the radius of the SMA wire used for morphing. It is obvious that for wires of radius equal to 0.5 mm angular rotation is 0 because it is not possible to bend the airfoil. Model C1v3b produces the maximum angular rotation, but the results regarding the mobile chordal length from Figure 125 indicate that its movement is confined to a region with length less than 10% of chord, so this high angular rotation cannot be used for effective morphing. If the radius of the wire actuators is increased above 1.5 mm there is a clear trend to increase the amplitude of the angular rotation but because this trend is smooth, a more detailed study must take place to decide if increasing actuator's radius pays off with better angular rotation.

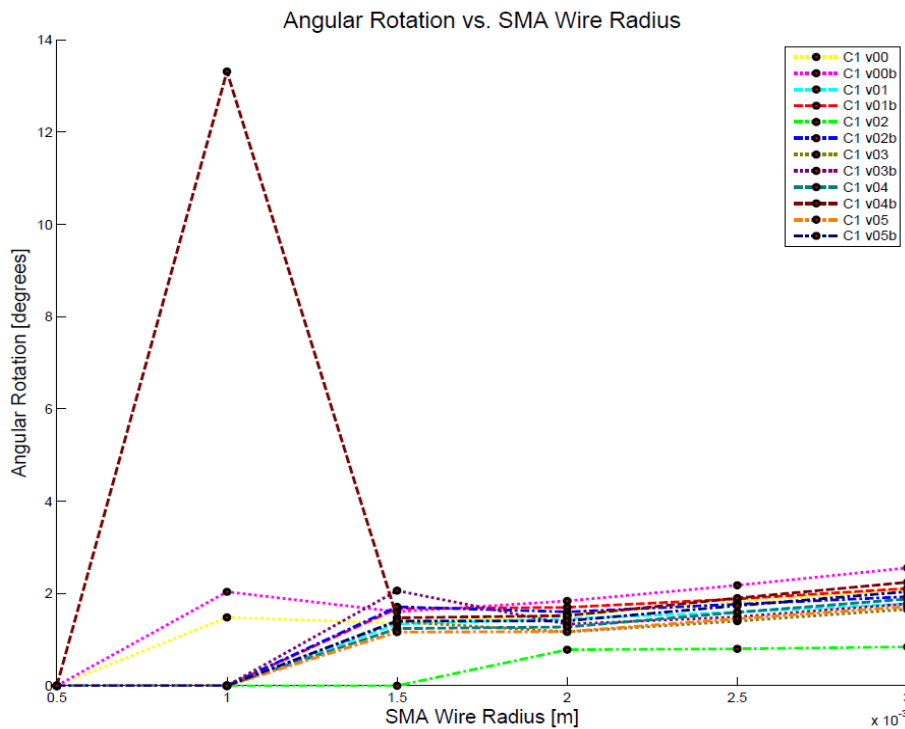


Figure 127: Concept 1 models angular rotation vs. SMA wire radius

In Figure 128 a close up of Figure 127 is presented in order to show in more detail the trend of the variation in angular rotation for each model. The most effective model configurations, regarding the produced angular rotation, are the models C1v0b, C1v1b and C1v4b. Here is clear that the expansion of the truss structure and the placement of actuators between web C and tail V have improved the response of the model. If the respective models without the expansion are considered, the difference in the angular rotation is about 0.5°. Although this might seem a small difference it may result in a wider variation of coefficient of lift for more cases of reduced rotational frequency of the blade.

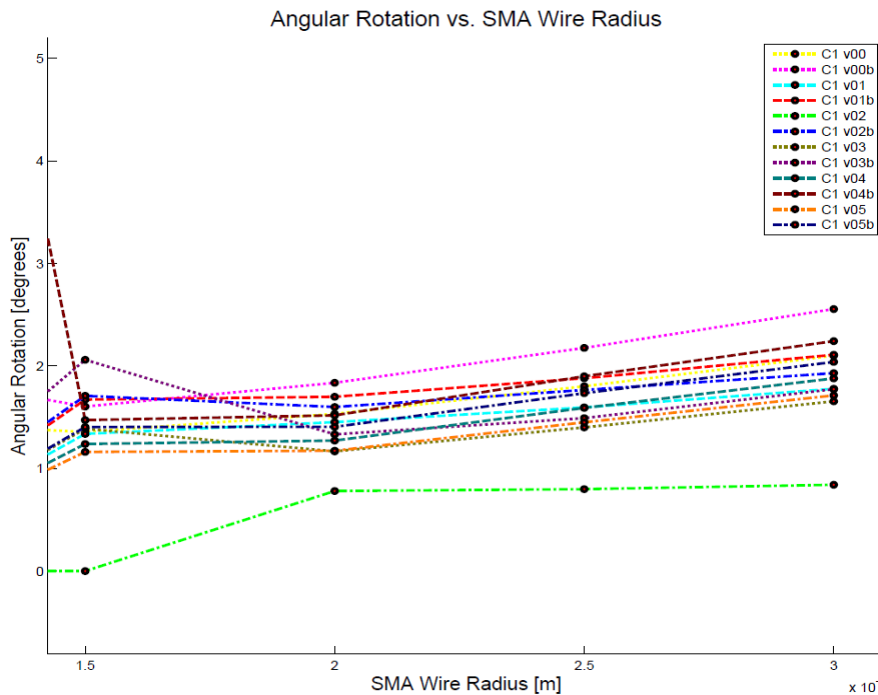


Figure 128: Concept 1 models zoomed region of Figure 127

Figure 129 shows the variation of maximum stress developed in SMA wire actuators with respect to their radius. As it is anticipated in almost every model the stress decreases while increasing their radius, because the same force created by certain thermal load is deduced to a larger surface.

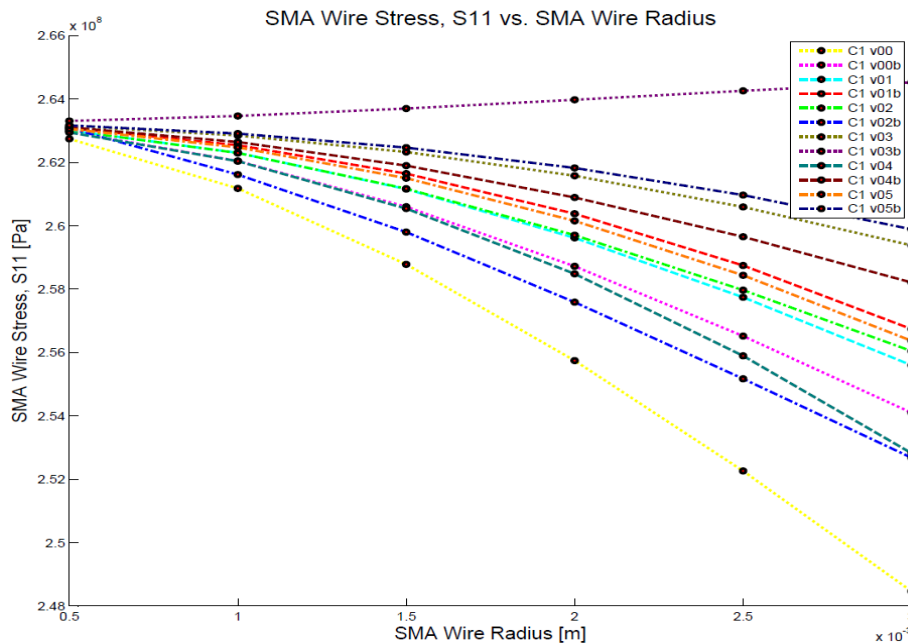


Figure 129: Concept 1 models actuators' maximum stress vs. SMA wire radius

The slight increase of stress in model C1v3 can be attributed to the different layout of the SMA wires and their support location. As the airfoil bends, the wires subject to mechanical load through

reaction forces from the support structure. When the developed stress increases the transformation temperature limits alter. Thus, the reaction forces from the support structure and antagonistic actuators may cause the activated actuators to transform differently in model C1v3 and lead to an increase in developed stress although wire radius is increased. For all the model cases the maximum developed stress is lower than the specification of the 270 MPa, but the most promising model are C1v0, C1v0b, C1v02 and C1v4, because they tend to have the most drastic decrease in developed stress when wires of radius of 1.5 mm or greater are used.

The next criterion that is studied is the martensitic volume fraction of the activated SMA wires at the end of each simulation. Martensitic volume fraction is required to have high values or values near it's initial in order for the reverse transformation to take place in less time. Figure 130 presents the value of martensitic volume fraction at the end of each simulation run for every model. It is obvious that martensitic volume fraction tends to decrease as the radius of the actuators increases. This happens because when the radius increases the developed stress decreases and this consequently lead to a decrease in transformation temperature thresholds. As these thresholds decrease the transformation tend to complete faster, so for a predefined temperature level martensitic volume fraction is going to decrease faster. If the radius of 1.5 mm is selected then models C1v3, C1v3b, C1v4b and C1v5b have the largest values of martensitic volume fraction at the end of simulation runs.

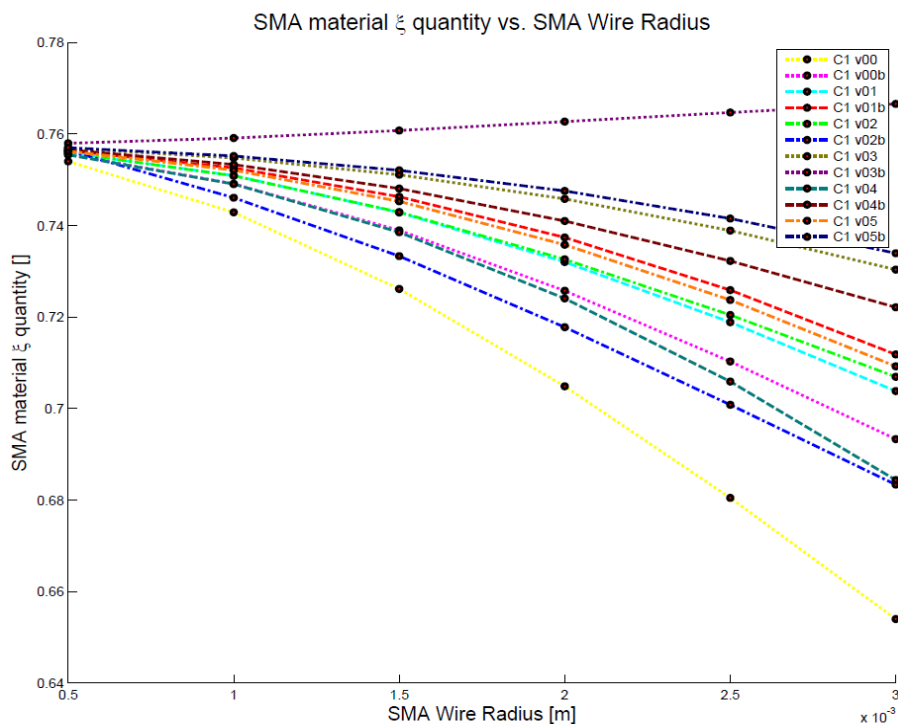


Figure 130: Concept 1 models martensitic volume fraction vs. SMA wire radius

In order to have a complete presentation of the results it is essential to measure the effect that implementation of the truss structure has on original airfoil structure's stiffness. For every model a force was applied on the chord end that meets trailing edge and the produced displacement was measured. The displacement was compared afterwards with the vertical displacement of the original airfoil structure when subjected to the same load. The results for each model as well as the original airfoil are presented in Figure 131. Clearly, the total stiffness of the structure is dramatically increased due to the implementation of the truss support structure. If a model of the present concept was to be studied further it should be optimized in order to lower airfoil's original structure stiffness as well as address the minimum number of truss support elements to have the

desired stiffness and the minimum weight, because the implementation of the truss elements leads to increase of the overall weight.

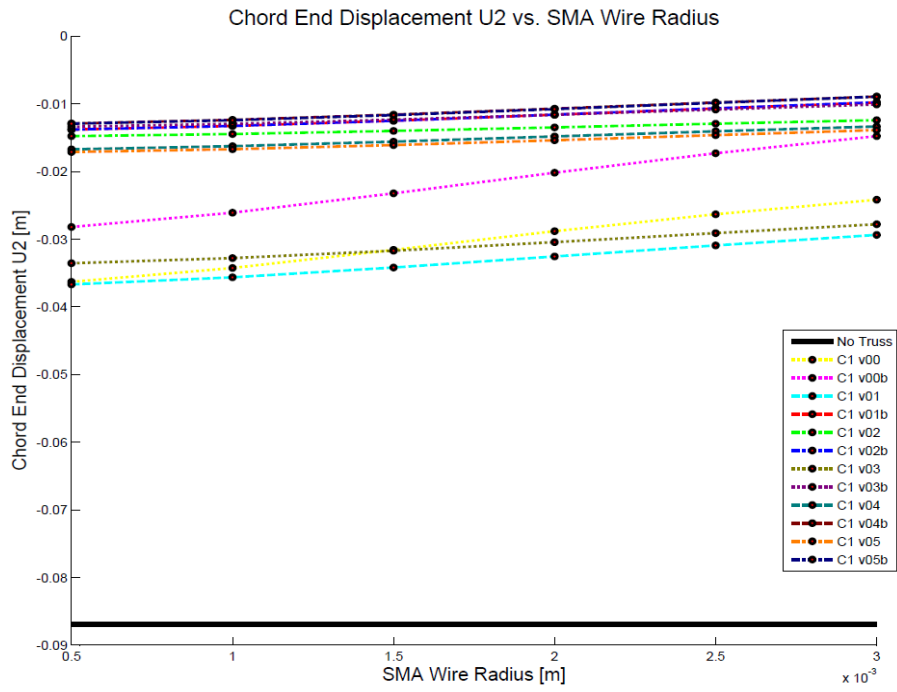
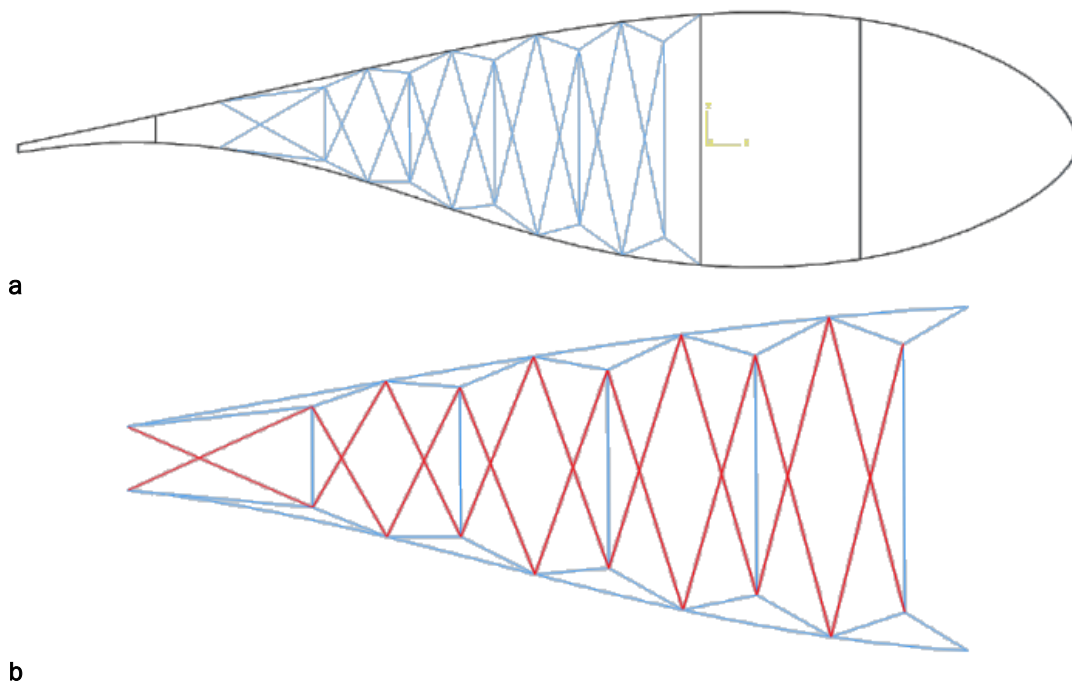


Figure 131: Concept 1 models vertical displacement of chord end

**Concept Category 2**

**Model C2v0b**

In this model an internal truss structure is implemented as in the previous models with the main difference lying on the way the trailing panels are connected. The trailing panels are separated into smaller portions that lie between the support truss elements and are connected to each other with pin joints.



**Figure 132: Model C2v0b (a) implementation of morphing structure and (b) truss structure with the SMA actuators**

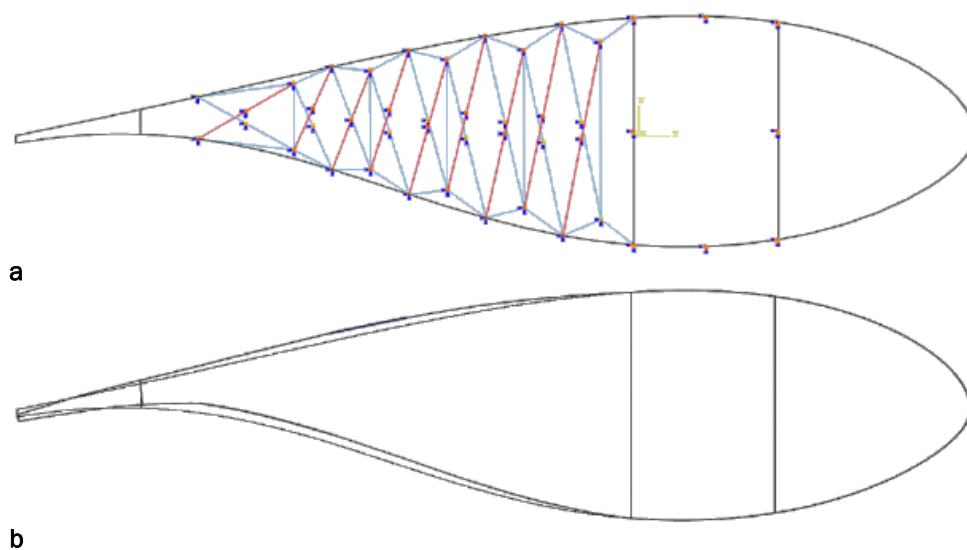


**Figure 133: Model C2v0b (a) SMA actuators activated and (b) the undeformed and deformed airfoil in real scale for  $r = 0.003$  m**

Table 64: Model C2v0b Effect of SMA wire radius on structural stiffness

Radius of SMA Wire Actuators		Vertical Displacement
ID	Assigned Value [m]	Value [m]
r <sub>1</sub>	0.0005	-3.3889E-02
r <sub>2</sub>	0.001	-2.5996E-02
r <sub>3</sub>	0.0015	-2.4556E-02
r <sub>4</sub>	0.002	-2.4010E-02
r <sub>5</sub>	0.0025	-2.3740E-02
r <sub>6</sub>	0.003	-2.3586E-02

Table 65: Model C2v0b Numerical results of lower sma wire actuators activation

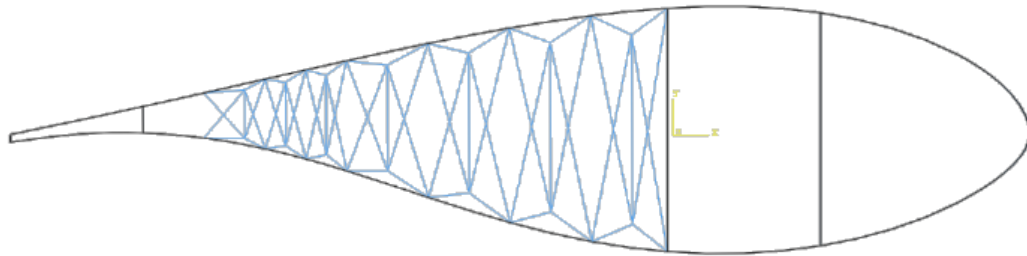
Radius of SMA Wire Actuators		Percent of Chord Length	Angle $\beta$	MVF	Maximum Stress (Actuators)	Maximum Stress (Composites)
ID	[m]	[%]	[°]		[Pa]	[Pa]
r <sub>1</sub>	0.0005	50	0.392	0.4830	2.2371E+08	1.8965E+07
r <sub>2</sub>	0.001	60	0.395	0.3816	2.0881E+08	5.8684E+07
r <sub>3</sub>	0.0015	60	0.408	0.2590	1.9054E+08	9.6955E+07
r <sub>4</sub>	0.002	60	0.434	0.1386	1.7235E+08	1.2257E+08
r <sub>5</sub>	0.0025	60	0.466	0.0279	1.5540E+08	1.4812E+08
r <sub>6</sub>	0.003	60	0.478	0.0145	1.3116E+08	1.6425E+08

Table 66: Model C2v0b Predicted  $C_L$  variation for each case study

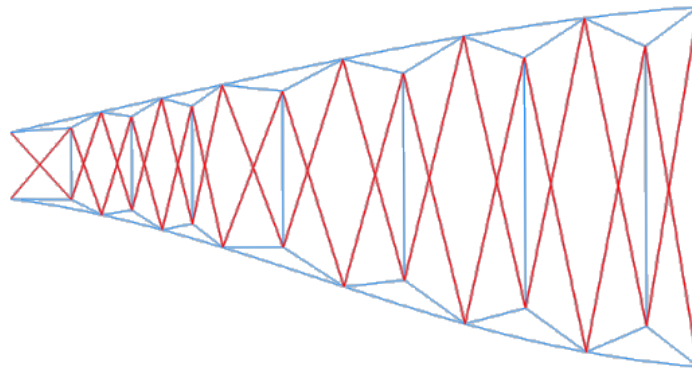
Radius of SMA Wire Actuators		$\Delta C_L$	
ID	[m]	for a.o.a. 0°	for a.o.a. 4°
r <sub>1</sub>	0.0005	0.05 up to k = 0.02	-
r <sub>2</sub>	0.001	0.05 up to k = 0.02	-
r <sub>3</sub>	0.0015	0.05 up to k = 0.03	0.05 up to k = 0.02
r <sub>4</sub>	0.002	0.05 up to k = 0.06	0.05 up to k = 0.05
r <sub>5</sub>	0.0025	0.05 up to k = 0.1	0.05 up to k = 0.08
r <sub>6</sub>	0.003	0.05 up to k = 0.1	0.05 up to k = 0.1

#### Model C2v1

This model is built in the same principle as model C2v0, but it uses more actuator pairs.

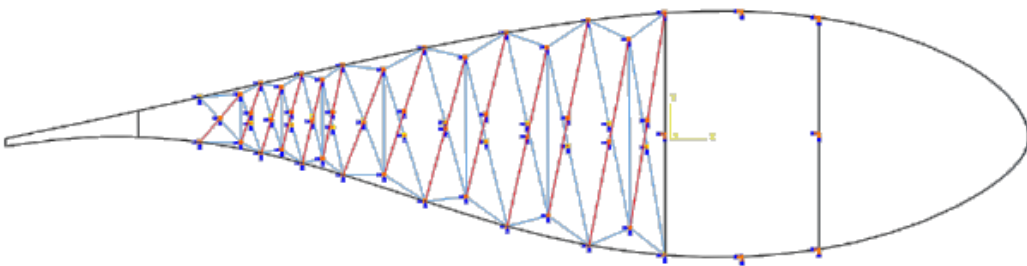


a

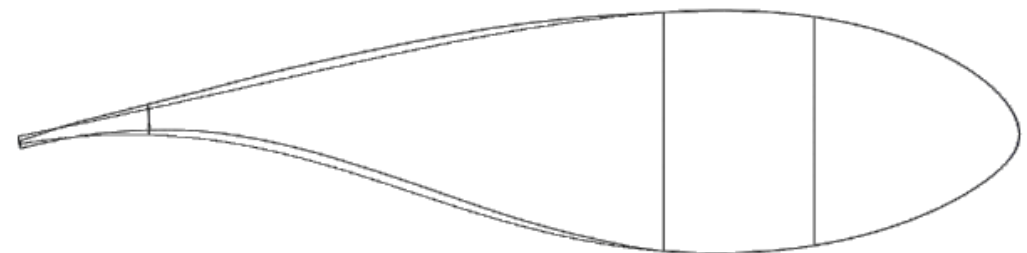


b

Figure 134: Model C2v1 (a) implementation of morphing structure and (b) truss structure with the SMA actuators



a



b

Figure 135: Model C2v1 (a) SMA actuators activated and (b) the undeformed and deformed airfoil in real scale for  $r = 0.003$  m

Table 67: Model C2v1 Effect of SMA wire radius on structural stiffness

Radius of SMA Wire Actuators		Vertical Displacement
ID	Assigned Value [m]	Value [m]
r <sub>1</sub>	0.0005	-1.5189E-02
r <sub>2</sub>	0.001	-1.2439E-02
r <sub>3</sub>	0.0015	-1.1698E-02
r <sub>4</sub>	0.002	-1.1405E-02
r <sub>5</sub>	0.0025	-1.1260E-02
r <sub>6</sub>	0.003	-1.1177E-02

Table 68: Model C2v1 Numerical results of lower SMA wire actuators activation

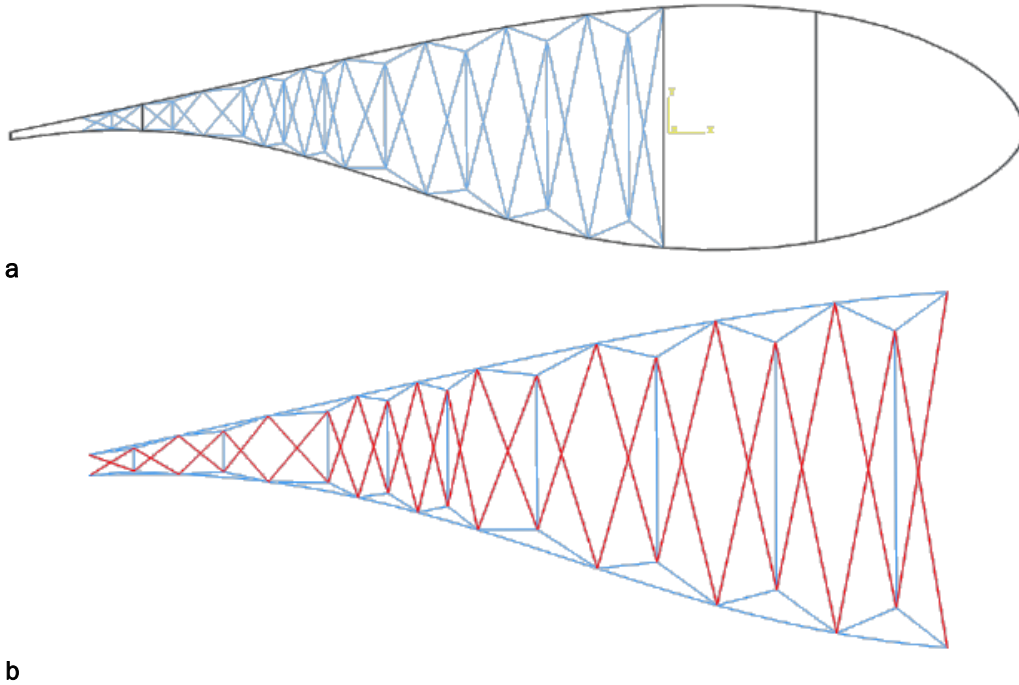
Radius of SMA Wire Actuators		Percent of Chord Length	Angle $\beta$	MVF	Maximum Stress (Actuators)	Maximum Stress (Composites)
ID	[m]	[%]	[°]		[Pa]	[Pa]
r <sub>1</sub>	0.0005	50	0.251	0.7199	2.5789E+08	4.2878E+07
r <sub>2</sub>	0.001	60	0.342	0.6725	2.5112E+08	9.6719E+07
r <sub>3</sub>	0.0015	60	0.370	0.6361	2.4590E+08	1.3373E+08
r <sub>4</sub>	0.002	60	0.389	0.6088	2.4197E+08	1.5877E+08
r <sub>5</sub>	0.0025	60	0.408	0.5872	2.3885E+08	1.7605E+08
r <sub>6</sub>	0.003	60	0.432	0.5689	2.3620E+08	1.8855E+08

Table 69: Model C2v1 Predicted  $\Delta C_L$  variation for each case study

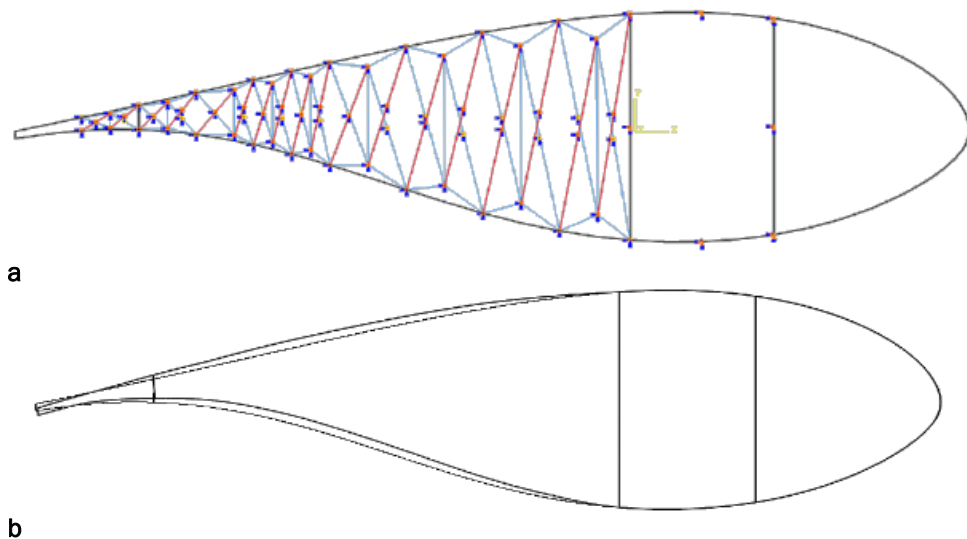
Radius of SMA Wire Actuators		$\Delta C_L$	
ID	[m]	for a.o.a. 0°	for a.o.a. 4°
r <sub>1</sub>	0.0005	-	-
r <sub>2</sub>	0.001	-	-
r <sub>3</sub>	0.0015	-	-
r <sub>4</sub>	0.002	-	-
r <sub>5</sub>	0.0025	0.05 up to k = 0.02	0.05 up to k = 0.02
r <sub>6</sub>	0.003	0.05 up to k = 0.05	0.05 up to k = 0.05

#### Model C2v2

This model is based on model C2v1, but it entails more actuator pairs implemented both in the region between web B and web C and between web C and tail V.



**b**  
**Figure 136: Model C2v2 (a) Implementation of morphing structure and (b) truss structure with the SMA actuators**



**b**  
**Figure 137: Model C2v2 (a) SMA actuators activated and (b) the undeformed and deformed airfoil in real scale for  $r = 0.003$  m**

Table 70: Model C2v2 Effect of SMA wire radius on structural stiffness

Radius of SMA Wire Actuators		Vertical Displacement
ID	Assigned Value [m]	Value [m]
r <sub>1</sub>	0.0005	-7.8191E-03
r <sub>2</sub>	0.001	-5.9235E-03
r <sub>3</sub>	0.0015	-5.3565E-03
r <sub>4</sub>	0.002	-5.1127E-03
r <sub>5</sub>	0.0025	-4.9846E-03
r <sub>6</sub>	0.003	-4.9080E-03

Table 71: Model C2v2 Numerical results of lower sma wire actuators activation

Radius of SMA Wire Actuators		Percent of Chord Length	Angle $\beta$	MVF	Maximum Stress (Actuators)	Maximum Stress (Composites)
ID	[m]	[%]	[°]		[Pa]	[Pa]
r <sub>1</sub>	0.0005	50	0.241	0.7199	2.5789E+08	4.4268E+07
r <sub>2</sub>	0.001	60	0.328	0.6725	2.5112E+08	9.6709E+07
r <sub>3</sub>	0.0015	60	0.366	0.6361	2.4590E+08	1.3373E+08
r <sub>4</sub>	0.002	60	0.399	0.6088	2.4197E+08	1.5877E+08
r <sub>5</sub>	0.0025	60	0.432	0.5872	2.3885E+08	1.7606E+08
r <sub>6</sub>	0.003	60	0.467	0.5688	2.3620E+08	1.8856E+08

Table 72: Model C2v2 Predicted  $C_L$  variation for each case study

Radius of SMA Wire Actuators		$\Delta C_L$	
ID	[m]	for a.o.a. 0°	for a.o.a. 4°
r <sub>1</sub>	0.0005	-	-
r <sub>2</sub>	0.001	-	-
r <sub>3</sub>	0.0015	-	-
r <sub>4</sub>	0.002	0.05 up to k = 0.02	0.05 up to k = 0.02
r <sub>5</sub>	0.0025	0.05 up to k = 0.06	0.05 up to k = 0.05
r <sub>6</sub>	0.003	0.05 up to k = 0.1	0.05 up to k = 0.1

### Interpretation of Analyses Results

The criteria on which the assessment of models is based are the same with the ones used to assess the models of concept 1. In Figure 138 the percentage of chord length with morphing capability at respect to the SMA wire radius is presented. From the aforementioned figure it is clear that the models of this concept achieve mobility of greater than 50% of chord length even by using wires with 0.5 mm radius. As the available data regarding variation of lift coefficient are limited to movement of a flap with length up to 50 % of the chord length the models chosen as most promising are C2v1 and C2v2.

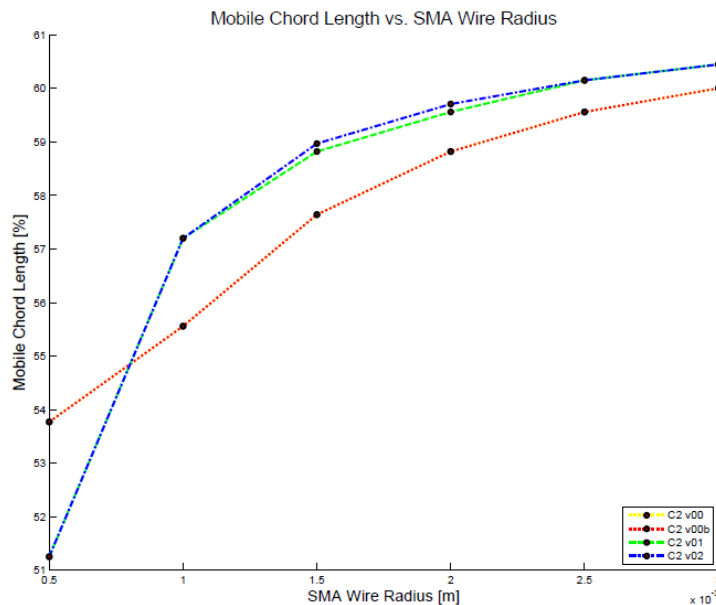


Figure 138: Concept 2 models chord length with morphing capability vs. sma wire radius for each model

Figure 139 presents the angular rotation  $\beta$  for each model versus the radius of the SMA wires. The response of model C2v0 and C2v0b stands out from the other models. It should be noted that red and yellow lines are identical and as a result it is safe to say that the difference in connections used in these models did not produce any difference regarding their response.

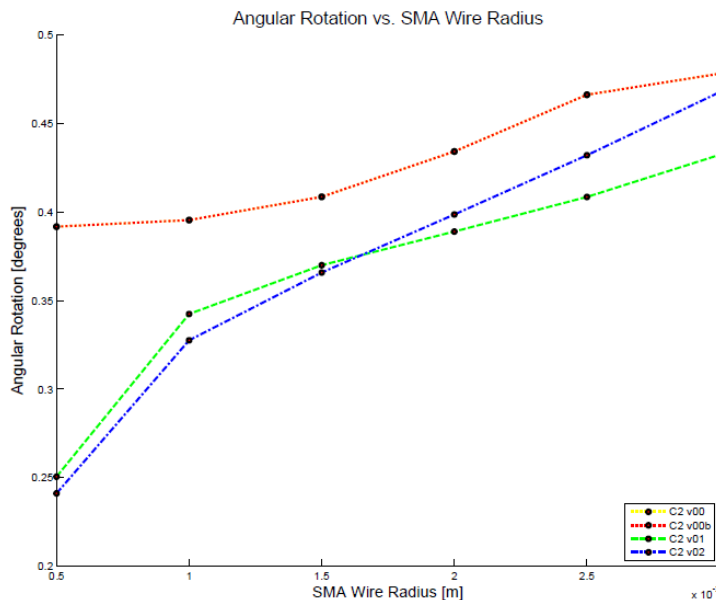


Figure 139: Concept 2 models angular rotation vs. SMA wire radius

The next variable that was studied for concept assessment is the maximum developed stress on the actuators and it is presented in Figure 140. Model C2v0b seems to have the optimum response among the models of this concept. Even when using wires with 0.5 mm radius the presented is less than 225 MPa. Although model C2v0b is by far the best option regarding developed stresses model C2v0 could be an alternative solution because of its simplicity when compared to model C2v0b. Similar are the results of martensitic volume fraction shown in Figure 141 but in this case the model that retains the higher value of martensitic volume fraction is the

best choice. For wires with radius 1.5 mm or less, the model C2v0 has the higher value of martensitic volume fraction while for radius greater than 1.5 mm model C2v2 is preferred.

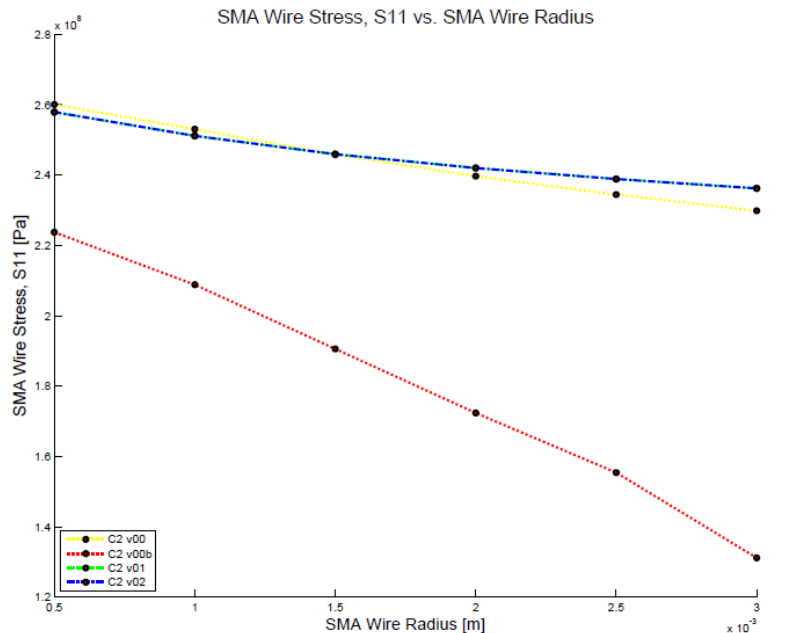


Figure 140: Concept 2 Models actuators' maximum stress vs. SMA wire radius

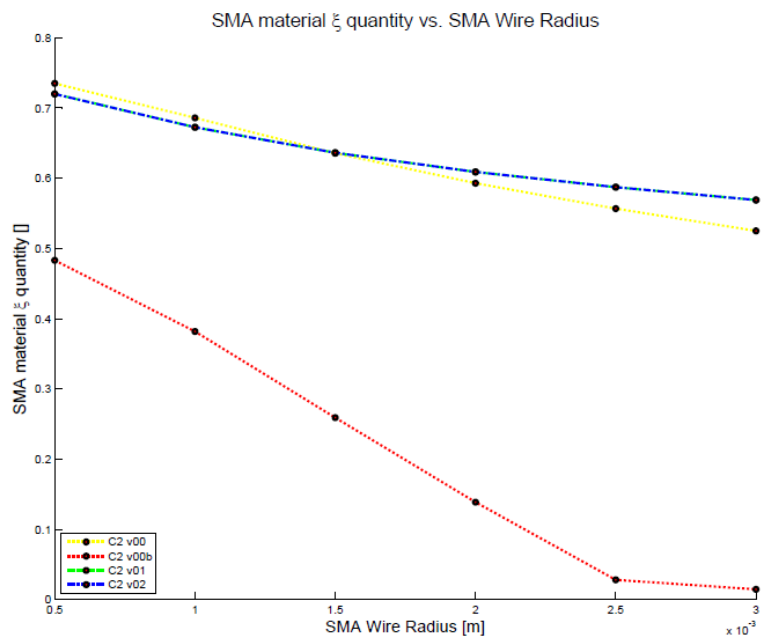


Figure 141: Concept 2 Models martensitic volume fraction vs. sma wire radius

Finally, in Figure 142 the increase in total structure stiffness is presented in terms of model's response when a mechanical point load is applied at the tip of the trailing edge. Until SMA wires radius reaches 1.5 mm an increase in structure's stiffness is noticed for every model. When radius is increased above 1.5 mm the variation in stiffness is saturated and can be almost negligible. In this concept models, like in first concept, the implementation of truss support structure and the antagonistic SMA wires increases the overall stiffness of the airfoil. Thus the need to address

changes in the configuration is essential to reduce the added weight, compensate the stiffness and optimize the structure.

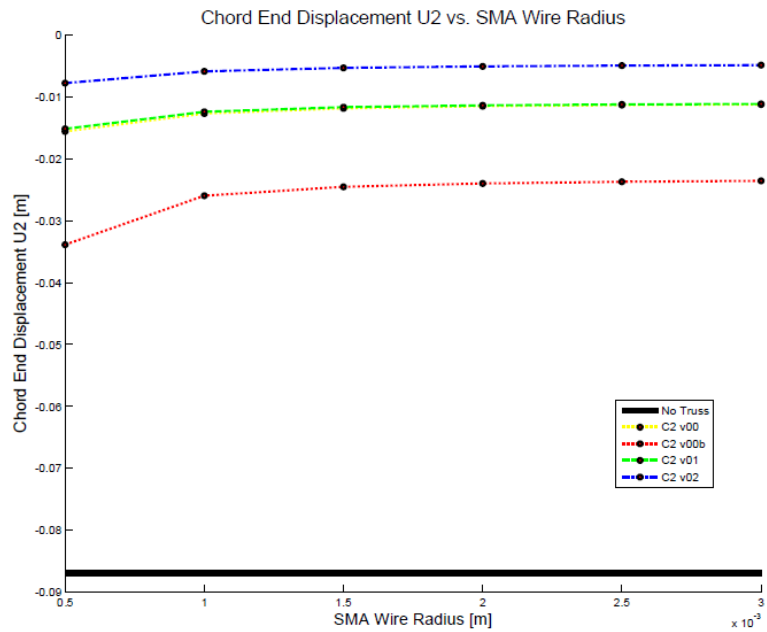
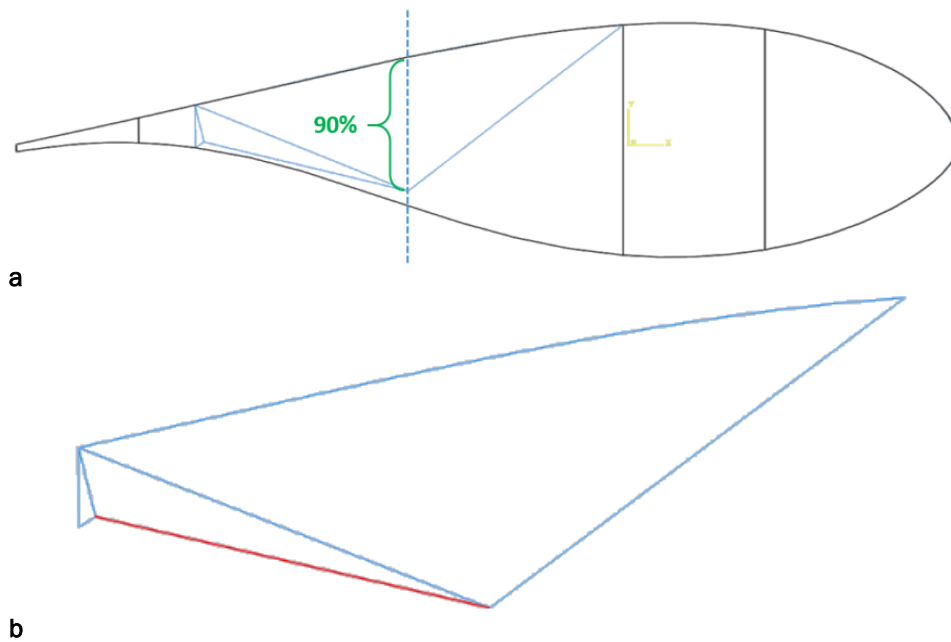


Figure 142: Concept 2 Models vertical displacement of chord end

**Concept Category 3**

**Model C3v0**

This model requires one SMA wire actuator to bend the airfoil. The wire is connected near web C and at a point in the middle of the distance between web B and web C with the rest of the airfoil. If an imaginary axis (dashed line in Figure 143 A) crosses the latter point and has direction parallel to vertical, Y, axis the distance of this point from the upper surface is 90 % of the distance between aerodynamic surfaces at this point.



**Figure 143: Model C3v0 (a) Implementation of morphing structure and (b) truss structure with the SMA actuators**

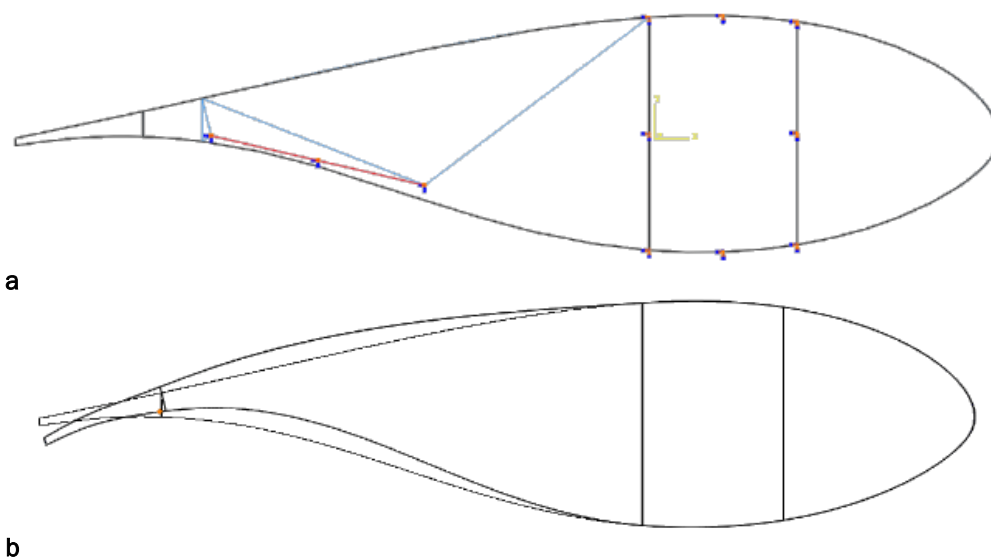


**Figure 144: Model C3v0 (a) SMA actuators activated and (b) the undeformed and deformed airfoil in real scale for  $r = 0.003$  m**

Table 73: Model C3v0 Effect of SMA wire radius on structural stiffness

Radius of SMA Wire Actuators		Vertical Displacement
ID	Assigned Value [m]	Value [m]
r <sub>1</sub>	0.0005	-3.1151E-02
r <sub>2</sub>	0.001	-2.3826E-02
r <sub>3</sub>	0.0015	-1.9964E-02
r <sub>4</sub>	0.002	-1.8026E-02
r <sub>5</sub>	0.0025	-1.6973E-02
r <sub>6</sub>	0.003	-1.6352E-02

Table 74: Model C3v0 Numerical results of lower SMA wire actuators activation

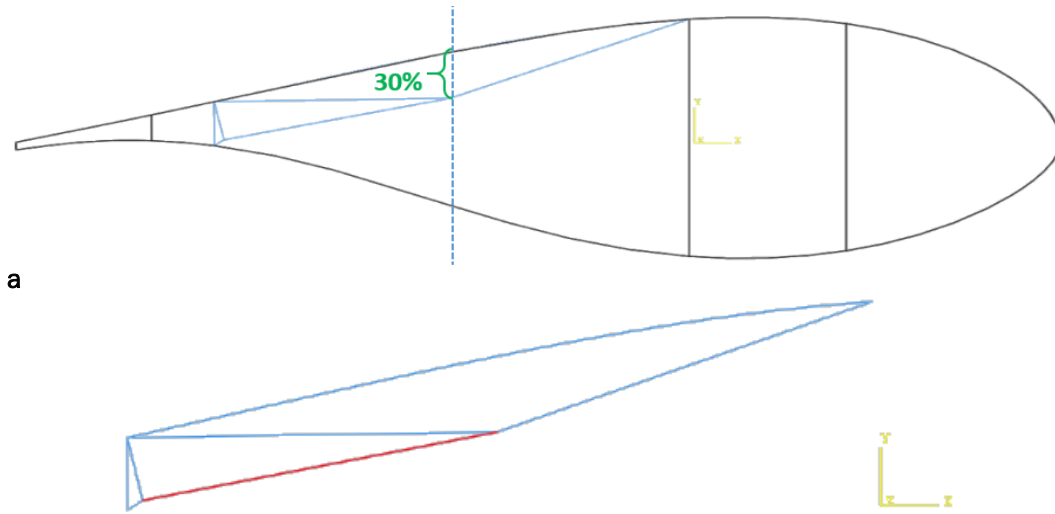
Radius of SMA Wire Actuators		Percent of Chord Length	Angle $\beta$	MVF	Maximum Stress (Actuators)	Maximum Stress (Composites)
ID	[m]	[%]	[°]		[Pa]	[Pa]
r <sub>1</sub>	0.0005	40	0.322	0.6740	2.5133E+08	2.7435E+07
r <sub>2</sub>	0.001	50	0.868	0.4595	2.2026E+08	9.6176E+07
r <sub>3</sub>	0.0015	60	1.524	0.1951	1.8092E+08	1.7775E+08
r <sub>4</sub>	0.002	60	2.001	0.0001	1.3588E+08	2.3733E+08
r <sub>5</sub>	0.0025	60	2.044	0.0001	8.8937E+07	2.4269E+08
r <sub>6</sub>	0.003	60	2.068	0.0001	6.2523E+07	2.4571E+08

Table 75: Model C3v0 Predicted  $C_L$  variation for each case study

Radius of SMA Wire Actuators		$\Delta C_L$	
ID	[m]	for a.o.a. 0°	for a.o.a. 4°
r <sub>1</sub>	0.0005	-	-
r <sub>2</sub>	0.001	0.1 up to k = 0.06	0.1 up to k = 0.05
r <sub>3</sub>	0.0015	0.15 up to k = 0.1	0.15 up to k = 0.02
r <sub>4</sub>	0.002	0.25 up to k = 0.02	0.2 up to k = 0.1
r <sub>5</sub>	0.0025	0.25 up to k = 0.03	0.25 up to k = 0.02
r <sub>6</sub>	0.003	0.25 up to k = 0.04	0.25 up to k = 0.02

#### Model C3v2

This model is based on the previous models with the difference lying on the fact that the support point for the right end of the SMA wire is positioned at 30% of the distance between the upper and lower aerodynamic surface.



**Figure 145: Model C3v2 (a) Implementation of morphing structure and (b) truss structure with the SMA actuators**

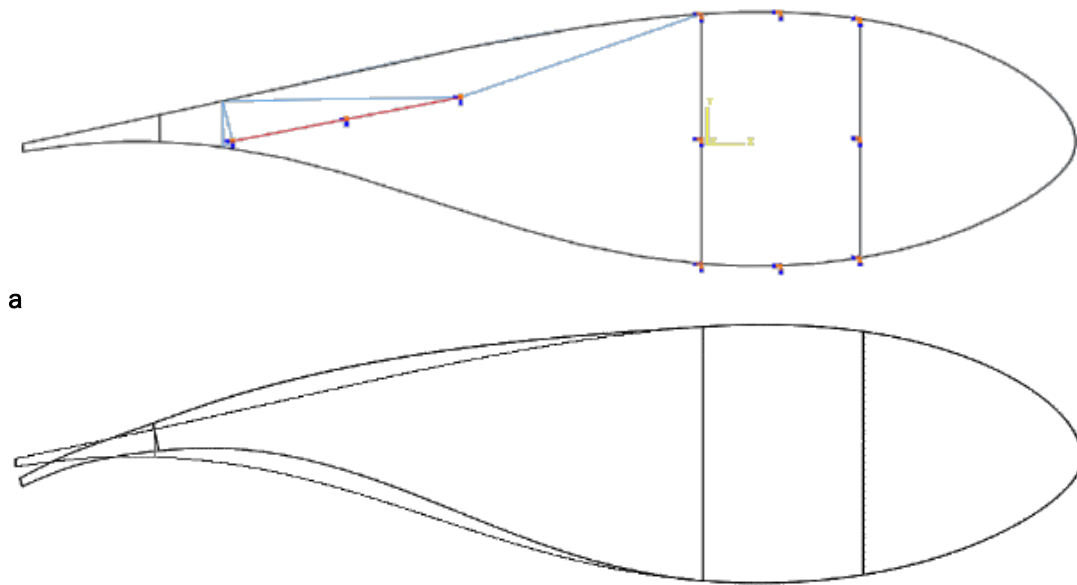


**Figure 146: Model C3v2 (a) SMA actuators activated and (b) the undeformed and deformed airfoil in real scale for  $r = 0.003$  m**

Table 76: Model C3v2 Effect of SMA wire radius on structural stiffness

Radius of SMA Wire Actuators		Vertical Displacement
ID	Assigned Value [m]	Value [m]
r <sub>1</sub>	0.0005	-3.0072E-02
r <sub>2</sub>	0.001	-2.2626E-02
r <sub>3</sub>	0.0015	-1.9133E-02
r <sub>4</sub>	0.002	-1.7478E-02
r <sub>5</sub>	0.0025	-1.6605E-02
r <sub>6</sub>	0.003	-1.6098E-02

Table 77: Model C3v2 Numerical results of lower SMA wire actuators activation

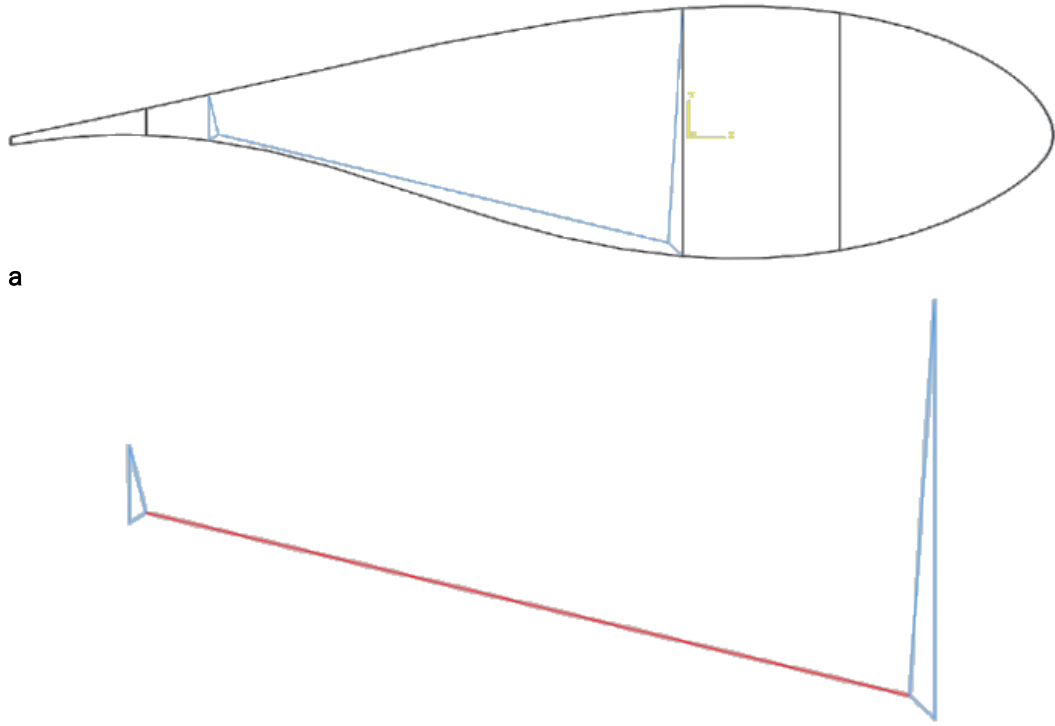
Radius of SMA Wire Actuators		Percent of Chord Length	Angle $\beta$	MVF	Maximum Stress (Actuators)	Maximum Stress (Composites)
ID	[m]	[%]	[°]		[Pa]	[Pa]
r <sub>1</sub>	0.0005	40	0.342	0.6526	2.4827E+08	2.9625E+07
r <sub>2</sub>	0.001	50	0.922	0.3946	2.1071E+08	1.0310E+08
r <sub>3</sub>	0.0015	60	1.563	0.0982	1.6618E+08	1.8295E+08
r <sub>4</sub>	0.002	60	1.801	0.0001	1.0872E+08	2.1277E+08
r <sub>5</sub>	0.0025	60	1.832	0.0001	7.0828E+07	2.1659E+08
r <sub>6</sub>	0.003	60	1.849	0.0000	4.9674E+07	2.1874E+08

Table 78: Model C3v2 Predicted  $C_L$  variation for each case study

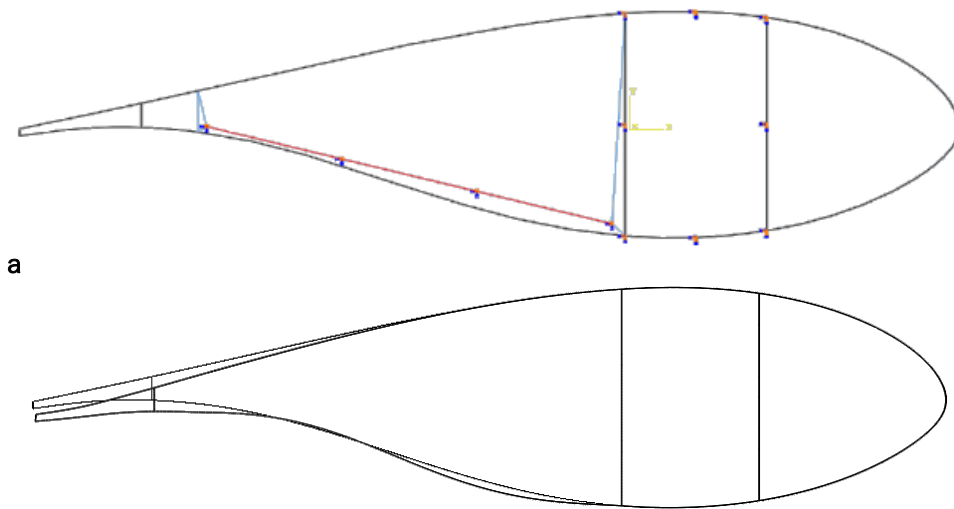
Radius of SMA Wire Actuators		$\Delta C_L$	
ID	[m]	for a.o.a. 0°	for a.o.a. 4°
r <sub>1</sub>	0.0005	-	-
r <sub>2</sub>	0.001	0.05 up to k = 0.09	0.05 up to k = 0.08
r <sub>3</sub>	0.0015	0.15 up to k = 0.1	0.15 up to k = 0.1
r <sub>4</sub>	0.002	0.2 up to k = 0.08	0.2 up to k = 0.06
r <sub>5</sub>	0.0025	0.2 up to k = 0.09	0.2 up to k = 0.07
r <sub>6</sub>	0.003	0.2 up to k = 0.09	0.25 up to k = 0.08

### Model C3v3

The presented model has a large SMA wire actuator and is located at the minimum possible distance from the lower aerodynamic surface.



**b**  
**Figure 147: Model C3v3 (a) Implementation of morphing structure and (b) truss structure with the SMA actuators**



**b**  
**Figure 148: Model C3v3 (a) SMA actuators activated and (b) the undeformed and deformed airfoil in real scale for  $r = 0.003$  m**

Table 79: Model C3v3 Effect of SMA wire radius on structural stiffness

Radius of SMA Wire Actuators		Vertical Displacement
ID	Assigned Value [m]	Value [m]
r <sub>1</sub>	0.0005	-4.1985E-02
r <sub>2</sub>	0.001	-4.1619E-02
r <sub>3</sub>	0.0015	-4.1142E-02
r <sub>4</sub>	0.002	-4.0657E-02
r <sub>5</sub>	0.0025	-4.0222E-02
r <sub>6</sub>	0.003	-3.9856E-02

Table 80: Model C3v3 Numerical results of lower SMA wire actuators activation

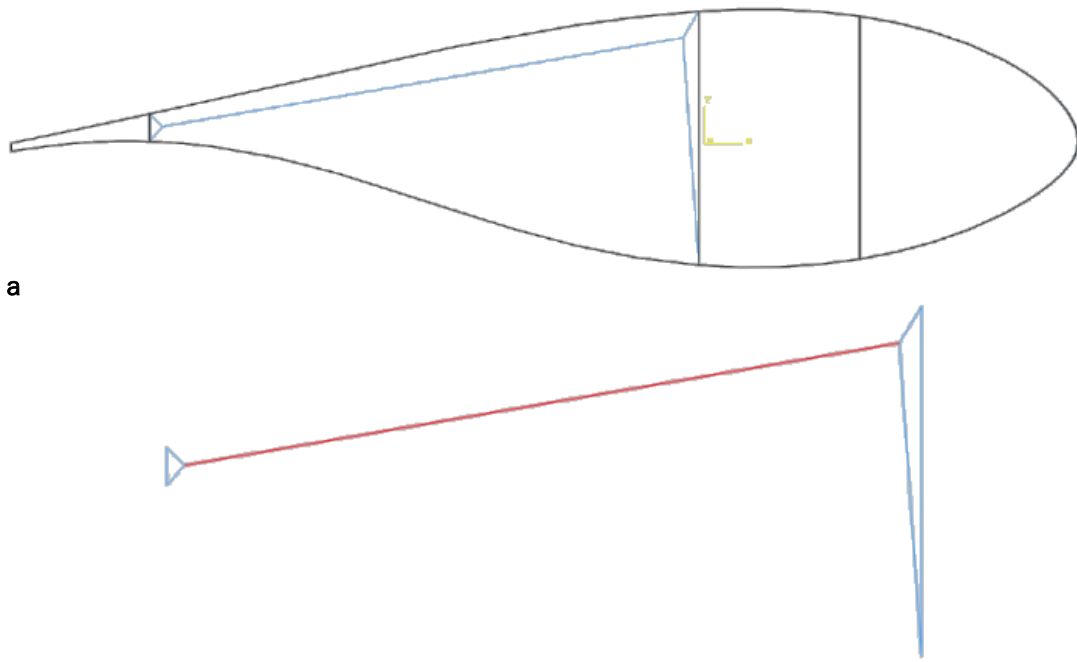
Radius of SMA Wire Actuators		Percent of Chord Length	Angle $\beta$	MVF	Maximum Stress (Actuators)	Maximum Stress (Composites)
ID	[m]	[%]	[°]		[Pa]	[Pa]
r <sub>1</sub>	0.0005	0	0.000	0.7494	2.6208E+08	5.0230E+06
r <sub>2</sub>	0.001	10	0.728	0.7244	2.5853E+08	1.9821E+07
r <sub>3</sub>	0.0015	60	0.399	0.6842	2.5279E+08	4.3609E+07
r <sub>4</sub>	0.002	60	0.654	0.6305	2.4510E+08	7.5166E+07
r <sub>5</sub>	0.0025	60	0.962	0.5657	2.3574E+08	1.1296E+08
r <sub>6</sub>	0.003	60	1.307	0.4923	2.2506E+08	1.5530E+08

Table 81: Model C3v3 Predicted  $C_L$  variation for each case study

Radius of SMA Wire Actuators		$\Delta C_L$	
ID	[m]	for a.o.a. 0°	for a.o.a. 4°
r <sub>1</sub>	0.0005	-	-
r <sub>2</sub>	0.001	-	-
r <sub>3</sub>	0.0015	-	-
r <sub>4</sub>	0.002	0.05 up to k = 0.1	0.05 up to k = 0.1
r <sub>5</sub>	0.0025	0.1 up to k = 0.1	0.1 up to k = 0.1
r <sub>6</sub>	0.003	0.15 up to k = 0.06	0.15 up to k = 0.05

#### Model C3v5

The last model is nearly the mirrored layout of model C3v3. The actuator is almost parallel and near to the upper aerodynamic surface while its length has been increased by extending the left end of the actuator up to web C.



**Figure 149: Model C3v5 (a) Implementation of morphing structure and (b) truss structure with the SMA actuators**

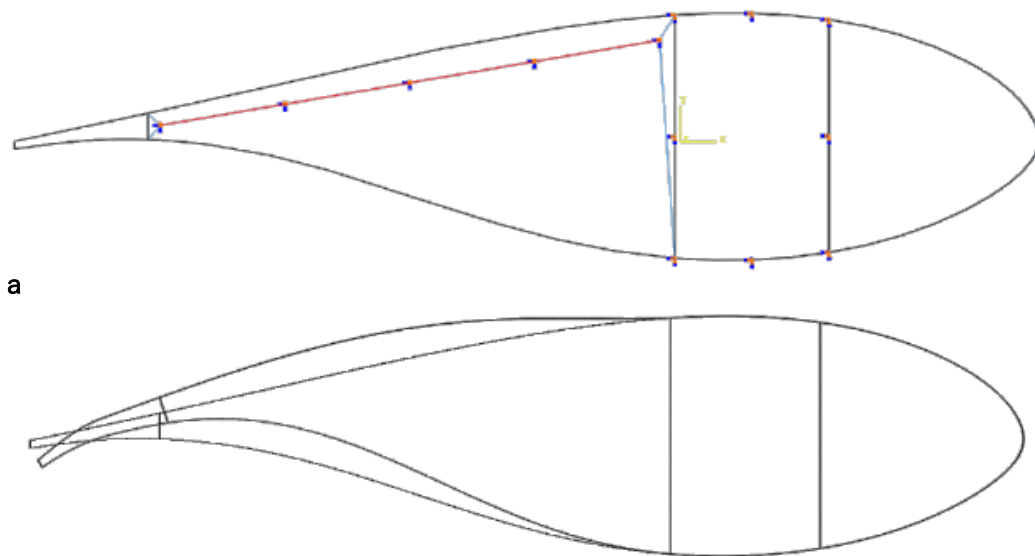


**Figure 150: Model C3v5 (a) SMA actuators activated and (b) the undeformed and deformed airfoil in real scale for  $r = 0.003$  m**

Table 82: Model C3v5 Effect of SMA wire radius on structural stiffness

Radius of SMA Wire Actuators		Vertical Displacement
ID	Assigned Value [m]	Value [m]
r <sub>1</sub>	0.0005	-4.3173E-02
r <sub>2</sub>	0.001	-4.2480E-02
r <sub>3</sub>	0.0015	-4.1650E-02
r <sub>4</sub>	0.002	-4.0881E-02
r <sub>5</sub>	0.0025	-4.0250E-02
r <sub>6</sub>	0.003	-3.9756E-02

Table 83: Model C3v5 Numerical results of lower SMA wire actuators activation

Radius of SMA Wire Actuators		Percent of Chord Length	Angle $\beta$	MVF	Maximum Stress (Actuators)	Maximum Stress (Composites)
ID	[m]	[%]	[°]		[Pa]	[Pa]
r <sub>1</sub>	0.0005	0	0.000	0.7457	2.6156E+08	1.7725E+07
r <sub>2</sub>	0.001	50	0.323	0.7102	2.5651E+08	6.9533E+07
r <sub>3</sub>	0.0015	50	0.628	0.6538	2.4844E+08	1.5153E+08
r <sub>4</sub>	0.002	60	1.020	0.5799	2.3780E+08	2.5785E+08
r <sub>5</sub>	0.0025	60	1.474	0.4930	2.2517E+08	3.8149E+08
r <sub>6</sub>	0.003	60	1.965	0.3976	2.1117E+08	5.1519E+08

Table 84: Model C3v5 Predicted  $\Delta C_L$  variation for each case study

Radius of SMA Wire Actuators		$\Delta C_L$	
ID	[m]	for a.o.a. 0°	for a.o.a. 4°
r <sub>1</sub>	0.0005	-	-
r <sub>2</sub>	0.001	-	-
r <sub>3</sub>	0.0015	0.05 up to k = 0.1	0.05 up to k = 0.1
r <sub>4</sub>	0.002	0.1 up to k = 0.1	0.1 up to k = 0.1
r <sub>5</sub>	0.0025	0.15 up to k = 0.1	0.15 up to k = 0.1
r <sub>6</sub>	0.003	0.25 up to k = 0.02	0.25 up to k = 0.1

### Interpretation of Analyses Results

As it can be seen in Figure 151, the percentage of chord length with morphing capability is almost fixed and exerts 50 % for all models with radius of the SMA wire equal to 2 mm or larger. Because the data of the charts relating the flap length and angular rotation are limited up to 50 % it is safe to assume that the maximum wire radius that gives the maximum morphing portion is the one of 1.5 mm. The models that have the optimum response regarding this criterion are C3v1, C3v2 and C3v4.

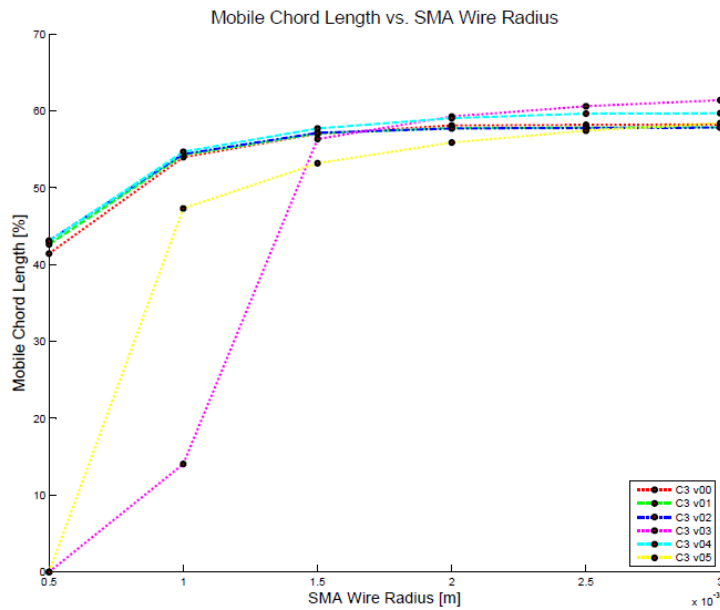


Figure 151: Concept 3 Models chord length with morphing capability vs. SMA wire radius for each model

The next criterion considered is the angular rotation of the morphed airfoil. From Figure 152 it can be derived that most of the models have a different response when the SMA actuator is activated. As radius of the actuator increases model C3v4 has the most abrupt change followed by C3v1 and C3v0.

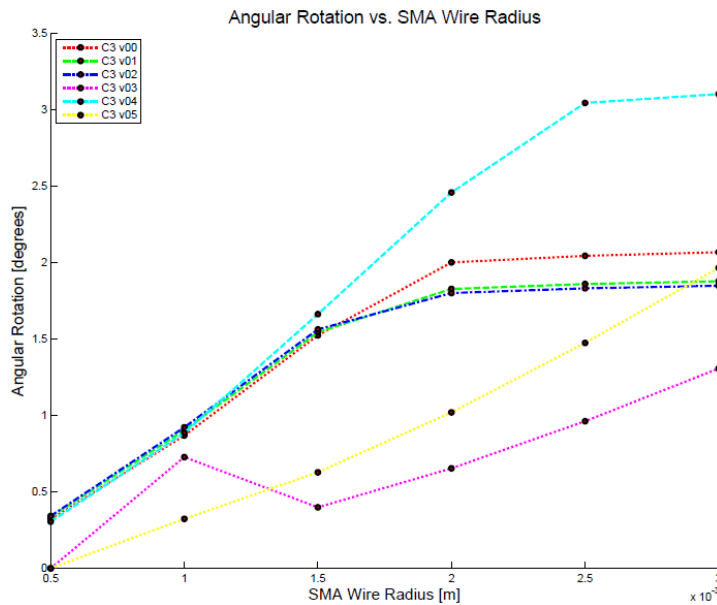


Figure 152: Concept 3 Models angular rotation vs. SMA wire radius

Regarding the maximum stress of the actuators at the end of each simulation run, it can be seen from Figure 153 that even when using actuators with radius of 0.5 mm the developed stress is below 270 MPa. As the radius increases the most intense decrease in stress is presented by models C3v2, C3v1 and C3v0.

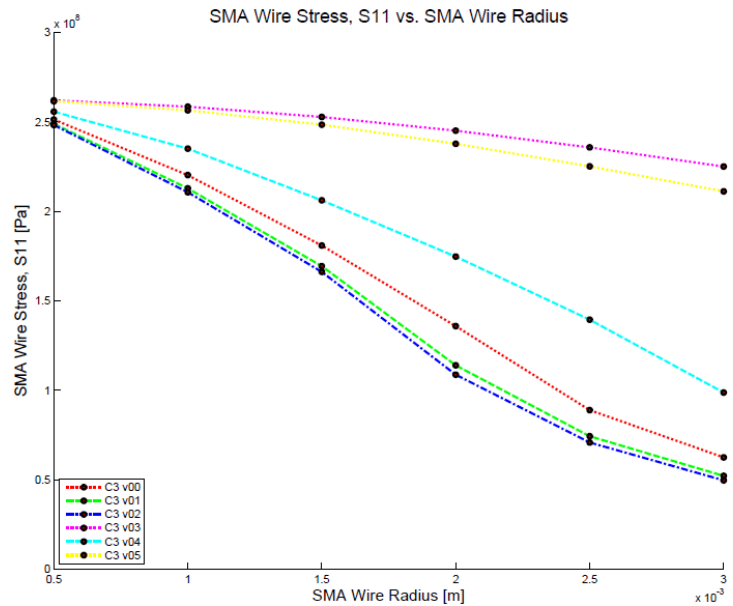


Figure 153: Concept 3 Models actuators' maximum stress vs. SMA wire radius

From Figure 154 it can be assumed that actuators of all models tend to have a substantial decrease in the martensitic volume fraction as the radius of the wire increases. In some models from radii of 2 mm and greater the martensitic volume fraction at the end of the analysis is zero. In this case the beginning of the transformation during cooling will require more time and a much higher temperature difference. Thus, regarding this criterion models C3v3 and C3v5 are selected as well as model C3v4 if the radius of actuator used is under 2 mm.

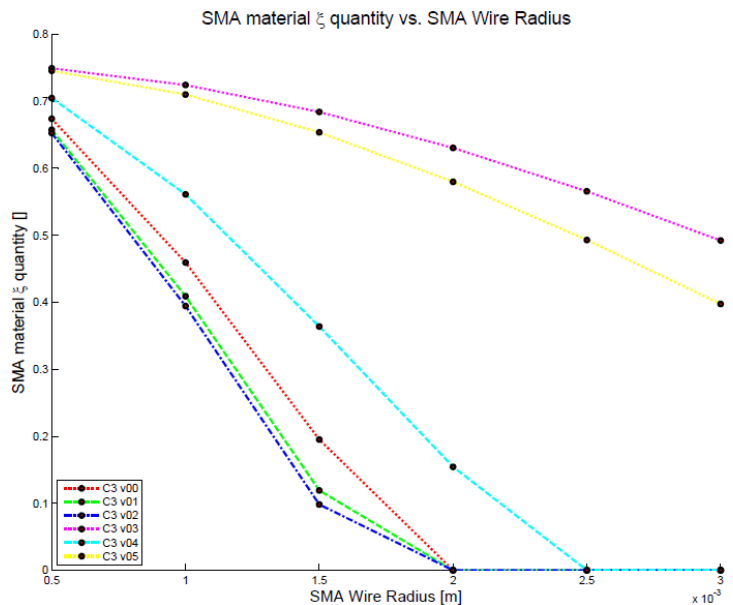


Figure 154: Concept 3 Models martensitic volume fraction vs. SMA wire radius

Finally, the vertical displacement of chord length with respect to the SMA wire radius is presented in Figure 155. Here, although the truss structures of the models are simple and have far less elements than the models of the previous concepts again there is a substantial increase in the overall stiffness of the structure.

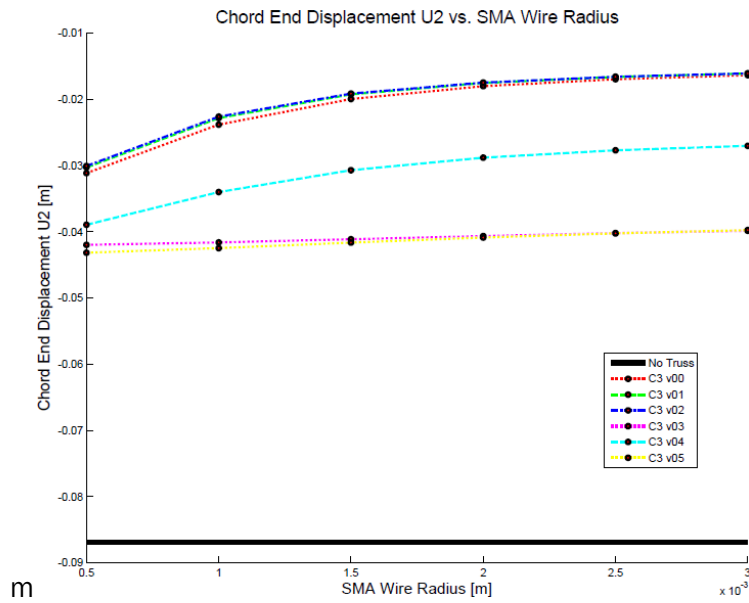


Figure 155: Concept 3 Models vertical displacement of chord end